HAL
open science

Fundamental study of nanofluidic transport : or How to reinvent the colander

Sophie Marbach

To cite this version:

Sophie Marbach. Fundamental study of nanofluidic transport : or How to reinvent the colander. Data Analysis, Statistics and Probability [physics.data-an]. Université Paris sciences et lettres, 2018. English. NNT : 2018PSLEE007 . tel-01877361

HAL Id: tel-01877361

https://theses.hal.science/tel-01877361v1

Submitted on 19 Sep 2018

HAL is a multi-disciplinary open access archive for the deposit and dissemination of scientific research documents, whether they are published or not. The documents may come from teaching and research institutions in France or abroad, or from public or private research centers.

L'archive ouverte pluridisciplinaire **HAL**, est destinée au dépôt et à la diffusion de documents scientifiques de niveau recherche, publiés ou non, émanant des établissements d'enseignement et de recherche français ou étrangers, des laboratoires publics ou privés.

THÈSE DE DOCTORAT

de l'Université de recherche Paris Sciences et Lettres
PSL Research University

Préparée à l'École Normale Supérieure de Paris

Étude fondamentale du transport nanofluidique
–
Comment réinventer la passoire ?

École doctorale n°564

PHYSIQUE EN ÎLE DE FRANCE

Spécialité PHYSIQUE STATISTIQUE ET HYDRODYNAMIQUE

COMPOSITION DU JURY :

M Jean-François Joanny
ESPCI, Paris, Président

M Jean-François Dufrêche
Univ. Montpellier, Rapporteur

M Peter Holdsworth
ENS, Lyon, Rapporteur

Mme Elisabeth Charlaix
Univ. Grenoble-Alpes, Examinateur

Mme Leticia Cugliandolo
Univ. Pierre et Marie Curie, Examinateur

M Olivier Pouliquen
Univ. Aix-Marseille, Examinateur

M David Dean
Univ. Bordeaux, Invité

M Lydéric Bocquet
ENS, Paris, Directeur de thèse

Soutenue par **Sophie Marbach**
le 15 Juin 2018

Dirigée par **Lydéric Bocquet**

ENS ÉCOLE NORMALE SUPÉRIEURE | PSL RESEARCH UNIVERSITY PARIS

Thèse de doctorat de
l'Université de recherche Paris Sciences et Lettres

Spécialité: Physique Statistique et Hydrodynamique

Fundamental Study of Nanofluidic Transport

or

How to reinvent the colander ?

---

présentée par

Sophie Marbach

afin d'obtenir le grade de
Docteur de l'Université de recherche Paris Sciences et Lettres

dirigée par
Lydéric Bocquet

Soutenance prévue le 15/06/2018 devant le Jury composé de

Pr. Jean-François Joanny	Président
Pr. Jean-François Dufrêche	Rapporteur
Pr. Peter Holdsworth	Rapporteur
Pr. Elisabeth Charlaix	Examinateur
Pr. Laetitia Cugliandolo	Examinateur
Pr. Olivier Pouliquen	Examinateur
Pr. Lydéric Bocquet	Directeur de Thèse
Pr. David Dean	Invité

Le savant n'étudie pas la nature parce que cela est utile; il l'étudie parce qu'il y prend plaisir et il y prend plaisir parce qu'elle est belle. Si la nature n'était pas belle, elle ne vaudrait pas la peine d'être connue, la vie ne vaudrait pas la peine d'être vécue. Je ne parle pas ici, bien entendu, de cette beauté qui frappe les sens, de la beauté des qualités et des apparences; non que j'en fasse fi, loin de là, mais elle n'a rien à faire avec la science; je veux parler de cette beauté plus intime qui vient de l'ordre harmonieux des parties, et qu'une intelligence pure peut saisir. – Henri Poincaré

Main table of contents

Acknowledgments **1**

Introduction **7**

1 Filtration today **7**
1 Back to the future : the origins of filtration 7
2 The tight link between osmosis and filtration 10
3 First developments of reverse osmosis filtering membranes 13
4 (Nano)Filtration today 14
5 What is the cost of filtration? 15
6 The limits of traditional filtration 16

2 Harnessing the nanoscale **19**
1 Why turn to fluids at the nanoscales ? 19
2 Nanofluidics: where new properties arise in fluids 20
3 Nanofluidics: a technological challenge 21
4 Nanofluidics : the future of filtration ? 23

3 New inventions with existing tools **24**
1 Bio-inspired materials 24
2 Geometrical and thermodynamic ideas 25
3 Inspiring from the Rules of Nature 26

4 Fluid transport at the nanoscale and beyond **26**

I Fundamental properties of fluids at the nanoscale **31**

Introduction **33**

1 A brief history of slippage **34**

2 Measuring minute flows through nanoscale pores **38**
1 The Landau-Squire jet : an indirect method to measure flows through nanoscale pores . . . 38
2 Evaluating the slip length in nanotubes . . . 40
3 The Landau-Squire plume : the counterpart with dyes . . . 44

3 Slippage in nanotubes **46**
1 Slippage depends on the topological nature of the material . . . 46
2 Slippage depends on the atomistic nature of the material . . . 47

4 Mathematical formulations of slip boundary conditions **49**
1 The friction or partial slip boundary condition . . . 49
2 A new paradox with irrotational boundary condition . . . 51
3 Mechanical energy dissipation between the fluid and an object . . . 52
4 Resolution of the irrotational boundary paradox . . . 55

Conclusion **56**
The multiple consequences of slippage at the interface . . . 56
What are the consequences for filtration? . . . 57

II The Osmotic Exchanger **59**

Introduction **61**

1 A clever filtration engine : Harnessing osmosis **63**
1 The serpentine geometry . . . 63
2 Transport equations and osmotic fluxes . . . 64
3 Results: spatial distributions, fluxes and optimal separation ability . . . 65

2 Hope for an efficient biomimetic filtration device **68**
1 Energetic cost for osmotic exchanger . . . 68
2 Power comparison to traditional sieving processes . . . 69

3 Experimental future of the kidney on a chip **71**
1 State-of-the-art experiment and challenges . . . 72
2 Experimental future explorations . . . 74

4 Understanding kidney filtration in the animal kingdom **75**
1 The mammalian kidney . . . 75
2 Desert birds . . . 76
3 Sharks and rays . . . 77

Conclusion **78**

III Out of equilibrium water transport **81**

Introduction **83**

1 Active selection across nanodoors **85**
1 The framework for permeance of active nano-pores 86
2 Consequences on selectivity 88
3 The experimental nanodoor 90

2 Active selection across nanochannels **95**
1 Do fluctuations enhance or decrease transport ? 95
2 Renormalization of transport due to pore shape fluctuations 96
3 Consequences from nano to milli fluidics 98

Conclusion **104**

IV New theories for nanoscale transport beyond equilibrium **107**

Introduction **109**

1 The kinetic approach of osmosis **111**
1 The limitation of the van 't Hoff theory 111
2 The Kedelm–Katchalsky framework and reflection coefficient 111
3 A kinetic approach to osmosis 112

2 Osmosis beyond the linear concentration regime **114**
1 Osmotic pressure at high concentrations 114
2 Diffusio-osmosis at high concentrations 115
3 Coupled osmotic effects 117

3 Osmosis out of equilibrium **118**

Conclusion **119**

Main conclusion and perspectives **121**

List of publications **124**
Active osmotic exchanger for efficient nanofiltration inspired by the kidney, Marbach, S. and Bocquet, L., Phys. Rev. X, **6**, 031008 (2016) 126
Massive radius-dependent flow slippage in carbon nanotubes, Secchi, E., Marbach, S., Nigués, A. , Stein, D., Siria, A. and Bocquet, L., Nature, **537**, 210 (2016) 136

Osmotic and diffusio-osmotic flow generation at high solute concentration. I. Mechanical approaches, Marbach, S., Yoshida, H. and Bocquet, L., J. Chem. Phys., **146**, 194701 (2017) 140
Osmotic and diffusio-osmotic flow generation at high solute concentration. II. Molecular dynamics simulations, Yoshida, H., Marbach, S. and Bocquet, L., J. Chem. Phys., **146**, 194702 (2017) 148
The Landau–Squire plume, Secchi, E., Marbach, S., Nigués, A. , Siria, A. and Bocquet, L., J. Fluid Mech., **826** (2017) 157
Active sieving across driven nanopores for tunable selectivity, Marbach, S. and Bocquet, L., J. Chem. Phys., **147**, 154701 (2017) 168

Appendices and references **181**

Methods **181**
1 Analytical Methods 181
2 Numerical Methods 189
3 Experimental Methods 197

References **201**

Acknowledgments

This dissertation would not have been fully complete without the constructive contributions of Elisabeth Charlaix, Leticia Cugliandolo, David Dean, Jean-François Dufrêche, Peter Holdsworth, Jean-François Joanny and Olivier Pouliquen. I am honored and pleased that they agreed to constitute my doctoral jury. I would like to thank in particular Jean-François Dufrêche and Peter Holdsworth who were in charge of reading through my entire manuscript and who brought forward a number of relevant comments and interrogations.

I am very grateful to and would like to pay tribute to my advisor, Lydéric Bocquet. I have acquired so much knowledge from his tutorship, and he has been of unwavering support in a variety of projects. We did have an infinite number of exciting discussions – see below in Fig. 1 – and there are a great number of things that I would like to say, but I must not spread out too much. There is one thing that I have learned and wish to highlight: *the great necessity of being humble, when faced to any question, from anyone* – or to put it in other words – really there are no good or bad questions, any question may lead to reasoning, learning, new ideas, and is never a waste of time (obviously to a certain extent).

The team I performed my PhD work in would not be complete without the presence of Alessandro Siria. I had the opportunity to work with him on the nanotube project, but also on the nanodoors. Alessandro brings a constant warmth and a precious knowledge to the team projects.

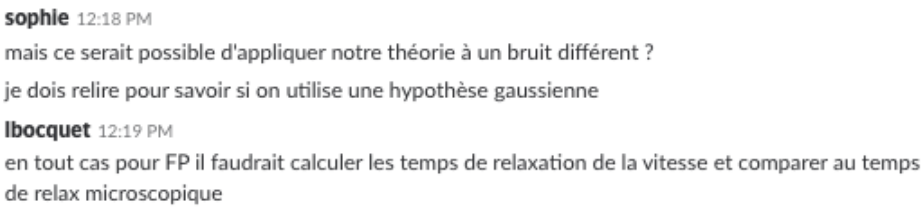

Fig. 1: Conversaton history

The entire lab was very helpful during these three years. I would like to thank Nora Sadaoui, Fabienne Renia, Annie Ribaudeau and Benoît Paulet for their patience, especially when I would ask for refunds sometimes in three different currencies at the same time. They have helped me organize the venue of my jury, and obviously I appreciate their kindness towards me. Thanks to Zaïre Dissi and Frédéric Desprez for bringing me constant support

on up-to-date software. Thanks to Didier Courtiade, Catherine Gripe, and Célia Ruschinzik for opening my lab door at least a hundred times when I would have forgotten my badge somewhere, and for moving the "marble" (a tetris game with a marble table of at least 500 kilograms). Thanks to José Palomo and Michael Rosticher for their help in the clean room and for discussing the fabrication part of the nanodoors.

It is time to thank all of the people I have closely collaborated with. They have greatly contributed to extend my scientific world and imagination. I have started my PhD with a project with Eleonora Secchi who was an inspiring colleague, extremely precise, rigorous, and from whom I have learned so much. Thanks to Derek Stein, who has added a lot of enthusiasm to the nanotube project. Thanks to Antoine Niguès as well, who has helped me substantially to try and shake these nanodoors up, and who is always good humored and happy to taste cakes. I would like to thank Hiroaki Yoshida, with whom I improvised a very intriguing project in a couple of months, and who taught me nearly everything I know on the LAMMPS software (that enabled me to check some very important things on the fluctuating walls project!), and last but not least, was also a lively addition to the team. Thanks to Nikita Kavokine, who is working on a thrilling topic and that I try to support by transferring my knowledge in simulations and analytics, and with whom I learn a lot as well. One of the most fruitful collaborations of my PhD was the one with David Dean, and I would like to thank him for his patience and his very productive work on this "fluctuating" project. We did not have a very precise idea of the question to start with, but we ended up with a very nice question solved and more questions to come. I am extremely glad of what we achieved together.

The team I worked in, the Micromegas Team, on the whole, is an extraordinary group, and I have met there incredible people : Jean-François Rupprecht (and his surprising but good jokes), Elisa Tamborini (who taught me the secret of membranes), Vojtech Kaiser (for the advice on sickness and garlic), Benoit Laborie (who trained me to experimental microfluidics), Jean Comtet (who "endured" with me to be the first generation of PhD students of the team at ENS), Luca Canale (for his general enthusiasm, his generous help on experiments, and all the great advice on food!), Anthony Poggioli (for the jokes as well), Adrien Benusiglio (and the lovely smile of Léon !), Joshua McGraw (who helped me figure out how to unglue carbon from the nanodoors), Antoine Lainé (for our shared vital need of the afternoon snack), Timothée Mouterde (for his overwhelming curiosity) and all of the new additions to the group for their enthusiasm : Alice Marcotte, Amin M'Barki and Christie Cherian. Finally, I would like to thank from the bottom of my heart, Laetitia Jubin, who was a precious support when lab life could become stressful, who is an impressive mind, and a great friend.

From time to time I was lucky enough to be able to pursue a collaboration with the "biophysics and morphogenesis" group in Germany, directed by Karen Alim. I went several times there. Each visit I did was always very relaxing and helped me generate even more creativity. I am indebted to Karen for inviting me so many times and for making these days so rich in ideas and experience. The "biophysics and morphogenesis" group is always very welcoming and lively, and I would like to thank especially one of them, Mirna Kramar, always

so generous and bright.

I had the chance to meet and spend time with several inspiring minds (both intellectually and personally) during my PhD. In this regard I would like to thank Benjamin Rotenberg, Marie-Laure Bocquet, Marie-Caroline Jullien, Stéphanie Descroix.

I would like to thank the CFM foundation who supported me financially, especially Marc Potters and Jean-Philippe Bouchaud, for their general interest, and the other PhD students who are inspiring. I would also like to thank the l'Oréal-UNESCO foundation for women in science, for it's support and the opportunity it gave me to meet inspiring and extraordinary women.

I must make a break and thank Shakira dressed up in Gazelle in Zootopia, for singing the dignified theme that could help any PhD student "*I won't give up, no I won't give in, Till I reach the end,* ***And then I'll start again***" – Try Everything.

Apart from the PhD life, hopefully friends are always there to increase the moments of joy and happiness, and I will name here especially those who have shared intimate links with my PhD: obviously the top scientific women of the DJFP : Lauriane Contamin, Marylou Gabrié, Danijela Markovic; William Legrand who had the initiative, the will and the brilliant idea to organize the Thésarium gustatifs (subformal gatherings of PhD students and a great amount of food to discuss one PhD topic) and who had the kindness to involve me; Amaury Hayat who allows me to talk endlessly of the research world and of what I do; and all the others for their support and their friendship: Sophie, Ariane, France, Aude N., Aude D., Marie D., Macha, Mathilde B., Mathilde L.,Quentin, Maxence, Marie B, Léa, Pierre, Pablo, Margaux, Paul-Hervé...*

My parents always believed in me and most importantly always helped me to achieve the projects I wanted to pursue so badly. During a PhD, one must be armed with patience and a love even stronger to support someone when one does not understand what she does ! They taught me the love of sharing and communicating with people who do not speak my mother tongue, and today that is part of my daily life, and I am very grateful. During my PhD I enjoyed several special moments with my big brother, and I would like to thank him for trusting me enough to speak during numerous lunch and snack times of boundary conditions in the Navier-Stokes equations. I also am grateful that he invited me to join a conference with him in les Houches – one of the most beautiful places in France.

Recently I realized that I had been using solely for my own work the analogy of the kitchen colander, when actually not only reverse osmosis membranes may benefit from this comparison. Zeolites, among other nanoporous materials with exotic frameworks, studied in particular by non other than the love of my life, Romain, may also be described by a colander. I am extremely grateful for his unwavering presence and support during those three years. I am indebted to him for listening to me blabber about, for the endless debates with pen and

*This list is obviously not full !

paper, for collecting and feeding all the best ideas, and all the worst. Today I am certain that two people who master the concept of the colander so well may only sustainably cook good food – if only we do not forget the pasta in the pan when we will draw again crystal meshes on the cooking plan.

Introduction

Filtration there and back again

Filtering specific molecules is a challenge faced for several vital needs: from biomedical applications like dialysis to the intensive production of clean water. The domain has been boosted over the last decades by the possibilities offered by nanoscale materials. Filtration is however always designed according to a sieving perspective: a membrane with small and properly decorated pores allows for the selection of the targeted molecules. This inevitably impedes the flux and transport, making separation processes costly in terms of energy.

Here I review the current status and performances of filtration with a very personal view. The reader is referred to the following books and article reviews for more information [1–4]. Then we introduce several innovative approaches to separation and filtration. We draw inspiration from biological systems (human kidney, aquaporins) and rationalize some new concepts for sieving. All these principles could be readily mimicked using existing technologies to build artificial dialysis devices or alternatives for advanced water recycling.

Chapter 1: Filtration today

1 Back to the future : the origins of filtration

Definition and etymology of filtration The definition from the french dictionnary for the noun *filtre* (*filter* in english) reads " Corps poreux (feutre, papier, charbon, etc.) au travers duquel on fait passer une substance liquide, gazeuse ou corpusculaire (la lumière, le courant électrique), pour la clarifier, l'épurer ou en séparer certains éléments." [5]* I find this definition somehow enlightning because it highlights some of the constitutive issues that we struggle with in the physics of filtration: firstly it defines the filter specifically by a porous material – highlighting that the filter is trully concieved as a sieve with holes and secondly it broadens the range of applications, talking more generally of separation. As is explained in [3], strictly speaking filtration implies *separation* of specific species, but *separation* does not necessarily imply *filtration*. Indeed species can be separated readily with electrical gradients or other means, not necessarily using an external boundary like a *filter*.

Similar definitions are found in english dictionnaries. According to the Thesaurus dictionnary of english [6], *to filter* means "to remove by the action of a filter", and a *filter* is "any substance, as cloth, paper, porous porcelain, or a layer of charcoal or sand, through which liquid or gas is passed to remove suspended impurities or to recover solids". Actually, *filter*

*Porous material (felt, paper, carbon, etc.) through which is passed any liquid, gas or corpuscular matter (light, electric current) to clarify, purify or separate some elements.

(or *filtre* in French – these words are trully transparent) comes from the Middle Ages Latin word *filtrum*. *Filtrum* does not in itself have a proper definition but is associated with "lana coactalis" (felt, or litterally "treaded hair fabric"), "centones" (something like a patchwork), or "fimbria" (a piece of cloth) – precisely the material that served to make the first filters. A passive, inert and porous materials (with very small holes) [7]*. In fact the word comes from a late latinization of a Germanic word, and this explains why the word is only defined by equivalent words, that describe its purpose. The concept of filtration thus inherits from the idea of the sieve with small holes to separate things – typically like the strainer used to separate pasta and water – and this dates back at least to the Middle Ages.

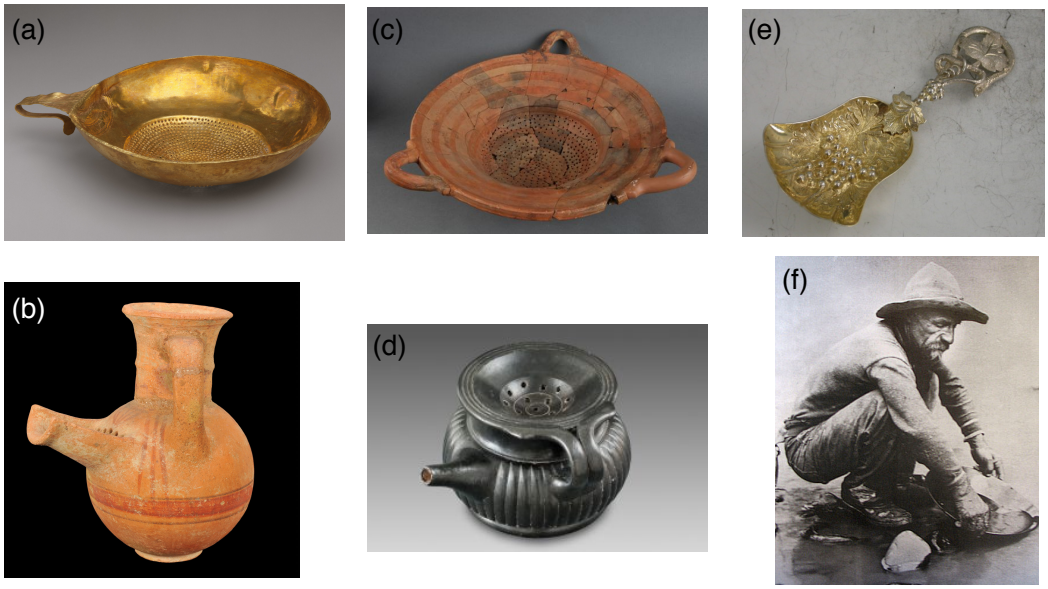

Fig. 1.1: **The strainer across ages**: (a) Egypt, Gold, 1279–1213 B.C., 12 cm, (Credits: Theodore M. Davis Collection, 1915) - MET museum, New-York; (b) Hebron, Iron Age ca. 800 B.C., strainer jug intended to filter a liquid - Aphrodite Ancient Art; (c) Lydia, Ceramic, mid-sixth century B.C., 35 cm, large strainer with three handles - Archeological Museum of Manisa, Turkey; (d) Italic Art, black ceramic, second half of the 5th century B.C., 7 cm, vessel with spout and strainer - Collection of the Phoenix Ancient Art ; (e) Victorian silver Caddy Spoon (designated for tea service), Hilliard & Thomason, Birmingham, 1881 - Collection of the Steppes Hill farm; (f) A fourty-niner gold-rusher at the American River during the californian gold rush, 1850 - from [8].

The strainer is not a modern tool. The first trace of strainers dates back from thousands of years ago. I found extremely well designed strainers dating from the Egyptian Reign 1200 years B.C. – see Fig. 1.1-a. The strainer was spread throughout civilizations and was later accompanied with more and more sophisticated forms of art – see Fig. 1.1-a to e.

But to what purpose were strainers used when the era of Italian Pasta had not yet begun?

*I am grateful for the help lent by Ferdinand Breffi, to struggle with this etymological search.

The answer is always in alcohol! Strainers were used to extract solid residues from beer or wine [9], sometimes even "strainer-glasses" were used to be able to extract the residues and drink at the same time [10]. Alcohol was actually a great driver for several other inventions in physics and chemistry, for instance the chemistry of distillation was onset by alcohol fabrication [11]*.

Strainers were used afterwards in various food presses (for example for making oil using filtration devices that were retaining the solid component); in the 17th century, when drinking tea became very popular, strainers were used for tea leaves... and I am not going to enumerate all the uses of strainers through the ages but somehow when I think of strainers I can not take my mind off the picture of gold-rushers in California, searching for the wanted precious gold through liters of river water – see Fig. 1.1-f.

Today we use filters of very different types, for a huge range of applications, to separate solids, liquids and gas; and if you still have a doubt on what we are talking about, I gathered the most common and simple examples of filters that we encounter in everyday life in Fig. 1.2.

Fig. 1.2: **The strainer today**: (a) Coffee strainer used to filter only the liquid part of coffee and avoid chunked coffee grains in the reservoir - credit from the Kitchen Shop; (b) Diesel particle filter - credit from my-cardictionary; (c) Colander for separating pasta and water.

Separating particles but of what size? I turn to the separation of species in liquid, mainly in water. Filtration is used also in gas and solid phases, but it is not the purpose of my thesis. The size of the separated particles is used to classify and define specific terms in filtration [12]. *Macro-filtration* is used for separating particles ranging from 1mm down to 5μm, then down to 0.1μm is *microfiltration*, and below this size, we use the term *ultrafiltration*. The limit of ultrafiltration is not so well defined and ultrafiltration covers essentially all particle sizes down to the smallest distinct particles (such as small colloids). All these filtration principles address the separation of particles *suspended* in liquid. The membranes (or filters) generally rely on size exclusion principles through dense porous arrays of polymers to distinguish and separate particles from the fluid.

Below ultrafiltration is *nanofiltration* and *reverse osmosis* (that will be properly defined

*I really like this book because I had to go to a special library to find it – the library of Archives

below). These filtration principles differ in the sense that they adress the separation of *dissolved* species in liquid. Most of the membranes used in this regime have no "proper holes" in them but "dissolve" one or more molecular species into the membrane itself [4, 13]. Separation occurs then because molecular species do not all diffuse as fast through the membrane. The different scales for filtration are summarized in Fig. 1.3.

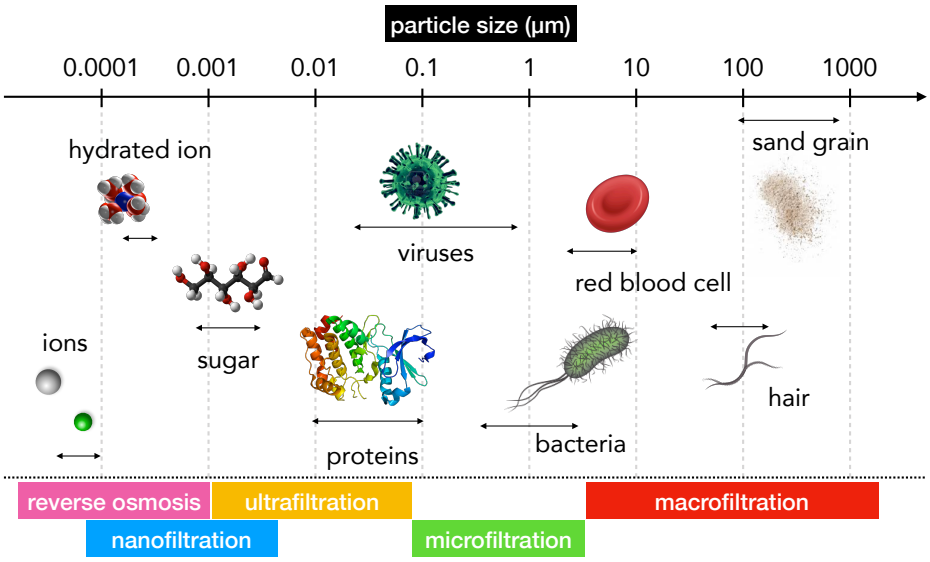

Fig. 1.3: **The different scales of filtration**: different particle types with typical sizes are represented according to their size and associated with a category of filtration – for example filtration of ions is a reverse osmosis or nanofiltration process. This image is freely inspired from [2].

2 The tight link between osmosis and filtration

One essential point to separate dissolved species is that at these scales, one can not just wait for dissolved species to "fall out" of little holes like water out of the (water+pasta) mix. At these scales one should "push" on the mix such that the desired component may transverse the membrane – similarly to pushing on the coffee strainer, in a way. This "pushing" mechanism is actually an applied pressure to beat the *osmotic pressure* that builds up at these scales.

An introduction to osmosis Osmotic transport is a subtle and non-trivial effect, that is harvested in numerous biological phenomena and applications, such as food processing in biological organisms [14, 15], reverse osmosis for desalination, and energy generation from salinity differences [4, 16–18], to name a few. Traditionally, osmotic transport is described as occurring across a semi-permeable membrane, *i.e.*, a membrane impermeable to the solute but permeable to the solvent, often water, see Fig. 1.4-d. If two reservoirs with different solute concentrations are put in contact via a semi-permeable membrane, an osmotic pressure builds

up between the compartments. This pressure drop is the driving force for a flux of water from the low concentration reservoir to the highly concentrated one, until the thermodynamic equilibrium is reached. For low solute concentrations, the osmotic pressure is expressed by the van 't Hoff law,

$$\Delta\Pi = k_B T \Delta c, \tag{1.1}$$

where Δc is the difference in solute concentration between the two reservoirs. [16] The van 't Hoff law is derived by equating the solvent chemical potential of the solvent across the membrane [19–23]. The osmotic pressure is accordingly defined in terms of equilibrium thermodynamic properties of the system.

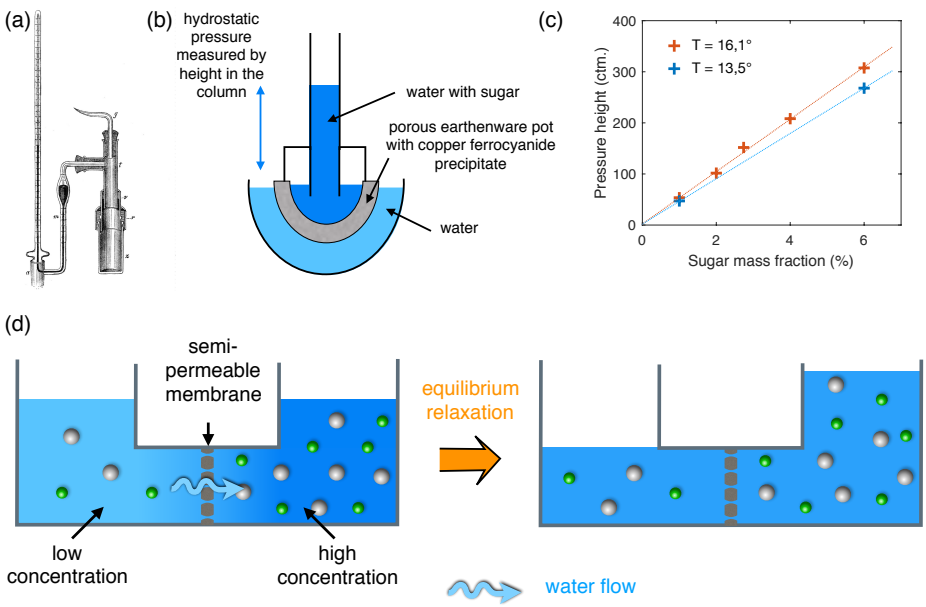

Fig. 1.4: **Osmosis principle**: (a) initial setup used by Pfeffer [24] to measure osmotic pressure; (b) schematic of the functioning principle of the Pfeffer cell; (c) data acquired by Pfeffer in Table 9 of [24] - the lines are a guide for the eye; (d) easy schematic of the principle of osmosis: if two compartments are separated by a semi-permeable membrane letting only water transverse, water will tend to go from the least concentrated compartment to the most concentrated compartment to equilibrate concentrations and decrease the chemical potential of the system. Initially the driving force for water flow is the osmotic pressure build-up between the two sides.

The theoretical background and ideas provided by van 't Hoff came just a few years after the first discovery of *osmotic pressure* by Pfeffer [24]. Pfeffer measured the hydraulic pressure between a solution of water with sugar and a solution of water only, separated by some porous earthware [25] and see Fig. 1.4-a to c. The theorization of the *osmotic pressure* at that time generated a lot of debate as to *which part of the liquid, the solute or the solvent* was generating the pressure contribution [26]. In fact, both components are implicated, and the story is just

not as simple. In 1901, van 't Hoff was awarded the first Nobel prize in chemistry for his work on the *osmotic pressure*.

To filter small dissolved species with sieves or membranes, one has to find a way to beat or bypass the osmotic pressure. For instance, to produce clear water from salty water (for instance like clarified seawater), one has to *concentrate even more* the already salty water compartment. To do so, one may apply a large hydrostatic pressure on the salty water compartment, larger than the osmotic pressure difference between the salty compartment and the clear compartment, and in this way may extract clear water by the semipermeable membrane, see Fig. 1.5. This process is more commonly referred to as *reverse osmosis*.

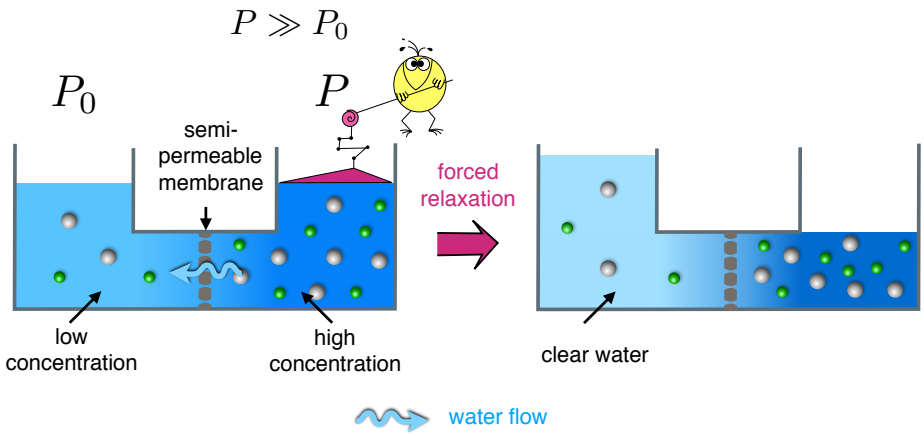

Fig. 1.5: **Basic principle to understand reverse osmosis**: as compared to osmosis in Fig. 1.4 if hydrostatic pressure is applied against osmotic pressure, the direction of the water flow may be reversed, and water may be concentrated on one side. The drawing is freely inspired from Les Shadoks - Jacques Rouxel.

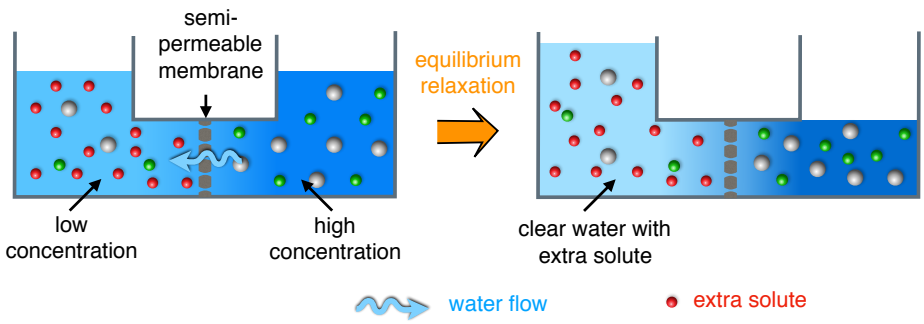

Fig. 1.6: **Basic principle to understand forward osmosis**: as compared to osmosis in Fig. 1.4 we can also reverse the sign of water flow by changing on purpose the concentration of solutes in both reservoirs. The osmotic pressure builds up according to the concentration of all the solutes.

Alternatively, one may "trick" the system by adding in the low concentration reservoir a specific extra solute. This specific solute will increase the osmotic pressure in its compartment. If it is sufficiently concentrated there, one may revert the osmotic pressure difference such that

the natural osmotic current will be from the salty compartment to the low salt compartment – see Fig. 1.6. This process is called *forward osmosis*. It is sometimes used for desalination, using an extra solute that may be easily evaporated from water (more easily than salt).

On top of that, and although this is somehow a shortcut, *pressure retarded osmosis* is similar in its process to reverse osmosis except for the fact that this time the osmotic pressure difference is harvested to produce energy. This form of energy is sometimes referred to as *blue energy* – see Fig. 1.8-d.

3 First developments of reverse osmosis filtering membranes

The idea of *reverse osmosis* to desalinate seawater arose in the 1950s. At that time, the first successful experiment was realized in 1958 and is reported in [27, 28]. A flat plastic film supported by a porous plate was used as a membrane. Pressure on a salty solution on top of the membrane was obtained by a *hand-operated* hydraulic pump, and concentrated brine was successfully obtained. The flow through these membranes were however extremely low, and thus not viable for commercial use. Subsequently a new membrane was developped by Loeb and Sourirajan [29], it was the first *asymmetric membrane* – see Fig. 1.7. It was a cellulose acetate membrane build by polymer assembly and evaporation, such that the pore density and geometry was different on one side and the other, and it allowed a significantly higher flow of clear water through [30]. Beforehand, membranes would either be completely impermeable to water, or would have such big holes that they would not block salt sufficiently. Subsequently membranes were commercially available from the 1960s onward.

With time assymetric membranes became more sophisticated. Ultimatly it was found that there was a difference in using them on one side or upside down [33]. Though this phenomenon was not understood at the time – and is still somewhat debated – it hints to sophisticated electronic and chemical effects occuring at the nanoscale in these devices. Composite membranes were developped in parallel and are structurally very different, mostly because they are made of heterogeneous materials. For example thin-film composite membranes are composed of a very thin and very selective film deposited on and grafted to a more solid structure with larger pores, that serves as a mechanically stable support for the thin film – see Fig. 1.7. There exists today a huge variety of thin film membranes and other classes of composite membranes [34], maybe one of the most famous of these is the class of nafion membranes that are used as proton exchange membranes: they are selective to protons (but also to other positively charges species), and are mainly used in proton-exchange membrane fuel cells that are good candidates for clean energy transport [35].

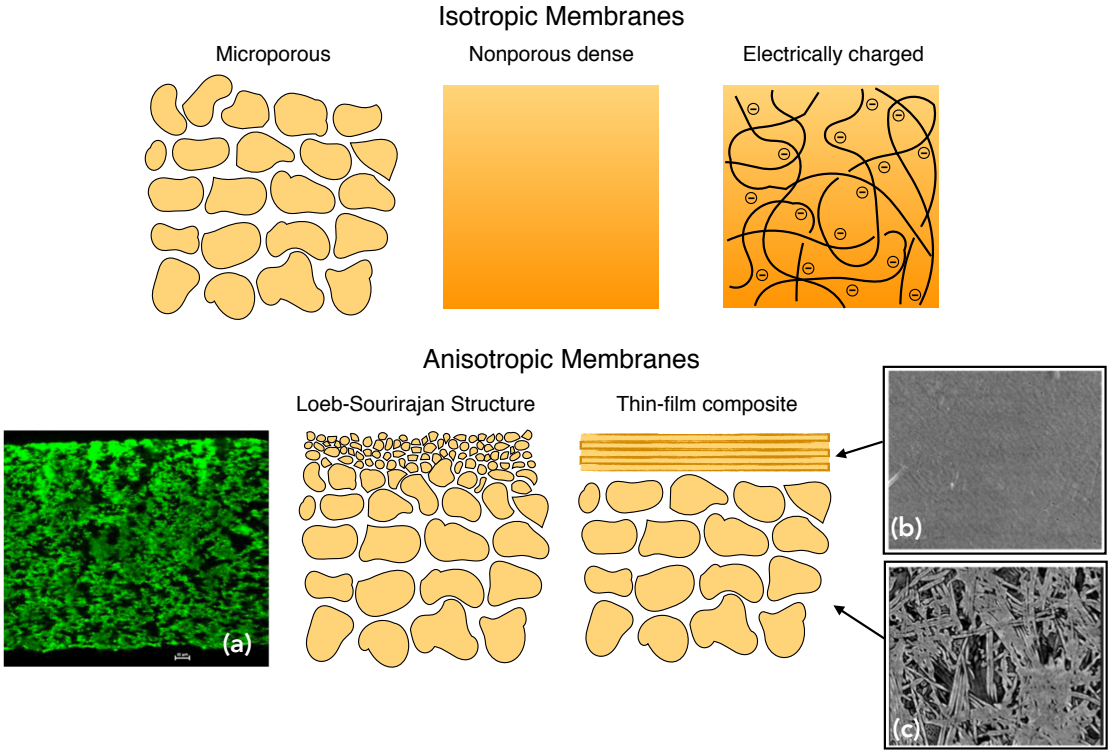

Fig. 1.7: **Schematic of typical membrane structures**: (freely adapted from [2]) Isotropic membranes have the same physico-chemical properties through the depth, while anisotropic membranes are generally assymetric either chemically or physically, with one side with a thin layer either made of the same but denser material or of a different material, *e.g.* a thin chemical layer. (a) Cross-sectional confocal laser scanning microscope image of an asymmetric polyethersulfone membrane. The membrane is stained with a fluorescent dye. The dense surface is at the top. The image is a square of 210μm and is from [31]. (b) and (c) X-ray computed tomography cross-section images of a SW30-XLE TFC RO membrane with a polyester backing layer (lower layer - c) and polysulfone support layer (upper layer - b). Images from [32].

4 (Nano)Filtration today

Filtering small particles has a huge range of applications [12] and interest for this topic is still growing [36]: from various water treatments, to numerous applications in food industry, not to forget oil purification. One of the main applications that this thesis is connected to is to clean water. Today access to clean water and cleaning water from industrial waste is a great challenge: still 663 million people worlwide lack access to drinkable water [4, 37], cleaning waste water is becoming a major challenge in oil and gas industries [38–40], and, going further, some new regulations will appear and require a zero liquid discharge for industrial waste [41, 42].

In fact, 3% of the total amount of water on Earth is fresh, and of this most of it is

frozen at the poles. On the whole only 9 million cubic kilometers of fresh water are readily accessible [43], but the majority of it is confined below earth. On a day to day basis, we consume an equivalent of 10-100 cubic kilometers of water [44]. Because fresh water is not directly accessible everywhere, and to cover the growing need for freshwater, two industrial approaches are growing: desalination and cleaning of waste water.

The idea that we could *turn sea water into fresh drinking water* dates at least from Aristotle (Meteorologica - II. 3): " Salt water when it turns into vapour becomes sweet and the vapour does not form salt water again, when it condenses. This I know by experiment" [11,45] – see Fig. 1.8-a. Desalination technologies have advanced through the years. Before *reverse osmosis*, desalination relied mostly on evaporation and distillation principles, that are particularly expensive. With the progress of reverse osmosis (RO) membranes, in 2009 58% of the newly installed desalination capacity relied on RO [46]. According to the International Desalination Association, in June 2015, 18,426 desalination plants operated worldwide, producing about 0.09 cubic kilometers per day, providing water for 300 million people.

A number of new "membrane based" or "osmotic based" ideas are explored for desalination: reverse osmosis, forward osmosis, electrodialysis (based on electric potential driving of salts) [47] but also capacitive dionization [48–50], biodesalination [51–53], shock electrodialysis based on the idea of combining salt recovery with a porous charged material [54], concentration polarization [55], and other techniques harnessing chemical phenomena like adsorption desalination [56].

A side yet critical issue for drinkable water is micropollutants, because of their variety [57], and also because they may be found in a great range of concentrations (from ng/L to μg/L) [4]. Some of these micropollutants are of great concern for health [58].

Alternatively some people try to perform ressource recovery from waste water [59–61], both to generate fresh water but also to find added value to the (solid) waste. Re-use and reclamation of waste water from industrial or municipal sources to restore it to potable quality seems like a good idea to achieve on-site sustainable wastewater treatment in cities – especially since pumping water over long distances is also very expensive [62, 63]. The technical challenge is great !

5 What is the cost of filtration?

In a context were sustainable development is a major issue, it is interesting to investigate the energetic cost of filtration processes, in particular of desalination. To make drinkable water, one should pass from 30g/L of dissolved salt to 1g/L [64]. From there if one evaluates the minimal thermodynamical cost to nearly double the salt concentration in the brine, that is in majority sodium chloride [65], one finds $\mathcal{P} = 0.69kWh/m^3$. RO consumes typically around $3-4kWh/m^3$ [46,47,66]. Lately, significant progress in this energy consumption was achieved

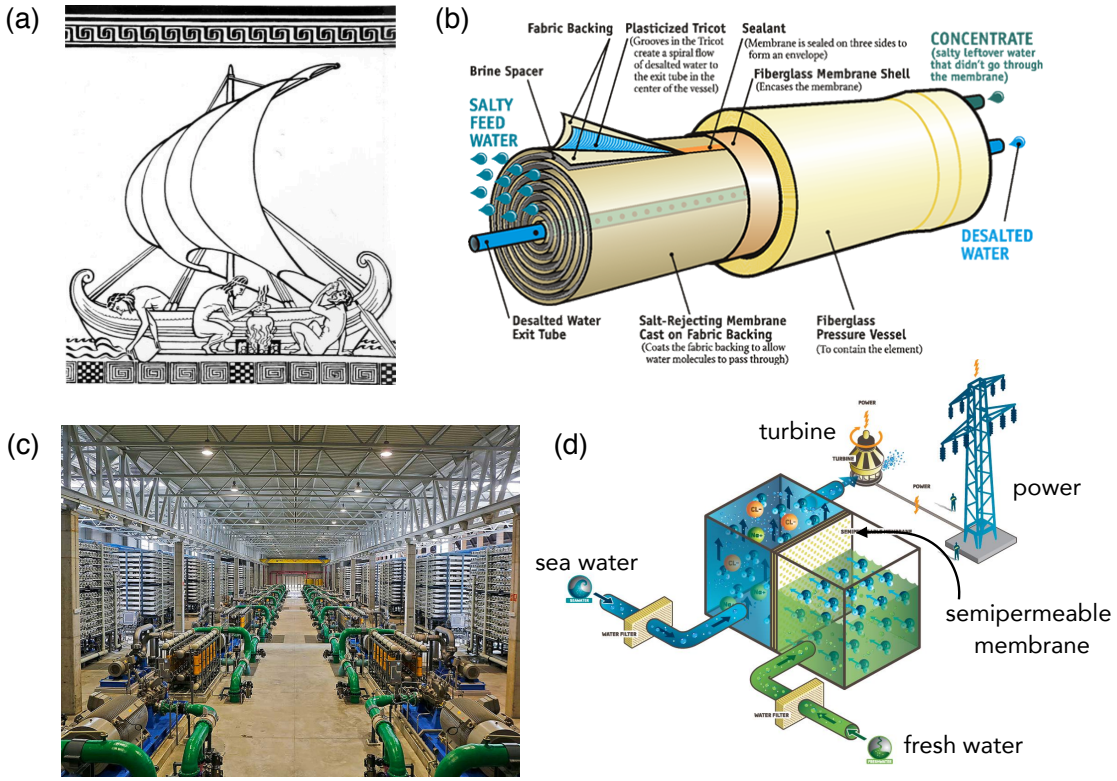

Fig. 1.8: **From Aristote to large scale desalination and blue energy**: (a) Vapor condensing in sponges reproduced from [45] – the original drawing source is uncertain; (b) Schematic principle of reverse osmosis cells. Those cells are assembled in series and parallel in large scale desalination plants like Torrevieja desalination plant (c). (d) One may also take advantage of salt concentration differences in sea and river water to produce *blue* energy via pressure retarded osmosis. The osmotic pressure imbalance between both sides produces a pressure gradient in the sea water compartment that drives a turbine that generates power. Image from Climate Tech Wiki.

by adding blue energy recovery units connected to RO plants [46, 66]. This amount is to be compared to the amount of energy consumed per inhabitant on earth, $117kWh/day$ (calculated from [67]). A person consumes about 3 m^3/day of fresh water (in terms of water flow [44]) such that about $10kWh/day$ are required to desalinate the consumed water. It seems rather reasonable to use about 10% of the consumed energy for water purposes (also including agricultural and industrial purposes) but this is neglecting the huge amount of energy that we use for transport !

6 The limits of traditional filtration

Traditional filtration conceived as a membrane technology allowing to separate particles faces several challenges, and I review some of the most important below.

Fouling Traditional filtration – in terms of a membrane separating the permeate from the brine – has a high propensity to fouling [66]. There are several types of fouling [4]: organic fouling by adsorption, scaling by deposition, and biological fouling – more details may be found in [4, 12]. This inevitably impedes the flux and transport of water through the membrane, and eventually the membrane has to be properly rinsed or disposed of. Surprisingly, fouling is not only due to large particles – larger than the typical pore size – but also to small particles accumulating and packing in flow "corners" [68]. Membrane deterioration on a general basis also occurs because of the high pressures implied to perform reverse osmosis. Understanding the dynamics of fouling is an essential requirement to be able to take action and design anti-fouling resistive membranes.

Intrinsic selectivity permeability limitation With the growing number of membranes, and their ever more sophisticated fabrication process, at some point consumers were lacking a faithful way to compare the performances of these various membranes. In 2005, Mehta and coworkers, introduced a concept already used for gas separation [69] to quantify the performances of membranes [70]. The idea is to compare the permeability of the membrane and the selectivity of the membrane (towards selection of the desired component).

Using [16, 71] one may write the total volume flux of the solution through the membrane:

$$Q = \mathcal{L}_{\text{hyd}}(\Delta p - \sigma \Delta \Pi) \tag{1.2}$$

where $\mathcal{L}_{\text{hyd}} = \kappa/\eta L$ is the solvent permeance, η is the channel permeability, σ the reflection coefficient, and L the thickness of the active layer of the membrane. Δp is the hydrostatic pressure drop between the two sides, and $\Delta\Pi$ the osmotic pressure as described by van 't Hoff Eq. 1.1.$\kappa = \varepsilon_p r_p^2/8$ is the Hagen-Poiseuille permeability with ε_p the membrane porosity. κ is usually the descriptor for water permeability through the membrane. Now one is interested in computing the selectivity properties of the membrane. There is a number of models to describe steric selection. One of the most famous from [72] derives a complete formula for rejection combining the original steric rejection result (assuming particles have a finite size and thus there is an exclusion zone for particles through the pore) [73] and also the idea that the particle is submitted to drag forces that make it move at a velocity different from that of the flow [74]. The model from [72] writes the rejection coefficient σ (in his work the rejection coefficient is written $\overline{R}_2$ but the more contemporary notation σ is used in my thesis) as

$$\sigma = 1 - \left[2\left(1 - \frac{a}{r_p}\right)^2 - \left(1 - \frac{a}{r_p}\right)^4\right] \exp\left(-0.1746\left(\frac{a}{r_p}\right)^2\right) \tag{1.3}$$

where r_p is the pore radius and a the particle size, and $r_p > a$. For $r_p < a$, $\sigma = 1$. σ is a measure for selectivity. In fact if $\sigma = 1$, there is full rejection of the solute, the membrane is fully semipermeable. Reciprocally, if $\sigma \simeq 0$, the solute can easily permeate through the membrane, and the membrane is permeable to the solute, and thus the effective osmotic pressure $\sigma\Delta\Pi$ drops to 0.

Consequently on may plot for every value of r_p given a certain particle size a the permeability versus the rejection coefficient [69] – and see Fig. 1.9-a. The model may be extended to account for pore size distribution [70, 75] and eventually was found to reproduce rather well experimental data on ultrafiltration membranes [70] and see Fig. 1.9-a inset. Permeability increases with r_p but rejection decreases with r_p. As a result it is nearly impossible to make a sieve both highly selective and highly permeable at the same time – while this is generally expected for practical applications. This result and limitation is generally referred to as the selectivity-permeability trade-off. One may not have both a very selective and very permeable membrane.

For nanofiltration membranes the story is slightly more complex. In fact membranes for selection at these scales are generally made of dense porous materials, and the process of translocation through the membrane is limited by solution diffusion and not by size exclusion. An empirical model was made to relate the water permeability and selectivity in dense porous membranes [76]. The solute permeability is assumed to be proportional to the cube of water permeability $P_s \propto P_w^3$, herein the selectivity $\propto P_w^{-3}$. This is a less rigorous framework – and could probably benefit from better understanding. In fact solute rejection is not so easy to quantify [77, 78] in particular because rejection is for instance highly dependent on bulk concentration. The empirical model was however been shown to be "rather well" connected to experimental measurements, see Fig. 1.9-b. All in all nanofiltration or reverse osmosis also suffers from the same trade-off criteria: selectivity and permeability *may not* be high at the same time. This has triggered extensive research to come up with new materials that may bypass this limitation. Be that as it may, *passive* materials will always suffer from a similar limitation, and to perform breakthrough progress, out-of-the-box ideas are required.

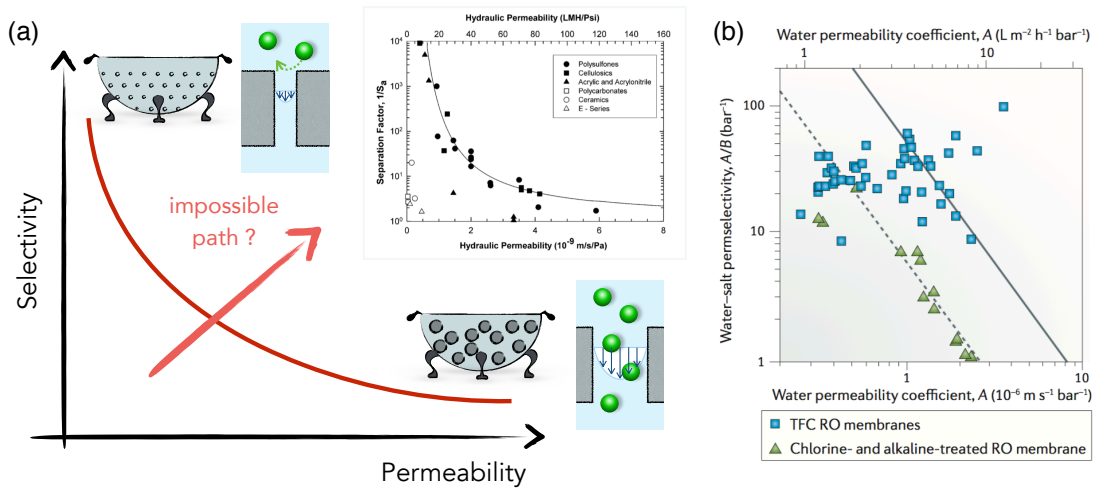

Fig. 1.9: **The selectivity-permeability trade-off**: (a) Selectivity-permeability trade-off for traditional porous membranes with cylindrical pores and (inset) experimental validation of the model, from [70]; (b) extension to reverse osmosis (RO) membranes; the lines are trade-off model fits for RO membranes [76]. Image from [4].

Traditional membranes lack molecular design level One of the main axis for progress today is the ability to perform high throughput selectivity [79] notably because that is the most critical condition to ensure high water or food quality. Indeed a higher water quality is required today [80] in terms of purity and removal of micropollutants is investigated for potable reuse [81–83]. Selectivity is also a key factor to increase the performance of desalination [4]. One of the limitations of membranes to achieve high selectivity is the lack of molecular design [84]. However with the materials and the techniques now at hand there is hope to design more advanced functionalized materials [85]; for example using the range of possibilities offered by metal organic frameworks [84]; exploiting binding sites to functionalize graphene nanosheets [86]; and tailor made carbon materials [87]. This state-of-the-art manipulation and fabrication of molecular scale designs was made possible in particular by the large advancement of research of fluids at the nanoscale.

Chapter 2: Harnessing the nanoscale

The visionary phrase of R. P. Feynman "*There is plenty of room at the bottom*" (1959 at Caltech University) was the onset for numerous scientific and technological developments harnessing the peculiar properties of the infinitesimal scales. There are still many effects to explore at those scales, in particular in terms of fluid transport at the nanoscale, and their transport properties through nanoscale constrictions like pores or channels [88, 89].

1 Why turn to fluids at the nanoscales ?

A decisive turnpoint in the study of nanoscale systems probably arose with the interest triggered by the discovery of nanoscale channels in biology. For example, one of the most famous family of these channels is the aquaporin family (the most common being AQP1 or CHIP-28). An aquaporin is a water-specific channel; aquaporins are present in many organs in the human being: they play a central role in the human kidney, but are also present in red blood cells [90]. Aquaporins were discovered in the 1990s by the group of Peter Agre – who was awarded the Nobel Prize for Chemistry in 2003 for his work on water channels [91, 92]. The striking specificity of aquaporins is that they are both highly selective to water *and* highly permeable: a single aquaporin allows 3 million water molecules through per second [93] – 3 orders of magnitude more than what is expected from continuum dynamics [88, 94]. Aquaporins present several intriguing features: surprisingly they are hydrophobic channels [95] but this actually helps to drive water fast within, they are extremely constricted [95] – only 3 Å

in diameter at the narrowest point, that allows for this selectivity –, and finally they present a sophisticated geometry that is believed to enhance the water permeability as well [96], see Fig. 2.1. All of these exceptional properties are intimately connected to its nanoscale (and even Angstrom-scale) structure – thus hinting to the striking and appealing properties of fluid flow at the nanoscale.

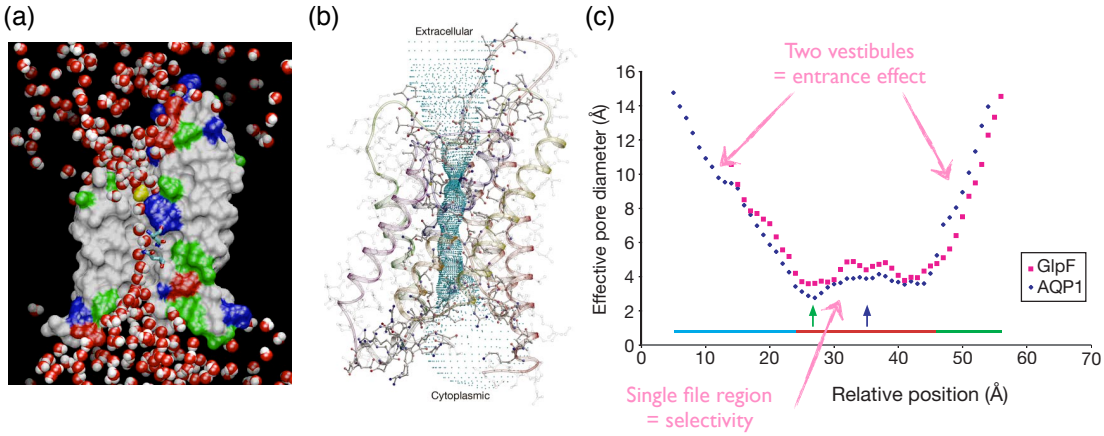

Fig. 2.1: **The aquaporin AQP1 water channel**: (a) Molecular dynamics simulation of water transversing an aquaporin channel. Still image from the video of [97]. (b) Pore profile of the aquaporin highlighted by an array of blue dots generated by the program HOLE38. The constriction region is visible. Image from [95]. (c) Effective pore diameter of the AQP1 and GlpF channels. Pore diameters were determined with AMBER-based van der Waals radii and analysed using the program HOLE38. The locations of the constriction region and the entrance regions are indicated in pink. Image adapted from [95].

2 Nanofluidics: where new properties arise in fluids

The aim of this thesis is to investigate existing properties and imagine new phenomenon that arise in ***transport of fluids at the nanoscale****..* Specifically, we are typically interested in water or dissolved species like ions being transported through nanoscale pores or channels. Transport may be induced by a variety of forces like electric potential driving, thermodynamic potential driving or simple diffusion. We focus on minute confinement of the flows (though not necessarily all dimensions nanoscale) because at these scales – as was seen for the dramatic confinement in aquaporins – new properties are expected to arise in fluids.

In this context, water is actually an emblematic molecule. Already in bulk water is an extremely sophisticated fluid – with its specific dielectric properties, the presence of a permanent dipole, its strong intermolecular interactions via hydrogen bonds – and possesses distinct thermodynamic properties from other liquids. In ultra-confined spaces this specificity also arises, and leads to anomalous phase transitions, and local regular space patterning inducing anomalous transport of the molecules [98–103].

But how to describe water at these minute scales ? At large scales water and fluids in general may be described by continuum equations like the Navier-Stokes equation, describing for instance the velocity field within the fluid. At very small scales however, water is composed of individual molecules. Obviously there must be a scale defining the transition between one description and the other – see Fig. 2.2 and [104]. This scale may be defined by a reasoning on time scales, stating that continuous laws fail when the relaxation time scale for microscopic fluctuations is greater than characteristic hydrodynamic time scales [88]. This criterion yields that continuous hydrodynamics fail around $1nm$, which is coherent with molecular dynamic simulations [88]. Already before reaching this extreme nanoscale confinement, one expects that classical continuum hydrodynamics have to be extended and modified to account for confining effects. For example, at these scales, the interactions of the fluid with the confining surface are expected to matter, and boundary conditions have to be adapted [105]. Memory effects or non-local collective effects arise [106]. Also molecule scale fluctuations may modify the flow at these scales and in particular transport by the flow [107, 108].

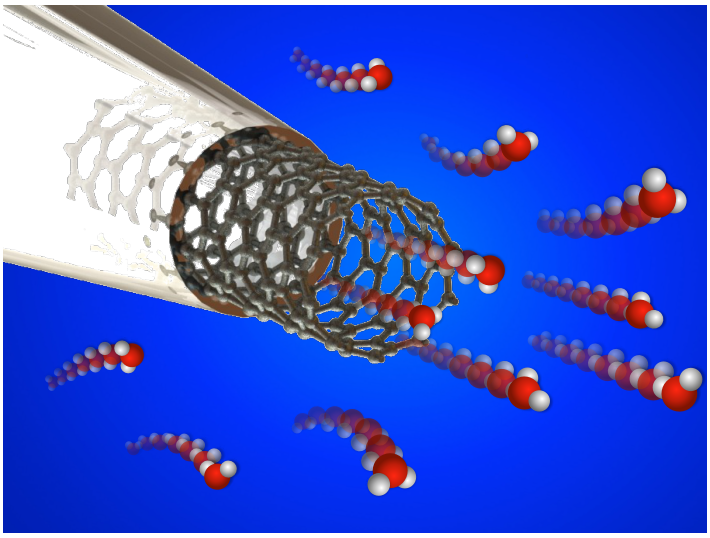

Fig. 2.2: **The paradigm of nanofluidics**: illustration of water flowing through a carbon nanotube, the water is both represented in a continuous way by the blue background but also in a discrete way showing its microscopic details, by the red and white molecules.

Beyond the challenge of understanding and modelling these corrections to continuum hydrodynamics, the question is to be able to *observe* and *measure* these nanoscale flows.

3 Nanofluidics: a technological challenge

Nanofluidics represent at least a double technological challenge for experiments: first, nano-objects such as channels or slits have to be assembled, which is obviously difficult because it requires nanomanipulation techniques, and second, *something* has to be measured properly – like flow, or ionic current – but direct measurements often fail because the currents involved

are too minute to be detected. Without going into the details I will just mention that the last two decades have seen impressive nanotechnology developments [4], and I give below a – non exhaustive ! – list of examples.

On the fabrication size, today we are able to design individual nanoscale structures. This is especially precious – not only because it shows that nanotechnology is mastered to the point of making individual details – but also to study with better accuracy individual channel or porin properties. Single nanopores may be carved or etched in membranes that are only an atomic layer thick [109, 110] and may be accordingly functionalized [86] – see Fig. 2.3-b. Extra thin polydymethylsulfate channels (less than 1 μm which is rather exceptional for such a material [111]) to single wall (sometimes less than a nanometer in diameter) nanotubes [18, 112–115] are designed, manipulated and inserted in devices – see Fig. 2.3-a. Carbon nanotubes are also easily functionalized [116]. The most impressive and recent example is probably the work by A. Geim and coworkers, to make nanoslits with a thickness determined in terms of a quantified and precise number of graphene sheet spacers. Such slits can reach confinement thicknesses down to 7Å [117, 118]. Other materials are triggering interest today. Harvesting the nanoscale properties of graphene oxide seems like a very promissing route [119, 120], but there is also the route of tailor-designed DNA origami channels [121, 122].

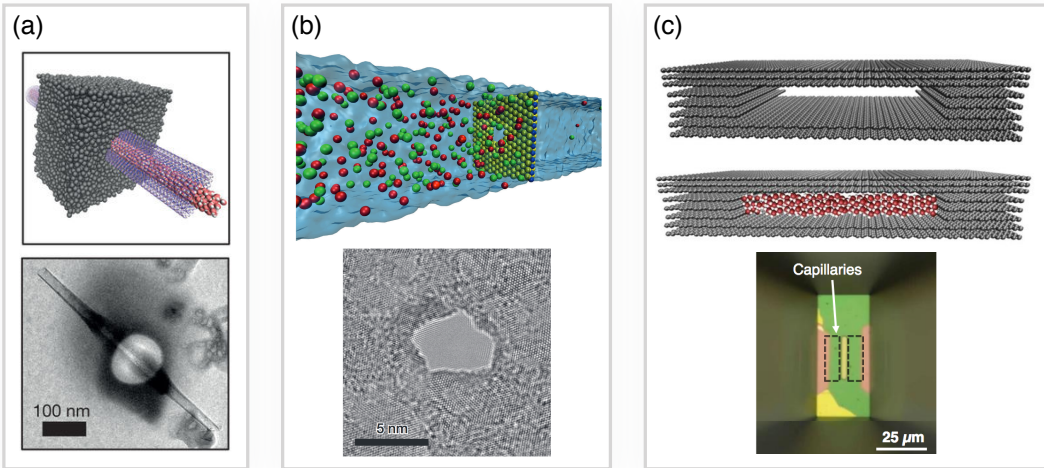

Fig. 2.3: **Nanofluidic technology**: (a) a single boron nitride nanotube inserted in a membrane, where ionic current is measured, from [18]; (b) a single MoS_2 layer is pierced by chemical etching of a single nanometric size (around 5 nm) pore, from [109]; (c) a nanoslit of a few Angstroms thick is designed by graphene sheet assembly from [118].

Through these systems, a number of nanofluidic-specific effects were observed, from specific ion exclusion effects [113,115,123,124] to anomalous ionic curent effects [125]. Extremely fast permeation of water in particular was measured through carbon nanotubes [114,115,126–128]. In all these situations, the challenge is ongoing to measure and quantify the specific origin of these effects.

4 Nanofluidics : the future of filtration ?

All these efforts on nanoscale fluidics are not disconnected to potential applications – and also the efforts of my thesis. At these scales, potentially it is possible to harvest specific properties for instance to bypass the selectivity-permeability trade-off. For instance, carbon nanotubes in the last decade have emerged as potentially extremely good candidates in terms of permeation and in terms of selectivity [114,115,126–128]. The problem remains – now that we have investigated the flows through individual structures – to upscale the devices. Indeed a carbon nanotube typically can flow about a fL/s, and that is – needless to say – orders of magnitude below the required flux for a desalination or water treatment plant. Therefore, efforts in terms of upscaling are ongoing, but for carbon nanotube based membranes, the difficulty is to properly align the tubes, and design a material that binds them solidly to one another. For now the designed membranes are too fragile [129, 130] to be used in such high-throughput devices.

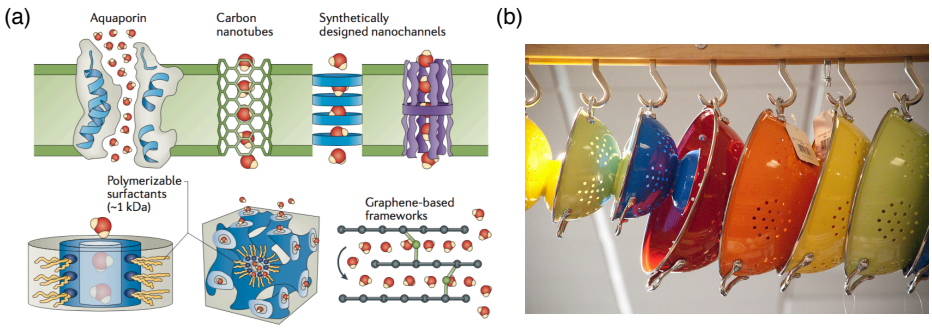

Fig. 2.4: **The variety of nanoscale pores**: (a) the accessible variety of nanoscales pores, image from [4]; (b) an array of strainers with different colors.

All in all, within the variety of new materials, the generic idea is always to design holes (pores) in a membrane, with specific physico-chemical properties that will allow to retain the desired component – see Fig. 2.4. Without denying all these remarkable advances, somehow one could make a parallel between these decorated pores and an array of differently colored strainers with different hole sizes – see Fig. 2.4. In fact all these new materials are designed according to a sieving perspective. Because of that, all new materials will also suffer at least in part from the selectivity-permeability trade-off. As a consequence, more imaginative strainers have to be invented; the dream being – see Fig. 2.5 – to invent a strainer that will extract the pasta instead of the water !

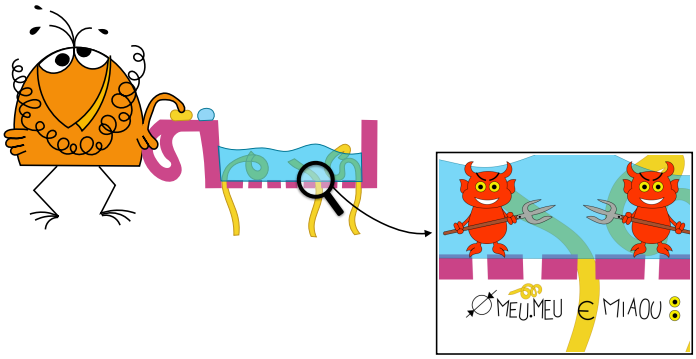

Fig. 2.5: **The unconfessed goal of my PhD**: to design a strainer that can selectively sort for the Pasta, a tool much more convenient than a regular strainer to eat tomato-sauce spaghetti, since you just have to click on it and the pasta goes in your plate.

Chapter 3: New inventions with existing tools

Inventing filters that do not look like traditional passive filters and that harvest original properties is not necessarily a new idea, but most importantly, does not necessarily require to use innovative materials. Several inventions may be designed using existing tools but new design principles. I review some of the paths followed below.

1 Bio-inspired materials

Today, "biomimetism" is a very fashionable approach to solve industrial or biomedical challenges but in fact it generates several fruitful ideas. For instance, to solve the fouling problem today new fouling resistant membranes are designed for instance inspired from fish scales [131,132]. The exceptionnal "glue" that mussels use to stick to rocks – polydopamine – was an inspiration to design coatings for highly selective nanofiltration membranes and water purification particles [133–135]. A variety of bio-inspired ideas are evaluated also to solve the water challenge in the coming years [136], like dew condensation on desert beetle skin thanks to nanostructures – those desert animals have adapted to very scarce water ressources [137]. Beyond the physical approach it is possible to build with state-of-the-art chemistry and bio-development tools highly selective bio-grown membranes [138] – that may encapsulate active

membrane transporters – or artificial transmembrane transporters [139]. This approach is however extremely specific and technical.

2 Geometrical and thermodynamic ideas

Continuing with biomimetism, it is also possible to inspire from strictly geometrical properties of biological porins. For instance the aquaporin dumpbell shape was shown to be connected to its high permeability [96] and was a source of inspiration for artificial dumpbell shaped porins [140].

Going further on geometric ideas, it is also possible to play on the lateral arrangement of the membranes. Today, most processes are performed in cross-flow (both fluids are flowed parallel to the membrane) instead of dead-end flow (fluids are flowed perpendicular to the membrane), which helps to increase the contact area and thus optimizes the time delay for equilibration to happen [2]. Most membranes are in fact rolled up and flowed in multiple layers to optimize even more contact area – see Fig. 1.8-b.

More interesting and innovative is to play with thermodynamics and combine different element phases. For instance [141] has achieved high permeability and low selectivity of dissolved species through nanoparticle base membranes where the inner phase is in a vapor state. Another idea is to design a fluidic membrane with particle entrapment at the interface, the hope being that maybe it is possible to retain small particles at the interface because they are unable to beat the capillary forces to transverse the liquid membrane [142, 143]. Even better, why not suppress the membrane and harvest hydrodynamic or electrostatic interactions to sort particles ? Hydrodynamic interactions [144] and surface acoustic waves [145, 146] have been used to sort particles in microfluidic devices – see Fig. 3.1, but the challenge remains to separate nanoscale dissolved species by a membrane-less device !

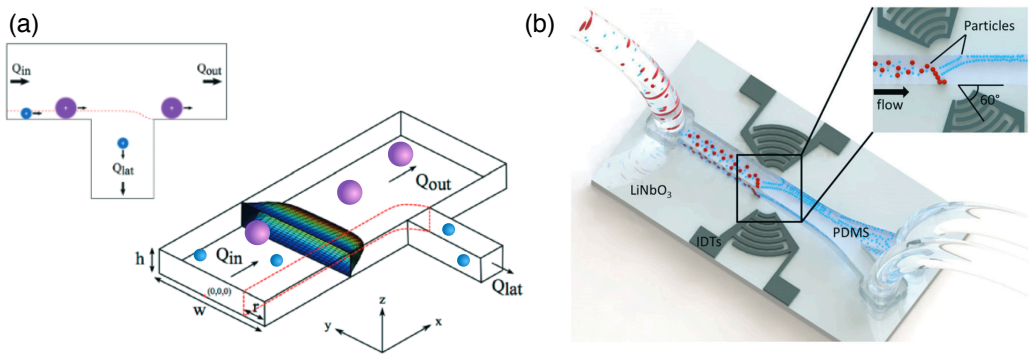

Fig. 3.1: **Membrane-less sorting of particles**: (a) a hydrodynamic sorter is able to differentiate two different particle sizes in a T-shaped microfluidic sorter. Image adapted from [144]. (b) surface acoustic waves are able to continuously differentiate particles of different sizes. Image from [146].

3 Inspiring from the Rules of Nature

Beyond bio-inspired-materials, one could build on rules observed in Nature to draw new design rules. For instance, while we are astonished by the exceptional selectivity and permeability properties of biological pores [94], biological porins demonstrate ubiquitous dynamical behaviors [147–149] that are not encompassed in current nanotechnology. Pore shape agitation – due to thermal fluctuations or in response to external stimuli – is believed to facilitate transport in biochannels [150–154], but its impact on transport in artificial pores remains largely unexplored. In a variety of larger scale organisms active processes enhance dispersion of particles by active mixing of water – for example cilia of coral species rely on active mixing for survival [155].

The idea of harnessing and understanding active transport in nanoscale devices is currently discussed [63]. For example the effect of pulsating flows in filters is studied [12] – also thanks to the theoretical background existing that was originally developped to study pulsating flows in blood vessels – but more ideas need to arise, and also theories have to be advanced to describe transport and selection *out-of-equilibrium*. This would have consequences in particular to help understand the basic rules to build ionic machineries like pumps [156] or individual molecule controllers [157].

Chapter 4: Fluid transport at the nanoscale and beyond

To bypass the limitations of current filters – especially the selectivity-permeability trade-off – new ideas have to be put forward. To build on innovative nanoscale transport, also more theoretical background has to be provided to be able to draw for example design rules or perform faithful predictions.

In my thesis I investigate several innovative approaches to separation and filtration. I draw inspiration from biological systems (the human kidney, biological channels like aquaporins) and rationalize some new concepts for sieving, based on simple models. These approaches rely on different alternative strategies: either exploring new topologies – typically by exploring the peculiar geometrical arrangement of the central filter unit of the kidney – or the idea of active sieving, with dynamically responsive channels and pores. All these principles could be readily mimicked using existing technologies to build artificial dialysis devices or alternatives for advanced water recycling.

In a broader perspective, these approaches open fundamental questions in the fields of statistical physics and fluid dynamics. In particular, traditional in-equilibrium quantities like osmotic pressure and permeability are not defined when the pore has an active component, yet one easily imagines that such concepts could be extended to these out-of-equilibrium situations. I thus also strive to provide substantial theories to answer these questions.

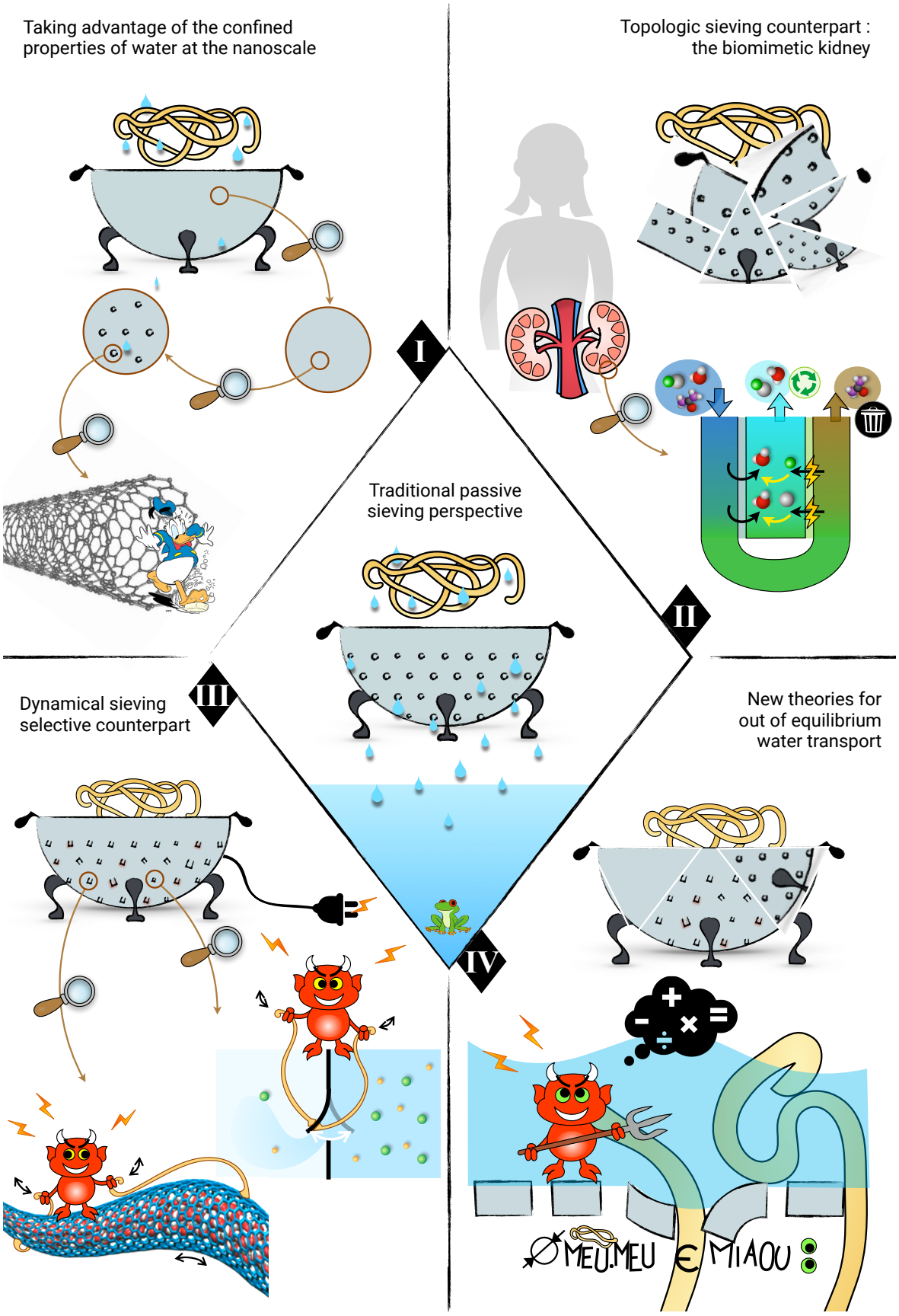
Taking advantage of the confined properties of water at the nanoscale
Topologic sieving counterpart : the biomimetic kidney
I
Traditional passive sieving perspective
II
III
Dynamical sieving selective counterpart
New theories for out of equilibrium water transport
IV
MEU.MEU
MIAOU

Part I

Fundamental properties of fluids at the nanoscale

or

a “ nano” investigation of filtration

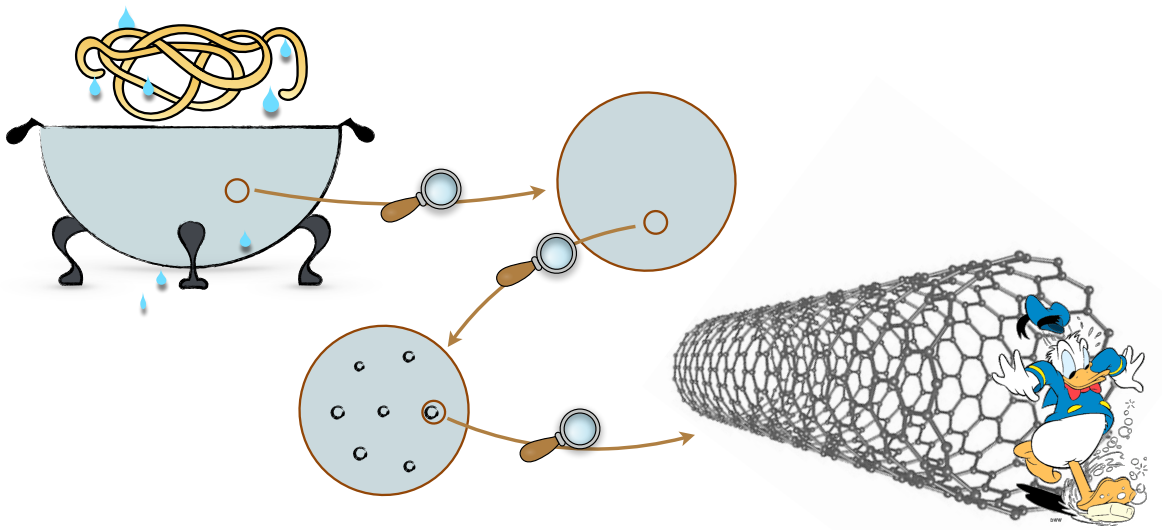

Introduction

"*God made the bulk, surfaces where invented by the devil*" (Wolfgang Pauli)

In the perspective of ever increasing the permeability and selectivity properties of membranes used for desalination and filtration, carbon nanotubes, boron nitride nanotubes, or graphene surfaces became increasingly popular from the beginning of year 2000. The first paper to report exceptional properties of water permeation through the interior of carbon nanotubes is a molecular dynamics demonstration [158]. The simulation showed that molecules would align in a single line, similarly as in aquaporins [90], and that would lead to ultrafast water conduction. This is similar to the effect of people gathered in a queue: if the files are split in several single files, the queue will be faster as if the file is a unique file with tumbling people inside.

These fundamental findings were soon followed by a number of experiments measuring water flows through membranes made of vertically aligned carbon nanotubes [126–128]. These measurements showed that the water flow was sometimes 4 orders of magnitude larger than the value expected in traditional tubes with friction at the boundary. What was more surprising was that these flow measurements were done in carbon nanotubes with sometimes a large radius (much larger than 2 nm), were the continuum theory is supposed to apply, and the discrete nature of water molecules should not intervene. These measurements are coherent with a nearly frictionless interaction between carbon and water; this is quantified by a slip length for water on carbon on the order of hundreds of nanometers and more. Numerous experiments and simulations were performed subsequently, and I refer the reader to the following reviews for more information [88, 159, 160].

Measurements and simulations have found that water flow over a flat graphene surface is typically of the order of a few nanometers [117, 161, 162], which is several orders of magnitude lower than the slippage calculated for water flow in carbon nanotube arrays [126–128]. The incoherence between flat graphene and rolled-up graphene into carbon nanotubes is large and also the values of expected slip lengths in carbon nanotubes exceed that for any other material [88, 105]. Although there was some debate on the values obtained because the experimental results were obtained on averages over a large number of carbon nanotubes with radius dispersion [163], the enhancement remained largely unexplained and the exact mechanisms of water transport inside the nanotubes and at the water-carbon interface continues to be debated [119, 160, 164, 165].

Some theoretical efforts have confirmed exceptionally low wall-fluid friction between carbon and water with molecular dynamics simulations [166, 167]. A striking discovery of these works is that surface friction decreases with the radius of the carbon nanotube, smaller tubes leading to faster flows. But the discrepancy – orders of magnitude – remains between the molecular dynamics works – that study the transport of water through properly defined and isolated carbon nanotubes – and the experimental investigations – that study arrays of a large number of nanotubes. This lack of validation arises because, even though controlled and systematic studies have explored transport (of ions, or other compounds) through individual nanotubes [18, 112, 159, 168–172], none has met the considerable technical challenge of unambiguously measuring the permeability of a single nanotube [160].

In this part I will make a brief review on what "slippage at the interface" means. Then I will introduce an indirect method to measure nanofluidic flows – of the order of a few fL/s – then I will discuss the results obtained for permeability and slippage in carbon and boron nanotubes. The important result here is that we demonstrate a definite link between the atomic nature of the confining surface and the hydrodynamic properties. I will then extend the discussion by exploring some remaining questions for slippage in flows perpendicular to curved environments. I will finish this part by broadening the discussion on nanofluidics as a potential application to filtration.

Chapter 1: A brief history of slippage

The scientific investigation of hydrodynamics dates back at least to the founding work of Archimedes, captured in his famous book "On Floating Bodies" in the 3rd century B.C. More observations were made by Leonardo da Vinci in the 15th century though none were published and in the 17th century, Newton establishes the presence of a "viscosity" force proportional to the velocity of the moving body in his founding *Principia* [173]. The 18th century is more fruitful for hydrodynamics but the effect of "viscosity" is still not well understood: Bernoulli establishes the theorem bearing his name [174], and d'Alembert, using Bernoulli's theorem, establishes the famous *d'Alembert paradox* stating that a body moving at constant velocity in a fluid with little viscosity is not submitted to any drag force [175]. A little later Euler establishes the system of equations describing Euler flows (inviscid flows) in [176]. A century later, in his essay [177], Navier finally establishes the consequences of "viscosity" that he typically describes as the forces exerted by the molecules of the fluid on the molecules of the fluid themselves, and puts together what is now known as the Navier-Stokes equation describing viscous flows in general. The equation is corroborated by Stokes a little later [178]

and today reads:

$$\rho\left(\partial_t \boldsymbol{v} + (\boldsymbol{v}.\boldsymbol{\nabla})\boldsymbol{v}\right) = -\boldsymbol{\nabla} p + f + \eta \Delta \boldsymbol{v} \tag{1.1}$$

where $\boldsymbol{v}$ is the velocity field of the fluid, ρ the volume mass, η the dynamic viscosity, p the pressure field and f the external volume forces exerted on the fluid (gravity, electric field...). The blue term is specifically the addition of Navier.

Some years later Reynolds establishes a non dimensional number to allow to distinguish between viscous flows and inviscid flows, today bearing his name [179]:

$$Re = \frac{VL}{\nu} \tag{1.2}$$

where V is the characteristic velocity of the fluid or body moving through the fluid, L a characteristic length scale, and $\nu = \eta/\rho$ the cinematic viscosity of the fluid. At high Reynolds numbers, (or at high velocities and low friction fluids like air for instance) Navier's equation reduces to Euler's equation and the drag on a body at constant speed vanishes. D'Alembert's paradox will only be released 150 years after his own work with the demonstration of Prandtl [180] that even at high Reynolds number there exists small boundary layers where viscosity matters and that are responsible for drag forces*.

This historical view shows in particular that it took centuries to understand what *viscosity* consisted in. In fact, Navier was the first to introduce the concept in fluid dynamics. Indeed it is the reasoning that there exists a balance between internal forces that led Navier to uncover the notion of friction between a fluid and the wall. At that time several experimental results could not be explained by the current status of fluid dynamics "[L]es equations [...] supposent que toutes les molécules du fluide sont susceptibles de [...] glisser sans effort sur les parois des vases dans lesquels le fluide est contenu." †. And this leads Navier to try and explore a new interaction within the fluid - namely repulsive interactions between molecules - otherwise pressure would make the fluid collapse "Une pression [...] tend à rapprocher les parties, qui résistent a cette action par des forces répulsives qui s'établissent entre les molécules voisines" ‡.

Parallel to Navier, in 1872 Boltzmann established a kinetic theory for gases - modelling the individual trajectories of the gas molecules [181]. Joined with the work of Maxwell who gives thermodynamic laws for the velocity distribution of the gas molecules [182], the Maxwell-Boltzmann kinetic theory was shown by the method of Chapman-Enskog [183, 184] to be equivalent to Navier-Stokes. In particular, the key point to recover the viscosity term of Navier is to consider the molecular interaction potentials.

If the particles of the fluid interact between them, they should also interact with the

*I like to talk about Prandtl because I sat in the office gathering all his old tools at the MPIDS in Göttingen

†"the equations suppose that all the molecules of the fluid can slide effortlessly on the walls of the pipes within which the fluid is contained"

‡A pressure tends to bring the parts closer, but they resist this action by repulsive forces that arise between neighbor molecules

molecules constituting the boundaries, and this gives the following relationship at the boundary – (see Fig. 1.1-a for the original formulation):

$$\left[\sigma(\boldsymbol{v}).\boldsymbol{n} + \frac{1}{b}\boldsymbol{v}\right]_{\tan} = 0, \tag{1.3}$$

where $\boldsymbol{n}$ is the normal to the surface (outwards), $\sigma(\boldsymbol{v}) := \frac{1}{2}\left(\nabla\boldsymbol{v} + (\nabla\boldsymbol{v})^T\right)$ and $[\boldsymbol{v}]_{\tan} = \boldsymbol{v} - (\boldsymbol{v}\cdot\boldsymbol{n})\boldsymbol{n}$ is the tangential component of vector $\boldsymbol{v}$ and $\boldsymbol{v}\cdot\boldsymbol{n} = 0$ when the membrane is impermeable. b was interpreted as a characteristic length today called the slip length [105] – this name was inspired from Maxwell's kinetic theory of gases who found a slip length of the order of the mean free path of the particles [185]–. Maxwell's kinetic theory of gas also points to the microscopic origin of the forces implying this boundary slippage. The microscopic interactions have been shown to give this macroscopic slip equation in a more formal way [186–188].

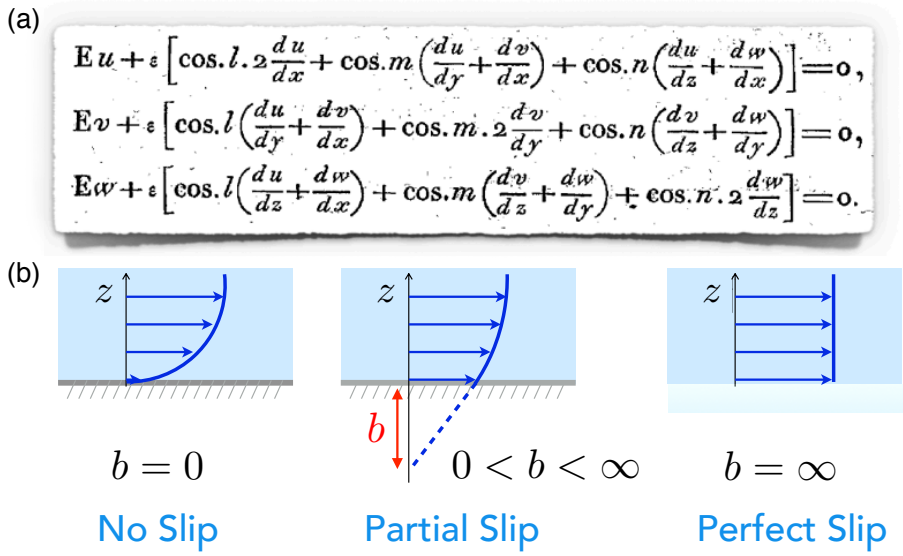

Fig. 1.1: **The meaning of slippage at the boundary**: (a) Exerpt of [177] introducing the condition on the velocity field (u, v, w) at a boundary. E, constant, corresponds to $1/b$ in the main text; (b) Different regimes of slippage from no slip to perfect slip boundary conditions. In between is partial slip. Slippage is interpreted in terms of a slip length b (the projection of the velocity field within the surface).

For a flow orthogonal to a flat surface, one finds:

$$\left.\frac{\partial v}{\partial z}\right|_{z=\text{wall}} = \left.\frac{v}{b}\right|_{z=\text{wall}}. \tag{1.4}$$

The slip length can be interpreted as the length scale required to prolongate the velocity field to zero within the wall – see Fig. 1.1-b. When the slip length $b = 0$ one recovers the traditional *no-slip* boundary condition: the velocity at the surface is zero. When the slip length $b = \infty$ one finds that the velocity field is not affected by the boundary, because no shear exists between the surface and the flow. This condition is called *perfect slip* boundary condition. It is typically the case for a free liquid interface (water and air for example).

As intuited in the explanations earlier, one expects an intimate link between the friction force F_{friction} at the interface and slippage. Indeed one may relate the friction coefficient λ to the slip length via:

$$b = \frac{\eta}{\lambda} \text{ where } F_{\text{friction}} = -\lambda \mathcal{A} v_{\text{wall}} \tag{1.5}$$

where $\mathcal{A}$ is the typical contact area [189–192]. The friction coefficient may be computed via a Grean-Kubo equilibrium approach from the individual forces applied on the individual water molecules (for instance in molecular dynamics simulations):

$$\lambda = \frac{1}{\mathcal{A} k_B T} \int_0^\infty \langle F_x(t) F_x(0) \rangle_{\text{eq}} \tag{1.6}$$

where k_B is the boltzmann constant, T temperature, x the direction parallel to the wall and the flow, and the average $\langle . \rangle_{\text{eq}}$ is an average over all particles at equilibrium. This approach typically allows to find a link between the structure at the interface (either the electronic or atomic rugosity) and the slippage of the particles, via the friction force correlation [191, 192]. By modifying the interface structure, and even explicitly patterning the interface, one may find ways to tune the *effective* slip length at the boundary [193, 194]. There exists a broad range of literature on this topic, that is not directly related to this thesis, and I report the reader to the the following reviews for more information [88, 105, 189, 195]. I will come back in Part III to another perspective on this matter.

From Navier's seminal work onwards, more than a century of experiments was coherent with the no slip boundary condition and the partial slip boundary condition disappeared from most textbooks [105]. Indeed the scientific world was lacking tools and materials to identify these small scale friction forces. With the appearance of the Surface Force Apparatus (SFA) in the 1970s [196] and the Atomic Force Microscope [197] in the 1980s, smaller forces were now measurable and several measurements were done for many different surfaces and fluids revealing slippage at the interface. With the SFA, J. Israelichvili found a slip length smaller than a few Angstroms for water between mica surfaces [198]. To cite only one example to put it in perspective some years later Cottin et al. [199] measured a slip length ranging from 50-200 nm for pyrex glass (with a coating of a self-assembled monolayer of octadecyltrichlorosilane) using (dynamic) SFA. A similar range of slip length measurements is possible with the AFM, for instance Henry et al. measured 80-140 nm slip length for water between silica/mica surfaces [200]. A very nice review and overview of slippage is found in [105].

In this context, water flows in carbon nanotubes where measured, and hinted that slip lengths of water on carbon would be of several 100 nm [126–128] while the slip length of water between graphene surfaces is only of about 10 nm [117, 161, 162].

Chapter 2: Measuring minute flows through nanoscale pores

I am indebted to Eleonora Secchi, A. Niguès, A. Siria, D. Stein, and L. Bocquet for their intense collobaration on the 2 chapters that follow. The two following chapters are connected to the publications [114, 201] reported p.134 and p.155

1 The Landau-Squire jet : an indirect method to measure flows through nanoscale pores

Measuring flows through individual nanotubes such as carbon nanotubes (CNTs) or boron-nitride nanotubes (BNNT) is a technical challenge because the flows through tubes at these scales are of the order of a few fL/s*, when experimental methods – when I started my PhD – are able only to measure flow rates as low as a few picoliters through nanocapillaries [202]. To put it in a nutshell, the strategy of "pushing" flow through the nanotube and waiting for a meniscus to be displaced is here totally impossible because water would evaporate before a significant move is done. For these reasons we turned to an indirect flow measurement through an individual tube. The strategy lies in the idea that we use the tube as the source for a water jet. The jet is characterized by a force [203] F_P. In the low Reynolds regime (characteristic of flows at these very small scales), one expects the force to scale as the Stokes viscous force $F_P \sim \eta R_t V$ where R_t is the tube radius and V the mean velocity emerging from the tube. Measuring the force is thus more accessible, since it scales as R_t when the direct measurement of the flux $Q \sim R_t^2 v$ scales as R_t^2.

We designed a nanofluidic set-up where a nanocapillary bridges two reservoirs: the tip is in the wide open fuidic cell, sandwiched between two glass slides – the glass slides are pertinent for both-sided microscope observation. The rear part of the nanocapillary is broader and filled with solution then sealed to a syringe pump that allows to apply a pressure. The fluidic cell is sealed but the pressure inside is the atmospheric pressure. Both reservoirs are filled with potassium chloride (KCl) solutions of chosen concentration and controlled pH, and the flow cell is seaded with 500-nm polystyrene particles. We then applied a pressure drop ΔP to

*a fL is a femto liter is 10^{-15} liters

the nanocapillary and tracked the resulting motion of the tracer particles under a microscope (see Fig. 2.1-a) to map the velocity profile of the flow (see Fig. 2.4-a). More details on the experimental design may be found in [114]. At the tip of the capillary – provided that the tip is sufficiently small – a jet emerges.

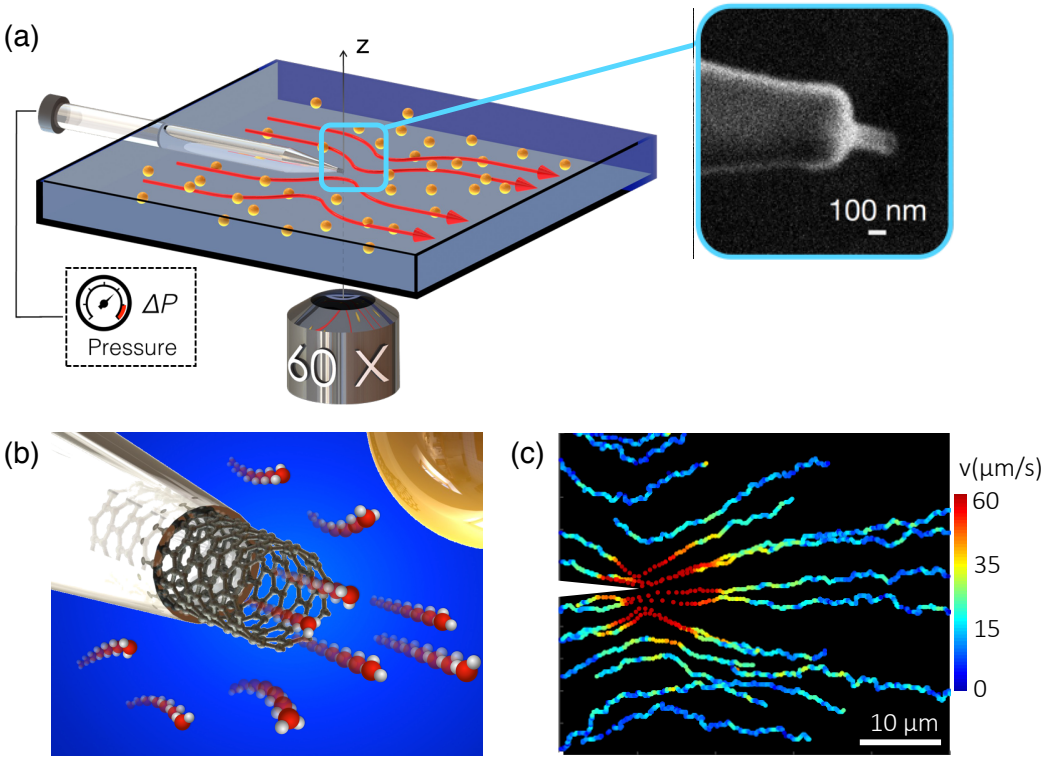

Fig. 2.1: **A nanotube creates a measurable flow**: (a) Sketch of the fluidic cell used to image the Landau-Squire flow set-up by nanojets emerging from individual nanotubes. Red arrows represent the Landau-Squire flow in the reservoir; orange spheres are tracer particles; z is the optical axis (inset) SEM image of a CNT inserted into a nanocapillary. The CNT has dimensions (R_t, L_t) = (50 nm, 1000 nm); (b) Sketch of a nanotube protruding from a nanocapillary tip. The flow of water molecules emerging from the nanotube is probed by the tracer particles (orange); (c) Trajectories of individual colloidal tracers in a Landau-Squire flow field in the outer reservoir. The color scale quantifies the velocity v of the tracer particles. The flow is driven by a nanojet from a CNT with dimensions (R_t, L_t) = (33 nm, 900 nm), with $\Delta P = 1.7$bar.

Another difficulty is to manipulate an individual carbon nanotube to insert it in the nanofluidic set-up. To do this, we adapted a technique for selecting and manipulating nanotubes of known length and diameter with a nanomanipulator operating inside a scanning electron microscope (SEM) [18,114]. We guided a nanotube into the tip of a laser-pulled glass nanocapillary with an orifice in the range 250-350 nm, and sealed it to the nanocapillary. The nanocapillary with the nanotube is placed within the fluidic cell and pressure is applied to the rear reservoir. The dimensions of the nanotubes and their integrity are determined by ionic transport measurement and by electron microscopy.

Upon application of pressure, for sufficiently large tubes ($R_t \geq 7$ nm for boron-nitride), a measurable flow is generated in the fluidic cell. The nanotube acts as the jet source and a long range flow is visible – see for instance Fig. 2.1-c where the flow extends significantly to several tens of microns. Indeed the flow generated by such a point source – called a Landau-Squire flow – [204, 205] behaves typically in $1/r$ where r is the distance to the tube tip. This $1/r$ decrease is thus long-lived, much longer then the flow for instance through a single pore within a membrane, that decreases as $1/r^2$ [206]. This second property also facilitates the measurement of the flow.

Note that the pressure has to be sufficiently large to beat random motion of the colloids. For very small nanotubes, the flux through the nanotube is lower and thus the force of the jet smaller, and thus the measured flow smaller. Pressures are limited by the cohesion strength of the tube to the nanocapillary, and thus for small nanotubes ($R_t \lesssim 10$ nm) it is not possible to distinguish the random motion and the Landau-Squire tracers. To measure flows through even more minute nanotubes, a significant improvement to the technique would have to be conducted (that would allow to decouple random motion) or another setup entirely would have to be designed.

2 Evaluating the slip length in nanotubes

The shape of the Landau-Squire flow illustrated in Fig. 2.4-b verifies:

$$v_r = \frac{F_P}{4\pi\eta}\frac{\cos\theta}{r} \text{ and } v_\theta = -\frac{F_P}{8\pi\eta}\frac{\sin\theta}{r} \tag{2.1}$$

where v_r and v_θ are the velocity components along the radial and orthoradial vectors where the origin is taken at the tip of the tube. F_P has the units of a force and characterizes the strength of the Landau-Squire jet.

2.1 The force of the Landau-Squire flow

One of the first tasks was to find the explicit relation between the force F_P and the mean flow emerging from the nanotube V. To do so, we performed a series of calibration experiments with theoretical support, on glass nanocapillaries without nanotubes. The nanocapillaries were sufficiently large to allow for a direct measurement of the flow (via the displacement of a meniscus of water flowed through the nanocapillary during a time interval).

Experimentally, we verified that $F_P = \alpha_{\text{exp}}\eta RV$ (where R is the radius of the capillary tip, and V the mean flow emerging from the capillary) with α_{exp} a constant close to 1. The experiments were performed using two independent methods. More details may be found in [114, 201]. Numerically, I performed simulations to compute the flow emerging from a nanocapillary with the exact same geometry as in the experiments. The idea of these

simulations is to compute the stationary flow described by Stokes equation (Navier-Stokes equation in the small Reynolds regime), with an inlet boundary condition in the capillary as an overpressure – see Fig. 2.2-a. The integration is done with a simulation method called *finite elements* using a software called Freefem++. It is specifically tricky in this situation because the description of the flow has to be done at very small scales (a few nanometers inside the nanotube) and at very large scales (several microns for the extension of the $1/r$ flow) at the same time. This required to be very meticulous in the simulation setup. Examples of flows obtained with the simulation are showed in Fig. 2.2-b to d. More details may be found in the supplement of [114].

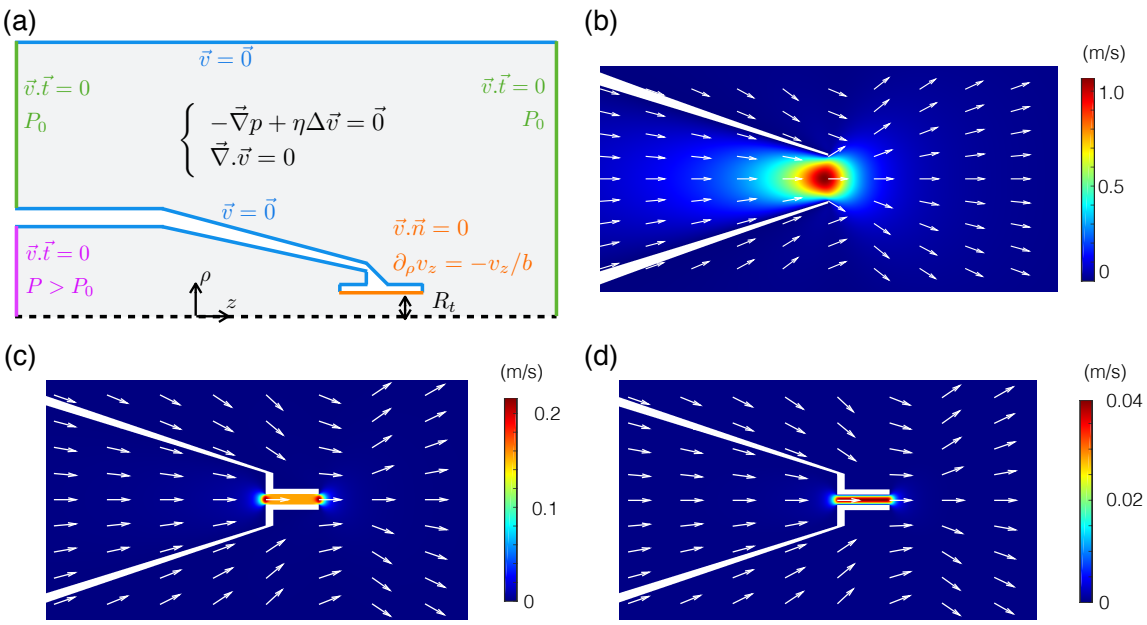

Fig. 2.2: **Finite element simulations of flow through a nanotube**: (a) Schematic of the simulation box for the finite element simulation, showing here an example geometry for a nanotube glued at the tip of a nanocapillary with a small triangular glue profile. The drawing is NOT at scale. The dashed line represents the revolution axis of the cylindrical geometry. The boundary conditions and the bulk equation solved are written in colors; (b) Flow amplitude at the nanocapillary tip (box size: 1.25 x 2.5 μm^2) (pipette minimal diameter : 250 nm) for the pipette alone; or (c) with a thin tube (inner diameter : 25 nm – box size: 1.15 x 2 μm^2) possessing perfect slip or (d) no slip inner wall boundary conditions.

Numerically, I verified that $F_P = \alpha(\gamma)\eta RV$ where α is a numerical prefactor. I performed extensive checks that showed that α was not dependent on R, little dependent on the thickness of the glass nanocapillary, not dependent on its rear radius, and not dependent on the inlet pressure P. The Stoke's friction law is thus well verified. Interestingly, α depends only on the capillary aperture angle γ, see Fig. 2.3. At small aperture angles, were the capillary becomes a tube, α reaches a constant close to 1. For large capillary angles, the parameter approaches zero. Indeed for $\gamma \to 90°$ the geometry approaches that of a pore in a wall, and

the flow is completely different. In this geometry it is the Sampson flow as $1/r^2$ [206], and the Landau-Squire flow as $1/r$ should indeed vanish. The monotonous dependence of α on γ looks rather simple, and one would expect to be able to find an analytical solution to this Stoke's problem. I tried several approaches but was rather unsuccessful.

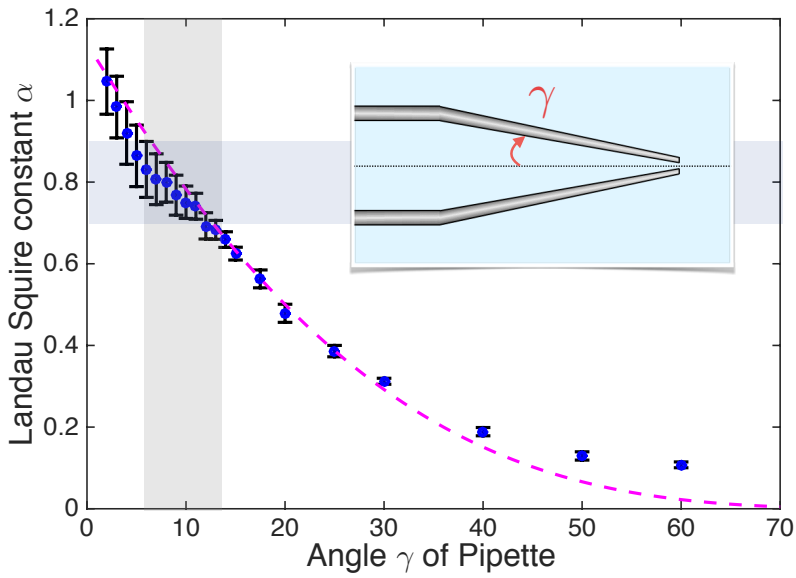

Fig. 2.3: **Landau-Squire profile**: Landau-Squire parameter α defined in the text as a function of the aperture angle of the capillary γ (in degrees). The grey area indicates the region of angles of capillary apertures used in the calibration experiments. The blue area indicates the corresponding range for α. The dots correspond to numerical simulations, and error bars correspond to the variability of α over the size of the observation box. The pink dashed line corresponds to an empirical fit of the data, and writes $\alpha = 1.1(1 - \sin\gamma)^2$.

As the capillaries used in the experiments were all pulled on the same laser puller, they all had very similar aperture angles. The numerical value of $\alpha(\gamma_{\text{exp}}) \sim \alpha_{\text{exp}}$. On a precise geometry we checked that we had excellent agreement between the experimental measurement and the numerical prediction. The calibration of the Stoke's law for the Landau-Squire force $F_P = \alpha(\gamma)\eta RV$ was thus well verified. Since the calibration was well done, we were thus able to use simulations of flows emerging from nanotubes to compute the corresponding α in those geometries, and from the experimentally measure F_P, compute the flow emerging from the nanotube V.

2.2 From flow to slip length

Performing several measurements of F_P at different pressure drops $\Delta P = P - P_0$ allows to compute in particular the permeability of the tubes via $\kappa = \eta L_t \pi R_t^2 \frac{V}{\Delta P}$, and $V = \frac{F_P}{\alpha \eta R_t}$. If the tube were a perfect no slip tube, one would expect for κ the Poiseuille permeability

$\kappa_{\text{no-slip}} = \frac{R_t^2}{8}$ such that one may compute the flow enhancement factor in the tube (the enhancement as compared to the no-slip case) as $\kappa/\kappa_{\text{no-slip}}$. We calculated this for the carbon nanotubes and found flow enhancement factors for carbon nanotubes up to $\kappa/\kappa_{\text{no-slip}} \simeq 23$ (for $(R_t, L_t) = (15, 700)$nm).

For a tube with slip length b the permeability is $\kappa_{\text{slip}} = \frac{R_t^2}{8}\left(1 + \frac{4b}{R_t}\right)$. From this equation one may expect to extract the slip length b from the measured value of κ. The story is actually a bit more complex. Indeed in the experimental setup one should take into account the permeability associated with entrance effects in the nanotube. It is possible to do so for instance using the formalism in [96], and find an approximate and better analytical estimate. Indeed there is an uncertainty on the evaluation of the constant for entrance effects, and for very small tubes the entrance effects count all-the-more since the force to push all the flow lines through such a small orifice is huge.

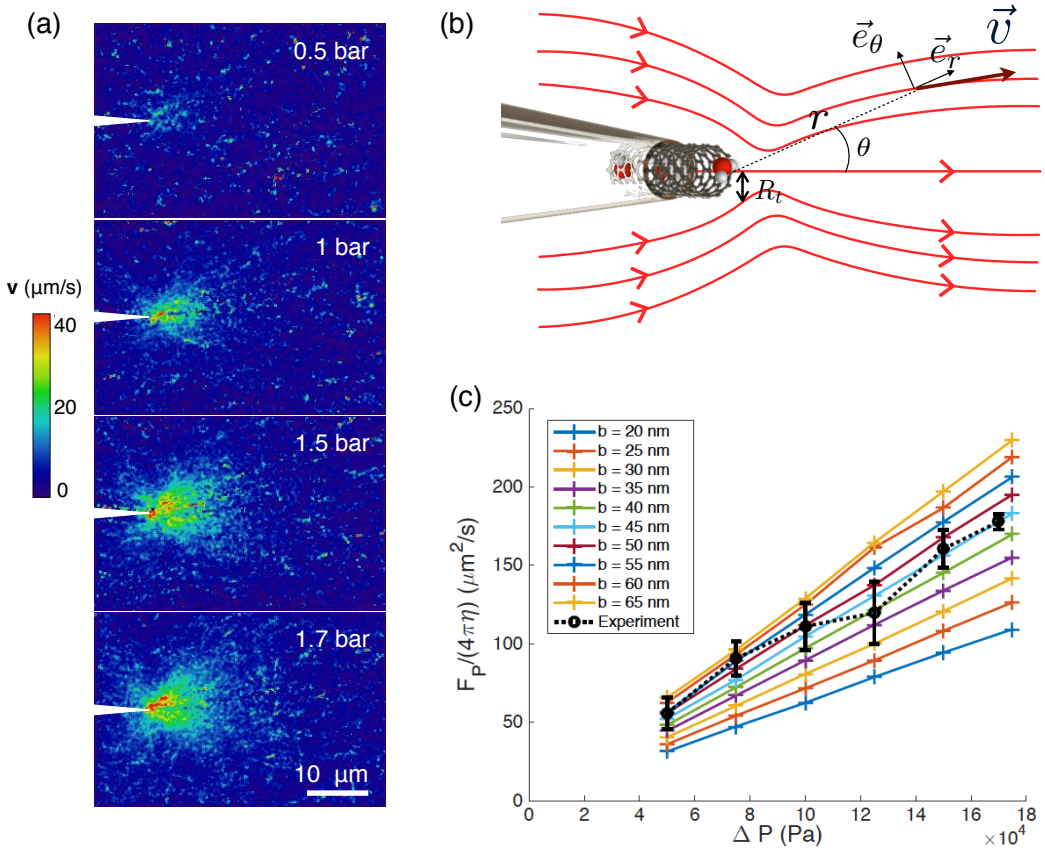

Fig. 2.4: **Evaluating the slip length from flow measurements**: (a) Maps of the velocity field near a CNT with $(R_t, L_t) =$ (33 nm, 900 nm) for various ΔP as indicated. (b) Schematic of the Landau-Squire flow field emerging from a nanocapillary with a nanotube. This flow is characterized by a force F_P as detailed in the text. (c) Dependence of the Landau Squire force $F_P/4\pi\eta$ on ΔP experimentally measured for the same CNT as in (a) and simulated for different slip lengths inside the CNT as indicated. In this experiment the slip length was evaluated to be $b = 45 \pm 10nm$.

Instead I performed several numerical simulations for each exact tube geometry using different slip lengths b inside the tube. I obtained numerically several values for $F_P(b)$ and compared them to the experimental data. Choosing the best match, I was able to evaluate the slip lengths, see for example Fig. 2.4. The slip lengths obtained numerically were coherent with the analytical estimations although all slightly smaller. I will comment the results obtained in the following chapter. Before moving on I would like to discuss briefly alternative methods for flow measurement through nanocapillaries, inspired from the Landau-Squire setting.

3 The Landau-Squire plume : the counterpart with dyes

Alternatively, one may look at the dispersion of particles within the Landau-Squire flow emerging from a tip and track the dispersion of these particles (either by using a fluorescent dye, or by using a reactive electrochemical compound) – see Fig. 2.5-a. I found that the concentration of particles diffusing through a Landau-Squire flow has a very simple form [201]

$$C(r,\theta) \simeq \frac{\Phi_0}{4\pi D r} \exp\left(\frac{Pe}{2}(\cos\theta - 1)\right). \tag{2.2}$$

A similar solution to this problem can be found in a more general form in [204], and the low Reynolds limit was obtained by [207]. Here Φ_0 is the initial flux of particles at the capillary tip, D the diffusion constant of the particles. The Peclet number Pe is connected to the Landau-Squire force $Pe = \frac{F_P}{4\pi\eta D}$. From the measurement of the concentration profile one sees that one could extract the Pe number and thus the Landau-Squire parameter F_P and thus the properties of the flow through the nanocapillary – as before.

We succesfully applied this method by tracking a fluorescent dye [201] and showed that we could measure with dyes a similar Landau-Squire force F_P as with particle tracking of colloids in the flow – see an example in Fig. 2.5–c. In this project I analyzed the experimental data and developed tools to investigate the dispersion profile reliably. One of the technical challenges is that an optical microscope equipped with epifluorescence produces a 2-dimensional image of a 3-dimensional fluorescence profile. The 2-d image thus suffers from vertical and non-local integration of the fluorescence signal. More commonly this is called the point spread function of the microscope. It can be bypassed using more advanced (more expensive) optical techniques like for example a confocal microscope.

We also investigated what signal could be captured by using a very thin carbon electrode that would thus "locally" measure the concentration of an electrochemically reactive compound. These experiments were conducted by Damien Quinton with the group of Manon Guille and Jérôme Delacotte. It is possible to measure reliably an electric current that depends on the applied pressure – see Fig. 2.5–b and I also showed that it is possible from this data to extract the Landau-Squire force and information on the flow emerging from the capillary. This work is unpublished but is another promising avenue to detect the flow

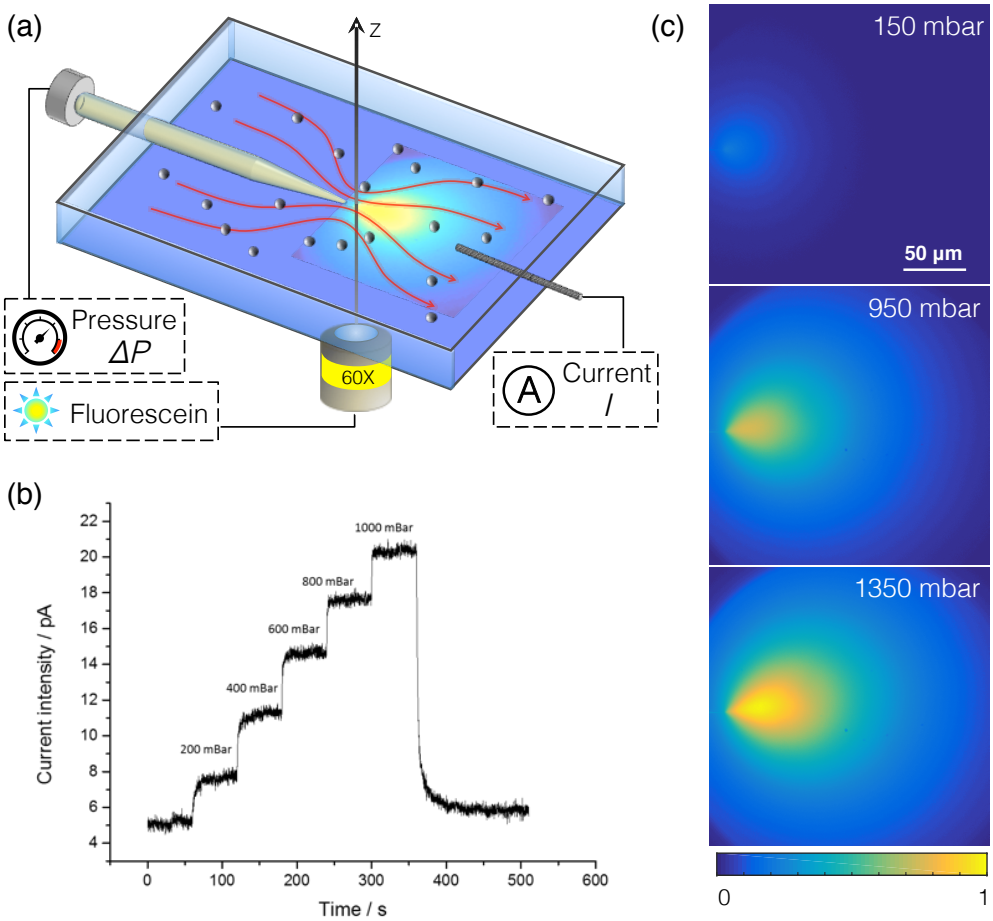

Fig. 2.5: **Other methods for indirect flow measurement**: (a) Schematic of the fluidic cell. Fluorescein and/or ferrocenemethanol is inserted in the nanocapillary. An optical microscope records the fluorescein intensity signal. A carbon fiber microelectrode of about 10μm in diameter, facing the capillary tip, records the electrochemical current. A second electrode, acting both as counter and pseudo-reference electrode, of Ag/AgCl is not shown. (b) Electrochemical current recorded at the microelectrode as a function of time before, during, and after injection at different pressures. Each pressure was applied for 1 min and gave rise to a step in current. The radius of the nanocapillary is 328 nm and it was filled with ferrocenemethanol at 100 μM and fluorescein at 50μM in phosphate buffer saline and was positioned at 60μm from the nanocapillary tip. The electrode potential was 350 mV with respect to the Ag/AgCl reference; Courtesy of *Damien Quinton*. (c) Experimental fluorescence profiles with increasing pressure drop. The nanocapillary is in a deionized water reservoir at pH 8, and filled with fluoresceinc at 1.5 mM. The intensity profiles are normalized with respect to the largest intensity measured. The radius of the nanocapillary is 120 nm. Data from [201].

emerging from very small capillaries such as nanotubes. We expect that the technical developments performed will allow to measure flows through individual biological channels such as aquaporins.

Chapter 3: Slippage in nanotubes

1 Slippage depends on the topological nature of the material

The results of (extracted) slip lengths from the Landau-Squire force measurements are reported in Fig. 3.1–c. The measurements and fits were done for 8 different nanotubes*; 5 nanotubes were carbon nanotubes (CNTs) and 3 were boron nitride nanotubes (BNNTs). CNTs and BNNTs have the same crystallography, but radically different electronic properties, with CNTs being semi-metallic and BNNTs insulating – see Fig. 3.1–a.

A first key observation from Fig. 3.1–c is that the slip length measured in CNTs strongly depends on the radius of the nanotube. As the nanotube becomes thinner, the slip length increases (highly non-linearly). This observation allowed us to resolve the long standing debate regarding the large difference in permeabilities reported previously using large-scale CNT membranes and graphene surfaces [119,160,164,165]. Indeed, if we overlap the different results found by previous experiments, we find that they can be placed nicely on the indicative trend line. The very large slip lengths obtained by [126,127] were indeed measured in arrays of extremely thin nanotubes. The slip lengths obtained by [165,208] were for larger nanotubes and correspond to the order of magnitude for similar sized nanotubes that we measured. At large radii, we find that the slip length diminishes, such that one may expect it to converge to a finite non zero value when the curvature radius becomes really large ... corresponding to the $\simeq$ 10nm slip length measured on flat graphene [117,161,162].

Very recent experiments have measured water flows through nanotubes with even smaller radii $\lesssim$ 1 nm [115] – the experiments were done for an assembly of nanotubes inserted in vesicles, and the measurement of flow was done with an indirect osmotic method. Through such small tubes, traditional fluid dynamics are expected to break down [88, 106] and one may not account for the high permeances measured in terms of a slip length. Even searching for a slip length b by accounting for the permeability measured in terms of the standard entrance and pore permeabilities yields a negative slip length, because the measured value

*There was a great technical challenge resulting in tremendous loss on the samples: first the nanotubes had to be inserted through the nanocapillaries, they had to be filled with water – which did not always work in particular for carbon nanotubes because graphene is hydrophobic – they had to survive conductance measurements to characterize their size especially their radius R_t and finally survive flow measurements with colloids sometimes sticking to the nanotube tip and blocking the flow definitely.

is too sensitive to the entrance effects and the precise geometry of the system. Aquaporins have a slightly smaller permeability as these very small nanotubes [115, 209], and their the slip lengths may be estimated to be $b \sim 3 - 10nm$ for an inner diameter of about $0.14nm$ – assuming a simple entrance effect [206]. However, this is far from describing the real mechanisms at play at these scales, and more advances describing single file – or extremely confined – transport could be made, along the lines of [208, 210, 211] for example accounting for reduced viscosity close to the tube walls.

Radius-dependent slippage was predicted inside CNTs with $R_t < 10$nm [166, 167] – see Fig. 3.1-b – and explained in terms of a curvature dependent friction [166]. Indeed when the radius of the nanotube shrinks, the incommensurability between the cristallography of the CNT and the water molecules changes, altering the electronic cloud that water molecules see. The initially "localized" electronic peaks will overlap with a shrinking curvature radius creating a "smoother" interface for water, that will thus slide with less friction. More evidence for the enhanced transport of water due to this incommensurability has been published recently [212]. The slip lengths found in the experiments confirm the expected trend, but exceed by far the values from the numerical predictions. The discrepancy shows that molecular dynamics – alone – is missing a descriptor for the situation.

2 Slippage depends on the atomistic nature of the material

A second key observation from Fig. 3.1 is the striking different behavior between BNNTs and CNTs. While the CNTs show large slippage dependent on the radius, BNNTs show absolutely no slippage. This is surprising because molecular dynamics simulations do not predict such differences [213, 214]. Indeed molecular dynamics do no take precisely into account the chemical interactions between the surface and the water, like adsorption and other effects. Recent explorations using *ab initio* simulations – that study the interactions of the electronic clouds of atoms – showed that electronic degrees of freedom can strongly affect the physical chemistry of the surfaces and lead to considerable difference in transport properties between BNNTs and CNTs [215], but even these predictions are insufficient to account for such a difference. More recent discoveries – and subsequent to our work – of adsorption phenomenon of water on the boron surface may help accounting for these differences [216]. [217] showed analytically that a link between electronic excitations and permeability could be established in carbon nanotubes, but not in BNNTs because they are insulating. [218] also pointed to the strong dependence of friction – and thus of permeability – on chirality, and also corroborated that the energy electrostatic landscape of CNTs is much smoother because of the absence of partial charges, thus reducing friction.

More detailed and systematic investigations could be done. On the experimental point of view, experiments at different salt concentrations would be insightful since the electronic properties (the surface charge) of carbon nanotubes is expected to increase with salt concentration [169] and permeability is thought to be affected significantly [219]. On the whole,

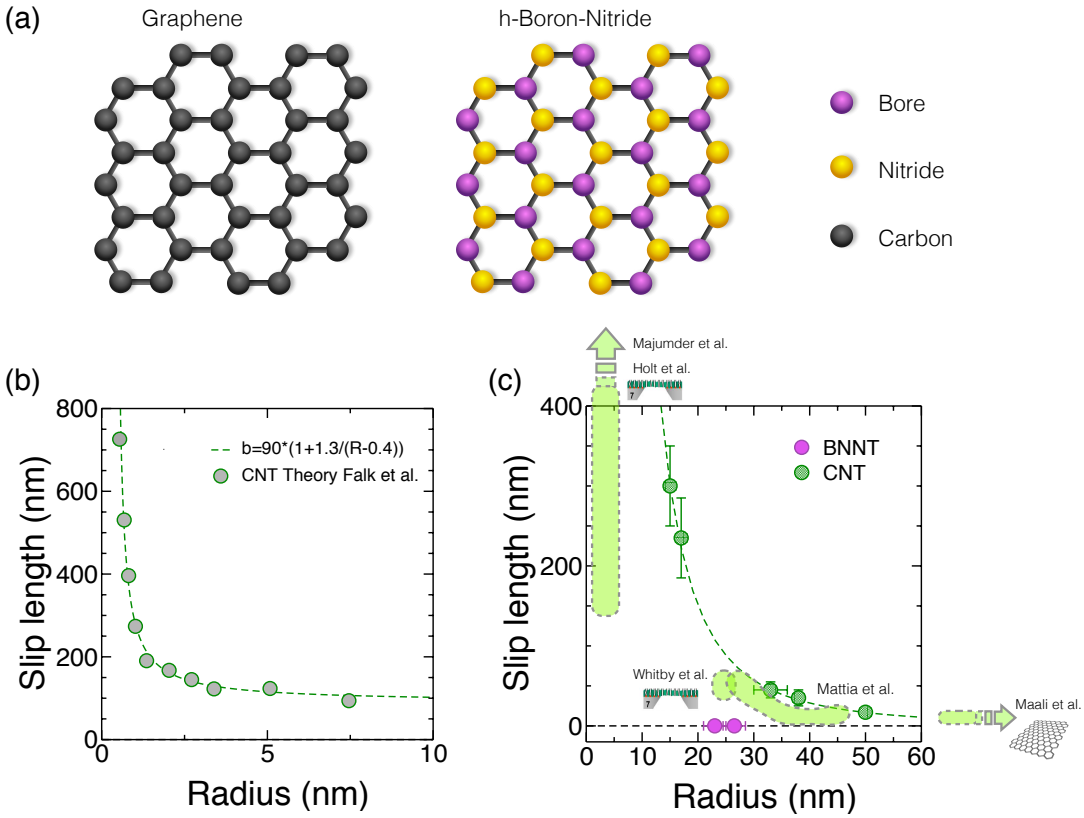

Fig. 3.1: **Slippage depends on the topological and atomistic nature of the material**: (a) Hexagonal structure of carbon forming graphene and hexagonal structure of boron nitride that are similar cristallographically but that differ in terms of their atomistic nature and also electronic properties; (b) Calculated slip length for molecular dynamics simulations of water through carbon nanotubes of different radius from [166]; (c) Measured slip length for different CNTs and BNNTs of different size [201] as a function of their inner radius. More data is added on the plot corresponding to measured slip lengths on arrays of carbon nanotubes (left) and on graphene (right). The corresponding references are indicated on the plot. The blue line is a horizontal line and the green dashed line is a guide for the eye.

these striking results of water slippage inside CNTs and BNNTs point to a certain link between the hydrodynamic flow and the electronic properties of the confining surface. Such links were not necessarily expected before, and are extremely interesting because they bridge the gap between hard (carbon) and soft (water) condensed matter physics.

Chapter 4: Mathematical formulations of slip boundary conditions

I am indebted to Frédéric Marbach for bringing up this problem at a restaurant table one day and for all the fun we had onwards. I acknowledge that I am only a physicist and that from this point on some of the mathematical science brought forward may be written with a slightly naive vocabulary.

When the boundary of a surface parallel to the flow stream is curved, then the Navier slip boundary condition will include in particular terms associated with the curvature of the surface. If one takes for instance flow past a circular sphere of radius a (with a spherical system of coordinates centered on the sphere (r, θ, φ)) one finds that the slip boundary condition Eq. 1.3 introduced by Navier writes:

$$\sigma_{r\theta}|_{r=a} = \frac{1}{r}\frac{\partial v_r}{\partial \theta}\bigg|_{r=a} + \frac{\partial v_\theta}{\partial r}\bigg|_{r=a} - \frac{v_\theta}{a}|_{r=a} = \frac{1}{b}v_\theta|_{r=a} \tag{4.1}$$

that can alternatively be written:

$$\frac{1}{r}\frac{\partial v_r}{\partial \theta}\bigg|_{r=a} + \frac{\partial v_\theta}{\partial r}\bigg|_{r=a} = \frac{1}{b_R}v_\theta|_{r=a} \tag{4.2}$$

where $b_R^{-1} = b^{-1} + a^{-1}$ is an effective slip length, more generally $b_R^{-1} = b^{-1} - R^{-1}$ with R the curvature of the surface with respect to the flow (so $R = -a$ for the sphere case) commonly called the *macroscopic* slip length [220]. Provided that the *microscopic* slip length is sufficiently large – or the curvature radius is positive and sufficiently small – , the *macroscopic* slip length may be negative, which *a priori* is rather surprising. But this does not mean that the surface creates negative friction, it just means that the stream lines have to bend and extend to follow the curvature of the flow – see Fig. 4.1.

1 The friction or partial slip boundary condition

Originally the partial slip boundary condition by Navier in [177] was written – and in math is usually written [221] – :

$$[\sigma(\boldsymbol{v})\boldsymbol{n} + \alpha\boldsymbol{v}]_{\tan} = 0, \tag{4.3}$$

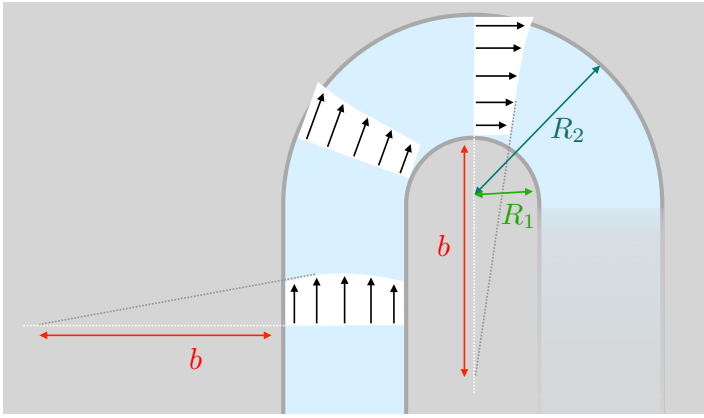

Fig. 4.1: **Apparent negative slip**: In the presence of a (sufficiently large) negative curvature radius (outer wall of the U channel) in a partially slipping channel one finds that the flow profile has an apparent negative slip length (the advection speed increases near the boundaries) because of the curvature of the medium. To phrase it differently, for conservation of mass particles that take the outer path of the U have a longer path and thus need to be faster.

where α (or $E = \alpha$ in the original book by Navier [177], and see Fig. 1.1) is a positive coefficient ($\alpha = 1/b$). Most of the mathematical results shown with $\alpha \geq 0$ can be extended to $\alpha < 0$ (from a strictly mathematical point of view, and in the time dependent case) and this because one may find energy estimations that absorb this lower order coefficient [221].

1.1 The irrotational or perfect slip boundary condition

For flat boundaries, the perfect slip boundary condition is written in any of the following equivalent conditions:

$$[\sigma(\boldsymbol{v})\boldsymbol{n}]_{\tan} = 0 \tag{4.4}$$

$$[\nabla \times \boldsymbol{v}]_{\tan} = 0 \tag{4.5}$$

In full generality, boundaries are not flat, and these conditions cease to be equivalent. To some extent, this has given rise to some confusion in the literature about which condition correctly describes a perfectly slipping boundary condition.

The boundary condition Eq. 4.4 can be seen as the limit when $\alpha \to 0$ of Eq. 4.3 (or $b \to \infty$, and called in physics the "perfect slip" boundary condition. It is used for example to account for free air-water interfaces [222,223]. The boundary condition Eq. 4.5 was first introduced by Jacques-Louis Lions in 2D in [224] and can be seen as a natural extension in 3D. This condition was used in many papers [225–230]– sometimes allowing to show mathematical results that have not yet been shown (and maybe are not true) with other boundary conditions, in particular the convergence of the Navier-Stokes equation to the Euler equation. In fact it is a more practical and convenient boundary condition because it does not generate (or at

least generates less) boundary layers. Indeed, if the Euler flow is irrotational, then it satisfies this boundary condition, and one sees that at low viscosity their is no need to establish a boundary layer to go from Navier-Stokes to Euler and match the boundary conditions.

1.2 The link between irrotational boundary condition and Navier boundary condition

The irrotational condition is actually a special case of Navier's boundary condition, where α is formally the *Weingarten map* A defined as $A(\boldsymbol{x})\boldsymbol{\tau} = \partial_{\boldsymbol{\tau}}\boldsymbol{n}$ for any tangential vector $\boldsymbol{\tau}$. In particular, in 2D A is twice the curvature $\kappa(\boldsymbol{x}) = 1/R(\boldsymbol{x})$ and thus with a slipping condition $\alpha = 2\kappa(\boldsymbol{x})$, it is equivalent to Navier's boundary condition. Note that α in this perspective has little physical sense since α is supposed to encapsulate the information about the interaction forces between the surface and the flow. More to the point, if the curvature is negative, one finds already that this would mean negative slippage, and is rather ill-defined physically.

1.3 Question

Since the irrotational boundary condition makes calculations so much easier for mathematicians, we ask if there is a physical meaning to this boundary condition. On the other hand, we are inspired by many works showing that the boundary conditions at the surface may take more general formulations beyond the linear proposition by Navier, for example at high shear rates non linear contributions appear [231–234] *. With that in mind, we also ask for more comprehension on the physical side on the consequences of the Navier boundary condition on forces in fluidic systems.

2 A new paradox with irrotational boundary condition

We work in normalized units, with a sphere of unit radius and a flow of unit speed at infinity. One checks that the Euler flow can be explicitly computed and is given in spherical coordinates by:

$$v_r = \left(1 - \frac{1}{r^3}\right)\cos\theta \quad \text{and} \quad v_\theta = -\left(1 + \frac{1}{2r^3}\right)\sin\theta. \tag{4.6}$$

This flow is the gradient of the potential:

$$\varphi = r\cos\theta\left(1 + \frac{1}{2r^3}\right). \tag{4.7}$$

*The first of the cited papers, by F. W. Brochard and P.-G. de Gennes, is rather funny: it contains no references, and is said to have been written at the end of a conference on a desk corner!

From Bernoulli's principle, the associated pressure is given by:

$$p = p_0 - \frac{1}{2}v^2 = p_0 - \frac{1}{2}\left(1 + \frac{1}{r^6}(1 - \frac{3}{4}\sin^2\theta) - \frac{1}{r^3}(2 - 3\sin^2\theta)\right). \tag{4.8}$$

The normalized pressure force in cartesian coordinates is:

$$\boldsymbol{F}_0 = \int_{\varphi=0}^{2\pi}\int_{\theta=0}^{\pi} p(1,\theta,\varphi)\begin{pmatrix}\sin\theta\cos\varphi\\ \sin\theta\sin\varphi\\ \cos\theta\end{pmatrix}\sin\theta d\theta d\varphi = \mathbf{0}. \tag{4.9}$$

We recover d'Alembert's paradox: there is no drag on the sphere.

Since the Euler flow is potential, it already satisfies the boundary condition Eq. 4.5, so there is no boundary layer at the first order. Moreover, $\Delta v = -\nabla\times(\nabla\times v) + \nabla(\nabla\cdot v) = 0$. Hence, the viscous term does not perturb the equation and the Euler flow is a solution of the Navier-Stokes equation with irrotational boundary condition. We compute the force on the sphere:

$$\boldsymbol{F}_\varepsilon = -\int_C \left(2\varepsilon\sigma(\boldsymbol{v}^0) - p^0\right)\boldsymbol{n} = \boldsymbol{F}_0 - 2\varepsilon\int_C \sigma(\boldsymbol{v}^0)\boldsymbol{n}. \tag{4.10}$$

We computed $\boldsymbol{F}_0 = \mathbf{0}$. We are left with the second term with $\varepsilon = 1/Re$. Using (Eq. 4.6) (see Methods) one checks that $\boldsymbol{F}_\varepsilon = \mathbf{0}$: there is absolutely no drag on the sphere even when the flow is viscous. This looks like a very perfect slip! However, there *should* be a non zero drag, even in the context of perfect slip boundary conditions. Since the stream lines have to be bend around the sphere, this should yield shear stress in any case, and generate drag. In this context, if one tries to define a slip length for the Euler flow, one finds a negative slip length $b = -a$, see Fig. 4.2-a. A negative slip length means that the object is accelerating particles and thus brings energy to the system. Indeed one may see that the flow lines are significantly accelerated at the vicinity of the sphere with the irrotational boundary condition, see Fig. 4.2-b. This is rather unlikely if no source of energy exists, and we thus propose to look at energy dissipation in the system to verify this hypothesis.

3 Mechanical energy dissipation between the fluid and an object

The flux of mechanical energy in the fluid is defined as $\boldsymbol{v}.\sigma(\boldsymbol{v})$ [235] (chap. 2). The rate per unit volume at which energy is being supplied by the work done by the stresses on an element of volume (neglecting the effect of body forces - so for instance gravity, that is not at play in our system) is thus: $\nabla.(\boldsymbol{v}.\sigma(\boldsymbol{v}))$. This work may be separated into three parts by developing the expression, where ultimately you manage to get rid of terms in $\nabla.\vec{v}$ because the fluid is incompressible. Nevertheless the rate at which energy is being supplied by the stresses on the total fluid volume is :

$$\mathcal{P}_{\text{stresses}} = \iiint_{\mathcal{V}} \nabla.(\boldsymbol{v}.\sigma(\boldsymbol{v}))d\tau = \oiint_{\mathcal{S}} \boldsymbol{v}.\sigma(\boldsymbol{v})\boldsymbol{n}dS \tag{4.11}$$

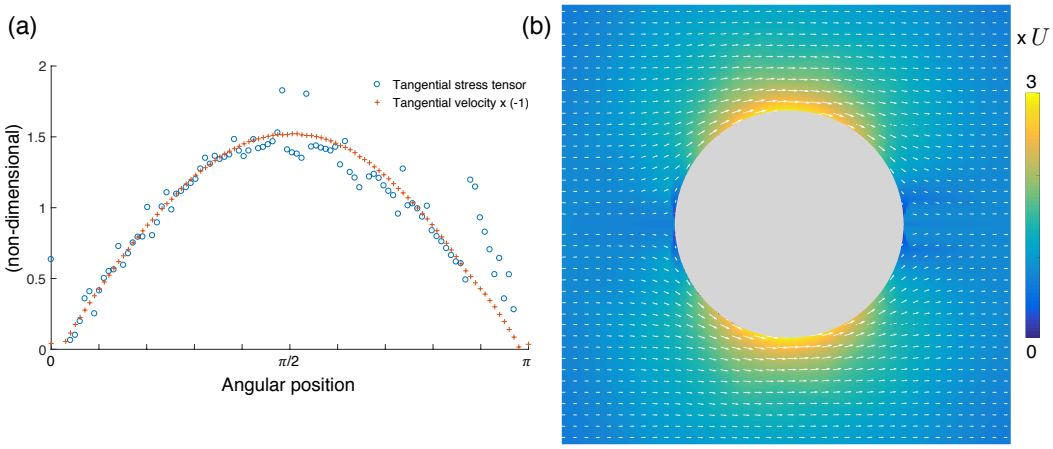

Fig. 4.2: **Negative slip in the Euler flow**: finite element simulation of the Euler flow around a sphere with irrotational boundary condition on the sphere (a) Comparison of the calculated tangential velocity and tangential stress on the sphere – the points for the stress are more scattered because they are less precise as they are a derivative – coherent with a slip length $b = -1$ in non-dimensional scale; (b) Euler flow around the sphere, the arrows in length are proportional to the norm of the local flow, with the far field flow being 1 in the $\boldsymbol{e}_z$ direction. The background color displays the amplitude of the flow fluid. Flow lines are significantly accelerated near the sphere interface.

where $\boldsymbol{n}$ is pointing outwards to the surrounding surfaces of the fluid. If one considers the spherical problem mentioned earlier, $\boldsymbol{n} = -\boldsymbol{e_r}$, and $v_r = 0$ at the boundary, resulting in (provided that the far field solution decays sufficiently fast ($|\boldsymbol{v}.\sigma(\boldsymbol{v})| = o(1/r^2)$) when $r \to \infty$):

$$\mathcal{P}_{\text{stresses}} = -2\pi \int_{\theta=0}^{\pi} v_\theta \sigma_{\theta r} \sin\theta d\theta \tag{4.12}$$

So this is the rate of energy supplied by the stresses on the fluid.

Another way of looking at it (see [236], p.24 of chapter 2, the appendix of [237]) is to think in terms of forces. Now consider a solid object in contact with the fluid. The elementary force produced by the object on the fluid is $d\boldsymbol{f} = \sigma(\boldsymbol{v}).\boldsymbol{n}dS$ where $\boldsymbol{n}$ is the normal to the interface pointing outwards from the fluid. As a consequence, the elementary work per unit time furnished by the object is : $\delta W = \boldsymbol{v}.d\boldsymbol{f}$ where $\boldsymbol{v}$ is the speed of the fluid at the interface. Thus the work per unit time produced by the object is :

$$\mathcal{P}_{\text{object}} = \oiint \boldsymbol{v}.\boldsymbol{\sigma}.\boldsymbol{n}dS. \tag{4.13}$$

To wrap it up, the power produced by the object or by the mechanical stresses is the same $\mathcal{P} = \mathcal{P}_{\text{object}} = \mathcal{P}_{\text{stress}}$, and is the work furnished to the fluid. Indeed it is by means of mechanical stresses that the object interacts with the fluid. We expect that $\mathcal{P} \leq 0$. *The object can not bring energy to the fluid.* Necessarily, the fluid either looses energy or energy does not change, because the system is isolated and its energy can not spontaneously increase (2nd principle of thermodynamics).

3.1 Application to the flow around a sphere with irrotational boundary condition

We have for the flow tensor $\sigma_{r\theta} = \frac{1}{2}\left(\frac{1}{r}\partial_\theta v_r + \partial_r v_\theta - \frac{v_\theta}{r}\right)$ and with the Euler flow above, we find first:

$$\sigma_{r\theta} = \frac{1}{2}\left(\frac{-1}{r}\left(1 - \frac{1}{r^3}\right)\sin\theta + \frac{3}{2r^4}\sin\theta + \frac{1}{r}\left(1 + \frac{1}{2r^3}\right)\sin\theta\right) \tag{4.14}$$

such that :

$$\begin{aligned}\mathcal{P} &= -2\pi\int_{\theta=0}^{\pi} v_\theta(r=1)\sigma_{r\theta}(r=1)\sin\theta d\theta \\ &= (9/2)\pi\int_{\theta=0}^{\pi}\sin^3\theta d\theta = 6\pi\end{aligned} \tag{4.15}$$

and coming back to real scale one finds $\mathcal{P} = 12\pi\mu U^2 a$ where a is the radius of the sphere. We find that $\mathcal{P} \geq 0$ – the sphere furnishes energy to the fluid – which as stated earlier is critically non physical. There is a forceless system that generates energy ! The full derivation checking the convergence of the far field to zero is reported in the Methods.

3.2 Application to the flow around a sphere with Navier boundary condition

We have

$$\mathcal{P} = \mathcal{P}_{\text{bound}} + \mathcal{P}_{\text{far}} = -2\pi\int_{\theta=0}^{\pi} v_\theta\sigma_{r\theta}\sin\theta d\theta + \mathcal{P}_{\text{far}} \tag{4.16}$$

such that if the system is perfectly slipping, namely $\sigma_{r\theta} = 0$, we find $\mathcal{P}_{\text{bound}} = 0$. There is thus a force of the flow on the sphere (and reciprocally) but this force does not dissipate any energy. This is coherent with the idea of *perfectly slipping*. This means that at the interface there is no shear stress between the interface and the fluid, and thus the energy dissipation is zero. It does not mean however that the total force acting on the sphere is zero, because flow lines are squeezed and induce a pressure field that induce a force. In the case of a no slip boundary condition, trivially $v_\theta = 0$ and $\mathcal{P}_{\text{bound}} = 0$. In this case there is no energy dissipation because at the interface the fluid is not moving. Now in the case of partial slip, we have (Eq. 4.1) and with $\sigma_{r\theta}|_{r=1} = \frac{1}{b}v_\theta|_{r=1}$ we find:

$$\mathcal{P}_{bound} = -4\pi\mu a\frac{1}{b}\int_{\theta=0}^{\pi} v_\theta^2(r=a)\sin\theta d\theta \leq 0 \tag{4.17}$$

and there is actually energy dissipation in this case because of the mechanical stresses.

The analytical expression for the flow can be found in the Stokes regime [235] such that:

$$v_\theta = -\frac{3}{2}U\sin\theta\frac{b}{1+3b/a} \tag{4.18}$$

and we find

$$\mathcal{P}_{bound} = -6\pi\eta U^2 a\frac{b/a}{(1+3b/a)^2}. \tag{4.19}$$

The far-field contribution $\mathcal{P}_{far}$ is non zero, and is exactly equal to the power consumed on the sphere by the net force on the sphere $\mathcal{F}$, such that $\mathcal{P}_{far} = \mathcal{F}U$. One can thus define the net energy dissipation as

$$\mathcal{P}^{\text{net}} = \mathcal{P} - \mathcal{F}U = \mathcal{P}_{bound} \tag{4.20}$$

The interesting point here is that one finds that at the local level there is a maximum of energy dissipation for $b = a/3$ and it is quite surprising. Nicely, this point corresponds to the maximal derivative of the drag force with respect to the slip length – see Fig. 4.3. This energy dissipation corresponds to waste energy that will probably be absorbed by heating the fluid. One could thus define an efficiency for pushing the sphere as $\eta = \mathcal{P}_{far}/|\mathcal{P}|$ which is optimal in particular for perfectly slipping boundaries.

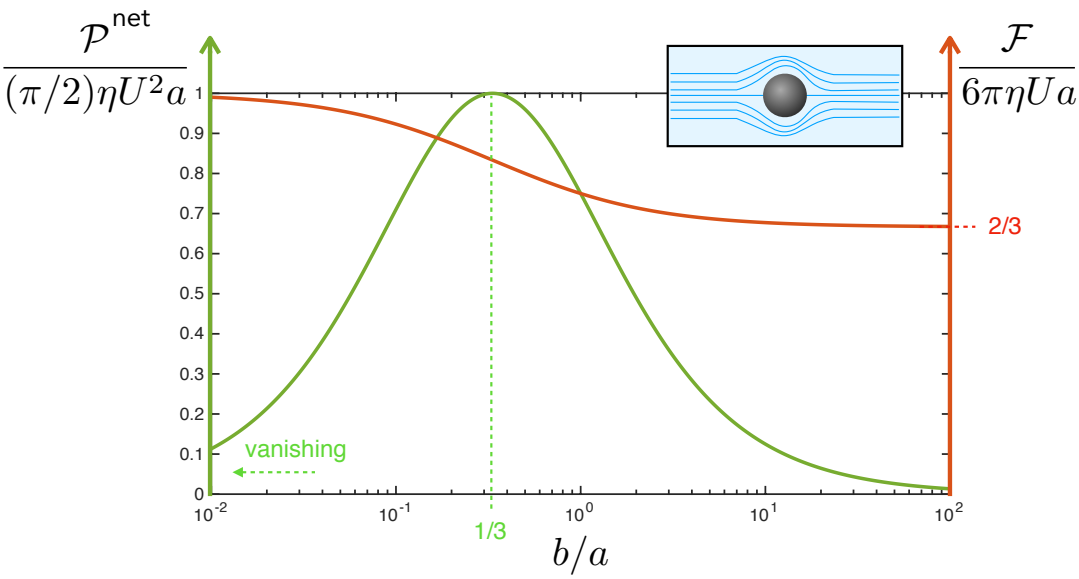

Fig. 4.3: **Dissipation and force of the Stokes' flow around a sphere**: Power dissipation in absolute value $\mathcal{P}$ normalized by its maximal value $(\pi/2)\eta U^2 a$ in $b/a = 1/3$ (in green) and drag force on a sphere in absolute value $\mathcal{F}$ normalized by its maximal value when the slip is zero $6\pi\eta U a$ from [235] (in orange). All variables are plotted as a function of the normalized slip length b/a. (Inset) Schematic illustration of flow lines around a sphere.

4 Resolution of the irrotational boundary paradox

More generally, since both conditions are equivalent provided that we make a Weingarten map between them, we find – if we apply the irrotational slip boundary condition – that on a small surface element δS:

$$\delta\mathcal{P}_{object} = +\boldsymbol{v}|_s.A(\boldsymbol{x})\boldsymbol{v}|_s\delta S = -2\kappa(\boldsymbol{x})\boldsymbol{v}|_s^2\delta S \tag{4.21}$$

where $\kappa(\boldsymbol{x})$ is the local curvature. In fact, for negative curvatures of objects (like the flow around the sphere, where the radius of curvature is $-a$), one finds that the object furnishes energy to the flow, which is non physical.

As a result, the irrotational slip boundary condition violates the second principle of thermodynamics and is thus non realistic to describe fluids at the vicinity of a *passive* interface. Now one may think of building up *active* interfaces, like self heating interfaces (think of the rear window of a car for example) or putting on micro-motors at the object surface !

Conclusion

The multiple consequences of slippage at the interface

To put this research in perspective, I would say that investigating how flows at *high* Reynolds numbers are modified by surface properties is of utmost importance in many fields, for instance to see how surface properties may affect friction on planes, cars etc – and thus reduce the consumption of fuel. Indeed, significant drag reduction has been shown to occur at high slippage on the surface [238–242], and was studied numerically for a variety of parameters [243]. Mathematically, the study of these phenomenons is very complex, due to the potentially singular behavior of boundary layer equations. These are problems connected to the boundary layer theory of Prandtl, and there remains in this field several open questions. More recently the impact of reduced friction on turbulence was more thoroughly described experimentally and numerically (with the use of Leidenfrost vapor layers around dropping spheres) [244–246]. These findings are coherent with the idea that increased slip allows to recover non turbulent flows at high Reynolds numbers, see in particular the theory of [222,223]. At this stage it would be extremely insightful to gain more mathematical insight on this question.

With a more scientific point of view, a very recent study was performed [247] and actually showed that molecular dynamics flowing in curved areas would reproduce the laws expected by Navier's partial slip boundary condition. The microscopic interactions (Boltzmann's equations) have been shown to give this macroscopic slip equation in a more rigorous way [186–188]. The Navier's partial slip (and perfect slip) boundary conditions seems thus to be the most physical law at the boundary to expect. Indeed, Navier's own derivation did adress these boundary conditions as being a direct translation of the forces between the surface molecules and the flow molecules. This corroborates the fact that the irrotational slip

boundary condition has no relevance whatsoever at a passive interface. More to the point it connects to the molecular origin of slippage and it is rather amazing to have seen this molecular origin appear especially with the measurement of slippage in the carbon and the boron nitride nanotubes [114].

What are the consequences for filtration?

Before discussing applicability of carbon nanotubes to filtration I find that it is interesting to go back to permeability. We measured permeabilities with $\kappa_{NT} = L_t \pi R_t \frac{F_P}{\alpha \Delta P}$ where α is the geometrical factor of the Landau-Squire flow, predicted numerically. The results for the different nanotubes are reported in Tab. 4.1. The intriguing result I find is that the permeability is roughly constant for all nanotubes, pointing to the fact that the organization of water molecules is the same whatever the CNT size, hinting to a sort of organized-file transport, that would in the end sum up to a single-file line for very small nanotubes with a radius close to 0.8nm [158].

$(R_t(nm), L_t(nm))_{\mathrm{CNT}}$	(50, 1000)	(38, 800)	(33, 900)	(17, 450)	(15, 700)
$k_{NT}(nm^2)$	660 ± 80	660 ± 120	720 ± 90	510 ± 50	670 ± 100

Tab. 4.1: **CNT-permeabilities** : Experimental measurement of the permeabilities for all CNTs measured in a nanocapillary with $\gamma = 5°$ and tip radius of the capillary $R_1 = 135nm$.

Because of this "organization" of water flow through CNTs, the permeabilities through these systems exceeds by several orders of magnitude the permeabilities through traditional thin film composite membranes [4,119,120] reaching similar – or better – properties as aquaporins [115].

The other advantage of nanotubes is that they are highly selective to salts provided that they are sufficiently small ($\lesssim$ 1 nm, much smaller than the CNTs used in our experiments) [115, 248]. This is a rather recent discovery, since early experiments membrane assemblies of carbon nanotubes were rather permeable to salts [4,126,127], essentially because they were made of too large nanotubes. In the prospect of increasing salt selectivity functionalization of the CNTs has been explored [124, 129, 219, 249–253] and has proved additional advantages like the reduction of fouling [129].

With these considerations, CNTs have all the requirements expected to beat the traditional permeability-selectivity trade-off, since they outperform the no slip Poiseuille flow. Recently a patent was published for carbon nanotube membranes for water filtration [254]. However designing arrays of carbon nanotube membranes is a technical challenge especially for upscaling [4, 119, 120]. The main issue is that to achieve high salt selectivity, extra small carbon nanotubes should be used ($\lesssim$ 1 nm), and thus the nanotubes should have a very narrow size dispersion. Synthesis at large scales of such nanotubes is becoming possible [130,255,256]

but now the issue is to assemble them in a regular way. Although some findings were done in terms of triggered self-assembly of nanotubes into a thin film composite membrane [257] the route to upscaling looks rather tedious and the fabricated membranes are extremly fragile. In this sense carbon nanotubes may not be the most attractive materials for water purification and desalination. A variety of other materials for filtration inspired by the channel geometry has also come into the picture, with sometimes more reliable techniques of fabrication though less amazing water properties [4, 209]. A promising avenue however lies in alternative materials based on graphene fabrication, like graphene oxide, or graphene-boron-nitride assymetric membranes [86, 117–120, 258, 259], that are slightly easier to produce and that would not suffer from the same issues for upscaling. On the whole, investigating ever more sophisticated materials may not be the best strategy to solve the challenges of filtration. Out of the box ideas have to be suggested and explored.

Part II

The Osmotic Exchanger

or

a “ topological” investigation of filtration

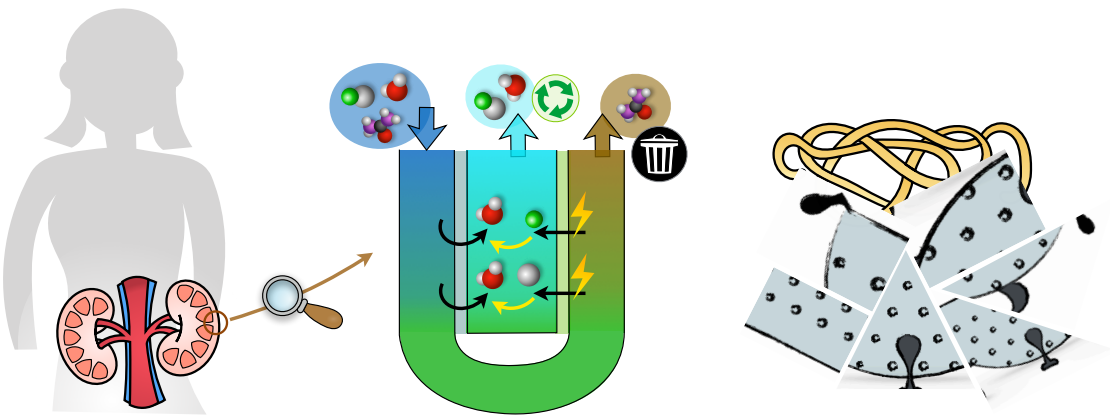

Introduction

In the perspective of improving water filtration, a necessary step for progress requires out-of-the-box ideas operating beyond traditional sieving separation principles. In this context it is interesting to investigate how biological systems are able to defy these constraints in their water cycle. They often rely on various forms of osmotically driven transport. For example in plants, osmosis is harnessed to drive water and sugars over long distances [15, 260, 261]. As we discuss below, filtration processes can also benefit from harnessing osmotic transport: this is the case in particular of the kidney.

Per day, the human kidney is capable of recycling about 200 L of water and 1.5 kg of salt, separating urea from water and salt at the low cost of 0.5 kJ/L [262] while readsorbing $\simeq$ 99% of the water input. The core of the kidney separation process lies in the millions of parallel filtration substructures called nephrons [262] – see Fig. 1. A striking feature is that the nephrons of all mammals present a precise loop geometry, the so-called Loop of Henle - in the shape of the letter "U". This loop plays a key role in the urinary concentrating mechanism and has been extensively studied from a biological and physiological point of view [262, 262–269]. The nephron operates the separation of urea from water near the thermodynamic limit, $\simeq$ 0.2 kJ/L [270], yet standard dialytic filtration systems, which are based on reverse osmosis and passive equilibration with a dialysate, require more than two orders of magnitude more energy [271]. Some attemps to build artificial devices mimicking the nephron were reported in the literature, but they rely on biological tissues or cell mediated transport, and cannot be easily scaled up and transferred to other separation devices [272–274]. Mimicking the separation process occurring in the kidney remains a challenge. Another interesting feature of the kidney as compared to standard filtration devices is that it operates at a remarkably low pressure – the arterial blood pressure – that is two orders of magnitude smaller than the pressure required for reverse osmosis [88].

In this part my goal is to take a physical perspective on the separation process at work in the nephron in order to decipher the elementary processes at work. This allows to propose a simple biomimetic design for an osmotic exchanger inspired by the kidney's Loop of Henle – see Fig. 1 –, combining a passive water permeation and an active salt pumping. Such an artificial counterpart can be implemented based on microfluidic elementary building blocks. As a side and intriguing note, I give some perspectives on how this understanding of the kidney function helps us enlighten some features of the animal kingdom.

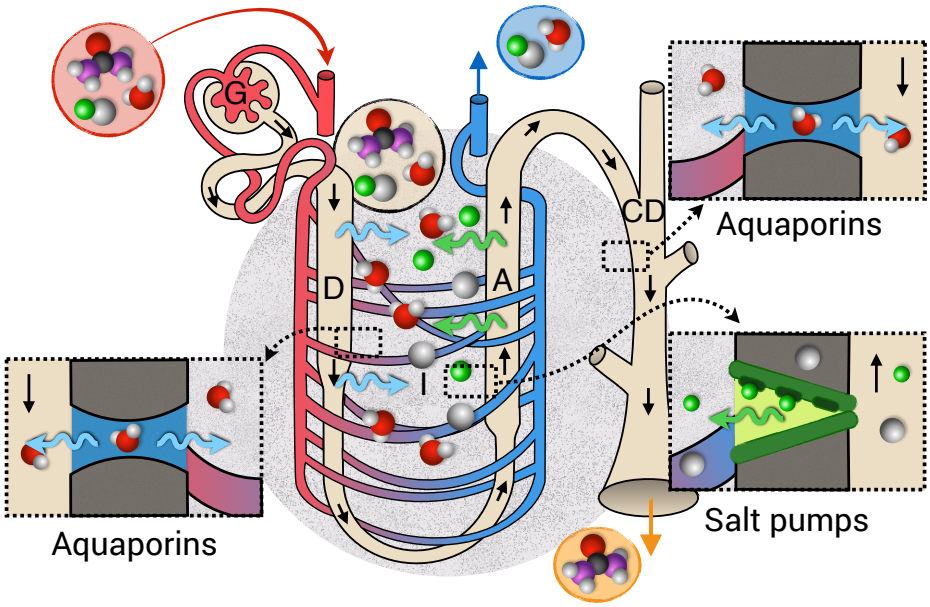

Fig. 1: **Schematic of the filtration process of urea through the nephron**. Urea, salt, and water arrive carried by the blood (red tubes and arrows) to the nephron. Urea, salt and water are separated from blood thanks to the glomureli (G); and subsequently sent into the loop of Henle (in beige) and will circulate down the descending limb (D), up the ascending limb (A) and then into the collecting duct (CD). The loop of Henle and the collecting duct are embedded in a dense tissue (the interstitium I), highly vascularized, that can exchange with the blood vessels. Along the descending limb, aquaporins on the wall allow water to traverse from the interstitium to the descending limb and reciprocally. Along the ascending limb, salt pumps on the wall use the dissociation energy of Adenosine-Tri-Phosphate (ATP) (the vector of energy in the body) to pump Sodium ions from the ascending limb to the insterstitium. Counter ions – Chloride ions – can traverse the walls by a simple carrier action to compensate charge imbalance [275]. As the amount of salt ions in the interstitium increases, the local osmotic pressure increases, and thus drives water out of the descending limb. As a result, urea is concentrated and subsequently eliminated by the collecting duct. On the walls of the collecting duct, also aquaporins are present and may allow for water reabsorption.

Chapter 1: A clever filtration engine : Harnessing osmosis

The following chapters are connected to the publication [270] reported p.124

Starting with physiological models of the nephron [264, 267], we revisit the detailed out-of-equilibrium flux balance along the exchanger, and build a minimal biomimetic model of the nephron.

1 The serpentine geometry

The model I consider is sketched in Fig. 1.1. It is a concentrating system that possesses the same primary features as the mammalian nephron: (i) a serpentine geometry consisting of (ii) a first U-loop (Henle's Loop, HL) with a descending limb (D) permeable only to water – a task performed by the aquaporins in the kidney –, while the second ascending limb (A) is coated with 'activator' pumps – accounting for the sodium pumps in the kidney – [262, 276–278]; (iii) this coil is embedded in a common loose material, permeable to both water and salt, the interstitium; (iv) the first U-loop is continued by another loop and the so-called collecting duct (CD), again permeable to water only. This model is inspired by the so-called central core models of the nephron [264, 267, 279–284]. Note that I do not take into account in this model the blood circulation, because it is not responsible for the concentration of urea in the kidney, it only consists in a parallel flow.

The initial solution entering the device from the D top is an aqueous solution with waste to be extracted – in the case of the kidney, urea–, with respective concentrations $[Water]^{\text{in}}$ and $[Waste]^{\text{in}}$. Aside from the specific geometry of the coil, an essential feature of the process is to use an 'osmotic activator' – in the case of the kidney, NaCl salt – that enters the D limb along with the mix, with concentration $[Osm]^{\text{in}}$. The terminology of 'osmotic activator' is justified by the role played by the salt in this separation process, and constitutes the main working principle of this loop: thanks to the U-loop geometry, the pumps in the A limb generate a salinity gradient in the interstitium which drags passively, via osmosis, the water from the D limb to the interstitium. The geometry of the loop of Henle thus plays the role of an *osmotic exchanger*.

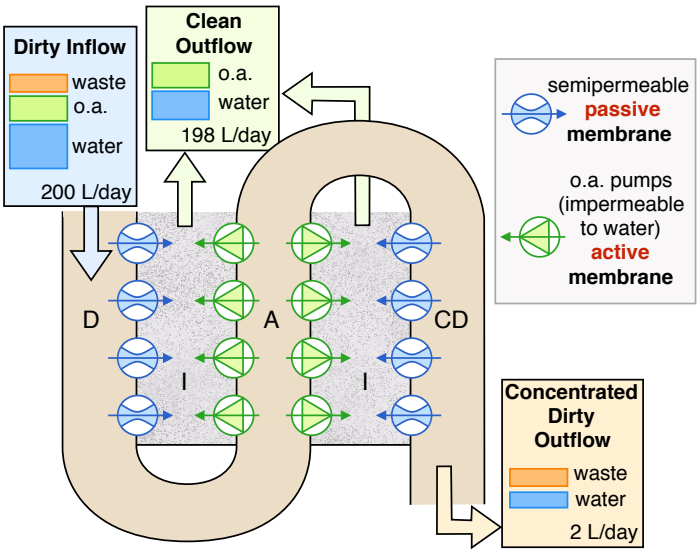

Fig. 1.1: **The osmotic exchanger filtration system.** Model for a concentrating device based on the geometry of Henle's Loop in the kidney. Water, waste and salt are carried through the loop of Henle, constituted of the descending limb (D), ascending limb (A) and continued by the collecting duct (CD). Each limb wall allows exchanges with the interstitium (I), enabling water and salt to evacuate the loop. The remaining waste is concentrated and evacuated by the collecting duct (CD).

2 Transport equations and osmotic fluxes

I now give the essential transport laws of the various components along the serpentine geometry, and ideas of the resulting fluxes. For the sake of simplicity, I develop a one dimension model along the tube length (this assumption can be justified [270] – typically a nephron limb is a few microns wide and millimetric in length [285, 286]).

Descending limb – Along the D limb, the water flux evolves due to the permeation of water under the osmotic pressure across the semi-permeable walls as [287]:

$$\frac{\partial v_D [Water]_D}{\partial x} = \frac{2P_f}{r} \ln\left(\frac{a_I^W}{a_D^W}\right) \tag{1.1}$$

where v is the velocity of the fluid, P_f the permeability of the D walls, r the radius of the limb, a^W the chemical activity of water – here, assumed to be proportional to the molar fraction of water –, D (resp. I) indices refer to variables in the descending limb (resp. the intersitium), and x is the main direction of the flow along the limbs. In the D limb, all other species are conserved.

The fluid velocity can be calculated thanks to conservation of mass in every limb. For instance in the D limb, this writes: $\frac{\partial v_D}{\partial x} = \overline{v}_{\text{Water}} \left(\frac{\partial [Water]_D}{\partial t} + \frac{\partial v_D [Water]_D}{\partial x}\right)$, with $\overline{v}_{\text{Water}}$ the molar volume of water. The hydrostatic pressure drop can be neglected [265].

Ascending limb – In the A limb, the salt – denoted in the following as the 'osmotic activator' – is actively pumped across the walls. We consider a general case where the pumps drive n osmotic activator molecules for an elementary energy cost. In the kidney, this is provided by the dissociation energy of one ATP molecule and the stoechiometry is believed to be 3 Na^+ for 1 ATP [275]. We write Michaelis-Menten kinetics to describe the activator concentration evolution in the A limb [288, 289]:

$$\frac{\partial v_A [Osm]_A}{\partial x} = -\frac{2nV_m}{r}\left(\frac{[Osm]_A}{K + [Osm]_A}\right)^n \tag{1.2}$$

where V_m is the maximum rate intake, K is the Michaelis constant, and A indices refer to variables associated with the A limb. All other species are conserved in the A limb. In particular, the membrane separating the A limb and the interstitium is considered impermeable to water.

Interstititum – In the Interstitium, equations similar to (Eq. 1.1) and (Eq. 1.2) are written for the salt and water concentrations, with the sign reversed for the terms on the right hand side. No waste is present in the interstitium. The velocity of the fluid is taken to be zero at the bottom of the interstitium.

The previous analysis yields a set of 11 coupled and self-consistent non-linear transport equations for the water, osmotic activator and waste concentrations, as well as for the velocities in the various compartments. At the entrance of the device, the fluxes of water, osmotic activator (salt) and waste are prescribed as q^{in}_{Water}, q^{in}_{Osm} and q^{in}_{Waste}. The integration of the previous system of equations yields the spatial distributions of each component and the outcoming water and waste fluxes, $q^{\text{out,CD}}_{Water}$ and q^{out}_{Waste}. (The whole set of equations may be found in [270])

3 Results: spatial distributions, fluxes and optimal separation ability

This complex system of differential equations is first solved numerically using standard methods, see Methods section. It is also possible to perform a systematic analysis of the transport equations at steady state, and find several analytical results. A typical numerical result is shown in Fig. 1.2 for the spatial evolution of the fluxes and molar fractions of the various components along the osmotic exchanger, at steady state. We overview now the results in order to gain some insight on the filtration process.

We start by looking at the absorption of the osmotic activator in the ascending limb (A). As highlighted in Fig. 1.2, salt reabsorbtion occurs typically over a length scale ℓ_c. This length scale can be constructed by balancing the input flux of osmotic activator, $q^{\text{in}}_{Osm} = \pi r^2 v^{\text{in}} [Osm]^{\text{in}}$ with the outward pumped flux, $q_{\text{pump}} = 2\pi r\, \ell_c\, V_m n$ (with V_m the intake rate

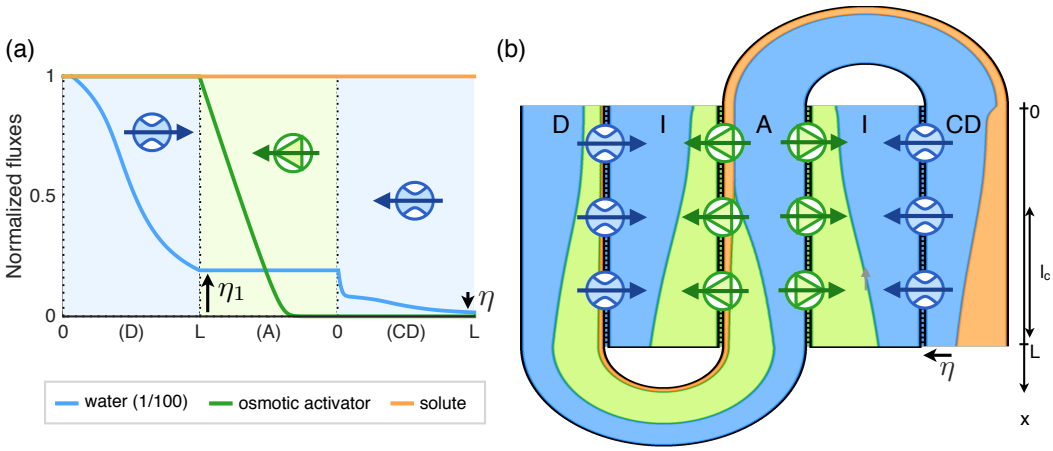

Fig. 1.2: **Spatial distributions of the fluxes and molar fraction in the osmotic exchanger** (a) Normalized fluxes of water, Osmotic activator (salt) and waste along the descending (D) and ascending (A) limbs and along the Collecting Duct (CD); in this graph, the water loss ratio $\eta = q^{\text{out,CD}}_{Water}/q^{\text{in}}_{Water}$ is the final normalized flux .(b) Spatial distribution of the molar fractions of water (divided by a scaling factor of 100), Osmotic activator and Waste along the D and A limbs and in the interstitium. Note that the interstitium exchanges with all three branches (D,A,CD); although 2 were plotted for convenience in this 2-dimensional view, they have the same composition. Numerical data are calculated with parameters $L = 4.3mm$, $P_f = 2500\mu m/s$, $n = 1$.

of the pumps), such that

$$\ell_c = \frac{q^{\text{in}}_{Osm}}{2\pi r V_m n}, \tag{1.3}$$

Using typical values for the various parameters entering this equation [270], we find $l_c \simeq 1mm$, which compares well to the total length of the nephron [285, 286]. Beyond that length scale, the activator uptake is negligible.

Because the velocity at the bottom of the interstitium vanishes, the osmotic activator accumulates there, increasing the osmotic pressure between the D limb and the interstitium. As a result, water is dragged out of the D limb into the interstitium. The concentration of osmotic activator in the D limb thus increases, and water leakage is possible until the osmotic pressure between the D limb and the interstitium equilibrates.

A simple yet key result can be obtained for the proportion η_1 of water flux remaining in the tube, after passage through the D and A limbs, *i.e.* the water loss ratio, $\eta_1 = q^{\text{out,A}}_{Water}/q^{\text{in}}_{Water}$, which characterizes the separation ability. It is obtained from the analysis of (Eq. 1.1) in the upper D limb:

$$\eta_1 = \frac{q^{\text{out,A}}_{Water}}{q^{\text{in}}_{Water}} \geq \eta_{1,\min} = \frac{[Waste]^{\text{in}}}{[Waste]^{\text{in}} + [Osm]^{\text{in}}}, \tag{1.4}$$

This lower bound can be interpreted physically in terms of the osmotic pressure balance between the D limb and the interstitium.

To achieve a good separation of waste from water in this device, the outflux of water $q_{Water}^{\text{out,A}}$ (flowing out with the waste), should be as small as possible, *e.g.* the water loss ratio η_1 should be as small as possible. Eq. 1.4 shows that the unrecovered water η_1 is limited by the initial molar ratio of the solute to be extracted to the one of the osmotic activator. So, no matter how efficient the activator pumps are or how high the water permeability of the membranes is, it is not possible to recycle more water from the system than $1-\eta_{1,\text{min}}$. Eq. 1.4 gives yet a simple understanding: a better waste concentration and higher water recycling ability is achieved when the osmotic activator/salt concentration is increased. Indeed, the larger the input salt concentration, the stronger the osmotic gradient in the interstitium that allows for an increased reabsorption of water.

For typical parameter values in the kidney, one computes $\eta_1 \sim 0.2$ and is limited from below by $\eta_{1,\text{min}} \approx 0.1$ after the first D and A limbs. At this point we note that such a water loss ratio is still in the high range of physiological data [262]. For a human being, with $\eta \sim 0.1$ and an average flux of fluid (water, urea and salt) through the nephrons of about 120 mL/min, the daily water loss would be tremendous, ~ 18 L, and accordingly not viable. This separation ability is also too low to be technologically relevant.

Remarkably, a solution to bypass this limitation has already been achieved by Nature. One may indeed observe that, in addition to the U geometry of the Henle loop, the nephron exhibits a third limb: the collecting duct (CD), that is only permeable to water as the D limb, see Fig. 1 and Fig. 1.2.

A key point is that this second limb is in contact with the same interstitium, therefore allowing to reabsorb water for a second time. A modified bound for the separation ability of the full osmotic exchanger is now given by:

$$\eta = \frac{q_{Water}^{\text{out,CD}}}{q_{Water}^{\text{in}}} \geq \eta_{\text{min}} = \left[\frac{[Waste]^{\text{in}}}{[Waste]^{\text{in}} + [Osm]^{\text{in}}}\right]^2 . \tag{1.5}$$

In Eq. 1.5, the square dependence, as compared to Eq. 1.4, originates from this second absorption step. Typically one finds now that $\eta_{\text{min}} \approx 0.01$, yielding a ~ 2 L daily water loss for a human being, very close to usual physiological observations [262]. This double loop device is therefore far more efficient than the simple Henle loop. Now, putting more limbs in series (for instance adding a third loop with a limb covered with osmotic activator pumps) does not improve further the performance because the osmotic activator uptake only happens in the first ascending limb. However, successive cycles in the osmotic exchanger system can be done, provided that a certain amount of osmotic activator is added to the mix before each new cycle.

I have demonstrated that the concentrating ability of the system may be increased by increasing the initial salt concentration. However, a higher salt concentration requires more energy to pump the salt from the A limb to the interstitium. This raises the question of the energetic performance of the exchanger.

Chapter 2: Hope for an efficient biomimetic filtration device

Beyond the separation ability estimate of the device, the energetic performance of the process remains to be assessed. From a physiological point of view, it is indeed vital for the kidney to operate at a minimal energy cost in view of the amount of water processed every day. Although some estimates of the free energy expense in models of nephron have been developed, they all fail to account for the energy provided by the salt pumps [269, 280, 290–293]. Also, it is important to compare the energy expense of such an osmotic exchanger to more standard filtration devices.

To simplify, we assume that the permeability, pump speed and tube length are adjusted so that η reaches its lower bound $\eta_{\min}$ in Eq. 1.4 or Eq. 1.5.

1 Energetic cost for osmotic exchanger

In the system described in Fig. 1.1, the energy consumption reduces to the energy required for the pumping of the osmotic activator along the A limb. The consumed power is written as $\mathcal{P} = \int_0^L \pi r^2 dx \frac{e_{ATP}}{n} N_{Osm}(x)$ with $N_{Osm}(x)$ the pumped flux of osmotic activator across the A membrane, and e_{ATP} the required energy to drive n osmotic activator molecules within a single pump, which in the case of the kidney corresponds to that of 1 ATP molecule. Using mass conservation $N_{Osm}(x) = -\frac{d}{dx}[v_A(x)[Osm](x)]$ and $v_A(L)[Osm]_A(L) = v_D(0)[Osm]_D(0)$, one may integrate explicitly the previous equation to obtain $\mathcal{P} = q^{\text{in}}_{Osm} e_{ATP}/n$. In the case of filtration through the Henle loop only (descending and ascending parts only)

$$\mathcal{P}_{HL} \underset{\eta\to 0}{\simeq} q^{\text{in}}_{Waste} \frac{e_{ATP}/n}{\eta}. \tag{2.1}$$

This is a simple and compact prediction showing that the power cost $\mathcal{P}$ diverges like the inverse of the water loss ratio η. As expected it becomes increasingly costly to obtain a higher separation of the waste, *i.e.* $\eta \to 0$ (see Fig. 2.1a, HL).

A much better energetic efficiency is actually reached by the full osmotic exchanger, in direct line with its improved separation ability. Since the interstitium is common to the U-loop and the collecting duct, the same amount of activator pumping is harvested to reabsorb

water both from the D limb and the CD. Thus, no further energetic cost is required as compared to the single U-loop. Collecting the results, one obtains:

$$\mathcal{P}_{HL+CD} \underset{\eta\to 0}{\simeq} q^{\text{in}}_{Waste} \frac{e_{ATP}/n}{\sqrt{\eta}}. \tag{2.2}$$

Eq. 2.2 demonstrates that the power consumption of the full osmotic exchanger is considerably reduced compared to the single U-loop (see Fig. 2.1-a). As a note this efficiency can be even more improved by performing subsequent cycles.

The above results can be compared to the minimal thermodynamic energy required for separation. The latter is estimated by computing the minimal work of separation for a given inward flux $\mathcal{P}_{Thermo} \simeq -q^{\text{in}}_{Waste} RT \ln(\eta)$. As shown in Fig. 2.1-a, this result is below the previous predictions in Eq. 2.1 and Eq. 2.2, as it should. However increasing the number of cycles as discussed above allows to get closer to this lower energetic bound.

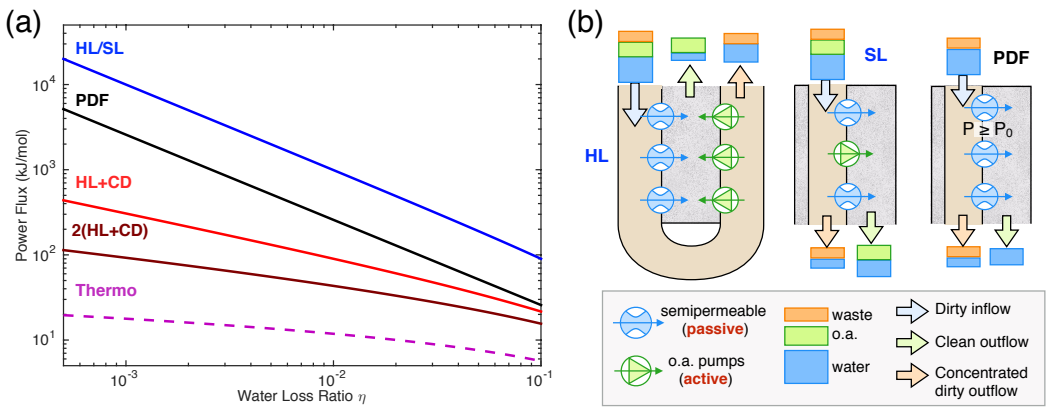

Fig. 2.1: **Comparison of filtration efficiencies of various systems** (a) Power required versus water loss ratio for the different systems. The data points are from the analytical expressions of the text. "2(HL+CD)" corresponds to 2 successive HL+CD cycles, with addition of osmotic activator in between the two cycles. "Thermo" corresponds to the minimal energy required to achieve a separation defined by a given water loss ratio. The nephron working conditions correspond to $\eta \approx 0.01$. (b) sketch of corresponding systems: HL: single U loop with ascending A and descending D limbs; HL+CD = double loop; SL = Single Limb; PDF = Pressure Driven Filtration. See text and [270] for detail.

2 Power comparison to traditional sieving processes

In the context of energy efficiency, it is of utmost interest to compare the previous exchanger device with other traditional filtration systems. For this purpose, we first consider a nanofiltration (reverse-osmosis like) system to extract the solute. This corresponds to a geometry with a single limb with water permeable walls, see Fig. 2.1-b. Water and waste only enter

the limb at a high pressure with the same composition as in the dirty inflow in the nephron. In this case, the high hydrostatic pressure allows to drive water out of the descending limb, against the osmotic pressure, and concentrates waste up to a certain degree, leaving a certain amount of water as compared to the beginning η. Accordingly this is a pressure driven filtration system (PDF). The power required to achieve this process is proportional to the mechanical energy to drive that amount of flow with the corresponding hydrostatic pressure drop and may be written as [270]:

$$\mathcal{P}_{PDF} \underset{\eta\to 0}{\simeq} q^{\text{in}}_{Waste}\frac{RT}{\eta}. \tag{2.3}$$

Interestingly, Eq. 2.3 is similar to Eq. 2.1 except for the thermal factor RT replacing the ATP energy, e_{ATP}/n. Quantitatively RT is of the order of 2.5kJ/mol, smaller than $e_{ATP}/n \simeq$ 10kJ/mol [294]. The two behave similarly as a function of η, see Fig. 2.1-a and the HL system and the PDF system are thus only different by a multiplicative factor. A major difference though is that the PDF system requires to bypass the osmotic pressure $P > P_0 \equiv RT[Waste]^{\text{in}}$ associated with the separation of the waste – as discussed in the introduction. As an alternative geometry, we also consider a 'single limb' system corresponding to a single limb where water permeable pores and activator pumps are intertwined on the wall of the limb (Fig. 1.2-b, SL). For this device we keep the osmotic activator in the solution. To some extent this system can be compared to currently used electrodialysis devices [295]. A simple analysis yields that the single limb system is basically equivalent to the HL, see Fig. 1.2 and [270].

Altogether, Fig. 1.2 demonstrates that the full osmotic activator, with one or more cycle, outperforms traditional filtration systems in terms of power efficiency, while working at small pressure.

Chapter 3: Experimental future of the kidney on a chip

These results show that with the double-loop geometry of the collecting duct in series with the Henle loop, Nature has evolved towards a most efficient geometry to filter out urea. From a technological point of view, it would be therefore highly inspiring to reproduce such a filtration device. This requires both the specific double-loop geometry highlighted above, and the use of an osmotic activator in the solution. We argue that all required ingredients are at our disposal to fabricate such an artificial nephron. Semi-permeable membranes will play the role of water permeable D and CD walls, replacing aquaporin-coated membranes. For salt – used as the osmotic activator – the ion pump functionality can be mimicked using a stack of ion-selective membranes, with an electric field as the driving force, similar in that spirit to electrodialytic processes [295]. Note that any ionic specie is in general a good candidate for osmotic activator, for it can be easily manipulated with electric fields – although monovalent species should be used to begin with – . Altogether modern microfabrication technologies developed for microfluidics would allow to directly mimick the set-up in Fig. 1.1, [296, 297] – see Fig. 3.1 –, with several devices possibly working in parallel (for more details, see [270]).

The steps towards the development of an experimentally working kidney on a chip are however not straightforward. The kidney on a chip requires to mount several different membranes in parallel in a microfluidic device, together with microelectrodes, thus necessitating to assemble some of the most advanced techniques of microfabrication including membranes in a very novel design [296–299]. The kidney on a chip could thus be the driving motor for the establishment of various new microfluidic tools. Altogether, mimicking an osmotic exchanger would allow the development of novel filtration devices and dialytic systems. A 'kidney on a chip' constitutes a paradigm change as compared to actual dialytic systems involving standard sieving process, which are difficult to miniaturize [300]: it allows for a compact design, with low energy consumption. Due to its low working pressure, it also allows to use soft materials in its design.

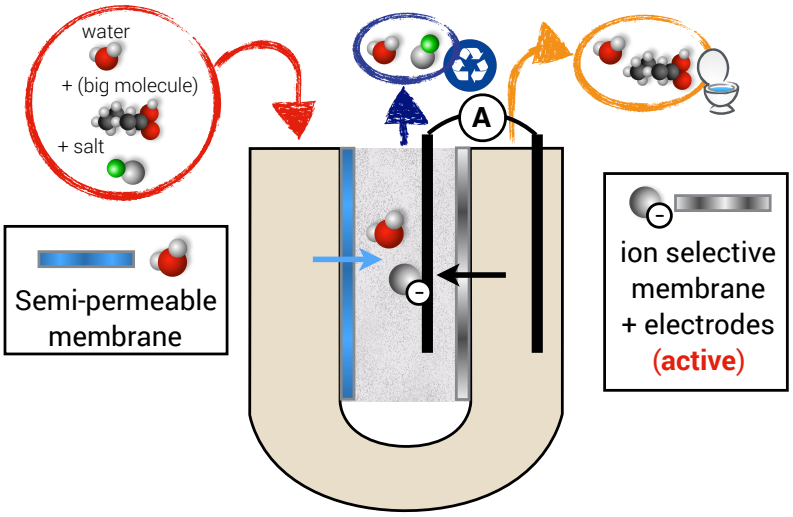

Fig. 3.1: **Experimental principle for a kidney on a chip** Schematic principle to mimic the central part of the nephron: Henle's Loop incorporating the descending limb, the ascending limb and the interstitium into microfluidic channels, communicating thanks to readily available membranes. A microfluidic channel is embedded in an interstitium, which is permeable to water and salt. The channel is separated from the interstitium by a semi-permeable membrane, only permeable to water; as well as by a cation exchange membrane which selectively allows the passage of K^+ under a given current or voltage drop imposed by electrodes.

1 State-of-the-art experiment and challenges

I am grateful to Benoit Laborie, Elisa Tamborini, and Anthony Poggioli for showing great interest in this project, and especially thank Benoit Laborie who conducted most of the following experiments.

Before assembling an entire loop, the individual parts (semi-permeable limb and ion pump) were designed and tested. The geometry is meant to separate two microfluidic channels made in polydimethylesiloxane (PDMS – classical material to design microfluidic chips) containing water with for instance KCl salt. A membrane with the good specific properties separates the two channels (for the semipermeable membrane, a STERLITECH membrane was used, were only the "active" top layer was detached from the support, and inserted into our device; for the cation exchange membrane, a FUMATECH FKE membrane was used, that is specifically designed for the transfer of K^+ ions. Ag/AgCl ultrathin electrodes were inserted into the membrane. If a current is imposed, K^+ ions are transferred through the membrane, and Cl^- ions are consumed (or created) at the electrodes. As a result, KCl may be "pumped" from one channel to another.) An example of a working setup of an ion pump is given in Fig. 3.2. A working semipermeable membrane can also be embedded in such a structure though the results are not reported here.

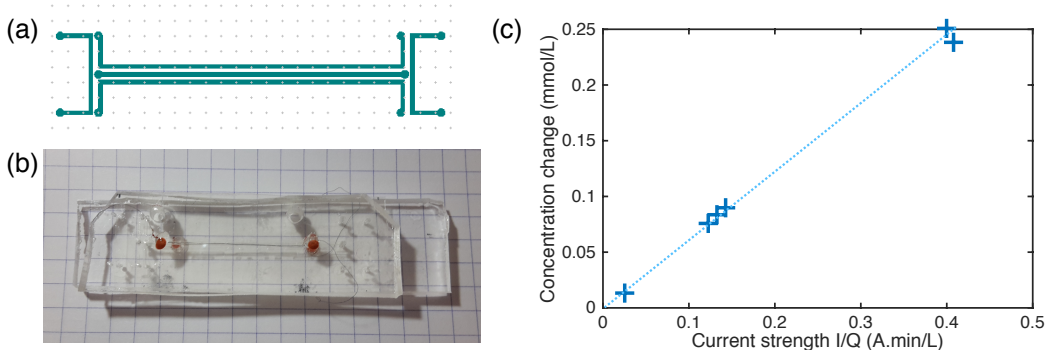

Fig. 3.2: **Experimental evidence for an ion pump channel** (a) Mask for the PDMS channels: the central channel is 600μm wide, 250μm high, and 40mm long. The parallel channels are meant to be filled by PDMS after alignment of the upper and bottom channels on both sides of the ionic selective membrane to attach the membrane to the structure. The membrane is a cation exchange membrane from FUMATECH, FKE. (b) Working setup (the small squares on the sheet below are 5mm). The membrane is transparent (FKE, thickness of about 50μm) and the electrodes (Ag/AgCl, 50μm in diameter) may be seen as small bright filaments. (c) Concentration drop at the end of the channel for an initial concentration in [KCl] of 10^{-3} mmol/L as a function of the applied current I between the electrodes and imposed flow Q through the channel. The line is a guide for the eye. *Data and setup from Benoit Laborie.*

I review below some of the main challenges for fabrication of these separate elements and for the assembly of the two of them into a kidney on a chip:

- **Insertion of a membrane in a microfluidic setup**; one of the main hardships was to avoid leakage of the channels through the borders of the membrane. The difficulty being that "gluing" the membrane to the PDMS with a waterproof joint was not necessarily obvious and rather membrane dependent. A tedious method was (as in Fig. 3.2) to use liquid PDMS with APTES ((3-Aminopropyl)triethoxysilane) in side channels – side channels are filled and then reticulated, hopefully clutching to the membrane –; another more practical method was to use double-sided tape.

- **Insertion and consumption of the electrodes**; the electrodes being extremely thin it is rather tedious to insert them into the long microfluidic channel. Another tricky hardship is that to pump salt from one side to another the electrodes are slowly consumed, and as they are extremely thin, after 30 min the electrodes are fully consumed, leaving no AgCl to be depleted. An idea to bypass this issue may be either to use different electrodes; or a mix of cation and anion exchange membranes with recombination with platinum electrodes for instance; or a reversible setup, capable of functioning both ways, such that once AgCl is fully depleted on one side, the whole setup is reversed.

- **Measurement of the output concentration**; a technical challenge is to measure the output concentration from the channel. Indeed, as the flux through the channel is rather

slow, a very small quantity of fluid is outputted (typically within 30 min barely 1mL may be obtained). To measure the conductance and thus the concentration of such a small amount of fluid, one should rely on alternative conductance measurements (other than the standard conductance probe that requires a few mL to make a measurement). A small microfluidic device with a thin deposit of gold electrodes was tested. It has a capacitive response depending on salt concentration. Ideally, the output fluid would directly enter this microfluidic chamber and the concentration of the fluid would be measured continually.

- **Assembly into the kidney on a chip**; ideally one would imagine to create a single interstitium and assemble both membranes on top of the interstitium. This is a clear technical challenge because serious leakage may occur between the interstitium and the point were the membranes are "attached" one next to the other. A way to bypass this issue is – instead of assembling membranes on a "single" interstitium – to assemble two U loops together, one on top of the other, with one side were branches are separated by a semipermeable membrane, and the other by the water pumps. The interstitium, now in the shape of a U loop, has to be flowing as well for the kidney on a chip to function.

2 Experimental future explorations

Pursuing the microfluidic approach with solid membranes is maybe not the most ideal path to design the kidney on a chip. Note that several authors have claimed to construct a kidney on a chip [301–303] but still none of them is capable of introducing and mimicking the advantageous geometry of the Loop of Henle. [304] acknowledges that this is still one of the great challenges.

Regarding the geometrical approach of the device, one may think about doing either true 3-dimensional microfluidics, with several stacks of membranes [305]; the trick being how to connect channels that are one on top of the other. This may be feasible with the recent progress in designing true 3-dimensional microfluidics [306, 307]. Another idea is to due real 2-dimensional microfluidics, in the sense that every channel is on a single layer, and channels are permeating via quasi vertical membranes. A way to do that is to *melt in* a component to act as the membrane. This was successfully done for ion selective membranes and semi-permeable membranes [308–310]. There are several other ideas to desalinate water or guide ions that could also be harvested in this purpose [55, 311].

Chapter 4: Understanding kidney filtration in the animal kingdom

1 The mammalian kidney

The mammalian kidney obviously encapsulates many more features than the ones that are explored in this "biomimetic approach".

For example, we took so far all parameters describing water leakage and activator uptake to be uniform along the tube. Introducing for instance a spatial variation of the distribution of pores along the descending limb could actually help reaching the lower bound limit of Eq. 1.4. Since water leakage is essentially limited in the upper part of the tube, where no supplementary activator uptake arrives from the facing part of the ascending limb, one expects that the distribution of pores should be larger at the top of the tube: this is confirmed by analytical results and numerical simulations (see [270]). A 3% decrease in the water loss ratio is observed when the pore density are distributed linearly from twice their original density at the top to 0 at the bottom. Interestingly physiological data show that the permeability is generally measured to be higher at the top of the descending limb than at the bottom, in agreement with the previous argument [276]. Similarly, varying the distribution of pumps can also help reaching the limit of Eq. 1.4. An increase in the distribution of pumps at the bottom of the kidney is observed experimentally [312]. From our analytic calculation, one can also predict that this corresponds to decreasing the water loss ratio. Numerically, a 6% decrease in the water loss ratio can be reached with only a 50% linear variation on the pump density, with higher density at the bottom.

The exploration of the mammalian kidney can be extended in many more ways – with a desire to improve the *physical* mechanisms at play, specifically how flow rates and other physical quantities impact the biological result – extensive and quantitative modelling is being performed already [267–269]. For instance, the role of periodic inflow – a consequence of periodic heartbeat – is an interesting question, it also connects to the idea that all of these processes are performed critically out of equilibrium. The transient establishment of the sharp concentration gradients should also be investigated.

2 Desert birds

Another conclusion of our analytical results is that the length scale of salt reabsorption ℓ_c does not depend on the length of the limb L in Eq. 1.3. As a result, even if L increases, salt will always be reabsorbed on the same length scale ℓ_c at the bottom of the ascending limb. However, the region of length $L - \ell_c$ at the top of the interstitium increases. In this region, concentrated salt coming from the bottom of the intersitium continues to be diluted by progressive water uptake under the osmotic pressure, see Fig. 1.2-b, as said earlier.

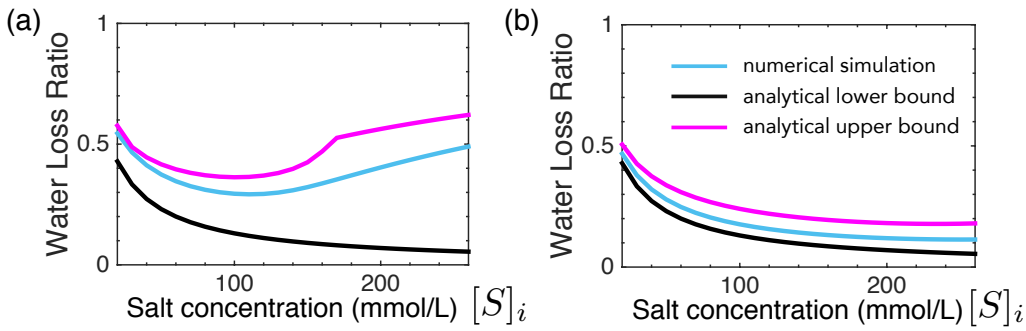

(c)

Name	House Sparrow	White-Crowned Sparrow
Visual		
Limb length	**2.2 mm**	**1.9 mm**
Migration	None	Migrating
Habitat	Arizona, dry seasons	Temperate forests

Fig. 4.1: **Influence of nephron length on reabsorption** Evolution of the water loss ratio (simulation and analyical estimates) with increasing initial salt concentration, for typical parameters of a rat kidney [270] and Michaelis-Menten constant $n = 1$, permeability of the descending limb $P_f = 1250\mu$m/s, and nephron length $L = 2.7$mm (a) and $L = 6$mm (b); (c) Comparison of very similar birds, the data is from [313] and the photos are a courtesy from *Manx Bird Photography*.

Note that it is also possible to derive an (approximate) upper analytic bound $\eta_{\max}$ for the water loss ratio η, by solving the equations on the species of the descending limb in the higher and deeper parts of the limb, see Supplemental of [270]. The upper bound $\eta_{\max}$ converges to the lower bound $\eta_{\min}$ defined by Eq. 1.4 in the limit of large pore permeability and/or long tube. For typical parameter values in the rat kidney, doubling the length decreases the

water loss ratio by 60% – see Fig. 4.1-a and b. It is fascinating to see that also in the animal kingdom evolution has followed these "rules" for animals living in draught conditions. For some time there were measurements that showed that the length of the limbs were correlated to the concentrating ability of the animals [314], however when more data became accessible the message was not as clear [315,316]. Obviously the concentration ability depends on many other parameters: the number of nephrons in the animal's kidneys, the flow rate in these kidneys (heart beat is not a constant in the animal kingdom !) and the rule of thumb does not apply. Be that as it may, [313] was able to compare two very close bird species (with similar body weight, and kidney weight *etc.*) and found that the specie living in the driest conditions had evolved to have a nephron length slightly longer than it's counterpart living in more temperate regions – see Fig. 4.1-c.

3 Sharks and rays

Another question about osmosis arises when thinking about animals living underwater. Indeed animals living in seawater and in freshwater do not face the same constraints at all. Animals living in seawater should protect themselves from dehydration because the osmotic pressure tends to empty them of their water, while it is the opposite for animals living in fresh water. I heard that salmons that leave the ocean to go upstream to reproduce in freshwater would generally die at the end of the journey – and I'm not sure wether this is a consequence of bear activity (eating them) or of them having a hard time to adapt to these rough water conditions – but some litterature does seem to corroborate the latter idea [317]. Most fish rely on scales to make their skin more impermeable to water.

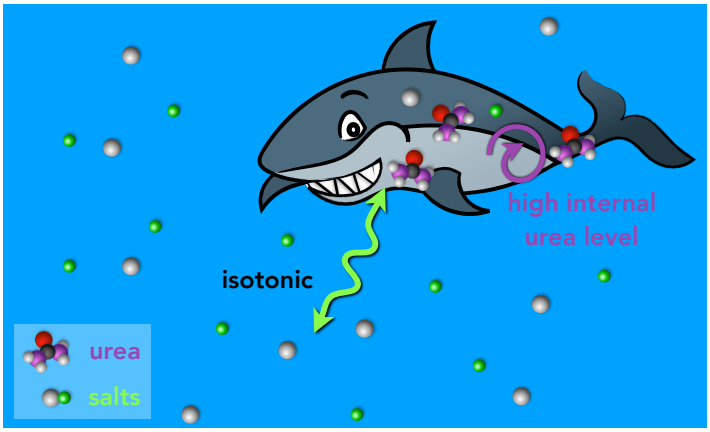

Fig. 4.2: **Osmoregulation of a shark** To face the osmotic pressure between the inner body and the surrounding seawater, sharks rely on high internal concentration of urea throughout their body.

Elasmobranchs (like sharks and rays), that do not have scales, harvest a different mechanism to control this high outflux of water by the skin: they increase the osmotic pressure inside their body in particular using urea [318–320]. When rays or sharks are killed – to eat

them essentially – the urea in their skin decomposes and creates ammonia that is very smelly and has a powerful taste. I never ate shark myself – this is forbidden by the United Nations Organization because sharks are mostly endangered species – but apparently shark meat is indeed very unusual – and apparently tastes very bad !

Conclusion

Altogether, mimicking an osmotic exchanger would allow the development of novel filtration devices and dialytic systems. A "kidney on a chip"constitutes a paradigm change as compared to actual dialytic systems involving standard sieving processes, which are difficult to miniaturize [300]: it allows for a compact design, with low energy consumption. Due to its low working pressure, it also allows to use soft materials in its design.

Such systems could be used advantageously in the pre-treatment stage of standard desalination processes. Pretreatment to separate the basic contaminants from salty water [66] typically costs more than 0.3 kWh/m^3 in reverse-osmosis plants [47,321] (to compare to the total power required to desalinate water, as stated in the Introduction, about $3-4$ kWh/m^3). Using recent progresses on ion selective membranes (e.g. monovalent selective) [322–324], the "kidney on a chip" geometry could effectively provide decontamination and deionization of targeted heavy ions and significantly diminish water hardness. This would reduce the corresponding energy cost and considerably improve the global energetic efficiency of the desalination process.

More inspiration could certainly be drawn from the kidney. For instance, the ionic pumps responsible for sodium reabsorption in the ascending limb are able to discriminate between sodium and potassium ions [275]. So far, no one but Nature succeeded in making such a monovalent specific membrane. One key feature of selection and filtration occurring respectively in these pores and in the nephron is that the transport is performed out-of-equilibrium. In the nephron, alternating heart beat and variable concentrations of components with time are a feature of transport that we have not explored. Also in the very selective aquaporines, fluctuations and vibrations of the molecular structure are seen [90] and their impact should be studied.

Part III

Out of equilibrium water transport

or

an “ active” investigation of filtration

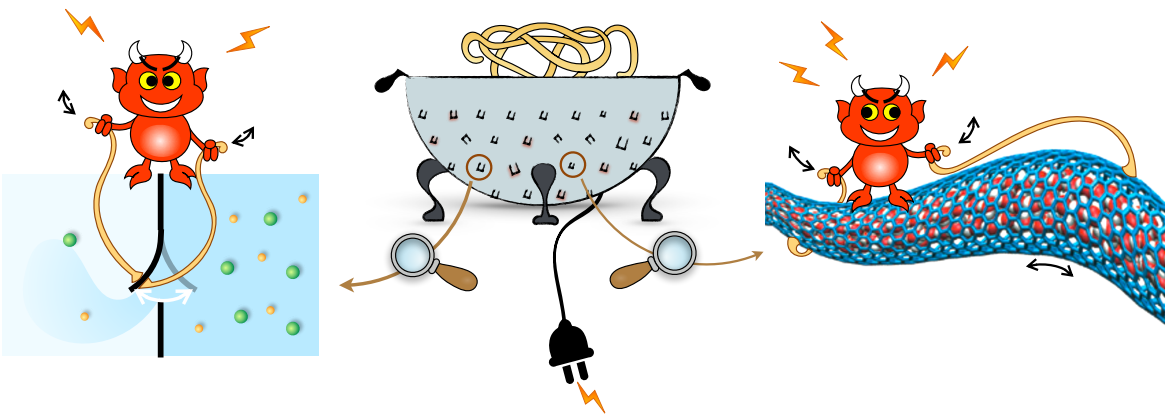

Introduction

"Everything that living things do can be understood in terms of the jigglings and wigglings of atoms". This quotation by R. P. Feynmann highlights the importance of fluctuations and dynamics in living matter. Transport and selection driven by fluctuations in biological nanopores is no exception to this rule and has been widely investigated [150–154, 325]. Surprisingly long lived fluctuations in molecular dynamics of proteins have been discovered and were very early believed to have an intimate connection to their selectivity properties [326]. In particular the selectivity of the potassium channel KcsA (see Fig. 1-d and e) is now attributed to the molecular scale fluctuations of the channel structure [151]. In other protein channels, Nature is even able to distinguish quasi similar ions, *e.g.* like sodium and potassium, [275]. Similar observations have been made in (non-living) fluid phases, where bulk hydrodynamic fluctuations dramatically affect nanoscale transport [327], see Fig. 1-a. More recently, numerical simulations have noted the impact of phonon modes in carbon nanotubes on the transport of particles confined within them [328–330], see Fig. 1-b. Going upscale, vascular motion in fungi – micron scale, see Fig. 1-c, intestinal contractions, and microfluidic surface waves affect transport, and at much larger scales, surface waves in oceans [331], are known to influence mixing and dispersion. While these observations – which span a considerable range of length scales – point to a quantitative impact of surface agitation on the transport and selection in confined geometries, a general theory, predicting the dependence of transport properties on the surface fluctuations, is lacking. Moreover, so far no artificial counterpart has been designed up to now to reach such a fine selectivity – as compared to Nature.

In this context I explored the possibility of *active sieving*, harnessing non-equilibrium dynamics to separate particles across nanopores. A Maxwell demon is the (utopian) prototypical system able to perform separation on the basis of transfer of information [332]. This corresponds accordingly to a non-equilibrium situation, baring some analogy with active matter, which allows to bypass to some extent the equilibrium constraints for better separation. Furthermore, I explored the possibility of *active transport*, mediated by surface fluctuations, and provided the general theoretical framework to quantify transport in this context.

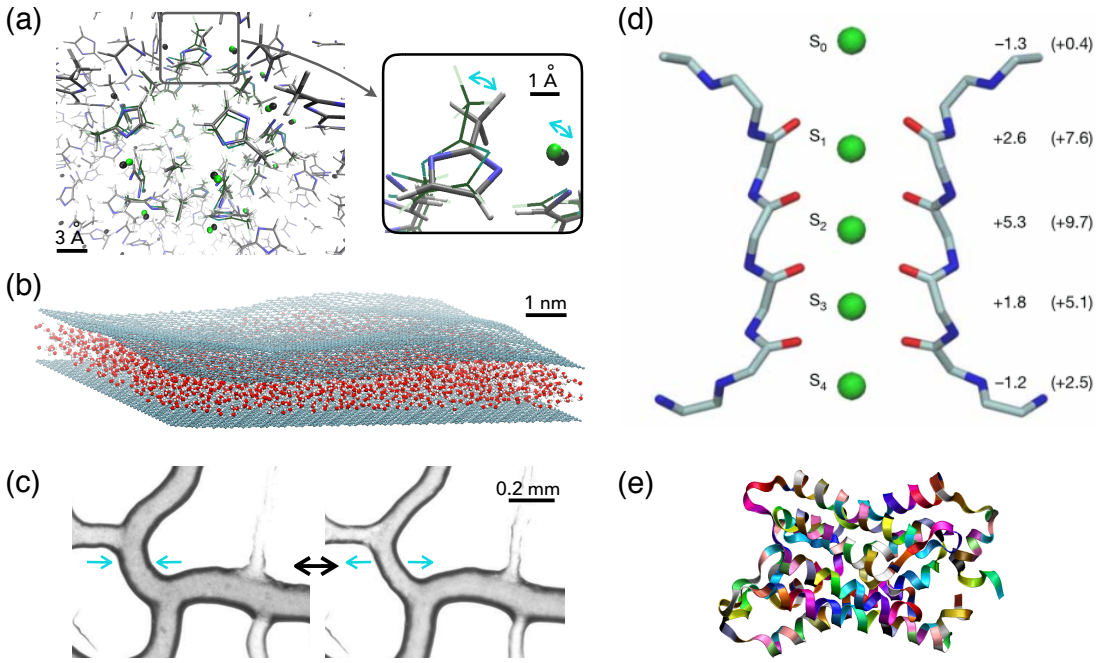

Fig. 1: **Active and passive fluctuations at the nano to micro scales influence transport**. (a) Superposition of a unit cell of the Zinc Imidazolate Framework-8 at 300 K at two time points separated by 3 ps (grey shade versus green shade). The right inset shows a zoomed view (*Courtesy of Romain Gaillac*) (b) Thermal surface ripples on graphene over water (c) Bright field image of an individual *physarum Polycephalum* demonstrating active periodic vascular contractions with time, with an amplitude typically ranging from the left image to the right (*Courtesy of Gabriel Amselem*). (d) Ion channel KcsA from [151] where the selective passage of K^+ ions is conditionned by fluctuations of the protein bonds. (e) Aquaporin AQP-1 ribbon representation from [333] where fluctuations at atomic scale should also influence the passage of water, that can only pass in a single file way.

Chapter 1: Active selection across nanodoors

The following chapter is connected to the publication [334] reported p.166

Here I explore a simple situation, where an external mechanical or electrical action modifies pore properties, thus creating some blind – "crazy" – Maxwell demon. Typical geometries of driven nanopores under consideration are sketched in Fig. 1.1: a driven nano-gate; a pore with a fluctuating size; or a pore whose surface charge may be externally gated. Such geometries are of special interest in the present study since they are amenable to further experimental investigations – see Fig. 1.1-d.

To model separation across these systems, I build on the pioneering work of R. Zwanzig in Refs. [335, 336], who considered the translocation rate of molecules through fluctuating pores. I consider as a supplementary ingredient that the opening of the nanopore is forced externally at a given frequency ω. This is the characteristic *active* part of the device.

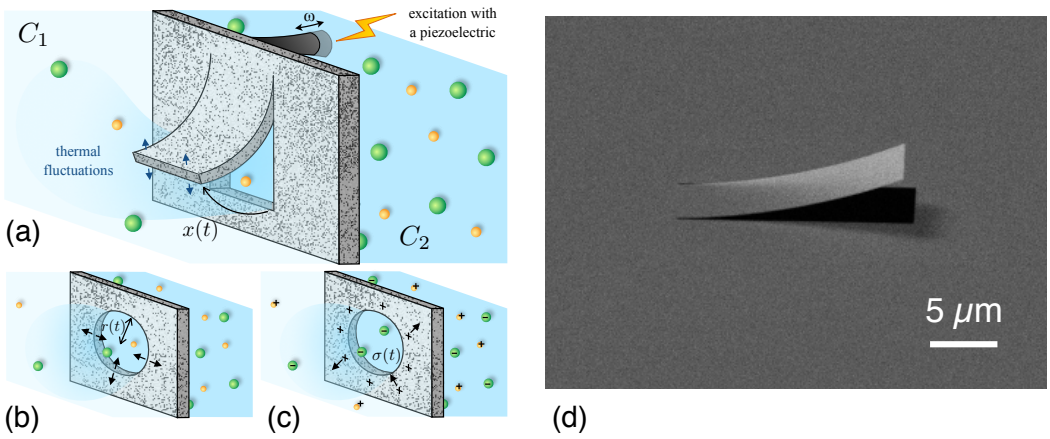

Fig. 1.1: **Active nano-doors**. (a) - A driven nanodoor in a membrane, submitted to opening by thermal fluctuations and by external application of a periodic excitation. (b) - Circular nanopore with fluctuating size and (c) - with fluctuating charge. (d) Scanning electron microscope $45°$ view of a Si-N membrane, with thickness $100nm$, carved by focused ion beam in the shape of a door. *This door was realized with the help of the IMPMC MEB-FIB platform at Université Pierre et Marie Curie.*

1 The framework for permeance of active nano-pores

I consider the effusion of a solute (with concentration C in a reservoir) across a nanopore. Pore gating which controls the translocation state across the nanopore is characterized by an internal parameter x: for example the radius of the pore, the door opening, or the surface charge, see Fig. 1.1. In line with Zwanzig's model of Refs. [335,336], I assume that the solute concentration C relaxes according to the following leakage equation:

$$\frac{dC}{dt} = -K(x)C, \tag{1.1}$$

where $K(x)$ is the x-dependent leakage constant. It is proportional to the mobility of the solute. It also depends on the characteristics of the gating. For steric gating, x is merely geometrical: for the circular pore in Fig. 1.1b, x is the radius r of the pore and $K(r) = k'r^2$, while for the nanodoor x is the aperture of the door and $K(x) = k|x|$. For electric gating – when the pore is charged, see Fig. 1.1-c, x is proportional to the surface charge of the pore Σ and for small nanopores one may model $K(x) = k" \sqrt{1+x^2}$ (see [270]). The constant k (resp. k' and k'') defines the mobility of the solute.

I am interested in the separation of small sized particles (say, ions, colloids, polymers...) effusing through nanometric sized pores. Accordingly the internal parameter x is further assumed to evolve dynamically due to (i) thermal noise – expected at the nanoscale –, and (ii) some external forcing which drives an oscillation. To simplify the discussion, I assume that the nanopore is excited such that its *average* opening x oscillates at a frequency ω, and I further model the effects of thermal noise by a simple Langevin equation for the excess internal parameter $\delta x = x - \langle x \rangle$:

$$\begin{aligned} \langle x \rangle &= x_0(t) = x_0 \sin(\omega t) \\ \frac{d\,\delta x}{dt} &= -\lambda \delta x + F(t) \end{aligned} \tag{1.2}$$

where $F(t)$ is a gaussian white noise. The second moment of δx is $\langle \delta x^2 \rangle = \theta$, and the fluctuation-dissipation theorem at equilibrium imposes $\langle F(t)F(t') \rangle = 2\theta\lambda\delta(t-t')$. The goal is now to obtain more information on the evolution of the solute concentration averaged over the noise: $\langle C(t) \rangle$.

From Eq. 1.1 and Eq. 1.2 it is possible to establish an equivalent Schmoluchowski equation (see the Methods for details) on the average value of C at time t and key feature x, $\bar{C}(x,t)$:

$$\frac{\partial \bar{C}}{\partial t} = -K(x)\bar{C} + \frac{\partial}{\partial x}\lambda\theta\frac{\partial \bar{C}}{\partial x} + \frac{\partial\left(\lambda(x-x_0) - \frac{dx_0}{dt}\right)\bar{C}}{\partial x} \tag{1.3}$$

The time-dependent concentration $\langle C(t) \rangle$ is accordingly defined as $\int \overline{C}(x,t)dx = \langle C(t) \rangle$. The Smoluchowski Eq. 1.3 can be solved analytically for some specific forms of $K(x)$ (in particular for $K(x) \propto x^2$). Alternatively I solve Eq. 1.3 numerically, to deduce the time

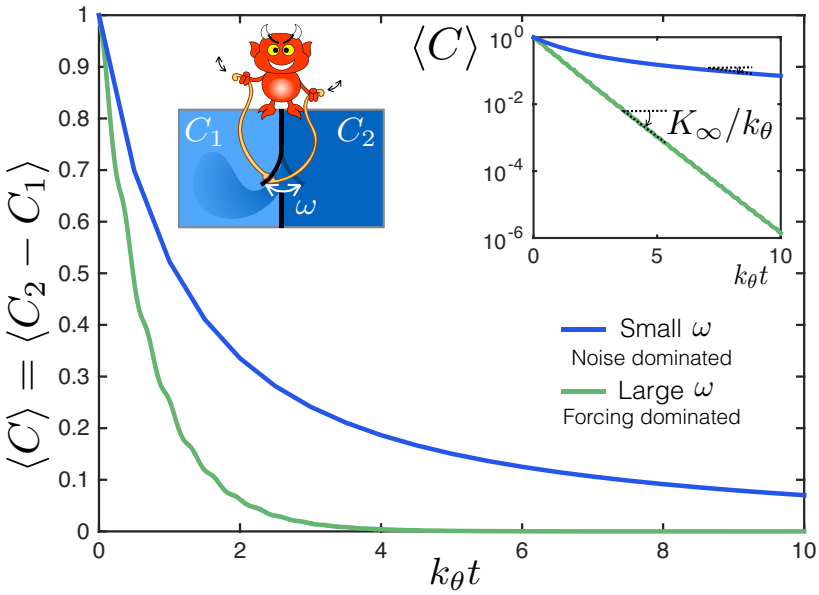

Fig. 1.2: **Relaxation of the difference in concentration between the two sides of a nanodoor**, averaged over noise. The data is a simulation result with $\lambda/k_\theta = 10^{-3}$, $\omega/k_\theta = 10^{-3}$, and $\omega/k_\theta = 1$. (*Inset, Left*) Illustration of a demon oscillating the nanodoor. (*Inset, Right*) Log scale of the previous graph and example of the extraction of the long time relaxation constant K_∞, the *permeance* of the system.

dependent averaged concentration $\langle C(t) \rangle$. I show in Fig. 1.2 an example for the averaged concentration $\langle C(t) \rangle$, here in the case of a nanodoor where $K(x) = k|x|$ (Fig. 1.1-a).

As a generic feature, one may show that $\langle C(t) \rangle$ is exponentially decaying at long times,

$$\langle C(t) \rangle \underset{t \to \infty}{\sim} \exp(-K_\infty t). \tag{1.4}$$

and this allows to define the *permeance* K_∞ of the system. Fast translocation of the solute corresponds to a large K_∞. The permeance K_∞ depends on the thermal damping λ, noise amplitude θ, but also on the external forcing (frequency ω and amplitude x_0). In the following, the goal is to identify some of the rules on how permeance depends on these antagonistic effects, and most of all how this affects selectivity. All of the rules describing the dependence of K_∞ on this wide number of parameters can be found in [334]. Units of lengths are given by $\sqrt{\theta}$, while time is given in terms of a renormalized parameter k_θ with units of an inverse time: for the nanodoor, $k_\theta = k\sqrt{\theta}$, while for the nanopore $k_\theta = k'\,\theta$.

2 Consequences on selectivity

2.1 Transport through the active pore

Let me discuss the various regimes at play. It is first interesting to explore the limiting behaviors at low damping ($\lambda \ll k'\theta$). This regime is actually relevant for ionic or liquid separation systems [151, 169], see for instance the experimental study of biological channels in Ref. [337] which is consistent with the low damping limit relaxation with $\lambda \propto 1/\eta$, with η the fluid viscosity. At high frequency, the forced oscillations become too quick for the thermal damping to rub them out and x reduces simply to its noise average $x \simeq x_0(t)$ such that $K_\infty \simeq (\omega/2\pi)\int K[x_0(t)]dt$. For the case of the circular pore one accordingly finds $K_\infty \sim k' r_0^2 \varepsilon^2/2$ in this regime. This is the *forcing dominated regime*, see Fig. 1.3-d. The behavior at low forcing frequencies ω, where noise dominates (see Fig. 1.3-c), is more subtle. According to Eq. 1.2, the gating variable will mainly diffuse with a diffusion coefficient $\mathcal{D}_x = \theta\,\lambda$. Over a time τ, the gating variable thus takes a typical value $\bar{x} \sim \sqrt{\mathcal{D}_x \tau}$. Now the passage time is itself fixed by K_∞^{-1}, so that one gets a self-consistent estimate for K_∞, as

$$K_\infty \underset{\substack{\omega \ll \omega_c \\ \lambda \ll k_\theta}}{\simeq} K\left[\bar{x} \sim \sqrt{\frac{\lambda\theta}{K_\infty}}\right] \tag{1.5}$$

For the circular nanopore, where x is the radius r and $K(r) = k' r^2$, one deduces accordingly $K_\infty \approx \sqrt{k'\,\lambda\theta}$. All these results may be recovered analytically [334]. This interpretation for K_∞ in Eq. 1.5 can be generalized to the other types of gates. For the nanodoor, for which $K(x) = k|x|$, Eq. 1.5 predicts $K_\infty \approx (k\lambda\theta)^{1/3}$, as can indeed be verified numerically [334].

The transition between the low and high frequency regimes results from the competition between the forced oscillations and the noise. In Eq. 1.2 the thermal fluctuations $f(t)$ compete with the forced oscillations $dx_0(t)/dt \sim \omega x_0(t)$ and the crossover between the two regimes occurs accordingly when $f(t) \sim dx_0(t)/dt$. Using the fluctuation-dissipation theorem, and taking a typical time-scale $\tau \sim k_\theta^{-1}$ this yields $\omega_c(\lambda) \sim \sqrt{k_\theta \lambda}$ for the critical frequency. This estimation matches perfectly the scaling obtained numerically for all systems of Fig. 1.1 and also with the full analytical expression for the circular pore of Fig. 1.1-b.

At high damping ($\lambda \gg k\theta$) noise renormalizes everything and $K_\infty \sim K(\sqrt{\theta})$, at high and low frequencies.

2.2 Consequences on selectivity

The different scalings suggest further that the permeance K_∞ exhibits a strongly contrasted dependence on the particle mobility (via k') in the low and high frequency regimes. Accordingly, at finite frequency, solutes with different mobilities will be separated by the active gate in a very different way as compared to the static (passive) nanopore.

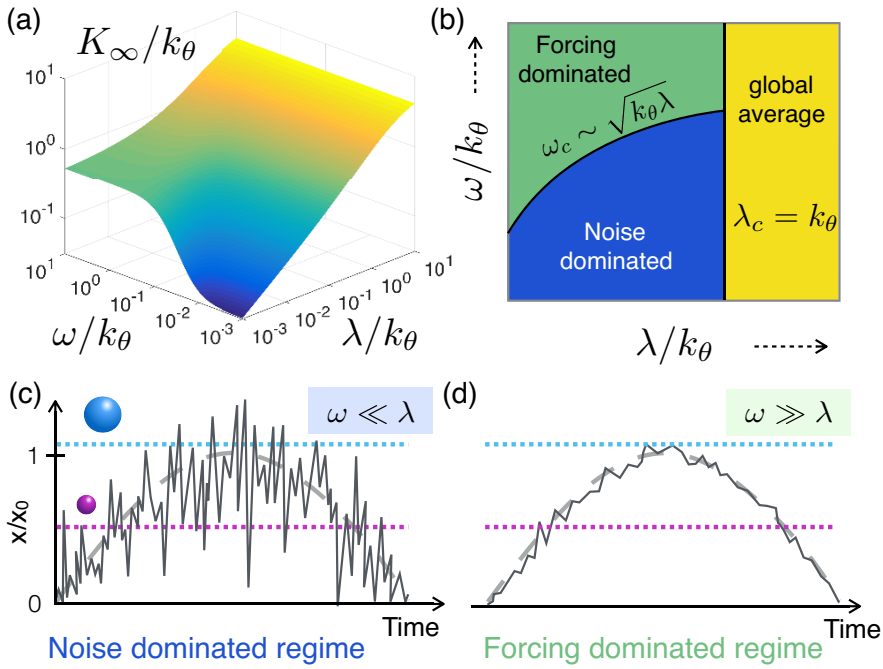

Fig. 1.3: **Universal diagram for permeance across an active pore**. (a) Analytical solution of the permeance K_∞ as a function of the forcing frequency ω and the thermal damping λ for the forced nanopore system ($r_0 = 2\sqrt{\theta}$ and $\varepsilon = 0.5$). (b) Universal phase diagram of the permeance K_∞ with ω and λ. (c) Schematic of the door opening x/x_0 (solid black line) in the noise dominated regime, where $\omega \ll \lambda$ and (d) in the forcing dominated regime, where $\omega \gg \lambda$.

This is highlighted in Fig. 1.4, where I show the permeance of the nanopore to particles of different permeabilities, corresponding to particles with different k', (here $k_1/k_2 = 100$ for illustration). The selectivity of the pore, defined in terms of the ratio of the permeances of the two particles, is plotted in Fig. 1.4-c. What is striking in this plot is that the selectivity is a strongly dependent function of the frequency (and furthermore non monotonous), so that the relative translocation rate of the two species can be finely tuned by the forcing frequency. This stems from the fact that the critical frequency ω_c for each particle is dependent on the particle mobility (via k'). Thus, a slower-diffusing particle will reach the forcing dominated regime at smaller frequencies. When the slower (blue) particle has just transitioned to the forcing dominated regime, the faster (purple) particle is still in the noise dominated regime, and the selectivity is reduced. This points to various non trivial avenues for 'on demand' sieving.

I emphasize that these results are not dependent on the choice of relative mobility, and here $k_1/k_2 = 100$ is chosen for readibility. In a more realistic case of ionic separation, for instance separating sodium and potassium, we would have $k^{(K^+)}/k^{(Na^+)} = 1.47$. [338] As a consequence, for low frequencies the selectivity $K_\infty^{(K^+)}/K_\infty^{(Na^+)} \sim \sqrt{k^{(K^+)}/k^{(Na^+)}} \sim 1.21$ and at high frequencies the selectivity increases: $K_\infty^{(K^+)}/K_\infty^{(Na^+)} \sim k^{(K^+)}/k^{(Na^+)} \sim 1.47$. Note

that this does not depend on the value of the noise damping parameter λ: as long as noise is signficant in the system, one will always find the critical frequencies from one regime to another.

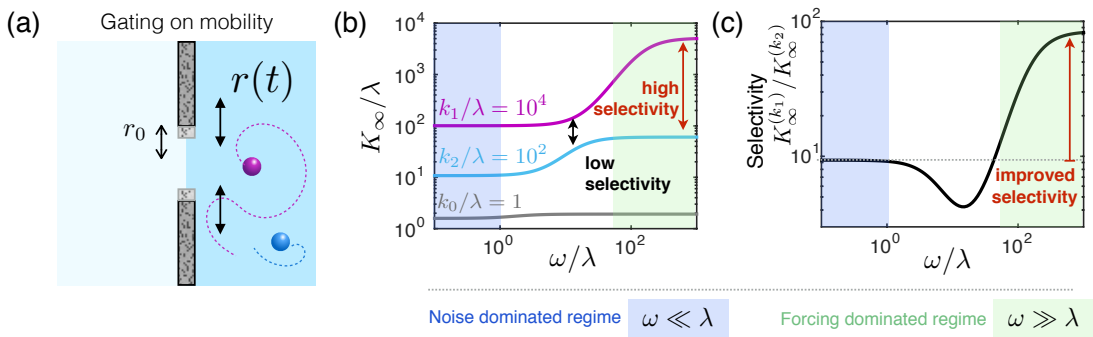

Fig. 1.4: **Selection on mobility**. (a) Schematic of gating through the fluctuating pore relying on mobility differences between particles. (b) Permeance K_∞/λ through the nanopore of two particles with mobility $k_1/\lambda = 10^4$ and $k_2/\lambda = 10^2$ as a function of the forcing frequency ω/λ, for small λ. (c) Selectivity of the nanopore to those particles, defined as the ratio of the permeances.

To phrase it in simpler words: this system typically acts like a rotating hotel door. Imagine Usain Bolt and a slower person trying to pass through the door. If the door is moving randomly (at low forcing frequencies, everything is dominated by noise) it will be very hard for both persons to go through. If the door is moving very quickly but in a very regular way (at high forcing frequencies, noise is covered), Usain Bolt will be able to go through, but not the slower person. This hints to the idea that to *sort particles on dynamical grounds, a dynamical sieve is the pertinent tool to use.* Interestingly, a similar effect has recently been observed in the nuclear pore complex, a biological pore responsible for the transduction of mRNA [339]. The mechanisms for selectivity of this pore are still debated, and is possibly linked to an effective spatiotemporal barrier of the nuclear pore complex. It has been observed that large (e.g. slowly diffusing) cargos see an effectively "high barrier" and thus are hindered in their passage through the pore; whilst small (e.g. fast diffusing) cargos have a high entrance probability [339].

3 The experimental nanodoor

I am indebted to Antoine Niguès and Alessandro Siria who seriously helped me in this problem, especially with the optics, Eleonora Secchi, Elisa Tamborini, Laetitia Jubin, and Benoit Laborie, who helped me on the fluidic measurements. I am obviously indebted to the rest of the experimental crowd for helping me out on a great number of related matters !

I give below some of the preliminary experimental results on the nanodoor system as showed in Fig. 1.2-d.

3.1 Ionic current through the steady nanodoor

As a first calibration experiment, I investigated how the door was reactive to an applied constant hydrostatic pressure. The nanodoor is embedded in microfluidic cell separating two reservoirs that are filled with KCl water – see Fig. 1.5-a. A voltage drop is imposed between the two reservoirs between two Ag/AgCl electrodes. As a result, a current establishes, consuming Cl^- at one electrode and forming Cl^- at the other; and K^+ is transported through the door. We measure the current response as a function of the voltage drop. More details on the experimental methods may be found in the Methods.

On top of that, I add a hydrostatic pressure controlled by a pressure pump and measure the response of the current. One expects that the pressure drop will induce a flow that will open the door on one side, and thus will change the ionic response to the voltage drop. In pratice I measure the streaming current (current at zero voltage due to surface charge on the nanodoor) and the conductance of the device with varying pressure drops – see Fig. 1.5-b. The results are given in Fig. 1.5-c to f, for two different salt concentrations.

Response of the streaming current. The response of the streaming current to increasing pressure drop is reported in Fig. 1.5-c and -e. The streaming current increases with the pressure drop, which is expected because for a simple pore, it should scale linearly with the pressure drop [88]. Clearly, the linear scaling is not fulfilled and something is going on – probably due to the fact that pressure is actually opening/closing the door and thus – since the pore area changes – the linear regime is not fulfilled. However, extracting a trend is not obvious from the data I have so far.

Response of the conductance: The conductance G is a direct (almost) measure of the effective open surface area for ions to traverse the door. With increasing negative pressure (so "on the right side" of the door) there is increase of the conductance, hinting to an increased opening of the door. With increasing positive pressure (so "on the left side" of the door) there is a decrease of the conductance, then an increase at higher pressures. Actually, the door is originally slightly deformed – opened – in one direction, because it was bombarded by ions or electrons for imaging. So effectively on this side pressure first closes the door and opens it again on the other side. Typically one has $G \propto \mathcal{A}$ where $\mathcal{A}$ is the typical opened surface area of the pore [88]. Thus one finds that the door opened by an angle $\delta\theta(\Delta P) = G(\Delta P)/G(\Delta P = 0)$ and thus by a total distance $\delta x(\Delta P) \simeq L\delta\theta(\Delta P)$ where $L = 27\mu m$ is the length of the door. One finds $\delta x(\Delta P = -400mbar, C = 10^{-3}M) \simeq 2\mu m$, and $\delta x(\Delta P = -400mbar, C = 10^{-2}M) \simeq 1\mu m$. These values seem pretty reasonable. From these we can evaluate the bending modulus knowing that for a uniformly applied force (like the pressure force in this case) one finds that the deflection angle is $\delta\theta = 2\Delta P L^3/Eh^3$ [340] and thus $E = 2\Delta P L^3/h^3\delta\theta \simeq\sim 200 - 400GPa$ which is rather in the range of measurements for silicon-nitride [341, 342].

All in all gathering information on pressure measurements on this system is not a straightforward process because the door is very sensitive to slight unsteadinesses in the pressure. I

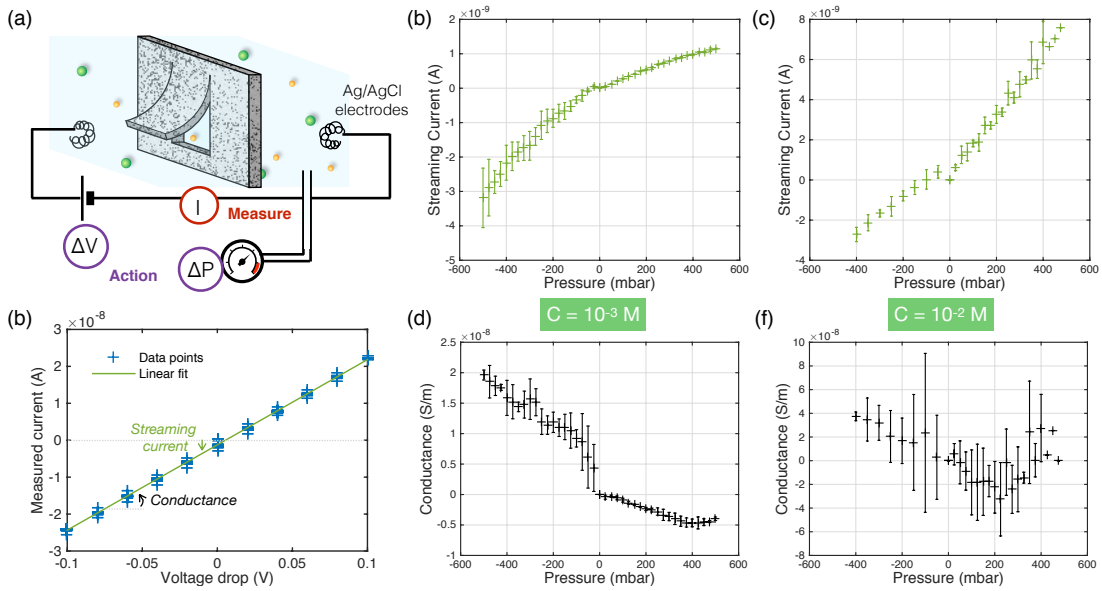

Fig. 1.5: **Response of the nanodoor to applied pressure**. (a) Schematic of the microfluidic cell, where a membrane with a carved nanodoor is embedded between two salt reservoirs. Ionic current I through the door is measured thanks to Ag/AgCl electrodes in response to a voltage drop ΔV between the reservoirs; a pressure ΔP can also be applied with a pressure controller. (b) Ionic current in response to an applied voltage drop (the points are registered every 1s for 10s at each voltage value, and several ramps are done) for a nanodoor with thickness $e = 500nm$, length $L = 27\mu m$ and width $W = L/3$ at pressure drop $\Delta P = 200mbar$; the streaming current and conductance are extracted from the linear fit of the data; for the same door, reported streaming current and conductance (where the 0 pressure drop value of the conductance was substracted from the data) at $10^{-3}M$ salt concentration – (c - d) – and $10^{-2}M$ – (e - f).($G(\Delta P = 0, C = 10^{-3}M) = 223 \pm 3nS/m$; $G(\Delta P = 0, C = 10^{-2}M) = 1290 \pm 40nS/m$); The results were averaged on at least 3 ramps of pressure with control experiment after each single measurement.

also performed measurements of streaming current under an applied concentration difference. The results are interesting to some limited extent, but for the sake of keeping this thesis to a reasonable size, they are not reported here.

3.2 Calibration of the spectrum of the nanodoor

Future work consists now in investigating the resonance modes of the nanodoor, and the typical amplitude of these modes; before putting it in water and actually measuring the response of transport to an active modification of the membrane. Indeed quick preliminary experiments showed that it was not straightforward to measure obvious changes in transport through the nanodoor while it was vibrating. This shows that we need to know precisely where

the door will be resonant to detect a significant change in transport. I show in Fig. 1.6 some of the ongoing work to investigate the door vibrations. I first tried to observe the nanodoor under a scanning electron microscope, and found that one could see some resonance in the door at some frequencies – see Fig. 1.6-b; unfortunately it is not the most convenient method to explore the nanodoors and thus I turned to a more meticulous set-up where I investigate the vibration modes of the door thanks to interferometry tools – see Fig. 1.6-c and more details in the methods; and the set-up itself is still being properly calibrated. One of the things that I still do not fully understand is the response of the interferometer system when I simply make a lateral map of the door – see Fig. 1.6-d. Indeed the image response, that one would expect to keep the symmetry axis of the door, breaks this symmetry. Understanding the interferometry images would allow then to choose a specific position with accuracy (at the free edge of the door for instance) and then perform an interferometry response to a piezo excitation in a range of frequencies. Since the interferometry scan is sensitive to the vertical distance from the tip of the fiber to the door (see Fig. 1.6-e, where the constructive and destructive interference are visible), this would allow in principle to detect the resonance frequencies of the door.

3.3 Perspectives on the experimental nanodoor

The aim of the experiments on the nanodoor is to bring out some non trivial properties of out-of-equilibrium sieving. In this prospect, we expect that – possibly – transport through different resonant doors (at different resonant frequencies – and thus different mobility versus door time constant characteristics) may present some interesting features. For this reason I have designed 10 different door sizes with *a priori* different resonance frequencies (computed from standard mechanics calculus). I have planned to pursue these experiments if time allows.

Another interesting feature with these doors – that will be discussed in Part IV – is that possibly one may operate some kind of *out-of-equilibrium osmotic driving*. Suppose one would find big dissoluble molecules like DNA strands or other polymers, with a gyration radius larger than the typical leak size through the sides of door. One may thus produce an osmotic pressure between one side – with a high concentration of these molecules – and the other side – with just clear water. A water flow will then establish towards the concentrated side, this water flow may open the door, and thus, the molecules may be allowed through. As a result, the osmotic pressure will drop, and the water flow will diminish, and the door may close. And we are back at the beginning. The story is certainly more complex, but one immediately sees that something totally unseen before is possible.

Investigating these new out-of-equilibrium sieving principles may be of great consequence for filtration. To add up, they lead to a number of fundamental physics questions.

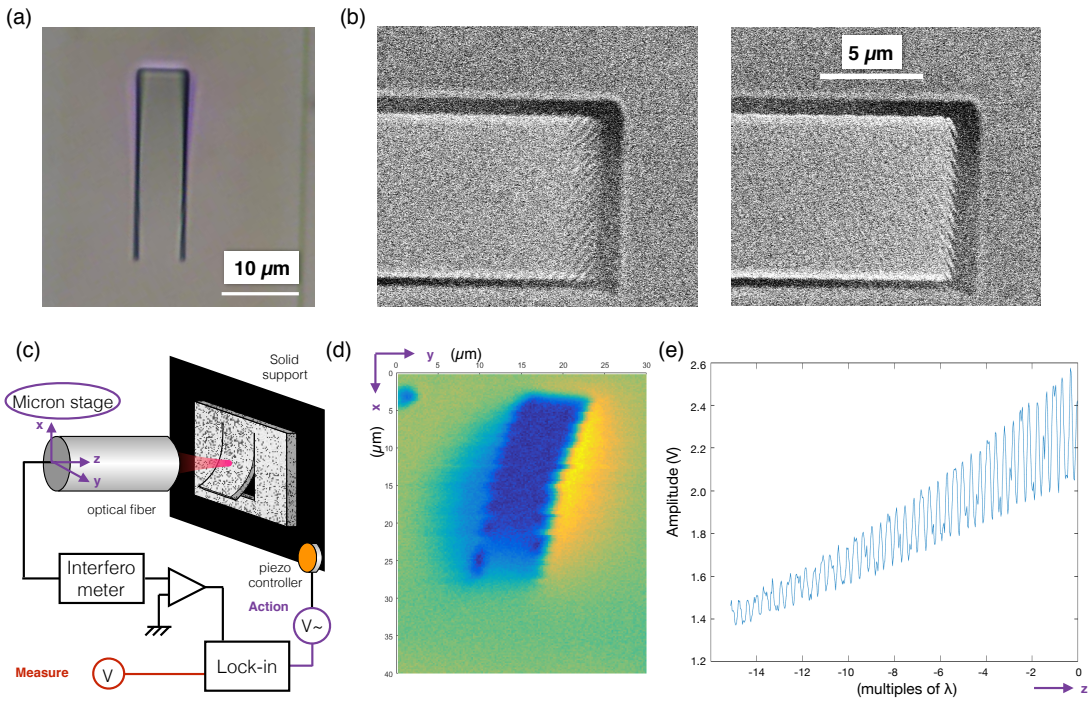

Fig. 1.6: **Response of the nanodoor to external vibrations**. (a) Bright field microscope image (50x) of a nanodoor with $e = 200nm$, $L = 36\mu m = 3W$. (b) Scanning electron microscope images of a similar door that is excited at 240 kHz thanks to a nearby piezo transducer - the door shows diagonal line patterns – due to its motion and the fact that the image is acquired line per line – that demonstrate that the door is reacting to the applied drive. (c) Schematic of the calibration experiment to measure the response of the door to an external excitation: a micron stage micromanipulator allows to displace an optical fiber on top of the nano-door, allowing to probe the response at different points along the door; the signal going back to the fiber is demodulated according to the initial signal and sent to an amplifier and measured via an acquisition card; the whole system can be coupled to a piezo controller and the signal may be analyzed with respect to the input piezo controller signal; (d) xy map of the nanodoor of (a) where yellow (resp blue) shade indicates regions of higher voltage response. The door is opened at the top of the figure; it is not clear yet how to interpret this image; (e) vertical approach on top of the same nanodoor and response in z, showing oscillations due to constructive and destructive interference as the path for the light to be reflected is a multiple or not of the wavelength λ.

Chapter 2: Active selection across nanochannels

I am especially indebted to Professor David Dean without whom the following research would not have been possible. The physics found is the result of an equilibrated 3 body research. The following chapter is connected to the publication [343] that is currently under review.

1 Do fluctuations enhance or decrease transport ?

Even the simple question: *do pore surface fluctuations along a pore enhance or diminish transport ?* is surprisingly difficult to answer. While surface fluctuations are naively expected to enhance diffusive transport via induced hydrodynamic flows – the presence of a flow field within a channel can enhance diffusive transport for instance via the canonical Taylor-Aris mechanism [344,345] –, geometrical bulges may entrap particles resulting in entropic slowing-down, as captured by the Fick-Jacobs framework [346, 347]. The more general situation of transport with temporally varying geometry remains open despite its obvious importance.

To tackle interest, I draw attention to a simulation investigating the effects of fluctuations on transport. I simulated with molecular dynamics (see the Methods for details) a confined water layer within two layers of graphene. The graphene layers are either fixed and perfectly flat – *fixed flat* configuration –, either the top graphene layer is composed of "free" carbon atoms, but still bound to one another to form the graphene – *thermal flexibility* –. The carbon atoms are submitted to atmospheric pressure that allows to maintain the confinement (the position of the flat layer in the *fixed flat* configuration was ajusted to match the average height of the flexible layer), and are thermalized at 300 K. This situation represents the impact of dynamic fluctuations at the interface on bulk transport. Last I explored a situation with a fixed top layer, but frozen in an undulated state of the *thermal flexibility* configuration. This configuration is called *fixed undulated*. I then measure the longitudinal mean square displacement of water molecules within the slit – see Fig. 2.1. Surprisingly, I find that in the *thermal flexibility* case, the displacement of molecules is greatly enhanced, as compared to the *fixed flat* case. In the *fixed undulated* case, displacement is decreased as compared to the *fixed flat* case, as expected from the Fick-Jacobs entropic trapping [346, 347]. The *fixed undulated* case must be connected somehow to the *thermal flexibility* case, since it represents the limit of extremely slow dynamics: as a consequence there must exist a regime of fluctuations that

enhances transport and one that diminishes transport. We thus require a formalism to be able to quantify when acceleration or trapping occurs.

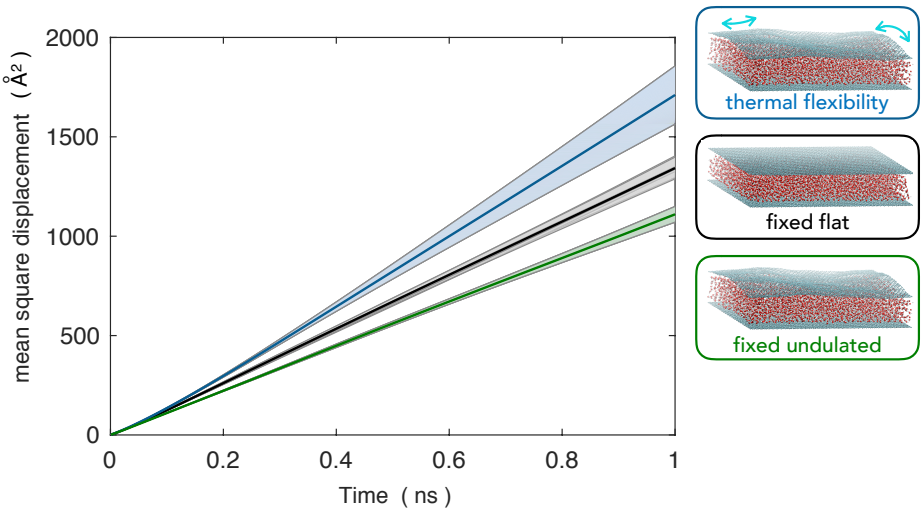

Fig. 2.1: **Graphene fluctuations strongly impact nanoconfined water transport**. Mean square displacement of water molecules between two graphene sheets as computed from molecular dynamics simulations (see the details in the Methods section). The graphene sheets are separated by an average distance of 18.6Å. The mean square displacement is computed on 6 to 12 independent runs, for the 3 situations detailed in the text, *thermal flexibility*, *fixed flat* and *fixed undulated*. When the graphene is flexible, the average vertical displacement of the graphene atoms is 1.35 Å.

In this chapter, I establish a general relationship between diffusive transport and the dynamical spectrum of surface fluctuations. Our framework applies to a variety of cases: the surface fluctuations can be induced by thermal noise or originate from non-equilibrium fluctuations induced by external stimuli. I give explicit applications of our formalism to several situations – specifically of nanopore transport [328, 329] – as well as to larger scale situations, for example active contractions in fungal species which influence nutrient transport [348–350]. As anticipated from the discussion above, I show that pore agitation can lead to an increase or decrease in transport, depending on an effective Péclet-like dimensionless number characterizing surface to bulk agitation.

2 Renormalization of transport due to pore shape fluctuations

Our theory starts with the perturbative analysis of the diffusion of a particle confined between fluctuating surfaces, typically like in Fig. 2.2. For simplicity, we consider a two dimensional model, but the results and the formalism can readily be extended to 3 dimensions [343]. The upper surface is located at $z = H + h(x,t)$, where H is the mean height and $h(x,t)$ represents fluctuations about this mean (x represents the coordinate along the channel and z the height coordinate). A tracer particle – for instance, a molecule of dye in the fluid – locally diffuses

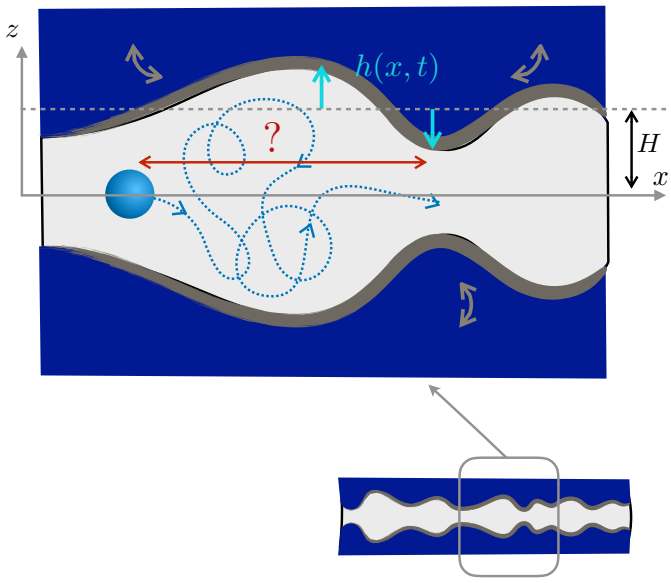

Fig. 2.2: **Schematic for calculating effective diffusion in a fluctuating nanochannel**. An interface fluctuates and/or is actively displaced by $h(x,t)$ from a reference height H. A particle (in light blue) is advected and diffuses within the medium.

with a bare diffusion constant D_0 and is advected by a hydrodynamic flow $\boldsymbol{u}$. The probability density $p(x,z,t)$ of the particle obeys the Fokker-Planck equation: $\partial_t p = -\boldsymbol{\nabla}.(\boldsymbol{u}p) + D_0 \Delta p$. In the case of thin channels, a standard expansion yields a reduced advection diffusion equation for the marginal probability density $p^*(x,t) = \int_0^{H+h(x,t)} p(x,z,t)dz$,

$$\partial_t p^* = -\partial_x \left(\overline{u}_x p^*\right) - D_0 \partial_x \left(\frac{\partial_x h}{(H+h)} p^*\right) + D_0 \partial_{xx} p^*. \tag{2.1}$$

where $\overline{u}_x = \frac{1}{H+h(x,t)} \int_0^{H+h(x,t)} u_x(x,z,t)dz$ is the height averaged longitudinal hydrodynamic flow. Incompressibility of the flow also gives $\partial_x \left((H+h)\overline{u}_x\right) = -\partial_t h$. Eq. 2.1 contains two advection terms which both depend explicitly on height fluctuations. The first is advection by the height averaged hydrodynamic flow – expected to enhance diffusion. The second term is present even in the absence of any fluid in the channel and represents the effect of spatial fluctuations. When h does not depend on time, the advection term is zero and the second term represents an entropic potential which slows down diffusion [346].

We analyze Eq. 2.1 via a perturbation expansion in the amplitude of the fluctuations of h (with $\langle h \rangle = 0$ where $\langle \cdot \rangle$ is an average over the thermal fluctuations). Using a diagrammatic expansion, and to first nontrivial order [351], we then demonstrated that the renormalized late time diffusion constant is given in terms of the spectrum of the pore surface fluctuations $S(k,\omega)$, as:

$$D_e = D_0 \left(1 - \frac{1}{H^2} \int \frac{dk\, d\omega}{(2\pi)^2} \frac{(D_0 k^2)^2 - 3\omega^2}{(D_0 k^2)^2 + \omega^2} S(k,\omega)\right), \tag{2.2}$$

where $S(k,\omega)$ is defined by $\langle \tilde{h}(k,\omega)\tilde{h}(k',\omega')\rangle = (2\pi)^2 \delta(k+k')\delta(\omega+\omega')S(q,\omega)$. Eq. 2.2 is

the main result of this section. The full derivation of this key result in 2D is reported in the Methods, and supplementary information is found in [343]. This equation can also be expressed in terms of the response function of the interface, related to the spectrum via fluctuation-dissipation, here calculated at an imaginary frequency [343]. Note also that a similar expression can be obtained for the wave-induced velocity drift, when in average (over noise or time) the surface undulations are not null.

At this stage, the formalism is completely general and can be used to compute the renormalized diffusion resulting from any pore or interface motion in terms of the pore or interface fluctuation spectrum. It may be interpreted as a generalization of the Ficks-Jacob formalism to dynamical confinement. It also applies both to the case where fluctuations originate from thermal noise, as well as active (non-equilibrium) fluctuations driven by external stimuli.

Eq. 2.2 highlights that the renormalization of the diffusion constant can be either positive or negative depending on the fluctuation spectrum: jiggling can both speed things up and slow things down ! Indeed, when the height field is frozen, we have $S(q,\omega) = (2\pi)\delta(\omega)S_f(q)$, where $S_f(q)$ is the spectral density of the spatial variations of the frozen height. Here we find $D_e/D_0 = 1-\langle h^2\rangle/H^2$, in agreement with Fick Jacobs [346,347]; diffusion is decreased. When the height fluctuations are very rapid in time, but they have a large spatial wavelength, we find $D_e/D_0 = 1+3\langle h^2\rangle/H^2$ and diffusion is enhanced. Indeed, what happens is that geometrical constrictions tend to slow down transport (exactly according to the Fick-Jacobs setting) but time dependence induces flow (by conservation of mass) which helps to stir and enhance transport – see Fig. 2.3. The shape of the fluctuating spectrum (in space k and time ω) will thus be critical to determine if transport is enhanced or decreased.

3 Consequences from nano to milli fluidics

In the following I give two example applications of this theory.

3.1 Transport in thermally fluctuating pores

Let's first focus on thermal fluctuations of a thin layer. Thin film dynamics can be analyzed within the lubrification approximation [352, 353] and in the limit of low Reynolds numbers. The fluctuation interface spectrum can be obtained from the Hamiltonian $\mathcal{H}[h]$ of the height fluctuations h. Typically $\mathcal{H}[h] = W\int_0^L dx\ \Phi(H+h,\partial_x h,\partial_{xx}h,....)dx$ for an energy functional Φ. Here W is the width of the slit, in the context of three dimensions and to simplify the discussion we assume that height fluctuations only occur along x. The energy functional depends on the Van der Waals interactions between the surfaces, possibly the discrete properties of the confined liquid [354–356] and also contributions associated with constraints fixing the

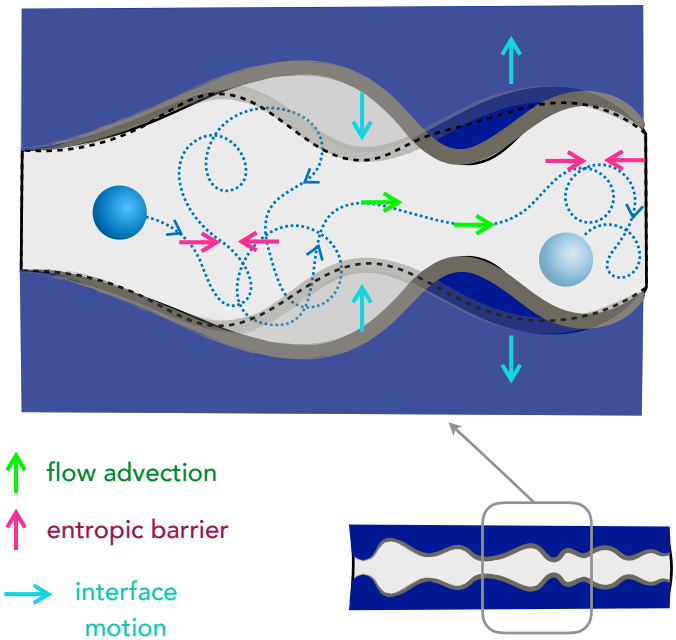

Fig. 2.3: **Mechanisms of transport renormalization in fluctuating nanochannels**. A particle (in light blue) is advected and diffuses within the medium. Transport is modified by advection in the flow induced by the temporal evolution of the interface and the entropic barriers induced by spatial variations of the interface.

average gap size. The dynamics for small height fluctuations are given by [352]

$$\partial_t h = -\partial_x((H+h)\overline{u}_x) = \partial_x\left(\lambda(H)\partial_x\frac{\delta\mathcal{H}}{\delta h} + \sqrt{\lambda(H)}\mathcal{N}\right) \tag{2.3}$$

with $\lambda(H)$ the permeance of the slit. The term $\mathcal{N}$ is a Gaussian white noise with $\langle\mathcal{N}(x,t)\mathcal{N}(x',t')\rangle = 2(k_BT/W)\delta(x-x')\delta(t-t')$ generated by hydrodynamic fluctuations within the liquid [352]. Note that wether fluctuations originate from initially from the bulk (in a sense of fluctuating hydrodynamics, because the system being nanoscale, the individual particle displacements can influence the dynamics) or at the surface (from fluctuations of surface bonds...) formally results in the same equations [352] and thus it is not necessary to account for both. Focusing more specifically on a thin film confined by an elastic membrane, the Hamiltonian takes the Landau form

$$\mathcal{H}[h] = \varphi(H)WL + \frac{W}{2}\int_0^L dx\ \left(\varphi''(H)h^2 + \kappa(H)(\partial_{xx}h)^2\right) \tag{2.4}$$

where $\varphi(H)$ is the free energy per unit area of a flat interface (verifying $\varphi'(H)=0$ for the equilibrium height H) and $\kappa(H)$ can be interpreted as the surface's bending rigidity. In this case $S(k,\omega) = 2k_BT\lambda(H)k^2/(\omega^2+k^4\lambda(H)^2(\varphi''+\kappa k^4)^2)$ and, directly, one finds using Eq. 2.2

$$D_e = D_0\left(1 + \frac{\langle h^2\rangle}{H^2}\left[\frac{4}{(1+D_0/D(H))^{3/4}} - 1\right]\right) \tag{2.5}$$

with $\langle h^2 \rangle = k_B T \ell^3 / 2\sqrt{2} W \kappa$, where $\ell = (\kappa/\varphi''(H))^{1/4}$ is the characteristic wavelength of the surface fluctuations. The quantity $D(H) = \lambda(H)\varphi''(H)$ is a diffusion coefficient scale associated with interface fluctuations. For no slip boundary, one has $D(H) = \frac{H^3}{12\eta}\varphi''(H)$, where η is the viscosity of the liquid. For a mobile interface with slip length b, $\lambda(H) = \frac{(H)^3}{12\eta} \cdot \frac{1+4b/(H)}{1+b/(H)}$, with η the viscosity of the fluid and b the slip length at the mobile interface. Other fluctuating confinement cases, with different Hamiltonians, geometries – *e.g.* tubes– and boundary conditions – *e.g.* partial slip –, can easily be analyzed, and further examples are given in [343], leading to qualitatively similar conclusions.

Eq. 2.5 shows that if bulk diffusion is large ($D_0/D(H) \geq \mathcal{M}_0$ with $\mathcal{M}_0 = 4^{4/3} - 1$), then effective diffusion will be reduced, *i.e.* $D_e \leq D_0$. Particles with high bare diffusivity see an effectively quenched surface profile which generates an entropic trapping potential, thus slowing down diffusion. On the other hand, for slowly diffusing particles, $D_0/D(H) \leq \mathcal{M}_0$, the fluctuation-induced advection enhances diffusion *i.e.* $D_e \geq D_0$. This results in a compensation effect –*robin hood effect* –, summarized in Fig. 2.4-a, whereby fast particles are slowed down and slow particles are sped up. This difference in effective diffusion as a function of bare diffusion has been observed in simulations of gas particles in metal organic frameworks [327] or water transport in biological porins [154]. Eq. 2.5 also describes typical low inertial phonon modes on an interface (like phonons on the surface of graphene or carbon nanotubes [343]). The impact of phonon modes of a carbon nanotube on confined water has indeed been measured to depend substantially on phonon frequency [328].

3.2 Active transport under externally driven pore shape

As a second example, let's consider a situation where the fluctuations of the pore's shape are driven *out-of-equilibrium* by an external stimulus. This situation is particularly interesting in the sense that the pore structure undergoes non-equilibrium fluctuations, therefore leading to out-of-equilibrium transport. In general, this situation can be accounted for by adding a force to Eq. 2.3 with a specific frequency ω_0 and wave number k_0. We consider here a propagating wave on the interface of a deforming tube with bare radius R, as : $\delta R(x,t) = a_0 \cos(\omega_0 t - k_0 x)$. In this context, the relevant driving spectrum is given by $S(k,\omega) = \pi^2 a_0^2 \left[\delta(\omega_0 + \omega)\delta(k_0 - k) + \delta(\omega_0 - \omega)\delta(k_0 + k)\right]$, and using the result of Eq. 2.2 for a tubular geometry we find:

$$D_e = D_0 \left(1 - \frac{a_0^2}{2R^2} \frac{1 - 3\left(D_\approx/D_0\right)^2}{1 + \left(D_\approx/D_0\right)^2}\right) \tag{2.6}$$

where $D_\approx = \omega_0/k_0^2$ can be seen as a diffusion coefficient associated with the surface wave packet. Interestingly, one recovers from Eq. 2.6 the two regimes highlighted previously, but now for the actively fluctuating surfaces: diffusion is enhanced or slowed down depending on whether the bare diffusion D_0 is lower or greater than the wave packet diffusion $D_\approx$. The results are summarized in Fig. 2.4-b. The exact same expression for effective diffusion may be obtained for propagating waves (only) within a different analytical framework [358–361].

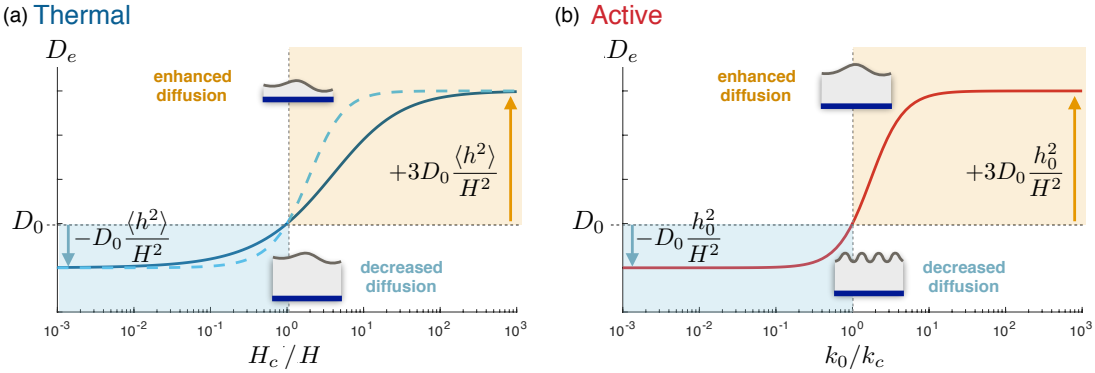

Fig. 2.4: **Renormalized diffusion under thermally fluctuating and actively driven surfaces.** (a) Renormalized diffusion D_e for a thermally fluctuating interface, as a function of the average upper interface height H. The vertical axis labels represent a change of one unit of $D_0\langle h^2\rangle/H^2$. The solid line is for no slip boundary conditions and the dashed is for a large slip length on both sides. φ is assumed for simplicity to be accounted for by a Hamaker expression, $\varphi(H) = PH + A/12\pi H^2$ with A a Hamaker constant and P a constant external pressure which fixes the average film height. $H_c = \frac{15A}{24\pi\eta D_0}$ is the critical height such that below (resp. above) this height, diffusion is enhanced, (resp. decreased). For a water film typically $A = 2\,10^{-20}$ J [196], and H_c =4nm. For slipping surfaces $H_c^2 \simeq \frac{15A}{4\pi\eta D_0}b$ for $b \gg H$, with a slip length $b \sim 10$nm [88], then $H_c \simeq 15$nm. Beyond the Hamaker framework, the disjoining contribution may exhibit layering contributions in very strong confinement [354, 357] which will result in additional and more complex effects on diffusive transport. (b) Renormalized diffusion D_e under actively fluctuating interface: D_e is plotted as a function of the excitation wave number k_0. k_c is the critical wavenumber defined as $k_c^2 = \omega_0/\sqrt{3}D_0$. For capillary waves on shallow water, one has $\omega_0^2 = \gamma k_0^3/\rho_0$ where ρ_0 is the density of water, such that $k_c = 3\gamma/\rho D_0^2$. Typically, $k_c \sim 10^{13}m^{-1}$ and we expect that capillary waves always enhance mixing. In many other cases the dispersion relation may be more complex, yielding a rich zoology of behaviors.

3.3 Spectral mixing across the scales: an effective Péclet

Altogether, for the in- and out- of equilibrium cases respectively, one can easily define a dimensionless Péclet-like number to characterize the transition from decreased to enhanced mixing. For equilibrium fluctuations, $Pe = D(H)/D_0$ with $D(H)$ the dispersion induced by surface-induced flow, while for active fluctuations, $Pe = D_{\approx}/D_0$, introducing active surface transport via $D_{\approx}$. One may accordingly expect that $Pe \sim \ell^2/D_0\tau$ where ℓ and τ are characteristic length and time scales of the fluctuations. An outcome of our theoretical framework is that this Péclet number enables to quantify the impact of surface fluctuations on the transport. Typically for high (resp. low) Péclet $Pe \geq 1$ (resp. $Pe \leq 1$), the transport is expected to increase (resp. decrease) under structural jiggling, see Fig. 2.5.

We gather in Fig. 2.5 a variety of systems where the structural agitation of the confinement

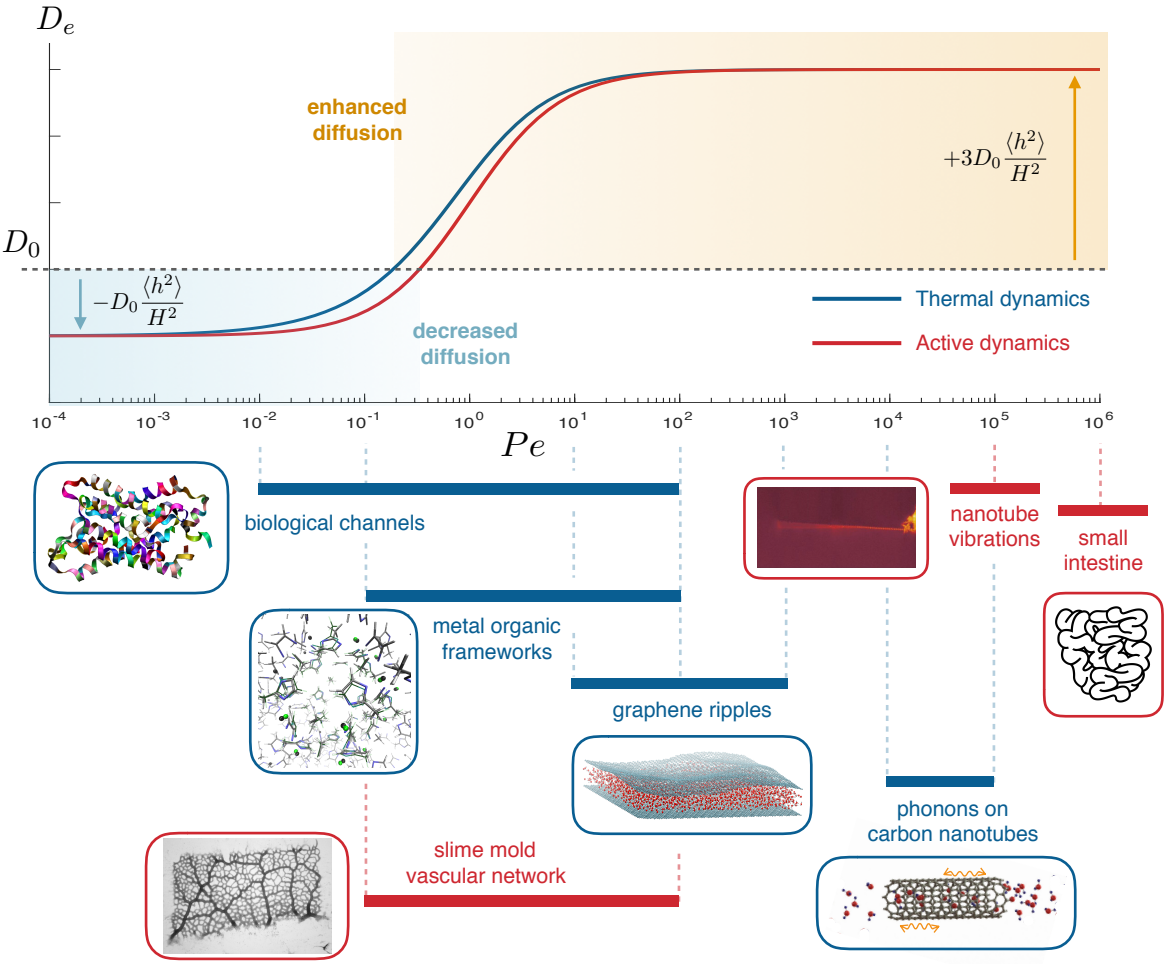

Fig. 2.5: **Enhanced or decreased transport under pore shape wiggling versus the dimensionless Péclet-like number for various fluid transporters**. Effective diffusion, in thermally or actively fluctuating pores, according to a thermal dynamics spectrum described by Eq. 2.5 or according to active dynamics described by Eq. 2.6. The diagram compares different fluid transporters, as described in the main text. (aquaporin for biological channels thanks to [333], slime mold courtesy from *Karen Alim* and vibrating nanotube from [362]).

is expected to impact particle transport. These fluctuating systems are classified according to their corresponding Péclet number – full details are given in [343] –:

- **Biological channels, like aquaporins**, will undergo thermal fluctuations with typically $Pe \sim 10^{-2} - 10^{2}$ [147,148] and indeed both behaviors were observed for water in a KscA channel [154]; the rate constants of transition through the gramicidin A channel for different ions – of thus different mobilities – are seen to be inverted at high and low frequencies of potential vibration (within the channel) [363].

- in **metal organic frameworks** the range is similar: small gas molecules like H_2 have

$Pe \leq 1$, and indeed such molecules are not accelerated by framework flexibility [327]; large gas molecules have $Pe \geq 1$, and indeed molecular diffusion is increased, well beyond perturbation theory.

- **Graphene sheets** show thermal ripples that are expected to affect water transport, typically with $Pe \sim 10^1 - 10^3$ [364, 365]. I have fully confirmed this behavior by performing the molecular dynamics simulations of water confined between graphene sheets: the thermally fluctuating sheets increase particle diffusion by 150% as compared to the flat rigid sheets, as detailed earlier in Fig. 2.1;
- Finally, we find that non-dissipative **phonon coupling** is in the range $Pe \sim 10^4 - 10^5$ and always enhances diffusion, in accordance with the observations of [328].

Going to actively driven dynamics, various examples include:

- **carbon nanotubes**, in which longitudinal mechanical vibrations could typically yield $Pe \sim 10^5$, echoing the numerical results from [366–370];
- the **small intestine**, which demonstrates contractile activity with typically $Pe \sim 10^6$ [371, 372]: evidence of an increased dispersion has also been observed (though not quantified) in a microfluidic device mimicking the contractions of the intestine [373];
- **Slime mold vascular networks** in which nutrient dispersion is characterized typically by $Pe \sim 10^{-1} - 10^2$ [349, 350, 374], and increasing for larger organisms. The latter example of nutrient dispersal in contracting vascular network of organisms is actually of particular interest since it is essential for survival to generate alternative strategies for fast nutrient dispersal. For example the unicellular organism *p. Polycephalum*, shown in Fig. 1-c, is composed of a connected network of veins, containing fluid cytoplasm that can deliver nutrients to the entire body: it exhibits nonstationary periodic shuttle flows [375] driven by a peristaltic wave of contractions [348] spanning the organism. For an individual like the one in Fig. 2.5with length $L = 8mm$, one has $k_0 \simeq 2\pi/L \sim 800m^{-1}$ and $\omega_0 \sim 0.06s^{-1}$ [375] one finds $D_{\approx} \sim 10^{-7}m^2/s$. This is two orders of magnitude larger than the bare diffusion of nutrient molecules with at most $D_0 \sim 10^{-9}m^2/s$, as indeed observed in simulations in [348]. The organisms with a small Pe number, and thus possibly with diminished transport, are typically small and in the early development stage [349]. This could hint to the idea that there is a minimal size for an organism to rely on peristalsis for enhanced transport.*

This figure highlights that a wide variety of situations, covering a huge range of scales, can be put in perspective under the framework of spectral mixing by confinement jiggling. Going further, it is possible to study the relative effect of coupled passive and active dynamics, for

*The study of this organism is part of a side project from my PhD [376], and I went several times to the MPIDS in Göttingen to work on this project. I find it rather amazing and beautiful that a single theory may be able to connect and describe carbon nanotubes and slime mold at the same time!

instance in biological membranes, with an active component [377], or nanoscale systems like nanotubes that are sensitive to thermal as well as activated vibrations [368].

Conclusion

All of these effects are described in a continuous framework, but obviously at the very small scales in biological channels or in nanoporous materials like Metal Organic Frameworks, the formalism developped above does not apply, because the molecular details become important – see for example Fig. 2.6. Now obviously the framework could be extended taking into account finite size effects on confinement [190, 378] but the idea of our work – so far – in the continuum framework is to deduce intuitive behaviors and "extrapolate" them at the nanoscale.

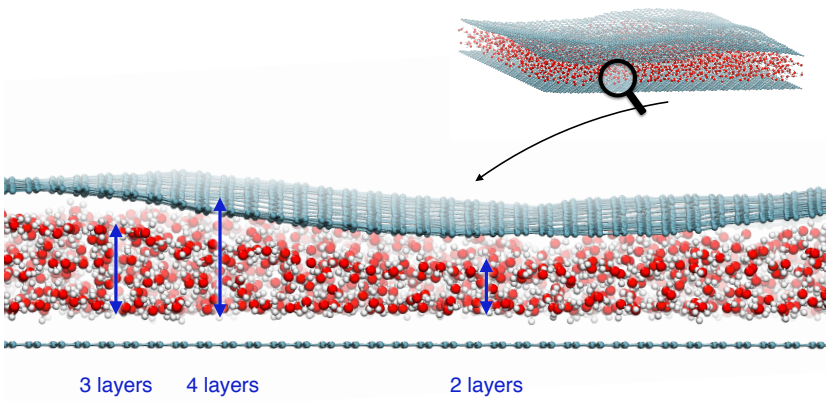

Fig. 2.6: **Nanoscale effects in fluctuating interfaces**. Simulation of a thermally fluctuating graphene layer on top of a few layers of water molecules. One distinctly sees that the graphene sheet deforms and allows locally only integer number of layers of water molecules. The 4 layer structure is in the background of the picture shown.

A simple rule of thumb that it is possible to take home from these results is that active systems possess the specific characteristic that they are able to *distinguish particles according to their dynamic properties* – like their mobility for instance – which is a radically different thing than the discriminating on steric properties like the particle size. As I pointed before: the active nanodoor acts like a gate allowing preferentially fast particles, and the active nanochannel acts like a regulator agent and slows particles that are too fast, and accelerates particles that are too slow. The active system adds more formally a characteristic time scale to the system, according to which dynamical properties of molecules may be distinguished.

Our formalism allows in particular to identify the key components to design active channels. The results here show that it is possible to tune actively the diffusion of species, therefore differentiating dynamically solutes as a function of their own Peclet number, providing the conditions for active separation [334]. In a different context, to improve the sensitivity of sequencing via translocation through nanopores, slowing-down of some species may indeed be required. Our results also demonstrate that this fine tuning is possible by harnessing out-of-equilibrium dynamics of the pore, with considerable implications for DNA sequencing [110, 379–384].

What I like about these systems is that they open a whole range of questions of thermodynamics out of equilibrium: now that the pores are effectively moving with time, what happens to the *osmotic pressure* or to the *permeability* of the pores, that are themselves defined *in equilibrium* ? These questions have direct applications to filtration and desalination and are discussed in the following Part.

Part IV

New theories for nanoscale transport beyond equilibrium

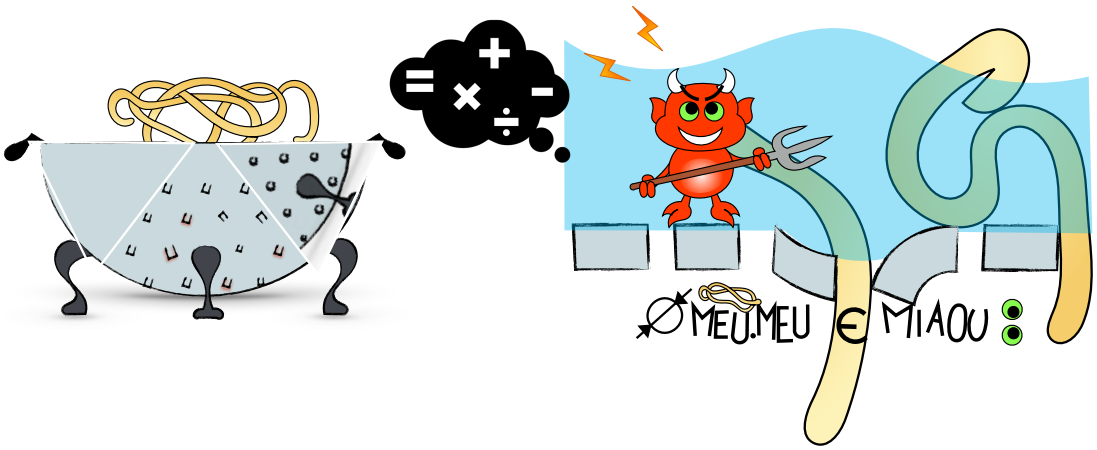

Introduction

As we have seen in the previous section, active motion of a pore drastically affects the transport of particles through this pore. This is expected to have consequences on the osmotic pressure. As highlighted by Kedem and Katchalsky in the context of membrane transport, there is an intimate symmetry link between permeance and osmosis [16]. When the nanopore fully rejects the solute particles, the membrane is semi-permeable (vanishing permeance) and an osmotic pressure is expected to build in the system. In the reverse case, the membrane is fully permeable (high permeance) and the osmotic pressure is zero. This link is highlighted by the flow induced by osmotic pressure [16] as seen in the main introduction:

$$Q = -\mathcal{L}_{\text{hyd}} \left(\Delta p - \sigma \Delta \Pi \right), \tag{1}$$

with $\Delta\Pi = k_B T \Delta C$, introducing the rejection coefficient σ, whose value is equal to 1 (resp. 0) for a semi- (resp. fully) permeable membrane; for a finite permeance K_∞ of the membrane, one then expects $1 - \sigma \propto K_\infty$ [16].

In the case of the fluctuating nanodoor (part III, chapter 1), the pore opens intermittently allowing for build-up and collapse of osmotic pressure. One can anticipate that in this case $\Delta\Pi = k_B T \langle C \rangle$ where $\langle C \rangle$ is the average concentration difference between the two sides. Consider an extended model with steric gating, with leakage law $K(x - x_p)\mathcal{H}(x - x_p)$ (where x_p is the size of the particle and $\mathcal{H}$ is the Heaviside function), such that the particle is allowed to pass only if the pore opening is greater than it's characteristic size. This leads to an effective permeance $K_\infty(\omega|x_p)$ – see Fig. 1-a and b. The corresponding solute flux $J_s = K_\infty \mathcal{V} \langle C \rangle$ (where $\mathcal{V}$ is the volume of the reservoir) can be identified to its definition $J_s = \bar{\mathcal{A}} \frac{D}{e} \alpha \langle C \rangle$ where $\bar{\mathcal{A}}$ is the average opening area of the pore, D the diffusion coefficient of the solute and e the thickness of the membrane; the permeability coefficient α is accordingly related to σ as $\alpha \propto 1 - \sigma$ [16].

Gathering definitions, one thus obtains the dynamical rejection coefficient in terms of selectivity:

$$\sigma(\omega) = 1 - \frac{K_\infty(\omega|x_p)}{K_\infty(\omega|x_p = 0)} \tag{2}$$

where the permeance of a particle with vanishing size $x_p = 0$ is used as normalization. This leads to a frequency dependent osmotic pressure, $\Delta\Pi(\omega) = \sigma(\omega) \times k_B T \langle C \rangle$. Note that this expression for the osmotic pressure is pertinent on time-scales longer than the time-dependent

forcing. The frequency dependence of the osmotic pressure is illustrated in Fig. 1-c. Tuning the frequency of the forcing therefore allows to modify 'on demand' the osmotic pressure across the active membrane.

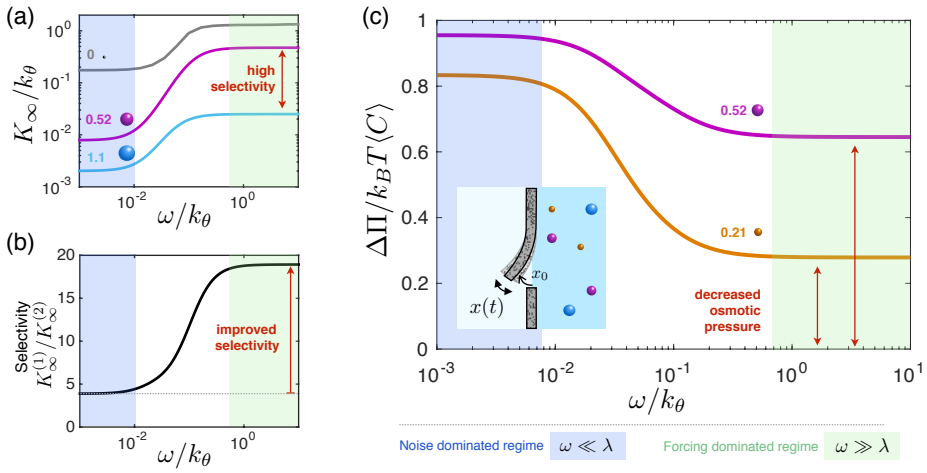

Fig. 1: **Gating with size can alter the osmotic pressure**: Effect of gating through the fluctuating door relying on size differences between particles (a) Permeance K_∞/k_θ through the nanodoor of two particles of different size (the smallest, purple is $0.52x_0$ in radius and the largest, blue, $1.1x_0$), as a function of the forcing frequency ω/k_θ, for small λ; (b) Selectivity of the nanodoor to those particles, defined as the ratio of their permeances; (c) Frequency dependent osmotic pressure through the nanodoor for two particles of different size (the largest, purple, is $0.52x_0$ in radius and the smallest, orange is $0.21x_0$) as a function of the forcing frequency ω/k_θ for small λ. (Inset) Schematic of gating through the fluctuating door relying on size differences between particles.

This sets the basic framework to show that osmosis may be strongly influenced by out-of-equilibrium effects. Although a very strong interest has been shown recently in investigated the osmotic pressure generated by *active fluids* in the vicinity of *passive semi-permeable membranes* [385–388] the osmotic pressure generated by a *passive fluid* in the vicinity of an *active membrane* remains completely unexplored. It is the object of the following part to set the basic ingredients to tackle some of the out of equilibrium aspects of osmotic pressure.

Chapter 1: The kinetic approach of osmosis

The beauty of thermodynamics is that there is often two ways to describe or reach the same result – and this generally adds physical comprehension. This is what I revisit below for the osmotic pressure, with, on the one side the thermodynamic approach of osmosis, and, on the other side, the mechanical approach of osmosis.

1 The limitation of the van 't Hoff theory

For low solute concentrations, the osmotic pressure is expressed by the van 't Hoff law,

$$\Delta\Pi = k_B T \Delta c, \tag{1.1}$$

where Δc is the difference in solute concentration between the two reservoirs [16]. The van 't Hoff law is derived by equating the solvent chemical potential of the solvent across the membrane [21–23]. The osmotic pressure is accordingly defined in terms of equilibrium thermodynamic properties of the system. An interesting, and quite counterintuitive, remark is that – provided it is semi-permeable – the membrane characteristics do not appear in this thermodynamic expression for the osmotic pressure. when the membrane is only *partially* impermeable to the solute, there is still a solvent flux driven by the solute concentration imbalance [389–392]. However the driving osmotic pressure is usually assumed to be reduced by a (dimensionless) rejection factor, say σ. Determining σ requires to describe the detailed mass and solute transport across the membrane, and this requires to go beyond the thermodynamic description.

2 The Kedelm–Katchalsky framework and reflection coefficient

To investigate where this rejection factor comes from, we need to take a broader perspective. Transport across a membrane is characterized within the framework of irreversible processes, via a transport matrix $\mathbb{L}$, relating fluxes to thermodynamic forces [16, 393, 394]

$$\begin{pmatrix} Q \\ J_s - cQ \end{pmatrix} = \mathbb{L} \times \begin{pmatrix} -\nabla p \\ -\nabla \mu \end{pmatrix}, \tag{1.2}$$

with Q and J_s denoting respectively the volume flux (per unit area) of the solution and of the solute through the membrane; $J_s - cQ$ is accordingly the excess flux of solute with respect to solute standardly advected with the flow cQ; c is the solute concentration, p is the pressure, and μ is the solute chemical potential. This matrix is symmetric according to Onsager's principle. Kedem and Kachalsky rewrote these transport equations in a more explicit form as [16, 71, 395, 396]

$$Q = -\mathcal{L}_{\text{hyd}} \left(\Delta p - \sigma k_B T \Delta c \right), \tag{1.3}$$

$$J_s = -\mathcal{L}_{\text{D}} \alpha \Delta c + c(1-\sigma) Q, \tag{1.4}$$

where $\mathcal{L}_{\text{hyd}} = \kappa/(\eta L)$ is the solvent permeance, with κ the permeability (in units of a length squared), η the fluid viscosity, and L the membrane thickness, and $\mathcal{L}_{\text{D}} = D/L$ is the solute permeability with D the diffusion coefficient of the solute. The Kedem–Kachalsky result introduces the reflection coefficient σ mentioned previously, that is dependent in particular on the relative permeability of the membrane to the solvent and the solute. [389, 390, 397] Interestingly, the non-dimensional coefficients ω and σ are expected to be linearly related, [16] as $1-\sigma \propto \alpha$ – as we show again in [398]. Note that the previous Kedem–Kachalsky equations are valid in the regime of dilute solute concentration, where the van 't Hoff relationship applies. Generalizing them to mixtures with arbitrary volume fractions requires to introduce the general thermodynamic expression for the osmotic pressure and its link to non-equilibrium transport remains to be developed.

3 A kinetic approach to osmosis

To highlight the mechanical balance underlying osmotic transport, we consider a simplified model where the effect of the membrane on the solute is described in terms of an energy barrier, see Fig. 1.1. Such an energy barrier is a crude but convenient description for the membrane, avoiding to enter into the details of the interaction of the solute with the membrane. It reduces the description to its minimal ingredients of partial or semi-permeability, and makes it amenable to explicit calculations. As I show below, it allows to explore in details how osmotic pressure builds up, even in the absence of a full semi-permeability of the membrane to the solute. Such a potential barrier can also be physically achieved; for example, it can be generated from a nonuniform electric field acting on a polar solute in a nonpolar solvent [399], or it can represent the nonequivalent interactions of solute and of solvent particles with a permeable membrane, *e.g.*, charge interactions [400, 401]. In the case of osmosis, this approach was first introduced by [393] in the low concentration regime, and generalized more recently by Picallo *et al.* to explore the osmotic transport across asymmetric perm-selective [401].

We consider a membrane separating two sub-volumes, containing a solvent and a solute. The concentration difference between the two volumes is $\Delta c = c_+ - c_-$. As introduced above, we assume that the membrane behaves as an external potential $\mathcal{U}$ on the solute *only*, but

not on the solvent molecules. It varies only along the x axis. We denote L the lateral range of the potential $\mathcal{U}$, so that $\mathcal{U}(-L/2) = \mathcal{U}(L/2) = 0$, and vanishes outside of this domain, see Fig. 1.1. The membrane is permeable to the solvent, with a permeance $\mathcal{L}_{\rm hyd}$, relating the flux Q to the pressure drop Δp in the absence of a concentration difference: $Q = -\mathcal{L}_{\rm hyd}\Delta p$.

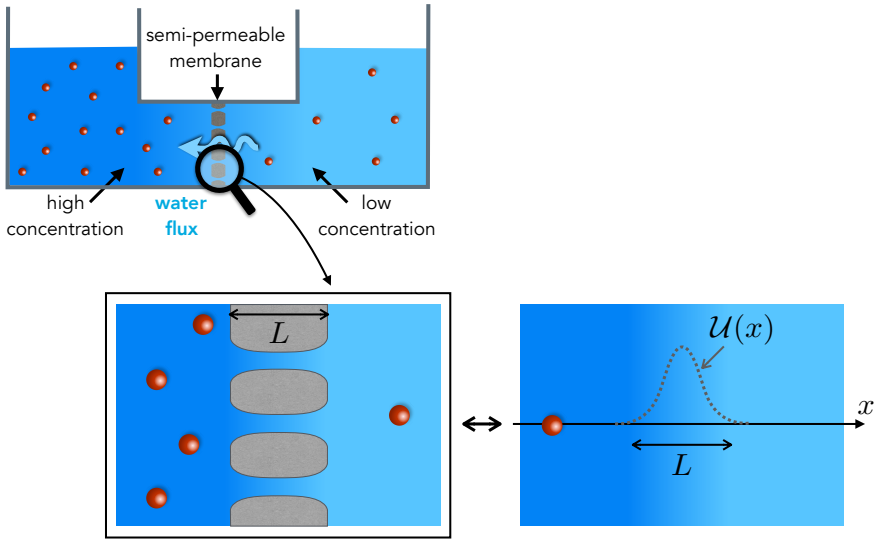

Fig. 1.1: **Kinetic approach of osmosis**: Illustration of the basic principle of osmosis, described by a membrane capable of differentiating water and the solute (in red), inducing a water flow. The membrane can be represented in terms of a longitudinal potential barrier $\mathcal{U}(x)$ for the solute.

Writing properly the stationary solute concentration and the force balance on the solvent allows to derive that the driving force inducing the solvent flow is written in terms of an apparent pressure drop, $-\partial_x \mathcal{P} = -\partial_x p + c(x)(-\partial_x \mathcal{U})$. The membrane, via its potential $\mathcal{U}$, will therefore create an average force on the fluid, which writes per unit surface

$$-\Delta\mathcal{P} = -\Delta p + \int_{-L/2}^{L/2} dx\, c\,(-\partial_x \mathcal{U}), \tag{1.5}$$

where ΔX means the difference of X between two sides. The second term of Eq. 1.5 can be interpreted as the osmotic contribution; one can calculate it explicitly using the concentration profile, to obtain

$$-\Delta\mathcal{P} = -\Delta p + \sigma\Delta\Pi. \tag{1.6}$$

This leads to the classical van 't Hoff law of the osmotic pressure, $\Delta\Pi = k_B T\Delta c$, and the expression of the reflection coefficient σ is obtained as

$$\sigma = 1 - \frac{L}{\int_{-L/2}^{L/2} dx'\, \exp[+\beta\mathcal{U}(x')]}. \tag{1.7}$$

The above result correctly recovers the case of a completely semi-permeable membrane (no solute flux across the membrane), *i.e.*, $\beta\mathcal{U} \gg 1$ in this limit, and thus $\sigma \to 1$, yielding

$-\Delta\mathcal{P} = -\Delta[p - \Pi]$. In the intermediate cases, although the membrane is permeable, a flow arises due to the solute concentration gradient even in the absence of a pressure gradient. When the potential is repulsive and small $\mathcal{U} \sim k_B T$, then $0 < \sigma < 1$; the flow is in the direction of increasing concentration and reversely. The total flux across the membrane is

$$Q = -\mathcal{L}_{\text{hyd}} \left(\Delta p - \sigma k_B T \Delta c\right). \tag{1.8}$$

Overall Eq. 1.8 agrees with the Kedem–Kachalsky result in Eq. 1.3.

Chapter 2: Osmosis beyond the linear concentration regime

I am especially indebted to Hiroaki Yoshida for his overall patience and great collaboration in this project. The following chapter is connected to the publications [398, 402] reported p.138 and p.146

Eq. 1.7 is derived in the case of a dilute dissolved solution. I now investigate some aspects of the osmotic pressure in high concentration regimes where Eq. 1.7 is not valid.

1 Osmotic pressure at high concentrations

Using the formalism described above, it is possible to derive a more general expression for the reflection coefficient – without making any assumption on the dilution regime – which takes the form:

$$\sigma = 1 - \frac{\int_{-L/2}^{L/2} \frac{dx'}{\lambda[c(x')]}}{\int_{-L/2}^{L/2} \frac{dx'}{\lambda[c(x')]} \frac{c_0}{c(x')}}, \tag{2.1}$$

where λ is the mobility of the solute particles, and c_0 is the average solute concentration far from the membranes; $c(x)$ is the stationary concentration distribution, see [398]. Since no assumption is made on the magnitude of c_0, this expression is valid beyond the dilute solute limit. In the dilute solute limit, the formula given in Eq. 2.1 reduces to the one derived by Manning [393], Eq. 1.7. In this regime, the concentration profile of the solute will alter the osmotic pressure and nonlinear feedback effects are seen.

We were able to visualize this dependence at high solute concentration, by performing molecular dynamics simulations (details are available in [402]). We simulated two reservoirs

separated by a potential membrane – see Fig. 2.1-a and b; at low and high concentration, for different barrier (membrane) strengths and computed the reflection coefficient – see Fig. 2.1-c. We observe the expected trend that for low barrier strengths, the reflection coefficient vanishes, and that is coherent with the fact that solute molecules are indeed allowed to pass. For high barrier strengths, the reflection coefficient reaches 1 in any case, which is coherent with the fact that beyond a critical strength, no solute molecule is allowed through. For the lower concentration (in blue) the data is coherent with the linear prediction of Eq. 1.7. For the higher concentration (in red), the prediction doesn't change and overestimates the reflection coefficient. The non-linear Eq. 2.1 however is perfectly coherent with the data.

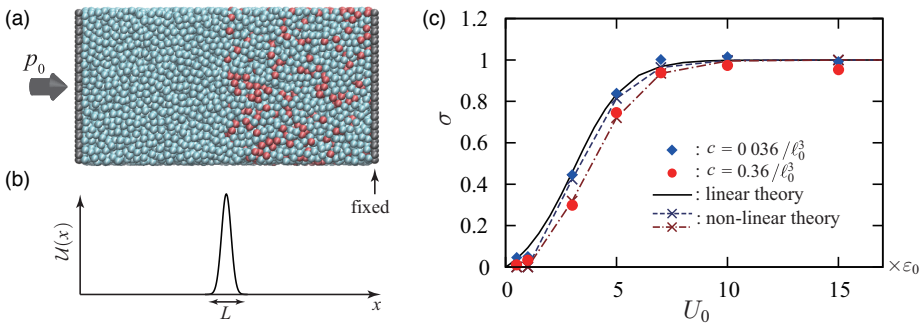

Fig. 2.1: **Osmotic pressure at high concentration**: *Figures from H. Yoshida* (a) Simulation setup of two fluid reservoirs with water (light blue) and solute (red), separated by a potential membrane. (b) Illustration of the energy barrier $\mathcal{U}(x)$ felt only by the solute particles – a gaussian rescaled. (c) Reflection coefficient σ versus height of the energy barrier U_0. The MD results are shown by the symbols. While the solid line is the theory for the low concentration regime given in Eq. 1.7, the dashed line and dash-dotted line are the results of the generalized theory Eq. 2.1. The data is rescaled in terms of Lennard-Jones units.

2 Diffusio-osmosis at high concentrations

2.1 A quick explanation of diffusio-osmosis

Osmosis is expected to occur under a solute imbalance across a semi-permeable membrane, which is permeable to the solvent but not to the solute. In contrast, diffusio-osmosis is a surface-driven flow occurring under solute gradients. It is an interfacially driven phenomenon, which takes its origin within the diffuse interfacial layer close to the surface where the solute interacts specifically with the surface. [403–405]. This form of transport has attracted increasing attention in the context of recent developments in micro- and nano-fluidic systems [391, 392, 406–408]. The basic principle underlying osmosis is the following [394]: a solute gradient (forced by an external chemical potential for example) is in the vicinity of a surface. The surface and the solute may interact for instance via chemical interactions. If the interaction is attractive – see Fig. 2.2-a – a solute gradient also builds up perpendicular

to the surface. This gradient induces – because of force balance – a pressure on the water flow, that is a higher where the concentration is greater. The resulting pressure difference drives a flow parallel to the surface. Note that in this case the flow is in the direction of the lower concentrations, thereby increasing the concentration difference.

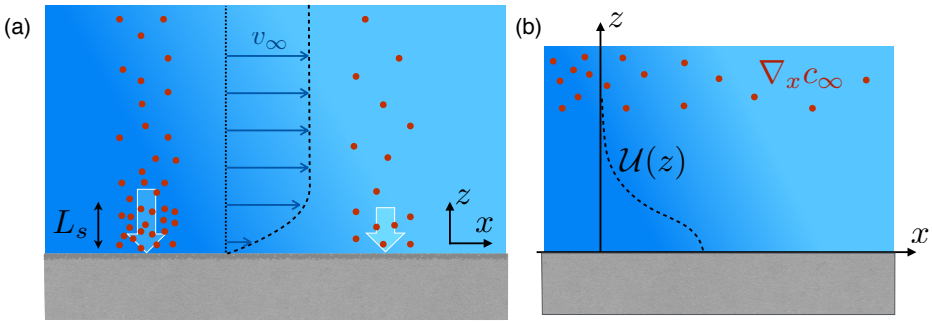

Fig. 2.2: **Diffusio-osmosis**: (a) Schematic principle of diffusio-osmosis, the solute in red is attracted by the surface. L_s is the typical width of the diffuse interface. The big light blue arrows represent the pressure build up. (b) Kinetic counterpart of the diffusio-osmotic setting.

2.2 Diffusio-osmosis beyond equilibrium

We explored similar questions of high concentration for diffusio-osmotic transport. We model the effect of the surface again by an energy barrier described in Fig. 2.2-b. Writing properly the force balance and the fluxes allows to obtain a transparent expression for the diffusio-osmotic velocity far from the surface as

$$v_\infty = K_{DO}\partial_x \Pi[c_\infty(x)], \tag{2.2}$$

with the diffusio-osmotic mobility K_{DO} given as

$$K_{DO} = -\frac{1}{\eta}\int_0^\infty dz'\, z' \left(\frac{c(x,z')}{c_\infty(x)} - 1\right). \tag{2.3}$$

Note that η can also be assumed to depend on the concentration c. In this case, $1/\eta$ in K_{DO} has to be integrated along z as well. Full detail can be found in [398]. The results for diffusio-osmosis in Eq. 2.2 and Eq. 2.3 are analogous to electro-osmosis and other surface-driven flows, with the mobility defined in terms of the first spatial moment of a density profile (solute concentration profile for diffusio-osmosis and charge density profile in the case of electro-osmosis).

To sum up, a solute gradient generates an interfacial flow of the fluid. As highlighted in Eq. 2.2, this flow takes its origin in an osmotic pressure gradient occurring within the diffuse layer close to the surface. This flow is quantified by the value of the diffusio-osmotic mobility K_{DO}, which is non-zero only if there is surface excess or surface depletion of the solute. As a rule of thumb, its sign will be dominantly determined by the adsorption $\Gamma =$

$\int_0^\infty dz'\ (c(x,z')/c_\infty(x) - 1)$. If there is a surface excess ($\Gamma > 0$), the flow of water goes towards the low concentrated area ($K_{DO} < 0$). Respectively, if there is a surface depletion, the flow of water reverses. But in case of a complex concentration profile, for instance with an oscillatory spatial dependence on z due to layering, the sign of K_{DO} may be expected to differ from the adsorption Γ. In this case, no obvious conclusion can be made for the direction of the diffusio-osmotic velocity and a full calculation has to be made.

The general expression for the diffusio-osmotic velocity, in Eq. 2.2 and Eq. 2.3, is very similar to the corresponding expression for the dilute solution, [403–405] but the result in Eq. 2.2 makes it very clear that the diffusio-osmotic flux is indeed driven by the thermodynamic osmotic pressure gradient $\partial_x \Pi[c_\infty(x)]$. This highlights in particular that osmotic flows and diffusio-osmotic flows are well named, because they originate in the same driving force, the osmotic pressure gradient. Numerical validation of this expression was also performed [402].

3 Coupled osmotic effects

While the previous derivations considered osmosis and diffusio-osmosis separately, one may consider a coupled situation in which both phenomena act jointly. In full generality, the two transport phenomena are intimately coupled in the force balance and the situation is complex to disentangle. However some conclusions can be drawn in the limit where the pore size is large as compared to the interaction range of the surface potential, *i.e.* small diffuse layer. I established that the flow across the membrane still obeys a general Kedem–Kachalsky formula as in Eq. 1.3, with Π the general osmotic force, but with a reflection coefficient which now contains the coupled effects of osmosis and diffusio-osmosis [398]:

$$\sigma = \sigma_O + \sigma_{DO} - \sigma_O \sigma_{DO}, \tag{2.4}$$

where σ_O is the osmotic reflection coefficient given by Eq. 2.1 and the diffusio-osmotic reflection coefficient is defined as $\sigma_{DO} = \eta K_{DO}/\kappa$, where K_{DO} given in Eq. 2.3 is the diffusio-osmotic reflection coefficient, and κ the permeability.

The last term in Eq. 2.4 accounts for a negative feedback coupling between osmosis and diffusio-osmosis. Although obtained in the limit of small diffuse layer, it exhibits a proper symmetry, as can be verified by considering various limiting situations. If the membrane is completely semi-permeable with $\sigma_O = 1$, then no solute flux occurs through the membrane and the diffusio-osmotic contribution in $\sigma_{DO}(1 - \sigma_O)$ vanishes. Reversely one also obtains $\sigma = 1$ when $\sigma_{DO} = 1$. A second note is that this coupled contribution hints to numerous possibilities to tune the flux through the membrane. With a given $\sigma_O < 1$, it is possible to enhance (respectively, diminish) σ – and thus the flux through the membrane – with a slight surface depletion (respectively, excess) on the surface. How this result may be generalized to any geometry remains to be explored.

Chapter 3: Osmosis out of equilibrium

Within this framework of a kinetic approach of osmosis, it is possible to study a great number of problems – in an "easy" way – and to investigate new effects on osmotic pressure and thus on filtration. For example, the osmotic pressure generated by active fluids in the vicinity of passive semi-permeable membranes has been explored with the kinetic approach [385–388]. The competition between two solute species trying to transverse a membrane – and with different affinities towards this membrane – was explored in this way [409]. Also transport through assymetric potential barriers were vastly explored, and specifically with a focus on osmotic flow properties [410, 411].

On the whole, already this approach was present and was used for a variety of barrier shapes in the 1980s [412] in particular to investigate consequences on permeability. At this time already, *how dynamical aspects* of the barrier shape, of the protein conformation, of the dynamics of the binding sites, etc. *would influence transport and permeability* was the main open question. Early molecular dynamics simulations – also limited by computational speeds – gave somewhat not a clear view on the basic mechanisms at play [413,414]. Surprisingly, this question is still open today. Specifically, how the osmotic pressure is affected by *membrane* dynamics is lacking a solid theoretical framework and behavioral rules. This is what I plan to investigate in the remaining months of my thesis.

Conclusion

In summary, I have revisited a kinetic theory to explore osmotic transport, that is able to encapsulate more details than standard thermodynamics. We have explored various forms of osmotic transport in the regime of high solute concentration. Both osmosis across model membranes and diffusio-osmosis at the interface with solid substrates were considered. We have specifically focused our approach on the mechanical balance leading to solvent flow under solute concentration gradients and explored the regime of high solute concentration. For high solute concentration gradients, the van 't Hoff expression for the osmotic pressure, $\Pi = k_B T c$, is replaced by its general thermodynamic counterpart, $\Pi = c\,\partial_c f - f[c] + f[c=0]$ (with f the free energy density), which is valid for an arbitrary composition of the "solvent"/"solute" mixture [415]*. Though it is not shown here (but in the full paper in [398]) this general expression of the osmotic pressure for mixtures, as obtained classically from the thermodynamic framework, emerges from the mechanical balance controlling non-equilibrium transport under solute gradients. It generalizes the existing results obtained in the dilute solute regime and was confirmed by simulations [402].

An interesting consequence of the result in Eq. 2.2 is that a non-linear "sensing" may originate from non-linearities of the osmotic pressure versus the solute concentration, inducing special coupling types echoing non linear sensing in biological channels [416]. This may occur, *e.g.*, for dense colloidal or polymer suspensions, as well as from a concentration dependent mobility K_{DO}.

In the case of osmosis, we considered a model membrane, where the details of the membrane are reduced to their minimal ingredients and modeled as an external potential acting on the solute. As shown above, this simplified picture is extremely fruitful to gain insight into the mechanical balance at play. But it also points to the fact that osmosis does not require *per se* a solid membrane to be expressed. One may consider experimental situations where such a potential is built on the basis of optical or electrical forces, using *e.g.* optical tweezers to repel "solute" particles, or dielectro-phoretic potential traps. Such "*osmosis without a membrane*" configuration would be highly interesting to develop, as it would simplify many aspects of clogging and pore blocking which occur for standard porous membranes. However designing such non-solid wells for molecular solutes, such as salts, remains a considerable challenge.

*This book is my great-spiritual-father's book, it was very useful to Hiroaki and me.

Main conclusion and perspectives

In my thesis I have strived to develop and understand some of the non-trivial equilibrium and out-of-equilibrium phenomena that govern nanofluidic transport – from understanding the impact of surface properties that have large consequences at these scales to more open questions on out-of-equilibrium consequences on transport. Obviously a number of challenges remain to be achieved: from experimental investigations to investigate and harness all these effects... to theoretical developments that are required to explore and understand the broad range of effects occurring at these scales. In particular, reaching the desired selectivity performances required for instance in biomedical treatment is still a challenge – for dialysis treatment in the case of kidney failure some waste molecules bigger than urea have yet to be controlled, and so far "only" grown cells from biological extracts are able to do so [138] – or in filtration and desalination (to bypass the famous permeability-selectivity trade-off).

Below I review some of the open questions that I have – and more broadly that are shared by the group and the community – on these topics.

What are the consequences of fluctuations at the nanoscale on macroscopic quantities ?

Following the questions that I tackled on the influence of simple fluctuations of pore opening and of surface confinement on transport, are a number of questions on the broad consequences of fluctuations at the small scale on microscopic or macroscopic properties. Some organisms even rely on excess noise [417] for selective transport and undoubtedly *harnessing* noise instead of *suffering* noise seems like a great open field to improve a number of processes (an example: [418]), in some sense going beyond the traditional fluctuation-dissipation picture of Kubo [419]. All in all this is a vague question, but for instance one concrete example question is to ask: what are the consequences of surface fluctuations in a channel on permeability ? And the underlying interest being : is it possible to enhance permeability given a certain fluctuation spectrum ? This would undoubtedly have consequences on filtration technology.

What can we expect from "angström" scale transport ?

Beyond the nanoscale description of water and ion transport, which includes most of the non-trivial surface effects that combine to flow transport, an atomistic or "angström" scale description of fluidic transport is required to describe transport in angström scale slits [118] or channels [112, 113, 125]*. Indeed at these scales transport becomes single-file like and non trivial effects are expected to occur, beyond the extrapolation of the continuous description.

This would allow to answer a variety of questions in particular connected to surprisingly high selectivity measurements in biological channels. For instance, gramicidin A — a model protein membrane, sharing some common features with the potassium channel KscA [420] – spontaneously forms a channel that leads to high selective currents [325, 421]. Transport through this channel is undoubtedly single file, due to the minute scales of the crosssection [416]. Interestingly, a number of nonlinear coupling effects arise in this channel: non-trivial interactions of cation fluxes [416], collaborative effects [422], non-linear conductance response to ion concentration [413]. A number of other effects are expected in these channels [423] including non trivial osmotic effects, but also in other "single-file" like channels: feedback of ions within the channel on transport in potassium channels [424] but also non-intuitive coupling of ions and active transport in giant squid nerves or axons [425, 426].

All these systems are currently lacking a detailed and extensive theory to account and model the observed effects. With a good theoretical framework, we may also be able to investigate the effects of fluctuating dynamics on the transport properties through these channels (for instance [414] showed non trivial coupling of motion of the binding sites to transport). And beyond, *understanding* the behavior of individual ions in channels could allow to *build* artificial ionic machines, that would open a whole new era of applications for filtration and biomedical applications.

What is the result of coupling various effects ?

Indeed complex behaviors are ongoing in biological channels, induced by a variety of forces: from electric gradients, chemical gradients, osmotic gradients, but also pressure or mechanical forces. The coupling of these effects induces sometimes non-linear responses because of strong interplay at these scales [423]†. For example, the streaming potential under a chemical gradient of gramicidin A channels is very special [427] and going to mechanical forces, some of them are key points responsible for "activating" specific ion channels like the piezo channels [428, 429]. Those mechanical sensors are vital for several biological functions and are a topic of ongoing research. Building their nanoscale physical counterparts would allow

*I am inspired for the following by the beautiful work started by Nikita Kavokine in my group.

†I am inspired for the following by the PhD thesis of Laetitia Jubin, one of my great labmates; and also the amazing theoretical work of Anthony Poggioli

not only to study and understand the elementary and surprising physics at play in these channels [430] but also to build their artificial counterparts for *e.g.* biomedical applications.

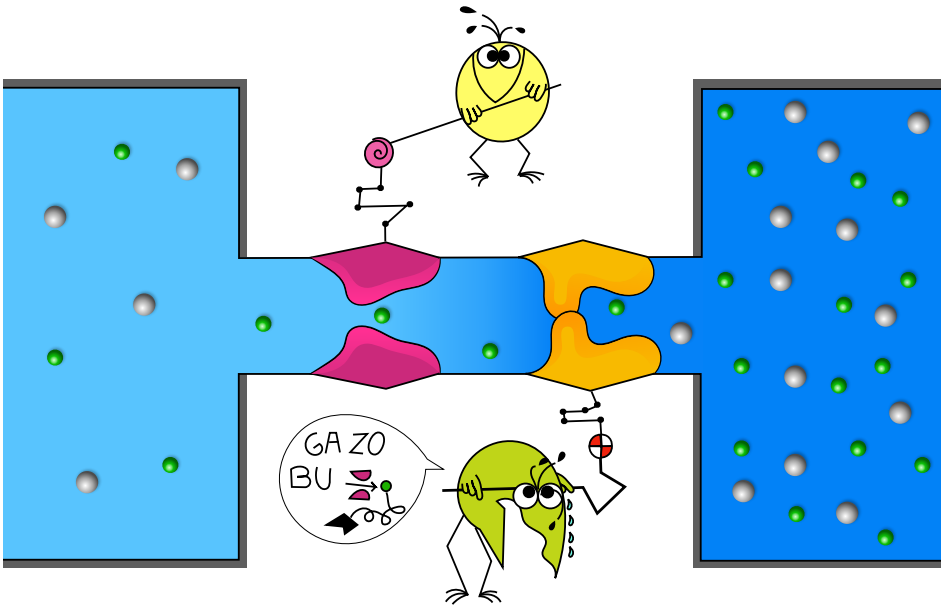

Principle of an ionic Shadok machine: A Shadok duet is trying to selectivity pump the green ionic particles through a channel thanks to a sophisticated Shadok pump design. The drawing is freely inspired from Les Shadoks - Jacques Rouxel.

List of publications

Publications linked to my PhD work:

[1] Marbach, Sophie et Lydéric Bocquet, "Active osmotic exchanger for efficient nanofiltration inspired by the kidney", *Physical Review X* 6(3), 031008 (2016).

[2] Eleonora Secchi, Marbach, Sophie, Antoine Niguès, Derek Stein, Alessandro Siria et Lydéric Bocquet, "Massive radius-dependent flow slippage in carbon nanotubes", *Nature* 537(7619), 210 (2016).

[3] Marbach, Sophie, Hiroaki Yoshida et Lydéric Bocquet, "Osmotic and diffusio-osmotic flow generation at high solute concentration. I. Mechanical approaches", *The Journal of Chemical Physics* 146(19), 194701 (2017).

[4] Hiroaki Yoshida, Marbach, Sophie et Lydéric Bocquet, "Osmotic and diffusio-osmotic flow generation at high solute concentration. II. Molecular dynamics simulations", *The Journal of Chemical Physics* 146(19), 194702 (2017).

[5] Eleonora Secchi, Marbach, Sophie, Antoine Niguès, Alessandro Siria et Lydéric Bocquet, "The Landau–Squire plume", *Journal of Fluid Mechanics* 826 (2017).

[6] Marbach, Sophie et Lydéric Bocquet, "Active sieving across driven nanopores for tunable selectivity", *The Journal of Chemical Physics* 147(15), 154701 (2017).

[7] Marbach, Sophie, David S. Dean et Lydéric Bocquet, "Transport and dispersion across wiggling nano-pores", *Nature Physics* (2018).

Publications from previous and adjacent works:

[1] Meng-Ju Sher, Niall M Mangan, Matthew J Smith, Yu-Ting Lin, Marbach, Sophie, Tobias M Schneider, Silvija Gradečak, Michael P Brenner et Eric Mazur, "Femtosecond-laser hyperdoping silicon in an SF6 atmosphere: Dopant incorporation mechanism", *Journal of Applied Physics* 117(12), 125301 (2015).

[2] Yu-Ting Lin, Niall Mangan, Marbach, Sophie, Tobias M Schneider, Guoliang Deng, Shouhouan Zhou, Michael P Brenner et Eric Mazur, "Creating femtosecond-laser-hyperdoped silicon with a homogeneous doping profile", *Applied Physics Letters* 106(6), 062105 (2015).

[3] Marbach, Sophie, Amélie Luise Godeau, Daniel Riveline, Jean-François Joanny et Jacques Prost, "Theoretical study of actin layers attachment and separation", *The European Physical Journal E* 38(11), 122 (2015).

[4] Marbach, Sophie, Karen Alim, Natalie Andrew, Anne Pringle et Michael P Brenner, "Pruning to increase Taylor dispersion in Physarum polycephalum networks", *Physical review letters* 117(17), 178103 (2016).

[5] Marbach, Sophie et Karen Alim, "Generalized Taylor dispersion in actively contracting pipes", *in writing* (2018).

Active Osmotic Exchanger for Efficient Nanofiltration Inspired by the Kidney

Sophie Marbach and Lydéric Bocquet*

Laboratoire de Physique Statistique, UMR CNRS 8550, Ecole Normale Supérieure, PSL Research University, 24 rue Lhomond, 75005 Paris, France

(Received 6 April 2016; revised manuscript received 5 June 2016; published 18 July 2016)

In this paper, we investigate the physical mechanisms underlying one of the most efficient filtration devices: the kidney. Building on a minimal model of the Henle loop—the central part of the kidney filtration—we investigate theoretically the detailed out-of-equilibrium fluxes in this separation process in order to obtain absolute theoretical bounds for its efficiency in terms of separation ability and energy consumption. We demonstrate that this separation process operates at a remarkably small energy cost as compared to traditional sieving processes while working at much smaller pressures. This unique energetic efficiency originates in the double-loop geometry of the nephron, which operates as an active osmotic exchanger. The principles for an artificial-kidney-inspired filtration device could be readily mimicked based on existing soft technologies to build compact and low-energy artificial dialytic devices. Such a "kidney on a chip" also points to new avenues for advanced water recycling, targeting, in particular, sea-water pretreatment for decontamination and hardness reduction.

DOI: 10.1103/PhysRevX.6.031008 Subject Areas: Fluid Dynamics

I. INTRODUCTION

Most modern processes for water recycling are based on sieving principles: A membrane with specific pore properties allows the separation of the permeating components from the retentate [1]. Selectivity requires small and properly decorated pores at the scale of the targeted molecules, and this inevitably impedes the flux and transport, making separation processes costly in terms of energy. It also raises structural challenges since high pressures are usually required to bypass the osmotic pressure. Lately, nanoscale materials—like state-of-the-art graphene, graphene oxides, or advanced membranes [2–6]—have raised hopes to boost the efficiency of separation processes. Yet, a necessary step for progress requires out-of-the-box ideas operating beyond traditional sieving separation principles.

In this context, it is interesting to investigate how biological systems are able to defy these constraints in their water cycle. They often rely on various forms of osmotically driven transport. For example, in plants, osmosis is harnessed to drive water and sugars over long distances [7,8]. As we discuss in this work, filtration processes can also benefit from osmotic transport: This is the case of the kidney.

Per day, the human kidney is capable of recycling about 200 L of water and 1.5 kg of salt, separating urea from water and salt at the low cost of 0.5 kJ/L [9] while readsorbing ≈99% of the water input. The core of the kidney separation process lies in the millions of parallel filtration substructures called nephrons [9]. A striking feature is that the nephrons of all mammals present a precise loop geometry, the so-called loop of Henle. This loop plays a key role in the urinary concentrating mechanism and has been extensively studied from a biological and physiological point of view [9–17] (see also Sec. I of Ref. [18] for a short review of the physiological literature). The nephron operates the separation of urea from water near the thermodynamic limit, ∼0.2 kJ/L (see Sec. V of Ref. [18]), yet standard dialytic filtration systems, which are based on reverse osmosis and passive equilibration with a dialysate, require more than 2-orders-of-magnitude more energy [19]. Some attempts to build artificial devices mimicking the nephron were reported in the literature, but they rely on biological tissues or cell-mediated transport and cannot be easily scaled up and transferred to other separation devices [20–22]. Mimicking the separation process occurring in the kidney remains a challenge.

In this work, our goal is to take a physical perspective on the separation process at work in the nephron in order to decipher the elementary processes at work. This allows us to propose a simple biomimetic design for an osmotic exchanger inspired by the kidney's loop of Henle—see Fig. 1—combining a passive water permeation and an active salt pumping. Such an artificial counterpart can be implemented based on microfluidic elementary building blocks.

A key feature of the process is merely geometrical: The U-shaped loop of Henle is designed as an active osmotic exchanger, with the waste separated from water and salt via a symbiotic reabsorption. Starting with physiological

*lyderic.bocquet@lps.ens.fr

Published by the American Physical Society under the terms of the Creative Commons Attribution 3.0 License. Further distribution of this work must maintain attribution to the author(s) and the published article's title, journal citation, and DOI.

models of the nephron [12,15], we revisit the detailed out-of-equilibrium flux balance along the exchanger. Our analysis allows us to obtain, to our knowledge for the first time, absolute theoretical bounds for its efficiency in terms of separation. Furthermore, we are able to predict analytically the energetic performance of the separation process. Comparing to alternative sieving strategies like reverse osmosis and nanofiltration, we show that this osmotic exchanger operates at a remarkably small energy cost, typically 1 order of magnitude smaller than other traditional sieving processes, while working at much smaller pressures. Our predictions further assess the key role played by the second part of the loop in order to reach optimal efficiency and low energy cost.

II. TRANSPORT EQUATIONS IN AN OSMOTIC EXCHANGER

A. Geometry of an osmotic exchanger

The model we consider is sketched in Fig. 1. It is a concentrating system that possesses the same primary features as the mammalian nephron: (i) a serpentine geometry consists of (ii) a first U-loop (Henle's loop, HL) with a descending limb (D) permeable only to water—a task performed by the aquaporins in the kidney—while the second ascending limb (A) is coated with "activator" pumps—accounting for the sodium pumps in the kidney [9,23–25]; (iii) this coil is embedded in a common loose material, permeable to both water and salt, the interstitium;

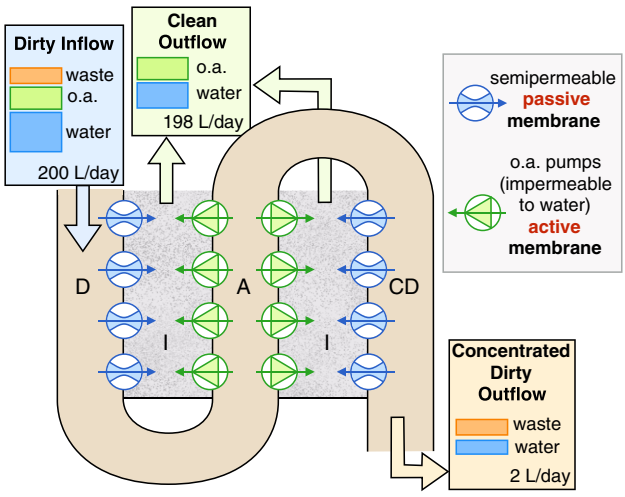

FIG. 1. The osmotic exchanger filtration system. Model for a concentrating device based on the geometry of Henle's loop in the kidney. Water, waste, and salt are carried through the loop of Henle, consisting of the descending limb (D) and ascending limb (A) and continued by the collecting duct (CD). Each limb wall allows exchanges with the interstitium (I), enabling water and salt to evacuate the loop. The remaining waste is concentrated and evacuated by the CD.

(iv) the first U-loop is continued by another loop and the so-called collecting duct (CD), again permeable to water only. This model is inspired by the so-called central core models of the nephron [12,15,26–31] (see also Sec. I of Ref. [x]). In our model though, we do not wish to accomplish a faithful description of the kidney and simplify the process to its elementary ingredients. This will also allow us to get detailed insights in the separation mechanism.

The initial solution entering the device from the D top is an aqueous solution with a waste to be extracted—in the case of the kidney, urea—with respective concentrations $[\mathrm{Water}]^{\mathrm{in}}$ and $[\mathrm{Waste}]^{\mathrm{in}}$. Aside from the specific geometry of the coil, an essential feature of the process is to use an "osmotic activator"—in the case of the kidney, NaCl salt—that enters the D limb along with the mix, with concentration $[\mathrm{Osm}]^{\mathrm{in}}$. The terminology of osmotic activator is justified by the role played by the salt in this separation process, and it constitutes the main working principle of this loop: Thanks to the U-loop geometry, the pumps in the A limb generate a salinity gradient in the interstitium that passively drags, via osmosis, the water from the D limb to the interstitium. In simple words, the work performed by the ionic pumps is further harvested to also drag water osmotically in the interstitium. The geometry of the loop of Henle thus plays the role of an osmotic exchanger.

B. Transport equations and osmotic fluxes

We now quantitatively analyze the transport of the various components along the serpentine geometry sketched in Fig. 1. For the sake of simplicity, we develop a one-dimensional modelization along the tube length. The coordinate along the tube is x, and the origin is located at the top of the D limb. The length of the tube from top to first loop is L [see Fig. 2(b)]. This simplification does not alter the main ingredients. One may indeed check that the equilibration of the concentrations by diffusion processes in the orthogonal direction is fast compared to the axial velocity of the fluid, so concentrations may be considered uniform in the orthogonal direction within each limb (but they may strongly differ from limb to limb). Moreover, the velocity of the fluid in the limbs is high enough that diffusion processes along the axial direction can also be neglected. We consider, for simplicity, the steady-state regime of the system.

In the following, we first focus on the single U-loop, e.g., the loop of Henle *per se* (D + A limbs), and then extend our analysis to the complete double-loop geometry (D + A limbs +CD).

1. Descending limb

Along the D limb, the water flux evolves because of the permeation of water under the osmotic pressure across the semipermeable D limb walls. Writing the infinitesimal water balance and osmotic fluxes [32] along a slice of the D

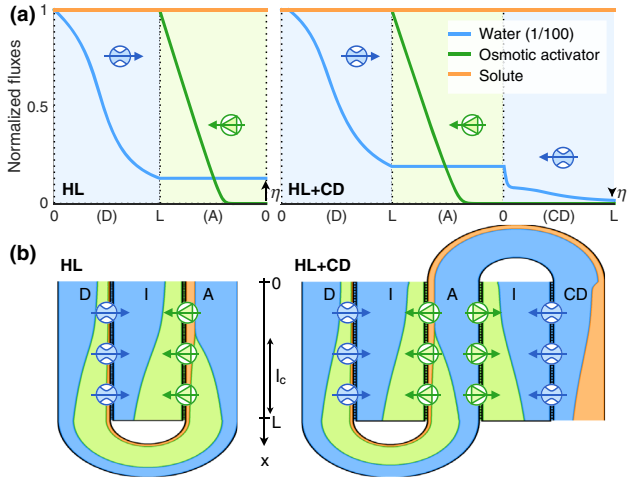

FIG. 2. Spatial distributions of the fluxes and molar fraction in the U-loop and full double loop (HL and HL + CD models). (a) Fluxes of water (divided by a scaling factor of 100), osmotic activator (salt), and waste along the D and A limbs, left panel; and along the CD for the HL + CD case; in this graph, the water loss ratio $\eta = q^{\rm out}_{\rm Water}/q^{\rm in}_{\rm Water}$ is the final normalized flux. (b) Spatial distribution of the molar fractions of water (divided by a scaling factor of 100), osmotic activator, and waste along the D and A limbs and in the interstitium. Note that in the (HL + CD) double-loop geometry, the interstitium exchanges with all three branches (D, A, CD); although two were plotted for convenience, they have the same composition. Numerical data are calculated with parameters $L = 4.3$ mm, $P_f = 2500$ μm/s, $n = 1$.

limb allows us to write the equation for the water flux along D as

$$\frac{\partial v_D[\mathrm{Water}]_D}{\partial x} = \frac{2P_f}{r}\ln\left(\frac{a_I^W}{a_D^W}\right), \tag{1}$$

where v is the velocity of the fluid, P_f the permeability of the D walls, r the radius of the limb, a^W the chemical activity of water—here, assumed to be proportional to the molar fraction of water—and D (resp. I) indices refer to variables in the D (resp. the interstitium). In the D limb, all other species are conserved.

The fluid velocity can be calculated thanks to conservation of mass in every limb. For instance, in the D limb, this is written $\partial v_D/\partial x = \bar{v}_{\rm Water}\{[(\partial[\mathrm{Water}]_D)/\partial t] + [(\partial v_D[\mathrm{Water}]_D)/\partial x]\}$, with $\bar{v}_{\rm Water}$ the molar volume of water. The hydrostatic pressure drop along each limb is ruled by Poiseuille flow. However, the pressure drop is significantly small [13] and is thus neglected. Accordingly, we can safely neglect, in Eq. (1), the contribution of the hydrodynamic pressure drop to the osmotic pressure drop.

2. Ascending limb

In the A limb, the salt, denoted in the following as the osmotic activator, is actively pumped across the walls. We consider a general case where the pumps drive n osmotic activator molecules for an elementary energy cost. In the kidney, this is provided by the dissociation energy of one adenosine triphosphate (ATP) molecule, and the stoichiometry is believed to be 3 Na^+ for 1 ATP [33]; Cl^- follows through the tissue walls and diffuses quickly to achieve electroneutrality [33]. We write Michaelis-Menten kinetics to describe the activator concentration evolution in the A limb [34,35]:

$$\frac{\partial v_A[\mathrm{Osm}]_A}{\partial x} = -\frac{2nV_m}{r}\left(\frac{[\mathrm{Osm}]_A}{K + [\mathrm{Osm}]_A}\right)^n, \tag{2}$$

where V_m is the maximum rate intake, K is the Michaelis constant, and A indices refer to variables associated with the A limb. The kinetics involved are assumed to be independent of the concentration of the osmotic activator in the interstitium, and furthermore, the energy requirement for the pump is assumed to be independent of the concentration of any of the constituents [33]. The kinetics described by Eq. (2) can be applied to various pumping mechanisms. All other species are conserved in the A limb. In particular, the membrane separating the A limb and the interstitium is considered to be impermeable to water.

3. Interstititum

In the interstitium, equations similar to Eq. (1) and (2) are written for the salt and water concentrations, with the sign reversed for the terms on the right-hand side. No waste is present in the interstitium. The velocity of the fluid is taken to be zero at the bottom of the interstitium.

III. RESULTS: SPATIAL DISTRIBUTIONS, FLUXES, AND OPTIMAL SEPARATION ABILITY

The previous analysis yields a set of 11 coupled and self-consistent nonlinear transport equations for the water, osmotic activator, and waste concentrations, as well as for the velocities in the various compartments. At the entrance of the device, the fluxes of water, osmotic activator (salt), and waste are prescribed as $q^{\rm in}_{\rm Water}$, $q^{\rm in}_{\rm Osm}$, and $q^{\rm in}_{\rm Waste}$. The integration of the previous system of equations yields the spatial distributions of the molar fractions of each component and the outcoming water and waste fluxes, $q^{\rm out}_{\rm Water}$ and $q^{\rm out}_{\rm Waste}$. The whole set of equations and boundary conditions is recalled in Sec. II of Ref. [18].

This complex system of differential equations is first solved numerically using standard methods, see Materials and Methods. Later, we also perform a systematic analysis of the transport equations at the steady state. This provides several analytical results for the spatial dependence of the concentrations and fluxes of the various components, as well as reliable estimates of the separation ability and energy cost of the system.

A typical numerical result is shown in Fig. 2 for the spatial evolution of the fluxes and molar fractions of the various components along the U-loop and double-loop geometries, at the steady state.

We now explore in detail the results in order to gain some insight on the filtration efficiency.

A. Osmotic activator pumping

We start the analysis by studying the absorption of the osmotic activator in the A limb. As highlighted in Fig. 2, what emerges from the numerical calculations is the existence of a characteristic length for reabsorption. This is confirmed by the analytical resolution of the transport equation for $[\mathrm{Osm}]_A$ and v_A in the A limb. Typically, this length scale can be constructed by balancing the input flux of the osmotic activator, $q_{\mathrm{Osm}}^{\mathrm{in}} = \pi r^2 v^{\mathrm{in}}[\mathrm{Osm}]^{\mathrm{in}}$, with the outward pumped flux, $q_{\mathrm{pump}} = 2\pi r \ell_c V_m n$ (with V_m the intake rate of the pumps), so that

$$\ell_c = \frac{q_{\mathrm{Osm}}^{\mathrm{in}}}{2\pi r V_m n}. \tag{3}$$

This result can also be obtained from the equations by approximating the spatial derivative of the activator flux $v_A[\mathrm{Osm}]_A$ in the A limb by its value at the bottom of the loop ($x = L$) in Eq. (2). This simplified expression for ℓ_c is then obtained under the assumption that $K \sim 30\ \mathrm{mmol/L} \ll [\mathrm{Osm}]^{\mathrm{in}} \simeq 100\text{–}200\ \mathrm{mmol/L}$ (Sec. III and Fig. S2 of Ref. [18]). Using typical values for the various parameters entering this equation (Ref. [18], Table 1), we find $l_c \simeq 1$ mm, which compares well to the total length of the nephron [36,37]. Beyond that length scale, the activator uptake is negligible.

Altogether, salt reabsorption occurs in a region of length ℓ_c close to the bottom of the U-loop. In the following, this allows us to split the effective domain of investigation into two different regions, where we can quantify every variable in the A limb: the deep domain, in a region of length ℓ_c close to the bottom, where osmotic activator or salt reabsorption happens on the length scale l_c; and the remaining higher domain.

A preliminary conclusion is that the length scale of salt reabsorption ℓ_c does not depend on the length of the limb L. As a result, even if L increases, salt will always be reabsorbed on the same length scale ℓ_c at the bottom of the A limb. However, the region of length $L - \ell_c$ at the top of the interstitium increases. In this region, concentrated salt coming from the bottom of the interstitium continues to be diluted by progressive water uptake under the osmotic pressure [see Fig. 2(b)].

B. Water reabsorption and optimal separation ability

With this result at hand, we can now turn to the detailed balance in water reabsorption. A key question is how much water may be extracted with this process. We analyze both the U-loop and the double-loop geometry.

Because the velocity at the bottom of the interstitium vanishes, the osmotic activator accumulates there, increasing the osmotic pressure between the D limb and the interstitium. As a result, water is dragged out of the D limb into the interstitium. The concentration of osmotic activator in the D limb thus increases, and water leakage is possible until the osmotic pressure between the D limb and the interstitium equilibrates.

1. Maximum separation ability in the U-loop

Let us start with the investigation in the U-loop. Because the exchanges between the interstitium and the limbs are well quantified, one may express the variables of the interstitium according to the variables of the D limb (unknown so far) and the variables of the A limb (with known approximates). Accordingly, a straightforward derivation allows us to obtain two self-consistent sets of equations for the variables of the D limb alone, which can be solved, although still complex. In Ref. [18], we report the details of the analytical calculations.

Beyond the detailed solutions, some helpful analytical predictions may be extracted from these calculations. This concerns, in particular, the proportion η of water flux remaining in the tube, i.e., the water loss ratio, $\eta = q_{\mathrm{Water}}^{\mathrm{out}}/q_{\mathrm{Water}}^{\mathrm{in}}$. In Fig. 3, we plot the numerical results for η as a function of the initial osmotic activator (or salt) concentration both in the U-loop and in the double-loop geometry discussed below.

A simple yet key result can be obtained for the water loss ratio, which characterizes the separation ability. It is obtained from the analysis of Eq. (1) in the upper part of the limb, by identifying that the flux of water through the semipermeable wall should always be directed from the D limb towards the interstitium (see Sec. IV of Ref. [18] for a detailed derivation). This is written as

$$\eta = \frac{q_{\mathrm{Water}}^{\mathrm{out}}}{q_{\mathrm{Water}}^{\mathrm{in}}} \geq \eta_{\mathrm{min}} = \frac{[\mathrm{Waste}]^{\mathrm{in}}}{[\mathrm{Waste}]^{\mathrm{in}} + [\mathrm{Osm}]^{\mathrm{in}}}, \tag{4}$$

where we recall that $[\mathrm{Waste}]^{\mathrm{in}}$ is the initial concentration of solute to be extracted arriving in the D limb and $[\mathrm{Osm}]^{\mathrm{in}}$ of osmotic activator.

This lower bound can be interpreted physically in terms of the osmotic pressure balance between the D limb and the interstitium. Indeed, for the water flux to be directed from D to I, the chemical balance requires that $a_I^W \leq a_D^W$ [see Eq. (1)]. This condition can be rewritten in terms of the various fluxes. On the one hand, the fluxes entering the D are $q_{\mathrm{Water}}^{\mathrm{in}}$ for water, $q_{\mathrm{Osm}}^{\mathrm{in}}$ for the osmotic activator, and $q_{\mathrm{Waste}}^{\mathrm{in}}$ for waste. On the other hand, by conservation of mass, the fluxes exiting the interstitium are $q_{\mathrm{Water}}^{\mathrm{in}} - q_{\mathrm{Water}}^{\mathrm{out}}$ for water, $q_{\mathrm{Osm}}^{\mathrm{in}}$ for the osmotic activator *if it has completely*

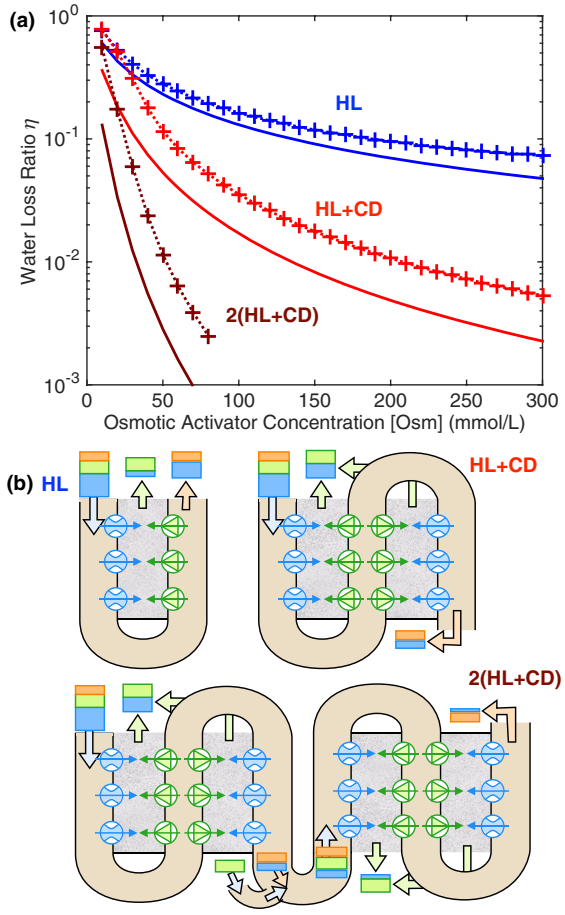

FIG. 3. Separation ability and minimal bounds. (a) Water loss ratio $\eta = q^{\rm out}_{\rm Water}/q^{\rm in}_{\rm Water}$ as a function of the initial concentration of osmotic activator $[{\rm Osm}]^{\rm in}$ (salt). Both the numerical results (crosses and dotted lines) and the predicted lower bounds (solid lines) are reported, for the single loop (HL), double-loop (HL + CD) and two double-loop cycles (2 HL + CD). The latter quantities are given by Eqs. (4) and (6) for the HL and HL + CD geometries, respectively. Numerical data are calculated with parameters $L = 4$ mm, $P_f = 2500$ μm/s, $n = 3$. (b) Schematics of the nephron-inspired systems studied in (a).

been reabsorbed, and 0 for the waste. In this minimal situation, the previous osmotic pressure balance yields

$$\frac{q^{\rm in}_{\rm Water} - q^{\rm out}_{\rm Water}}{q^{\rm in}_{\rm Water} - q^{\rm out}_{\rm Water} + q^{\rm in}_{\rm Osm}} \leq \frac{q^{\rm in}_{\rm Water}}{q^{\rm in}_{\rm Water} + q^{\rm in}_{\rm Osm} + q^{\rm in}_{\rm Waste}}, \quad (5)$$

and some simple algebra allows us to recover Eq. (4).

Note that it is also possible to derive an (approximate) upper analytic bound $\eta_{\rm max}$ for the water loss ratio η, by solving the equations on the species of the D in the higher and deeper parts of the limb, see Supplemental Material Sec IV.C. The upper bound $\eta_{\rm max}$ converges to the lower bound $\eta_{\rm min}$ defined by Eq. (4) in the limit of large pore permeability and/or a long tube (Supplemental Material Fig. S3). For typical parameter values in the kidney, doubling the permeability decreases the water loss ratio by 20% and doubling the length decreases it by 60%. The lower bound on η can also be approached, i.e., $\eta_{\rm max} \to \eta_{\rm min}$, by allowing for a nonuniform spatial distribution of the water permeability along the D walls or of the pumps along the A walls (Supplemental Material Sec. III-C), as observed in nature. In the general case, the lower bound for η in Eq. (4) provides a good approximation for the variational dependence of η versus the initial osmotic activator (or salt) concentration, as shown in Fig. 3.

The minimal bound on the water loss ratio in Eq. (4) is a key result because it provides a fundamental measure of the separation ability of the system. To achieve a good separation of waste from water in this device, the outflux of water $q^{\rm out}_{\rm Water}$, including the waste, should be as small as possible; e.g., the water loss ratio η should be as small as possible. Equation (4) shows that the uncovered water η is limited by the initial molar ratio of the solute to be extracted to the one of the osmotic activator. So, no matter how efficient the activator pumps are or how high the water permeability of the membranes is, it is not possible to recycle more water from the system than $1 - \eta_{\rm min}$.

Another way to interpret the result of Eq. (4) is to think of the osmotic exchanger as a concentrating device for the waste, i.e., any solute to be separated from water. The concentrating ability of this system, namely, $[{\rm Waste}]^{\rm out}/[{\rm Waste}]^{\rm in}$, can accordingly be expressed as a function of η as $[{\rm Waste}]^{\rm out}/[{\rm Waste}]^{\rm in} = 1/\eta$. Therefore, Eq. (4) is also a measure of the maximal concentrating ability of the system.

For typical parameter values in the kidney, the water loss ratio is $\eta \sim 0.2$ and is limited from below by $\eta_{\rm min} \approx 0.1$ after the first U-loop of Henle. At this point, we note that such a minimal water loss ratio is still in the high range of physiological data [9]. For a human being, with $\eta \sim 0.1$ and an average flux of fluid (water, urea, and salt) through the nephrons of about 120 mL/min, the daily water loss would be tremendous, about 18 L, and accordingly not viable. This separation ability is also too low to be technologically relevant.

2. *Maximum separation ability in the double loop*

Remarkably, a solution to bypass this limitation has already been achieved by nature. One may indeed observe that, in addition to the U geometry of the Henle loop, the nephron exhibits a second limb: the so-called collecting duct, which is only permeable to water as the D limb (see Figs. 1–4).

A key point is that this second limb is in contact with the same interstitium, therefore allowing the reabsorption of water for a second time. From the theoretical point of view, the analysis follows the same lines as above (see Sec. VIII of Ref. [18]). The concentration of salt in the interstitium is still assumed to be well mixed or homogeneous in the

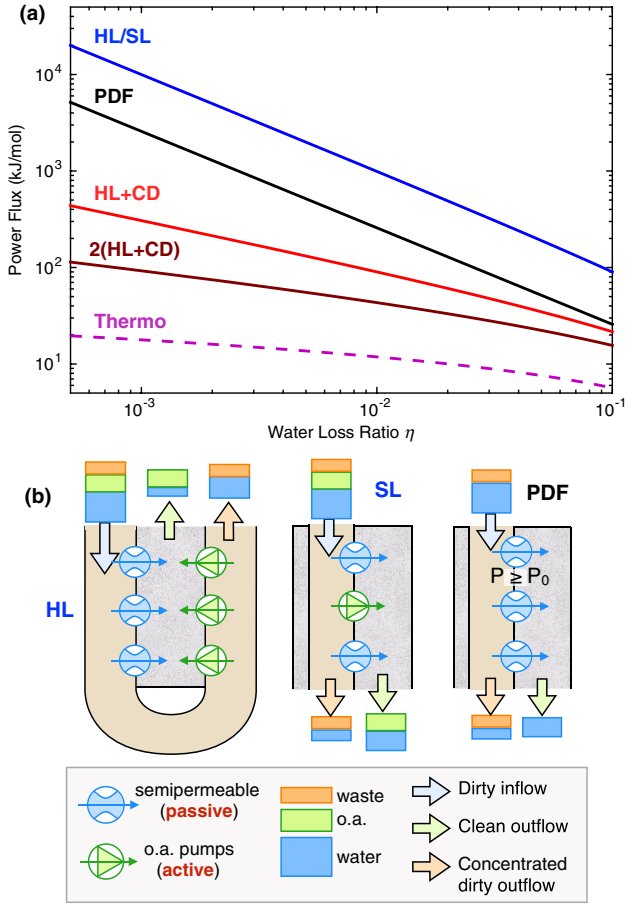

FIG. 4. Comparison of filtration efficiencies of various systems. We show power required versus water loss ratio for the different systems. The data points are from the analytical expressions of the text. Here, 2(HL + CD) corresponds to two successive HL + CD cycles, with the addition of osmotic activator in between the two cycles. Thermo corresponds to the minimal energy required to achieve a separation defined by a given water loss ratio. The nephron working conditions correspond to $\eta \approx 0.01$. Inset: Sketch of corresponding systems. Here, HL is for a single U-loop, HL + CD is a double loop, SL is a single limb, and PDF is for pressure-driven filtration. See text for detail.

orthogonal direction. Water is reabsorbed along the CD, following a permeability law similar to Eq. (1), the key difference being that the solute entering the CD has a different composition than the solute entering the D limb. A modified bound for the separation ability of the double-loop geometry is now given by

$$\eta \geq \eta_{\min}^{\mathrm{HL+CD}} = \left[\frac{[\mathrm{Waste}]^{\mathrm{in}}}{[\mathrm{Waste}]^{\mathrm{in}} + [\mathrm{Osm}]^{\mathrm{in}}}\right]^2. \tag{6}$$

In Eq. (6), the square dependence, as compared to Eq. (4), originates from this second absorption step. As above, the lower bound can be reached with an adjustment of geometrical and physiological parameters of the loops. Typically, one now finds that $\eta_{\min}^{\mathrm{HL+CD}} \approx 0.01$, yielding a nearly 2 L daily water loss for a human being, very close to usual physiological observations [9]. This double-loop device is therefore far more efficient than the simple Henle loop, Fig. 3. As for the single U-loop, the lower bound for η in Eq. (6) provides a good approximation for the variational dependence of η versus the initial osmotic activator (or salt) concentration (see Fig. 3).

Now, putting more than two loops in series (for instance, adding a third loop with a limb covered with osmotic activator pumps) does not further improve the performance because the osmotic activator uptake only happens in the first ascending limb. However, successive cycles in the HL + CD system can be done, provided that a certain amount of osmotic activator is added to the mix before each new cycle. In the case of two (respectively, N_c) successive cycles, if the concentration of the osmotic activator at the beginning of each HL + CD cycle is reinitiated, the minimal water loss ratio will be that defined by Eq. (6), now squared (respectively, to the power N_c). The improvement yielded for two cycles is also plotted in Fig. 3.

Equation (6) is the first main result of this paper. In a compact formula, it summarizes how the double-loop geometry acts as an osmotic exchanger to efficiently concentrate a waste. A better waste concentration and higher water recycling ability is achieved when the osmotic activator or salt concentration is increased. Indeed, the larger the salt concentration input, the stronger the osmotic gradient in the interstitium that allows for an increased reabsorption of water. However, a higher salt concentration requires more energy to pump the salt from the A limb to the interstitium. This raises the question of the energetic performance of the HL and HL + CD systems, in particular, if we want to consider them as useful working filtration devices.

IV. ENERGETIC PERFORMANCE OF THE OSMOTIC EXCHANGER

Beyond the separation ability estimate of the device, the energetic performance of the process remains to be assessed. From a physiological point of view, it is indeed vital for the kidney to operate at a minimal energy cost in view of the amount of water processed every day. Although some estimates of the free-energy expense in models of nephron have been developed, they all fail to account for the energy provided by the salt pumps [17,27,38–41]. Also, it is important to compare the energy expense of such an osmotic exchanger to more standard filtration devices.

To simplify, we assume that the permeability, pump speed, and tube length are adjusted so that η reaches its lower bound $\eta_{\min}$ in Eq. (4) or Eq. (6), depending on the geometry, respectively, U-loop or double loop.

A. Energetic cost for the single- and double-loop osmotic exchanger

In the system described in Fig. 1, the energy consumption reduces to the energy required for the pumping of the osmotic activator along the A limb. The consumed power is written as

$$\mathcal{P}_{\mathrm{HL}} = \int_0^L \pi r^2 dx \frac{e_{\mathrm{ATP}}}{n} N_{\mathrm{Osm}}(x), \tag{7}$$

with $N_{\mathrm{Osm}}(x)$ the pumped flux of the osmotic activator across the A membrane and e_{ATP} the required energy to drive n osmotic activator molecules within a single pump, which in the case of the kidney, corresponds to that of 1 ATP molecule. Using mass conservation, $N_{\mathrm{Osm}}(x) = -(d/dx)[v_A(x)[\mathrm{Osm}](x)]$ and $v_A(L)[\mathrm{Osm}]_A(L) = v_D(0)[\mathrm{Osm}]_D(0)$, one may integrate explicitly the previous equation to obtain

$$\mathcal{P}_{\mathrm{HL}} = q^{\mathrm{in}}_{\mathrm{Osm}} e_{\mathrm{ATP}}/n \underset{\eta\to 0}{\simeq} q^{\mathrm{in}}_{\mathrm{Waste}} \frac{e_{\mathrm{ATP}}/n}{\eta}. \tag{8}$$

This is a simple and compact prediction showing that the power cost $\mathcal{P}$ diverges like the inverse of the water loss ratio η. As expected, it becomes increasingly costly to obtain a higher separation of the waste, i.e., $\eta \to 0$ [Fig. 4(b), HL].

This result describes the power consumption for the single-loop exchanger. A much better energetic efficiency is actually reached by the double-loop system, in direct line with its improved separation ability. Indeed, since the interstitium is common to the U-loop and the collecting duct, the same amount of activator pumping is harvested to reabsorb water both from the D limb and the CD. Thus, no further energetic cost is required as compared to the single U-loop. Collecting the results, one obtains

$$\mathcal{P}_{\mathrm{HL+CD}} \underset{\eta\to 0}{\simeq} q^{\mathrm{in}}_{\mathrm{Waste}} \frac{e_{\mathrm{ATP}}/n}{\sqrt{\eta}}. \tag{9}$$

Equation (9) demonstrates that the power consumption of the double-loop system is considerably reduced compared to the single U-loop [Fig. 4(a)].

In the case of two successive cycles in the HL + CD system, with the addition of the same amount of osmotic activator to the mix before each new cycle as considered above, the energy expense is doubled—since the osmotic activator has to be readsorbed twice—but the minimal water loss ratio is squared. A two-cycle process yields a power cost $\mathcal{P}_{2\times(\mathrm{HL+CD})} \simeq 2q^{\mathrm{in}}_{\mathrm{Waste}}(e_{\mathrm{ATP}}/n)/\eta^{1/4}$, further optimizing the energy efficiency of the process for small values of η [see Fig. 4(a)]. A N_c-cycle process would accordingly operate at a power cost $\mathcal{P}_{2\times(\mathrm{HL+CD})} \simeq N_c q^{\mathrm{in}}_{\mathrm{Waste}}(e_{\mathrm{ATP}}/n)/\eta^{1/2N_c}$.

The above results can be compared to the minimal thermodynamical energy required for separation. The latter is estimated by computing the minimal work of separation for a given inward flux. After some algebra (see Sec. V of Ref. [18]]), this can be expressed in the simple form $\mathcal{P}_{\mathrm{Thermo}} \simeq -q^{\mathrm{in}}_{\mathrm{Waste}} RT \ln(\eta)$. As shown in Fig. 4(a), this result is below the previous predictions in Eqs. (8) and (9), as it should. However, increasing the number of cycles as discussed above allows us to get closer to this lower energetic bound.

Equation (9) is the second main result of this paper.

B. Power comparison to traditional sieving processes

In the context of energy efficiency, it is of utmost interest to compare the previous exchanger device with other traditional filtration or concentration systems. For this purpose, we first consider a nanofiltration (reverse-osmosis-like) system to extract the solute. This corresponds to a geometry with a single limb with water-permeable walls and acts as a pressure-driven filtration system (PDF) [see Fig. 4(b)]; no osmotic activator is required in this case. Water and waste only enter the limb at a high pressure with the same composition as in the dirty inflow in the nephron. In this situation, the hydrodynamic pressure drop is included in Eq. (1), and we similarly define the water loss ratio η as the ratio between the outward to inward flux of water through the limb (e.g., η is the ratio of water flux between the clean outflow and the dirty inflow). In this case, the high hydrostatic pressure allows us to drive water out of the descending limb, against the osmotic pressure, and concentrates waste up to a certain degree (see Sec. VII of Ref. [18] for details). If small components are also present in water—such as salt—and are also allowed to pass through the semipermeable membrane, the principle remains the same and the results are unchanged. The power required to achieve this process is proportional to the mechanical energy to drive that amount of flow with the corresponding hydrostatic pressure drop. The pressure drop may be further linked to the water loss ratio η. Some straightforward calculations along this idea, as detailed in Sec. VII of Ref. [18], allow us to predict the power required to achieve this process as

$$\mathcal{P}_{\mathrm{PDF}} \underset{\eta\to 0}{\simeq} q^{\mathrm{in}}_{\mathrm{Waste}} \frac{RT}{\eta}. \tag{10}$$

Interestingly, Eq. (10) is similar to Eq. (8) except for the thermal factor RT replacing the ATP energy, e_{ATP}/n. Quantitatively, RT is of the order of 2.5 kJ/mol, smaller than $e_{\mathrm{ATP}}/n \simeq 10$ kJ/ mol [42]. The two behave similarly as a function of η (see Fig. 4), and the HL system and the PDF system are thus only different by a multiplicative factor. A major difference, though, is that the PDF system requires us to bypass the osmotic pressure $P > P_0 \equiv \mathrm{RT}[\mathrm{Waste}]^{\mathrm{in}}$ associated with the separation of the

waste. This pressure can reach a few atmospheres depending on the concentration of the solute to extract, and such "reverse-osmosis-like" nanofiltration requires a high mechanical integrity of the material.

As an alternative geometry, we also consider a "single-limb" system corresponding to a single limb where water-permeable pores and activator pumps are intertwined on the wall of the limb [Fig. 4(a), SL]. For this device, we keep the osmotic activator in the solution. A similar analysis as for the single U-loop shows that the single-limb system is basically equivalent to the HL [see Fig. 4(b) and Sec. VI of Ref. [18]].

Altogether, Fig. 4 demonstrates that the double-loop exchanger, with one or more cycles, outperforms traditional filtration systems in terms of power efficiency while working at small pressure.

V. DISCUSSION

These results show that with the double-loop geometry of the collecting duct in series with the Henle loop, nature has evolved towards a most efficient geometry to filter out urea. From a technological point of view, it would therefore be highly inspiring to reproduce such a filtration device. This requires both the specific double-loop geometry highlighted above and the use of an osmotic activator in the solution. We argue that all required ingredients are at our disposal to fabricate such an artificial nephron. Semipermeable membranes will play the role of water-permeable D and CD walls, replacing aquaporin-coated membranes. For salt used as an osmotic activator, the ion pump functionality can be mimicked using a stack of ion-selective membranes, with an electric field as the driving force, similar in spirit to electrodialytic processes [43]. Note that any ionic species is, in general, a good candidate for an osmotic activator, for it can be easily manipulated with electric fields—although monovalent species should be used to begin with. Altogether, modern microfabrication technologies developed for microfluidics would allow us to directly mimic the setup in Fig. 1 [44,45], with several devices possibly working in parallel (for more details, we suggest a detailed implementation of the device in Sec. IX of Ref. [18]).

From the point of view of transport, such an artificial device can be described by the very same equations as above, Eqs. (1)–(4). The pumping energy is replaced by the electric power required to displace the ions, which is written as $e = \mathcal{F}\Delta\mathcal{V}/2$ for pumping under a voltage drop $\Delta\mathcal{V}$ across the ion-selective membranes and replacing e_{ATP}/n. The power consumption thus takes an expression similar to Eq. (9):

$$\mathcal{P}_{\mathrm{elec}} \underset{\eta\to 0}{\simeq} q^{\mathrm{in}}_{\mathrm{Waste}} \frac{\mathcal{F}\Delta\mathcal{V}/2}{\sqrt{\eta}}, \tag{11}$$

now with $\mathcal{F}\Delta\mathcal{V}/2 \simeq 5$–$50$ kJ/mol (using a value of $\Delta\mathcal{V} \simeq 0.1$–$1$ V [43]).

Altogether, mimicking an osmotic exchanger would allow the development of novel filtration devices and dialytic systems. A "kidney on a chip" constitutes a paradigm change as compared to actual dialytic systems involving a standard sieving process, which are difficult to miniaturize [46]: This allows for a compact design, with low energy consumption. Because of its low working pressure, this also allows us to use soft materials in its design.

Such systems could also be used advantageously in the pretreatment stage of standard desalination processes. Pretreatment to separate the basic contaminants from salty water [1] typically costs more than 1 kJ/L in reverse-osmosis plants [47,48]. Contrary to standard electrodialysis, one key point of the kidney on a chip is that the extraction of ions is done from the brine. Using recent progress on ion selective membranes (e.g., monovalent selective) [49–51], the kidney-on-a-chip geometry could effectively provide decontamination and dionization of targeted heavy ions and significantly diminish water hardness. This would reduce the corresponding energy cost and considerably improve the global energetic efficiency of the desalination process.

More inspiration could certainly be drawn from the kidney. For instance, the ionic pumps responsible for sodium reabsorption in the ascending limb are able to discriminate between sodium and potassium ions [33]. So far, only nature has succeeded in making such a monovalent specific membrane.

ACKNOWLEDGMENTS

We are grateful to L. Bankir, D. Fouque, and A. Edwards for interesting discussions on the kidney. The authors are grateful for the fruitful comments of B. Rotenberg, A. Siria, J.-F. Joanny, and R. Karnik. S. M. acknowledges funding from a J. P. Aguilar grant of the CFM Foundation. L. B. acknowledges support from ERC-AG *Micromegas*.

[1] M. Elimelech and W. A. Phillip, *The Future of Seawater Desalination: Energy, Technology, and the Environment*, Science **333**, 712 (2011).

[2] T. Humplik, J. Lee, S. C. O'Hern, B. A. Fellman, M. A. Baig, S. F. Hassan, M. A. Atieh, F. Rahman, T. Laoui, R. Karnik, and E. N. Wang, *Nanostructured Materials for Water Desalination*, Nanotechnology **22**, 292001 (2011).

[3] M. Heranian, A. B. Farimani, and N. R. Aluru, *Water Desalination with a Single-Layer* MoS_2 *Nanopore*, Nat. Commun. **6**, 8616 (2015).

[4] J. K. Holt, Hyung G. Park, Y. Wang, M. Stadermann, A. B. Artyukhin, C. P. Grigoropoulos, A. Noy, and O. Bakajin, *Fast Mass Transport through Sub-2-Nanometer Carbon Nano-tubes*, Science **312**, 1034 (2006).

[5] R. K. Joshi, P. Carbone, F. C. Wang, V. G. Kravets, Y. Su, I. V. Grigorieva, H. A. Wu, A. K. Geim, and R. R. Nair, *Precise and Ultrafast Molecular Sieving through Graphene Oxide Membranes*, Science **343**, 752 (2014).

[6] A. Siria, P. Poncharal, A.-L. Biance, Rmy Fulcrand, X. Blase, S. T. Purcell, and L. Bocquet, *Giant Osmotic Energy Conversion Measured in a Single Transmembrane Boron Nitride Nanotube*, Nature (London) **494**, 455 (2013).

[7] K. H. Jensen, E. Rio, R. Hansen, C. Clanet, and T. Bohr, *Osmotically Driven Pipe Flows and Their Relation to Sugar Transport in Plants*, J. Fluid Mech. **636**, 371 (2009).

[8] S. M. Henton, *Revisiting the Münch pressure–Flow Hypothesis for Long-Distance Transport of Carbohydrates: Modelling the Dynamics of Solute Transport Inside a Semipermeable Tube*, J. Exp. Bot. **53**, 1411 (2002).

[9] R. Greger and U. Windhorst, *Comprehensive Human Physiology: From Cellular Mechanisms to Integration* (Springer-Verlag, Berlin, 1996).

[10] C. W. Gottschalk and M. Mylle, *Evidence that the Mammalian Nephron Functions as a Countercurrent Multiplier System*, Science **128**, 594 (1958).

[11] L. Bankir, N. Bouby, and M. M. Trinh-Trang-Tan, *2 The Role of The Kidney in the Maintenance of Water Balance*, Baillière's Clinical Endocrinology and Metabolism **3**, 249 (1989).

[12] J. L. Stephenson, *Concentration of Urine in a Central Core Model of the Renal Counterflow System*, Kidney international **2**, 85 (1972).

[13] P. J. Palatt and G. M. Saidel, *Countercurrent Exchange in the Inner Renal Medulla: Vasa Recta-descending Limb System*, Bull. Math. Biol. **35**, 431 (1973).

[14] S. R. Thomas, *Inner Medullary Lactate Production and Accumulation: A Vasa Recta Model*, Am. J. Physiol. Renal Physiol. **279**, F468 (2000).

[15] D. Foster, J. A. Jacquez, and E. Daniels, *Solute Concentration in the Kidney-II. Input-Output Studies on a Central Core Model*, Math. Biosci. **32**, 337 (1976).

[16] A. T. Layton, *A Mathematical Model of the Urine Concentrating Mechanism in the Rat Renal Medulla. I. Formulation and Base-Case Results*, Am. J. Physiol. Renal Physiol. **300**, F356 (2010).

[17] A. Edwards, *Modeling Transport in the Kidney: Investigating Function and Dysfunction*, Am. J. Physiol. Renal Physiol. **298**, F475 (2010).

[18] See Supplemental material at http://link.aps.org/supplemental/10.1103/PhysRevX.6.031008 for details on analytical derivations and computations.

[19] Phoenix X 36 brochure (Gambro, 2009), https://www.baxter.com/assets/downloads/products_expertise/renal_therapies/Phoenix_X36_Hemodialysis_System.pdf.

[20] J. Borenstein, E. Weinberg, B. Orrick, C. Sundback, M. Kaazempur-Mofrad, and J. Vacanti, *Microfabrication of Three-Dimensional Engineered Scaffolds*, Tissue Eng. Part A **13**, 1837 (2007).

[21] J. Kim, F. Garzotto, F. Nalesso, D. Cruz, J. Kim, E. Kang, H. Kim, and C. Ronco, *A Wearable Artificial Kidney: Technical Requirements and Potential Solutions*, Expert Rev. Med. Dev. **8**, 567 (2011).

[22] P. Armignaco, F. Garzotto, M. Neri, A. Lorenzin, and C. Ronco, *Wak Engineering Evolution*, Blood purification **39**, 110 (2015).

[23] C.-L. Chou, M. A. Knepper, A. N. Hoek, D. Brown, B. Yang, T. Ma, and A. S. Verkman, *Reduced Water Permeability and Altered Ultrastructure in Thin Descending Limb of Henle in Aquaporin-1 Null Mice*, J. Clin. Invest. **103**, 491 (1999).

[24] S. Nielsen, J. Frkiaer, D. Marples, T. H. Kwon, P. Agre, and M. A. Knepper, *Aquaporins in the Kidney: From Molecules to Medicine*, Physiol. Rev. **82**, 205 (2002).

[25] R. Greger and E. Schlatter, *Presence of Luminal k+, a Prerequisite for Active NaCl Transport in the Cortical Thick Ascending Limb of Henle's Loop of Rabbit Kidney*, Pflügers Arch. **392**, 92 (1981).

[26] J. A. Jacquez, D. Foster, and E. Daniels, *Solute Concentration in the Kidney—I. A Model of the Renal Medulla and Its Limit Cases*, Math. Biosci. **32**, 307 (1976).

[27] J. Stephenson, *Concentration Engines and the Kidney: I. Central Core Model of the Renal Medulla*, Biophys. J. **13**, 512 (1973).

[28] J. Stephenson, *Concentration Engines and the Kidney: II. Multisolute Central Core Systems*, Biophys. J. **13**, 546 (1973).

[29] J. Stephenson, *Concentration Engines and the Kidney: III. Canonical Mass Balance Equation for Multinephron Models of the Renal Medulla*, Biophys. J. **16**, 1273 (1976).

[30] J. Stephenson, R. Tewarson, and R. Mejia, *Quantitative Analysis of Mass and Energy Balance in Non-ideal Models of the Renal Counterflow System*, Proc. Natl. Acad. Sci. U.S.A. **71**, 1618 (1974).

[31] J. Stephenson, *Models of the Urinary Concentrating Mechanism*, Kidney international **31**, 648 (1987).

[32] A. Finkelstein, *Water Movement through Lipid Bilayers, Pores, and Plasma Membranes* (John Wiley & Sons, NewYork, 1987).

[33] R. Greger and E. Schlatter, *Properties of the Basolateral Membrane of the Cortical Thick Ascending Limb of Henle's Loop of Rabbit Kidney*, Pflügers Arch. **396**, 325 (1983).

[34] B. Yang and J. M. Sands, *Urea Transporters* (Springer Science+ Business Media, Dordrecht, 2014).

[35] R. P. Garay and P. J. Garrahan, *The Interaction of Sodium and Potassium with the Sodium Pump in Red Cells*, J. Physiol. **231**, 297 (1973).

[36] M. A. Knepper, R. A. Danielson, G. M. Saidel, and R. S. Post, *Quantitative Analysis of Renal Medullary Anatomy in Rats and Rabbits*, Kidney international **12**, 313 (1977).

[37] H. Koepsell, W. Kriz, and J. Schnermann, *Pattern of Luminal Diameter Changes along the Descending and Ascending Thin Limbs of the Loop of Henle in the Inner Medullary Zone of the Rat Kidney*, Z. Anat. Entwickl.-Gesch. **138**, 321 (1972).

[38] J. Newburgh, *The Changes which Alter Renal Osmotic Work*, J. Clin. Invest. **22**, 439 (1943).

[39] A. Layton, *Mathematical Modeling of Kidney Transport*, Wiley Interdiscip. Rev.: Syst. Biol. Med. **5**, 557 (2013).

[40] B. Hargitay and W. Kuhn, *The Multiplication Principle as the Basis for Concentrating Urine in the Kidney*, J. Am. Soc. Nephrol. **12**, 1566 (2001); Reprinted from Chemie **55**, 539 (1951).

[41] S. Hervy and S. R Thomas, *Inner Medullary Lactate Production and Urine-Concentrating Mechanism: A Flat Medullary Model*, Am. J. Physiol. Renal Physiol. **284**, F65 (2003).

[42] B. Alberts, J. Lewis, M. Raff, K. Roberts, and P. Walter, *Molecular Biology of the Cell*, 4th ed. (Garland-Science, New York, 2002).

[43] J. W. Post, J. Veerman, H. V. M. Hamelers, G. J. W. Euverink, S. J. Metz, Kitty Nymeijer, and C. J. N. Buisman, *Salinity-Gradient Power: Evaluation of Pressure-Retarded Osmosis and Reverse Electrodialysis*, J. Membr. Sci. **288**, 218 (2007).

[44] B. B. Sales, M. Saakes, J. W. Post, C. J. N. Buisman, P. M. Biesheuvel, and H. V. M. Hamelers, *Direct Power Production from a Water Salinity Difference in a Membrane-Modified Supercapacitor Flow Cell*, Environ. Sci. Technol. **44**, 5661 (2010).

[45] J. de Jong, R. G. H. Lammerink, and M. Wessling, *Membranes and Microfluidics: A Review*, Lab Chip **6**, 1125 (2006).

[46] W. H. Fissell, H. D. Humes, A. J. Fleischman, and S. Roy, *Dialysis and Nanotechnology: Now, 10 Years, or Never?*, Blood purification **25**, 12 (2007).

[47] R. Semiat, *Energy Issues in Desalination Processes*, Environ. Sci. Technol. **42**, 8193 (2008).

[48] C. Fritzmann, J. Löwenberg, T. Wintgens, and T. Melin, *State-of-the-Art Reverse Osmosis Desalination*, Desalination **216**, 1 (2007).

[49] R. K. Nagarale, G. S. Gohil, and V. K. Shahi, *Recent Developments on On-Exchange Membranes and Electromembrane Processes.*, Adv. Colloid Interface Sci. **119**, 97 (2006).

[50] J. Li, M.-I. Zhou, J.-y. Lin, W.-y. Ye, Y.-q. Xu, J.-n. Shen, C.-j. Gao, and B. Van der Bruggen, *Mono-valent Cation Selective Membranes for Electrodialysis by Introducing Polyquaternium-7 in a Commercial Cation Exchange Membrane*, J. Membr. Sci. **486**, 89 (2015).

[51] S. C. O'Hern, M. S. H. Boutilier, J.-C. Idrobo, Y. Song, J. Kong, T. Laoui, M. Atieh, and R. Karnik, *Selective Ionic Transport through Tunable Subnanometer Pores in Single-Layer Graphene Membranes*, Nano Lett. **14**, 1234 (2014).

doi:10.1038/nature19315

Massive radius-dependent flow slippage in carbon nanotubes

Eleonora Secchi[1], Sophie Marbach[1], Antoine Niguès[1], Derek Stein[1,2], Alessandro Siria[1] & Lydéric Bocquet[1]

Measurements and simulations have found that water moves through carbon nanotubes at exceptionally high rates owing to nearly frictionless interfaces[1–4]. These observations have stimulated interest in nanotube-based membranes for applications including desalination, nano-filtration and energy harvesting[5–10], yet the exact mechanisms of water transport inside the nanotubes and at the water–carbon interface continue to be debated[11,12] because existing theories do not provide a satisfactory explanation for the limited number of experimental results available so far[13]. This lack of experimental results arises because, even though controlled and systematic studies have explored transport through individual nanotubes[7–9,14–17], none has met the considerable technical challenge of unambiguously measuring the permeability of a single nanotube[11]. Here we show that the pressure-driven flow rate through individual nanotubes can be determined with unprecedented sensitivity and without dyes from the hydrodynamics of water jets as they emerge from single nanotubes into a surrounding fluid. Our measurements reveal unexpectedly large and radius-dependent surface slippage in carbon nanotubes, and no slippage in boron nitride nanotubes that are crystallographically similar to carbon nanotubes, but electronically different. This pronounced contrast between the two systems must originate from subtle differences in the atomic-scale details of their solid–liquid interfaces, illustrating that nanofluidics is the frontier at which the continuum picture of fluid mechanics meets the atomic nature of matter.

Measuring the pressure-driven flow of water through individual carbon nanotubes (CNTs) and boron nitride nanotubes (BNNTs) with well-defined radii (R_t) and lengths (L_t) requires overcoming two considerable challenges. First, when R_t decreases to the nanoscale, the flow rate through a tube drops too rapidly for even state-of-the-art flow-rate measurements to detect. Flow rates as low as a few picolitres per second have been measured through single nanocapillaries[18], but such a rate is still about three orders of magnitude higher than the sensitivity required to probe mass flow through a single nanotube. Our approach avoids this problem by focusing instead on the flow that a fluid jet entrains outside a nanotube (see Fig. 1) and on the scaling property of the jet hydrodynamics[19]. The external flow is characterized by a driving force F_P that originates in the fluid momentum transfer at the tube opening[20,21] and scales linearly with R_t, so the flow velocities remain measurably large even when R_t shrinks to nanometre-scale dimensions. The second challenge is fabricating an experimental system for manipulating and using a single nanotube, in the form of a nanofluidic needle with a single nanotube protruding from the tip. To do this, we adapted a technique for selecting and manipulating nanotubes of known length

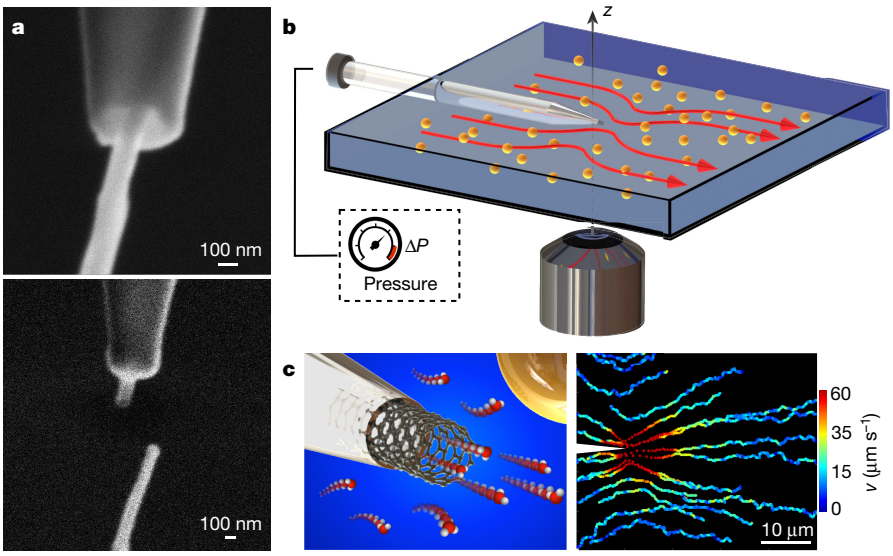

Figure 1 | Nanojet experimental set-up. a, SEM image of a CNT insertion into a nanocapillary (top) and after sealing (bottom). The CNT has dimensions of $(R_t, L_t) = (50\,\text{nm}, 1{,}000\,\text{nm})$. **b**, Sketch of the fluidic cell used to image the Landau–Squire flow set-up by nanojets emerging from individual nanotubes. Red arrows represent the Landau–Squire flow in the reservoir; orange spheres are tracer particles; z is the optical axis. **c**, Left, sketch of a nanotube protruding from a nanocapillary tip. The flow of water molecules emerging from the nanotube is probed by the tracer particles. Right, trajectories of individual colloidal tracers in a Landau–Squire flow field in the outer reservoir. The colour scale quantifies the velocity v of the tracer particles. The flow is driven by a nanojet from a CNT with dimensions of $(R_t, L_t) = (33\,\text{nm}, 900\,\text{nm})$, with $\Delta P = 1.7$ bar. Both reservoirs contained water with 10^{-2} M KCl.

[1]Laboratoire de Physique Statistique, Ecole Normale Supérieure, PSL Research University, 75005 Paris Cedex 05, France. [2]Physics Department, Brown University, Providence, Rhode Island 02912, USA.

© 2016 Macmillan Publishers Limited, part of Springer Nature. All rights reserved.

and diameter with a nanomanipulator operating inside a scanning electron microscope (SEM)[9]; see Supplementary Methods 1 and Supplementary Video 1. We guided a nanotube into the tip of a laser-pulled glass nanocapillary with an orifice in the range 250–350 nm. The dimensions of the nanotubes were determined by ionic transport measurements and by electron microscopy (see Supplementary Methods 2 and 4). For this study we tested five different CNTs with dimensions (in nanometres) of $(R_t, L_t) = (15, 700)$, $(17, 450)$, $(33, 900)$, $(38, 800)$ and $(50, 1{,}000)$, and three different BNNTs with dimensions (in nanometres) of $(R_t, L_t) = (23, 600)$, $(26, 700)$ and $(7, 1{,}300)$; see Supplementary Methods 2 and 4 and Supplementary Table 1.

The nanotube at the tip of the glass capillary bridged two macroscopic fluid reservoirs: one inside the capillary and another in the wide, transparent flow cell into which the capillary was placed (see Fig. 1b and Supplementary Methods 3). We filled both reservoirs with potassium chloride (KCl) solutions of a chosen concentration C_s and controlled pH, and seeded the flow cell with 500-nm polystyrene tracer particles. We then applied a pressure drop ΔP to the capillary and tracked the resulting motion of the tracers under a microscope (see Fig. 1b) to map the velocity profile of the flow (see Figs 1c and 2). Flow measurements were performed with salt concentration $C_s = 10^{-3}$ M or $C_s = 10^{-2}$ M. Low salinity is required during the tracking experiments to prevent salt-induced colloid aggregation.

Ag/AgCl electrodes inserted into either reservoir were used to measure the ionic conductance across the nanotube before and after each fluidic experiment to ensure the integrity of the device, as well as to obtain information on the dimensions and the surface charge density of the nanotube (see Supplementary Methods 4). These electrodes were grounded during flow measurements.

Owing to the needle geometry of the system, the pressure-driven flow through the nanotube sets up a flow in the outer reservoir called a Landau–Squire nanojet[18,20,21]. The Landau–Squire solution of the Navier–Stokes equations at low Reynolds number predicts radial and angular components of the flow velocity of $v_r = \frac{F_P}{4\pi\eta}\frac{\cos\theta}{r}$ and $v_\theta = -\frac{F_P}{8\pi\eta}\frac{\sin\theta}{r}$, respectively, where r is the radial distance from the tip, θ is the angle relative to the symmetry axis of the jet and η is the viscosity[20]. F_P is the driving force of the jet applied at the origin. Figure 2a, b shows that our measurements of the flow field around single nanotubes agree well with the Landau–Squire prediction. The inset of Fig. 2b further highlights the long-range $1/r$-dependence of the Landau–Squire flow, which extends over tens of micrometres despite the nanometre-scale size of the source of the flow.

From our analysis of the Landau–Squire flow, we extracted experimental values of F_P for each nanotube and ΔP. The results, presented in Fig. 2c, show a linear relationship between F_P and ΔP. To gain insight into the permeability of the nanotubes, we begin by observing that the mass flow rate and F_P are both proportional to ΔP and, hence, proportional to one another. The viscous origin of F_P at low Reynolds numbers as well as dimensional considerations motivate the definition $F_P = \alpha\eta R_t v_{NT}$, where $\alpha = \mathcal{O}(1)$ is a geometry-dependent numerical prefactor and v_{NT} is the average fluid velocity inside the nanotube. The permeability of the tube k_{NT} is defined by $v_{NT} = \frac{k_{NT}}{\eta}\frac{\Delta P}{L_t}$. Combining these expressions, F_P, k_{NT} and ΔP are related by $F_P(\Delta P) = \frac{\alpha R_t k_{NT}}{L_t}\Delta P$.

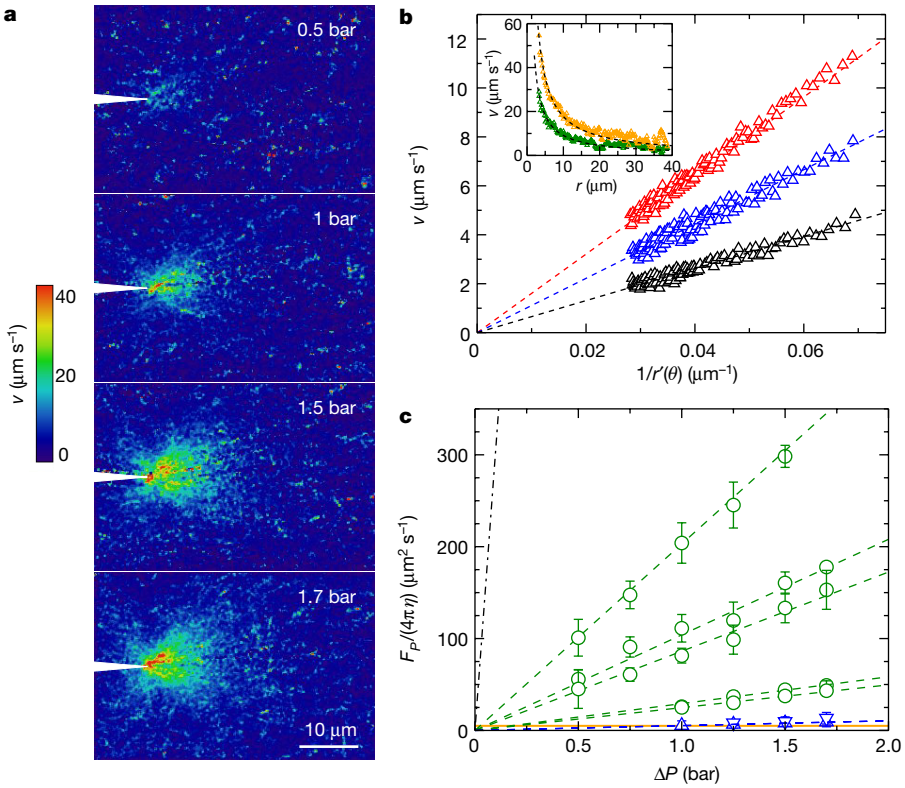

Figure 2 | Measurement of Landau–Squire flows driven from nanotubes. a, Maps of the velocity field near a CNT with $(R_t, L_t) = (33\text{ nm}, 900\text{ nm})$ for various ΔP as indicated ($C_s = 10^{-2}$ M and pH 6). **b**, Magnitude of mean particle velocity v as a function of $r'(\theta) = 2r/\sqrt{1 + 3\cos^2\theta}$ for $\Delta P = 0.5$ bar (black), $\Delta P = 1$ bar (blue) and $\Delta P = 1.5$ bar (red). Dashed lines are fits of the Landau–Squire prediction. Inset, particle velocity along the jet axis ($\theta = 0$) versus distance from the nanotube, for $\Delta P = 0.75$ bar (green) and $\Delta P = 1.7$ bar (orange); the dashed line is a $1/r$ fit. **c**, Dependence of $\frac{F_P}{4\pi\eta}$ on ΔP for CNTs (green circles) and BNNTs (blue triangles). CNT dimensions (in nanometres) are, from top to bottom, $(R_t, L_t) = (50, 1{,}000)$, $(33, 900)$, $(38, 800)$, $(15, 700)$ and $(17, 450)$; BNNT dimensions (in nanometres) are $(R_t, L_t) = (26, 700)$ and $(23, 600)$. The salt concentration is $C_s = 10^{-3}$ M, except for the 33-nm CNT, which was studied at both $C_s = 10^{-3}$ M and $C_s = 10^{-2}$ M without a detectable difference. Dashed green lines are linear fits from which the permeability was calculated. The orange line indicates the lowest detectable flow strength. The black dashed line corresponds to the results of a control experiment using a nanocapillary without a nanotube (see Supplementary Methods 5). Error bars correspond to the uncertainty in the slope in **b**, estimated from at least three measurement replicates at each ΔP.

© 2016 Macmillan Publishers Limited, part of Springer Nature. All rights reserved.

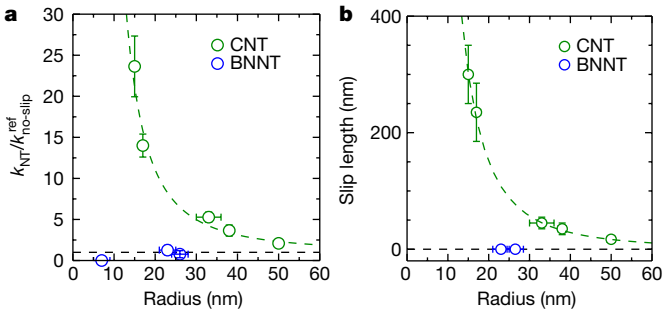

Figure 3 | Permeability and slip length of individual CNTs and BNNTs. **a**, Normalized permeability ($k_{NT}/k^{ref}_{no\text{-}slip}$) of CNTs (green) and BNNTs (blue) as a function of nanotube radius R_t. The permeability of the BNNT with $R_t = 7$ nm was below the experimental detection limit and is indicated as $k_{NT} = 0$ for completeness. Error bars correspond to the experimental errors on F_P. **b**, Dependence of the experimentally determined slip length inside CNTs (green) and BNNTs (blue) on R_t. Error bars correspond to the uncertainty in the permeability. Salt concentration is $C_s = 10^{-3}$ M, except for the 33-nm CNT, which was studied at both $C_s = 10^{-3}$ M and $C_s = 10^{-2}$ M without a detectable difference. Iin both panels, the horizontal dashed lines indicate the no-slip prediction ($k_{NT}/k^{ref}_{no\text{-}slip} = 1$) and the green dashed lines are guides to the eye. The error bars on the radius correspond to the experimental uncertainty in the electric characteristics (see Supplementary Methods 2 and 4). The values of the slip lengths are reported in Supplementary Tables 2 and 3.

According to this equation, the slope of the plots in Fig. 2c provides an estimate of the nanotube permeability, so we can already see that the permeability of CNTs is greatly enhanced as compared with BNNTs. But, to properly quantify the permeabilities, we need to know the value of α. We calculated α from the precise relationship between F_P, v_{NT} and ΔP that we obtained by numerically solving the full hydrodynamic Landau–Squire flow. Furthermore, because α could be sensitive to details of the geometry of the nanotube and the tip, we repeated our calculations for every nanotube device, taking in account its particular geometry as measured by SEM (see Supplementary Methods 6). This exhaustive study, which combines numerical hydrodynamic calculations with experimental benchmarking using nanocapillaries, is summarized in Supplementary Methods 5. Our study showed that $\alpha \approx 0.3$ for the nanotube devices considered in Fig. 2a, b, with only small variations between nanotubes. Having removed all uncertainty from the value of α, we obtained accurate values for k_{NT} from the experimental dependence of F_P on ΔP. Figure 3a presents the dependence of k_{NT} on R_t for every nanotube. The permeabilities are normalized by a simple no-slip reference, $k^{ref}_{no\text{-}slip} = R_t^2/8$, corresponding to a nanotube of the same size with a no-slip boundary condition at its surface. Note that the flow from the smallest BNNT tube, with $R_t = 7$ nm, was below the detection limit.

We attribute the enhanced permeability of the CNTs to hydrodynamic slippage at the carbon surface[12,13,22,23]. The fundamental way to account for this is to introduce a slip length b and to apply Navier's slip boundary condition to the fluid at the nanotube surface. We included the slip condition in our numerical analysis of the hydrodynamics of each nanotube device and obtained experimental b values by matching the computed flow rate enhancement due to surface slippage with the measured permeability data in Fig. 3a (see Supplementary Methods 6). This analysis, which uses the geometry of each nanotube device and takes into account hydrodynamic entrance effects at the nanotube ends, offers the most accurate estimation of b possible. The permeability and b can also be quantitatively obtained from an analytical model of hydrodynamic resistances in series, using the Sampson formula to account for both Poiseuille flow with slippage inside the nanotube and entrance effects[24]; see Supplementary Tables 2 and 3.

The peculiar nature of the water–carbon interface inside CNTs is revealed in Fig. 3b, which presents the experimentally determined slip length as a function of R_t. A first key observation is that the slip length is strongly radius-dependent, reaching 300 nm inside the smallest CNT investigated here. This observation allows us to resolve a long-standing debate regarding the large difference in permeabilities reported previously[2–4,25] using large-scale CNT membranes. The results of those studies are consistent with a decreasing permeability enhancement factor for larger nanotubes, and the range of slip lengths they report is fairly compatible with what we have measured. Our results also explain why the slip lengths measured previously inside CNTs were consistently much larger than the values measured on planar hydrophobic and graphite surfaces[13,26], for which b is typically a few tens of nanometres at most. From a theoretical perspective, the transport behaviour of water inside CNTs has been the subject of numerous studies, mostly using molecular dynamics simulations[12,13]. Radius-dependent slippage was predicted inside CNTs with $R_t < 10$ mn (refs 22, 23) and rationalized in terms of curvature-dependent friction[23]. The results presented here confirm the predicted trend, but the measured slip lengths far exceed the numerical predictions. This discrepancy suggests that molecular dynamics simulations do not represent the interfacial dynamics well at a quantitative level, echoing similar limitations encountered in studies of slippage at hydrophobic surfaces[13].

A second key feature of Fig. 3c is the vastly different behaviour of CNTs and BNNTs, with the latter showing no substantial slippage of water. The comparison is illuminating because CNTs and BNNTs have the same crystallography, but radically different electronic properties, with CNTs being semi-metallic and BNNTs insulating. That these nearly identical channels exhibit very different surface flow dynamics is unexpected: molecular dynamics simulations using semi-empirical interfacial parameters predict similar flow behaviour through CNTs and BNNTs[27,28]. More recent *ab initio* simulations predict that the friction of water on carbon surfaces is lower than on boron nitride surfaces[29], but even these predictions strongly underestimate the difference observed here. The stark differences in flow behaviour must therefore originate in subtle atomic-scale details of the solid–liquid interface, including the electronic structure of the confining material. A more detailed understanding will require a systematic theoretical investigation of physico-chemical factors that could affect surface friction, such as chemical surface dissociation or specific ion adsorption. Useful information could also be gained by measuring the slip behaviour in CNTs at high salt concentrations, a regime in which the surface charge of CNTs is expected to increase[15].

The unexpected slippage behaviour inside CNTs and BNNTs points to a hitherto not appreciated link between hydrodynamic flow and the electronic structure of the confining material. This opens up a new avenue for research that could bridge the gap between hard and soft condensed matter physics. We also expect that, with further improvements in sensitivity, the methods we have developed will enable the direct measurement of water transport through biological channels such as aquaporins.

Received 11 May; accepted 15 July 2016.

1. Hummer, G., Rasaiah, J. C. & Noworyta, J. P. Water conduction through the hydrophobic channel of a carbon nanotube. *Nature* **414,** 188–190 (2001).
2. Majumder, M., Chopra, N., Andrews, R. & Hinds, B. J. Nanoscale hydrodynamics: enhanced flow in carbon nanotubes. *Nature* **438,** 44 (2005); erratum **438,** 930 (2005).
3. Holt, J. K. *et al.* Fast mass transport through sub-2-nanometer carbon nanotubes. *Science* **312,** 1034–1037 (2006).
4. Whitby, M., Cagnon, L., Thanou, M. & Quirke, N. Enhanced fluid flow through nanoscale carbon pipes. *Nano Lett.* **8,** 2632–2637 (2008).
5. Nair, R. R., Wu, H. A., Jayaram, P. N., Grigorieva, I. V. & Geim, A. K. Unimpeded permeation of water through helium-leak-tight graphene-based membranes. *Science* **335,** 442–444 (2012).
6. Joshi, R. K. *et al.* Precise and ultrafast molecular sieving through graphene oxide membranes. *Science* **343,** 752–754 (2014).
7. Park, H. G. & Jung, Y. Carbon nanofluidics of rapid water transport for energy applications. *Chem. Soc. Rev.* **43,** 565–576 (2014).
8. Liu, H. *et al.* Translocation of single stranded DNA through single-walled carbon nanotubes. *Science* **327,** 64–67 (2010).

© 2016 Macmillan Publishers Limited, part of Springer Nature. All rights reserved.

9. Siria, A. *et al.* Giant osmotic energy conversion measured in a single transmembrane boron nitride nanotube. *Nature* **494,** 455–458 (2013).
10. Geng, J. *et al.* Stochastic transport through carbon nanotubes in lipid bilayers and live cell membranes. *Nature* **514,** 612–615 (2014).
11. Guo, S., Meshot, E. R., Kuykendall, T., Cabrini, S. & Fornasiero, F. Nanofluidic transport through isolated carbon nanotube channels: advances, controversies, and challenges. *Adv. Mater.* **27,** 5726–5737 (2015).
12. Whitby, M. & Quirke, N. Fluid flow in carbon nanotubes and nanopipes. *Nat. Nanotechnol.* **2,** 87–94 (2007).
13. Bocquet, L. & Charlaix, E. Nanofluidics, from bulk to interfaces. *Chem. Soc. Rev.* **39,** 1073–1095 (2010).
14. Lee, C. Y., Choi, W., Han, J.-H. & Strano, M. S. Coherence resonance in a single-walled carbon nanotube ion channel. *Science* **329,** 1320–1324 (2010).
15. Secchi, E., Niguès, A., Jubin, L., Siria, A. & Bocquet, L. Scaling behavior for ionic transport and its fluctuations in individual carbon nanotubes. *Phys. Rev. Lett.* **116,** 154501 (2016).
16. Qin, X., Yuan, Q., Zhao, Y., Xie, S. & Liu, Z. Measurement of the rate of water translocation through carbon nanotubes. *Nano Lett.* **11,** 2173–2177 (2011).
17. Lorenz, U. & Zewail, A. Observing liquid flow in nanotubes by 4D electron microscopy. *Science* **344,** 1496–1500 (2014).
18. Laohakunakorn, N. *et al.* A Landau–Squire nanojet. *Nano Lett.* **13,** 5141–5146 (2013).
19. Eggers, J. & Villermaux, E. Physics of liquid jets. *Rep. Prog. Phys.* **71,** 036601 (2008).
20. Landau, L. D. & Lifshitz, E. M. *Fluid Mechanics* Vol. 6 of *Course of Theoretical Physics* 81–83 (Pergamon, 1959).
21. Squire, H. B. The round laminar jet. *Q. J. Mech. Appl. Math*. **4,** 321–329 (1951).
22. Thomas, J. A. & McGaughey, A. J. H. Reassessing fast water transport through carbon nanotubes. *Nano Lett.* **8,** 2788–2793 (2008).
23. Falk, K., Sedlmeier, F., Joly, L., Netz, R. R. & Bocquet, L. Molecular origin of fast water transport in carbon nanotube membranes: superlubricity versus curvature dependent friction. *Nano Lett.* **10,** 4067–4073 (2010).
24. Sampson, R. A. On Stokes's current function. *Phil. Trans. R. Soc. A* **182,** 449–518 (1891).
25. Mattia, D., Leese, H. & Lee, K. P. Carbon nanotube membranes: from flow enhancement to permeability. *J. Membr. Sci.* **475,** 266–272 (2015).
26. Maali, A., Cohen-Bouhacina, T. & Kellay, H. Measurement of the slip length of water flow on graphite surface. *Appl. Phys. Lett.* **92,** 053101 (2008).
27. Suk, M. E., Raghunathan, A. V. & Aluru, N. R. Fast reverse osmosis using boron nitride and carbon nanotubes. *Appl. Phys. Lett.* **92,** 133120 (2008).
28. Hilder, T. A., Gordon, D. & Chung, S.-H. Salt rejection and water transport through boron nitride nanotubes. *Small* **5,** 2183–2190 (2009).
29. Tocci, G., Joly, L. & Michaelides, A. Friction of water on graphene and hexagonal boron nitride from ab initio methods: very different slippage despite very similar interface structures. *Nano Lett.* **14,** 6872–6877 (2014).

Supplementary Information is available in the online version of the paper.

Acknowledgements L.B. and A.S. thank U. Keyser for discussions. E.S., A.N., S.M. and A.S. acknowledge funding from the European Union's H2020 Framework Programme/ERC Starting Grant agreement number 637748 — NanoSOFT. L.B. and D.S. acknowledge support from the European Union's FP7 Framework Programme/ERC Advanced Grant Micromegas. S.M. acknowledges funding from a J.-P. Aguilar grant. L.B. acknowledges funding from a PSL chair of excellence. We acknowledge funding from ANR project BlueEnergy.

Author Contributions L.B. and A.S. conceived and directed the research. A.N. and A.S. designed and fabricated the nanotube devices. E.S and D.S. designed the fluidic cell. E.S. performed the measurements. The data were analysed by E.S., S.M. and L.B.; S.M. conducted the numerical analysis with input from the other authors. All authors contributed to the scientific discussions and the preparation of the manuscript.

Author Information Reprints and permissions information is available at www.nature.com/reprints. The authors declare no competing financial interests. Readers are welcome to comment on the online version of the paper. Correspondence and requests for materials should be addressed to L.B. (lyderic.bocquet@lps.ens.fr) and A.S. (alessandro.siria@lps.ens.fr).

Reviewer Information *Nature* thanks J. Eijkel and A. Michaelides for their contribution to the peer review of this work.

© 2016 Macmillan Publishers Limited, part of Springer Nature. All rights reserved.

THE JOURNAL OF CHEMICAL PHYSICS **146**, 194701 (2017)

Osmotic and diffusio-osmotic flow generation at high solute concentration. I. Mechanical approaches

Sophie Marbach,[1,a)] Hiroaki Yoshida,[1,2,b)] and Lydéric Bocquet[1,c)]
[1]*LPS, UMR CNRS 8550, Ecole Normale Supérieure, PSL Research University, 24 Rue Lhomond, 75005 Paris, France*
[2]*Toyota Central R&D Labs., Inc., Nagakute, Aichi 480-1192, Japan*

(Received 3 March 2017; accepted 3 April 2017; published online 16 May 2017)

In this paper, we explore various forms of osmotic transport in the regime of high solute concentration. We consider both the osmosis across membranes and diffusio-osmosis at solid interfaces, driven by solute concentration gradients. We follow a mechanical point of view of osmotic transport, which allows us to gain much insight into the local mechanical balance underlying osmosis. We demonstrate in particular how the general expression of the osmotic pressure for mixtures, as obtained classically from the thermodynamic framework, emerges from the mechanical balance controlling non-equilibrium transport under solute gradients. Expressions for the rejection coefficient of osmosis and the diffusio-osmotic mobilities are accordingly obtained. These results generalize existing ones in the dilute solute regime to mixtures with arbitrary concentrations. *Published by AIP Publishing.* [http://dx.doi.org/10.1063/1.4982221]

I. INTRODUCTION

Osmotic transport is a subtle and non-trivial effect that is harvested in numerous biological phenomena and applications, such as food processing in biological organisms,[1,2] reverse osmosis for desalination, and energy generation from salinity differences,[3–6] to name a few. Traditionally, osmotic transport is described as occurring across a semi-permeable membrane, i.e., a membrane impermeable to the solute but permeable to the solvent, often water, see Fig. 1. If two reservoirs with different solute concentrations are put in contact via a semi-permeable membrane, an osmotic pressure builds up between the compartments. This pressure drop is the driving force for a flux of water from the low concentration reservoir to the highly concentrated one, until the thermodynamic equilibrium is reached. For low solute concentrations, the osmotic pressure is expressed by the van 't Hoff law,

$$\Delta\Pi = k_{\mathrm{B}}T\Delta c, \tag{1}$$

where Δc is the difference in the solute concentration between the two reservoirs.[3] The van 't Hoff law is derived by equating the solvent chemical potential of the solvent across the membrane.[7–9] The osmotic pressure is accordingly defined in terms of equilibrium thermodynamic properties of the system. An interesting, and quite counterintuitive, remark is that—provided it is semi-permeable—the membrane characteristics do not appear in this thermodynamic expression for the osmotic pressure. Now, when the membrane is only *partially* impermeable to the solute, there is still a solvent flux driven by the solute concentration imbalance.[10–12] However the driving osmotic pressure is usually assumed to be reduced by a (dimensionless) rejection factor, say σ. Determining σ requires describing the detailed mass and solute transport across the membrane, and this requires going beyond the thermodynamic description. From a general perspective, transport across a membrane is characterized within the framework of irreversible processes, via a transport matrix $\mathbb{L}$, relating fluxes to thermodynamic forces[3,13,14]

$$\begin{pmatrix} Q \\ J_s - cQ \end{pmatrix} = \mathbb{L} \times \begin{pmatrix} -\nabla p \\ -\nabla \mu \end{pmatrix}, \tag{2}$$

with Q and J_s denoting, respectively, the volume flux (per unit area) of the solution and of the solute through the membrane; c is the solute concentration, p is the pressure, and μ is the solute chemical potential. This matrix is symmetric according to Onsager's principle. The question then amounts to characterizing the coefficients of this matrix associated with osmotic gradients. Kedem and Katchalsky rewrote these transport equations in a more explicit form as[3,15]

$$Q = -\mathcal{L}_{\mathrm{hyd}}\left(\Delta p - \sigma k_{\mathrm{B}}T\Delta c\right), \tag{3}$$

$$J_s = -\mathcal{L}_{\mathrm{D}}\omega\Delta c + c(1-\sigma)Q, \tag{4}$$

where $\mathcal{L}_{\mathrm{hyd}} = \kappa/(\eta L)$ is the solvent permeance with κ the permeability (in units of a length squared), η the fluid viscosity, and L the membrane thickness, and $\mathcal{L}_{\mathrm{D}} = D/L$ is the solute permeability with D the diffusion coefficient of the solute. The Onsager symmetry relations for Eq. (2) can be verified by exploring two limiting cases: the situation where $\Delta p = 0$ yields $Q = \sigma\mathcal{L}_{\mathrm{hyd}}c\Delta\mu$ (using $\Delta\mu = k_{\mathrm{B}}T\Delta c/c$ in the dilute case) and the situation where $\Delta c = 0$ yields $J_s - cQ = \sigma\mathcal{L}_{\mathrm{hyd}}c\Delta p$, as expected. The Kedem–Katchalsky result introduces the reflection coefficient σ mentioned previously that is dependent in particular on the relative permeability of the membrane to the solvent and the solute.[10,16] Interestingly, the non-dimensional coefficients ω and σ are expected to be linearly related,[3] as

a)Electronic mail: sophie.marbach@lps.ens.fr
b)Electronic mail: h-yoshida@mosk.tytlabs.co.jp
c)Electronic mail: lyderic.bocquet@lps.ens.fr

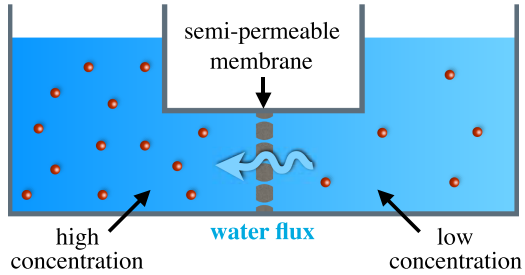

FIG. 1. Geometry of osmosis. A semi-permeable membrane allows transport of water upon a solute concentration difference.

$1 - \sigma \propto \omega$, a result that we will recover below. Note that the previous Kedem–Katchalsky equations are valid in the regime of dilute solute concentration, where the van 't Hoff relationship applies. Generalizing them to mixtures with arbitrary volume fractions requires introducing the general thermodynamic expression for the osmotic pressure and its link to non-equilibrium transport remains to be developed.

In this paper, our goal is to get some insight into the physical principles of osmosis, while exploring the high solute concentration regime. We will make use of a mechanical approach to osmosis, which is particularly illuminating to identify the force balance underlying the osmotic phenomenon. We will consider the two situations of bare osmosis across membranes and diffusio-osmosis at solid interfaces. Osmosis is expected to occur under a solute imbalance across a semi-permeable membrane, which is permeable to the solvent but not to the solute. In contrast, diffusio-osmosis is a surface-driven flow occurring under solute gradients. This form of transport has attracted increasing attention in the context of recent developments in micro- and nano-fluidic systems.[11,12,17–20]

To highlight the mechanical balance underlying osmotic transport, we will consider a simplified model where the effect of the membrane on the solute is described in terms of an energy barrier, see Fig. 2(a). Such an energy barrier is a crude but convenient description for the membrane, avoiding entering into the details of the interaction of the solute with the membrane. It reduces the description to its minimal ingredients of partial or semi-permeability and makes it amenable to explicit calculations. As we show below, it allows us to explore in detail how osmotic pressure builds up, even in the absence

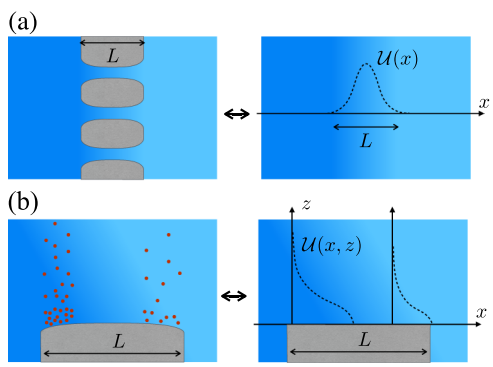

FIG. 2. From the hydrodynamic picture to the mechanical approach. (a) Geometry of osmosis: from the membrane type approach to the mechanical approach describing the membrane as a potential on the solute. (b) Geometry of diffusio-osmosis: from a zoomed surface-solute interaction to a description with a potential on the solute.

of a full semi-permeability of the membrane to the solute. We note furthermore that such a barrier potential can also be physically achieved; for example, it can be generated from a nonuniform electric field acting on a polar solute in a nonpolar solvent,[21] or it can represent the nonequivalent interactions of solute and solvent particles with a permeable membrane, e.g., charge interactions.[22,23] In the case of osmosis, this approach was first introduced by Manning[13] in the low concentration regime and generalized more recently by Picallo *et al.* to explore the osmotic transport across permselective charged nanopores.[23]

On the basis of this mechanical approach, a further objective of our study is to explore osmotic phenomena in the regime of high solute concentration, where the "solute" and the "solvent" are two components of a mixture with arbitrary molar fraction. In this case, thermodynamics predicts that the thermodynamic force driving motion is a generalized osmotic pressure taking the formal expression[24]

$$\Pi(c) = c\frac{\partial f}{\partial c} - f[c] + f[c=0], \tag{5}$$

with f the free energy density (see Appendix A for a reminder). However, how this osmotic pressure is expressed in terms of mechanical balance across a membrane (osmosis) or along an interface (diffusio-osmosis) has not been explored up to now. Our goal in the present work is accordingly to highlight how this thermodynamic expression connects to the (local) mechanical balance for osmosis and diffusio-osmosis.

II. FROM A THERMODYNAMIC TO A MECHANICAL APPROACH TO OSMOSIS

We consider a membrane separating two sub-volumes, containing a solvent and a solute. The concentration difference between the two volumes is $\Delta c = c_+ - c_-$. As introduced above, we assume that the membrane behaves as an external potential $\mathcal{U}$ on the solute *only*, but not on the solvent molecules. It varies only along the x axis. We denote L the lateral range of the potential $\mathcal{U}$, so that $\mathcal{U}(-L/2) = \mathcal{U}(L/2) = 0$ and vanishes outside of this domain, see Fig. 2(a). Still we consider that the membrane is permeable to the solvent, with a permeance $\mathcal{L}_{\rm hyd}$, relating the flux Q to the pressure drop Δp in the absence of a concentration difference: $Q = -\mathcal{L}_{\rm hyd}\Delta p$.

We first recall results for the dilute solute regime and then extend the results to the high concentration case.

A. Dilute solute concentration

Before considering the general case of the high solute concentration, we first revisit the case of the dilute solute concentration, as explored in Refs. 13 and 23, which allows us to give the flavor of the approach. In the 1D geometry described above, the stationary solute concentration $c(x)$ obeys a Smoluchowski equation

$$\begin{aligned} 0 = \partial_t c &= -\partial_x J_s \\ &= -\partial_x\left(-D\partial_x c + \lambda c\left(-\partial_x \mathcal{U}\right) + vc\right), \end{aligned} \tag{6}$$

where D is the diffusion coefficient and $\lambda = D/k_{\rm B}T$ the mobility, with $k_{\rm B}$ and T being the Boltzmann constant and the temperature, respectively. We further assume a low Péclet number

limit, $\mathrm{Pe} = vL/D \ll 1$, such that the convective term of Eq. (6) is negligible. This is valid for low permeability (nanoporous) membranes. Since the solute current across the membrane J_s is constant in time and spatially uniform, Eq. (6) is explicitly solved with respect to the concentration,

$$c(x) = -\Delta c\, e^{-\beta\mathcal{U}(x)} \frac{\int_x^{L/2} dx' \, \exp[+\beta\mathcal{U}(x')]}{\int_{-L/2}^{L/2} dx' \, \exp[+\beta\mathcal{U}(x')]}, \tag{7}$$

where $\beta = 1/k_\mathrm{B}T$.

Now let us focus on the force balance. It is crucial to remark that the membrane will act on the fluid as an external force, $-\partial_x\mathcal{U}$, exerted on the solute molecules. But due to action-reaction, this force acts on the fluid volume globally. This is, for example, highlighted in the force balance on the fluid, as represented by the Stokes equation along the x direction,

$$0 = -\partial_x p + c(x)(-\partial_x\mathcal{U}) + \eta\nabla^2 v, \tag{8}$$

where p is the fluid pressure and v is the flow velocity of the fluid in the x direction. The driving force inducing the solvent flow is accordingly written in terms of an apparent pressure drop, $-\partial_x\mathcal{P} = -\partial_x p + c(x)(-\partial_x\mathcal{U})$. The membrane, via its potential $\mathcal{U}$, will therefore create an average force on the fluid, which writes per unit surface as

$$-\Delta\mathcal{P} = -\Delta p + \int_{-L/2}^{L/2} dx\, c\,(-\partial_x\mathcal{U}), \tag{9}$$

where Δ means the difference of quantity between two sides. The second term of Eq. (9) can be interpreted as the osmotic contribution; one can calculate it explicitly using the concentration profile given in Eq. (7), to obtain

$$-\Delta\mathcal{P} = -\Delta p + \sigma\Delta\Pi. \tag{10}$$

This leads to the classical van 't Hoff law of the osmotic pressure, $\Delta\Pi = k_\mathrm{B}T\Delta c$, and the expression of the reflection coefficient σ is obtained as

$$\sigma = 1 - \frac{L}{\int_{-L/2}^{L/2} dx' \, \exp[+\beta\mathcal{U}(x')]}. \tag{11}$$

Equation (10) is often referred to as the Starling equation in the physiology literature, see, e.g., Ref. 25.

The above result correctly recovers the case of a completely semi-permeable membrane (no solute flux across the membrane), i.e., $\beta\mathcal{U} \gg 1$ in this limit, and thus $\sigma \to 1$, yielding $-\Delta\mathcal{P} = -\Delta[p - \Pi]$. In the intermediate cases, although the membrane is permeable, a flow arises due to the solute concentration gradient even in the absence of a pressure gradient. When the potential is repulsive and small $\mathcal{U} \sim k_\mathrm{B}T$, then $0 < \sigma < 1$; the flow is in the direction of increasing concentration. When the potential is attractive, then $\sigma < 0$ and the flow reverses. Integrating Eq. (8) over the membrane area ($\mathcal{A}$) and thickness (L) allows us to express the total flux Q as

$$Q = -\mathcal{L}_\mathrm{hyd}\,(\Delta p - \sigma k_\mathrm{B}T\Delta c)\,. \tag{12}$$

Here one may formally define the permeability κ in terms of the averaged flow as $(1/\mathcal{A}L)\int\int dx\, d\mathcal{A}\,\nabla^2 v \equiv -Q/\kappa$, and the corresponding permeance $\mathcal{L}_\mathrm{hyd} = \kappa/(\eta L)$. These parameters, κ and $\mathcal{L}_\mathrm{hyd}$, take into account the detailed geometric specificities of the pores in the membrane. Overall Eq. (12) agrees with the Kedem–Katchalsky result in Eq. (3).

We recall that according to Ref. 3 the reflection coefficient σ and the factor ω are linked by a linear relationship in the form $1 - \sigma \propto \omega$, for diffusion through the membrane. The origin of this symmetry relationship is easily apparent from the general expression of the solute flux J_s. From the steady state condition of Eq. (6), the solute flux is expressed as

$$J_s = -\lambda c\, \partial_x\,(\mu_\mathrm{id}[c] + \mathcal{U})\,, \tag{13}$$

where $\mu_\mathrm{id}[c] = k_\mathrm{B}T\ln(c/c^*)$ is the chemical potential of the ideal (dilute) solution with the solute concentration c, with c^* being a reference concentration. The first term can be rewritten as $-\lambda\partial_x\Pi$, with $\Pi = k_\mathrm{B}Tc$. The flux J_s is spatially homogeneous ($\partial_x J_s = 0$), so that one deduces

$$\begin{aligned} J_s &= -\lambda\left(\frac{\Delta\Pi}{L} - \frac{1}{L}\int_{-L/2}^{L/2} dx\, c(x)(-\partial_x\mathcal{U})\right) \\ &= -\frac{\lambda}{L}\,(1-\sigma)\,\Delta\Pi, \end{aligned} \tag{14}$$

and in the present case, $1 - \sigma = \omega$. Note that the contribution of the total flux Q to the solute flux J_s is recovered when the convective term of Eq. (6) is accounted for.[13]

B. High solute concentration

We now generalize the mechanical approach to the case of a mixture with a high solute concentration. As stated earlier, the osmotic pressure is expected in this regime to deviate from its van 't Hoff limit $\Pi = k_\mathrm{B}Tc$ and is now defined in terms of the general thermodynamic expression given in Eq. (5) (as recalled in Appendix A).[24]

In this regime, the solute flux J_s entering the Smoluchowski equation for the solute now writes as

$$J_s = -\lambda[c(x)]\, c(x)\partial_x\,(\mu[c(x)] + \mathcal{U}(x))\,, \tag{15}$$

where $\mu[c]$ is the chemical potential of the solute and $\lambda[c]$ the solute mobility, possibly depending on the concentration. The fluid equation of motion remains similar as above, in Eq. (8), with the membrane acting on the fluid in the form of an external force $c(x)(-\partial_x\mathcal{U})$, leading to an average force as in Eq. (9).

At equilibrium, fluxes are vanishing and the equilibrium concentration $c_0(x)$ thus obeys

$$\mu[c_0(x)] + \mathcal{U}(x) = \mu_\mathrm{res}, \tag{16}$$

where $c_0(-L/2) = c_0(L/2) = c_\mathrm{res}$, such that $\mu[c_\mathrm{res}] = \mu_\mathrm{res}$. Now when there is a concentration difference δc_0 of the solute between the reservoirs, solvent and solute fluxes build up. In contrast to the dilute case above, one cannot solve exactly the previous equations for $c(x)$. However, one may explore the case of a small concentration difference between the reservoirs and compute the perturbation from equilibrium. This leads to a change in the concentration profile $c(x)$, which we write as $c(x) = c_0(x) + \delta c(x)$. At the boundaries, one has $\delta c(-L/2) = 0$ and $\delta c(L/2) = \delta c_0$. Equivalently, this can be expressed in terms of a chemical potential difference of the solute between the reservoirs, $\Delta\mu = \mu'[c_\mathrm{res}] \times \delta c_0$, where $\mu' = \partial\mu/\partial c$.

To lowest order in $\delta c(x)$, the flux in Eq. (15) now writes as

$$J_s = -\lambda[c_0(x)]\, c_0(x)\partial_x \left(\frac{\partial \mu}{\partial c}[c_0(x)]\, \delta c(x)\right). \tag{17}$$

Since $\partial_x J_s = 0$ in the stationary state, this equation is solved with respect to $\delta c(x)$,

$$\delta c(x) = -\frac{J_s}{\mu'[c_0(x)]} \int_{-L/2}^{x} \frac{dx'}{\lambda[c_0(x')]\, c_0(x')}. \tag{18}$$

Using the boundary condition $\delta c(L/2) = \delta c_0$, we obtain the following expression for the flux,

$$J_s = -\frac{1}{\int_{-L/2}^{L/2} \frac{dx'}{\lambda[c_0(x')]\, c_0(x')}} \Delta\mu, \tag{19}$$

and deduce the concentration profile $\delta c(x)$ as

$$\delta c(x) = \frac{\Delta\mu}{\mu'[c_0(x)]} \frac{\int_{-L/2}^{x} \frac{dx'}{\lambda[c_0(x')]\, c_0(x')}}{\int_{-L/2}^{L/2} \frac{dx'}{\lambda[c_0(x')]\, c_0(x')}}. \tag{20}$$

Using this solution for the density profile, we can now compute the corresponding driving force due to the solute acting on the fluid, according to Eq. (9),

$$\int_{-L/2}^{L/2} dx\, \delta c(x)(-\partial_x \mathcal{U}) = c_0(L/2)\mu'[c_0(L/2)]\delta c(L/2) - \mu'[c_0(L/2)]\delta c(L/2) \frac{\int_{-L/2}^{L/2} \frac{dx'}{\lambda[c_0(x')]}}{\int_{-L/2}^{L/2} \frac{dx'}{\lambda[c_0(x')]\, c_0(x')}}, \tag{21}$$

where we used the equilibrium condition $\partial_x(\mu[c_0(x)] + \mathcal{U}) = 0$ to simplify the expressions.

This expression can be rewritten in terms of the thermodynamic osmotic pressure in Eq. (5), noting that

$$\Delta\Pi = \Pi(c_{\rm res} + \delta c_0) - \Pi(c_{\rm res}) = c_{\rm res}\mu'[c_{\rm res}]\delta c_0. \tag{22}$$

The average force on the membrane in Eq. (21) can accordingly be re-expressed as

$$\int_{-L/2}^{L/2} dx\, \delta c(x)(-\partial_x \mathcal{U}) = \sigma\Delta\Pi, \tag{23}$$

where the reflection coefficient σ is now defined as

$$\sigma = 1 - \frac{\int_{-L/2}^{L/2} \frac{dx'}{\lambda[c_0(x')]}}{\int_{-L/2}^{L/2} \frac{dx'}{\lambda[c_0(x')]} \frac{c_{\rm res}}{c_0(x')}}. \tag{24}$$

Equation (24) takes into account the non-linearities that arise from the deviation from the simple Boltzmann distribution and the dependence of mobility on concentration. The driving force is formally the same as in Eq. (10), and the solvent flux takes accordingly the form

$$Q = -\mathcal{L}_{\rm hyd}\left(\Delta p - \sigma\Delta\Pi\right), \tag{25}$$

with Π the general thermodynamic expression in Eq. (5).

Similarly to the discussion leading to Eq. (14), we also find

$$J_s = -\frac{1}{\int_{-L/2}^{L/2} \frac{dx'}{\lambda[c_0(x')]}}(1-\sigma)\Delta\Pi, \tag{26}$$

showing that the coefficients σ and ω are again related as $1 - \sigma = \omega$.

Altogether, this derivation unifies the thermodynamic and the mechanical perspectives on the osmotic pressure.

III. DIFFUSIO-OSMOTIC TRANSPORT AT HIGH SOLUTE CONCENTRATIONS

We now explore similar questions for diffusio-osmotic transport. Diffusio-osmosis corresponds to the generation of the solvent flow under a salinity gradient, close to a solid surface, see Fig. 3. It is an interfacially driven phenomenon, which takes its origin within the diffuse interfacial layer close to the surface where the solute interacts specifically with the surface.[14,26,27] Its effects were explored in various experimental works.[5,11,12,20] However only the regime of dilute solutes has been considered up to now, and we generalize the concepts to mixtures with a high volume fraction of the "solute" versus the "solvent" (solute and solvent being actually two components of a mixture). This will allow us to highlight the links between diffusio-osmosis and the generalized thermodynamic osmotic pressure, as introduced in Eq. (5), and how it builds up.

The geometry is described in Fig. 3. We consider a flat surface with a solute gradient along the membrane. We denote by x the coordinate parallel to the surface and by z the one orthogonal to the surface. The solute concentration gradient far from the surface is $\partial_x c_\infty$ and is assumed to be uniform along x. Similarly to the mechanical approach for osmosis across a membrane, we introduce an external potential $\mathcal{U}(z)$ from the surface, which acts only on the solute; one noticeable difference to the previous membrane case is that it now acts perpendicular to the solid surface and solute gradient (i.e., depending on z but not on x). Typically, $\mathcal{U}$ is strong near the surface within a thin layer and vanishes far from the surface.

We first focus on the solute distribution. We assume a thin diffusive layer, i.e., the equilibrium along z is fast, so that the gradient along the surface (along x) is small compared with the gradient orthogonal to the surface (along z). In this case, local equilibrium establishes,

$$\mu[c(x,z)] + \mathcal{U}(z) \simeq \mu[c_\infty(x)]. \tag{27}$$

In the dilute regime where $\mu[c] = k_{\rm B}T\ln(c/c^*)$, we find $c(x,z) = c_\infty(x)\exp(-\mathcal{U}(z)/k_{\rm B}T)$, as discussed above. It can be more complex for a high concentration c of the solute. In general, depending on the interaction potential $\mathcal{U}$, a surface excess or a surface depletion of the solute will occur at the surface.

This equation may be interpreted in terms of a mechanical balance introducing the generalized osmotic pressure. Indeed, using the local equilibrium condition Eq. (27), one

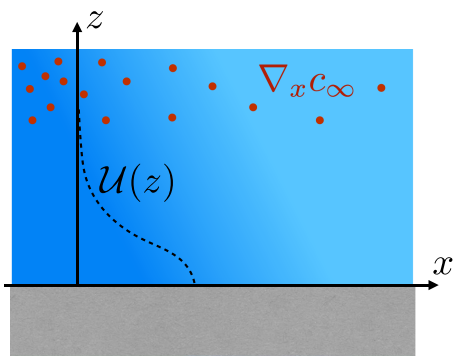

FIG. 3. Geometry of diffusio-osmosis only. Far from the surface, there is a uniform gradient of the solute $\nabla_x c_\infty$ parallel to the surface. The solute undergoes an external potential $\mathcal{U}(z)$.

gets $c(-\partial_z \mathcal{U}) = c\partial_z \mu = c\partial_z (\partial f/\partial c) \equiv \partial_z \Pi[c]$ (the latter two equalities being also a consequence of the Gibbs-Duhem relationship). Accordingly, one deduces that the local force (along z) acting on the fluid due to the wall can be interpreted in terms of the osmotic pressure as

$$c(-\partial_z \mathcal{U}) = \partial_z \Pi[c]. \tag{28}$$

Let us now turn to the fluid transport equation. It is described again by the Stokes equation

$$0 = -\nabla p + c(-\nabla \mathcal{U}) + \eta \nabla^2 \vec{v}. \tag{29}$$

First, the projection along the z direction (with a vanishing component of the velocity v_z) yields $0 = -\partial_z p + c(-\partial_z \mathcal{U})$. Using the previous result of Eq. (28), one can rewrite this pressure balance as $\partial_z(p - \Pi) = 0$ and obtain

$$p(x,z) - p_\infty = \Pi[c(x,z)] - \Pi[c_\infty(x)]. \tag{30}$$

Note that here, $\Pi[c]$ indeed takes the full expression of the osmotic pressure described in Eq. (5).

This result then allows us to obtain the solvent velocity profile. Indeed, injecting the pressure from Eq. (30) into the Stokes equation projected along x gives

$$0 = \eta \partial_z^2 v_x - \partial_x(\Pi[c(x,z)] - \Pi[c_\infty(x)]). \tag{31}$$

One then obtains the velocity field in terms of the osmotic pressure,

$$v_x(x,z) = \frac{1}{\eta}\int_0^z dz' \int_{z'}^\infty dz'' \partial_x(\Pi[c_\infty(x)] - \Pi[c(x,z'')]). \tag{32}$$

Here the no-slip boundary condition at the surface and a vanishing velocity gradient at infinity have been assumed.

This expression can be rearranged using again the Gibbs-Duhem relation, $d\Pi = c d\mu$ (see Eq. (5)), leading to

$$v_x(x,z) = \frac{1}{\eta}\int_0^z dz' \int_{z'}^\infty dz'' \left(c_\infty(x) - c(x,z'')\right) \partial_x \mu[c_\infty(x)]. \tag{33}$$

Note that we used $\partial_x \mu[c(x,z)] = \partial_x \mu[c_\infty(x)]$ resulting from the local equilibrium in Eq. (27). Finally, using $c_\infty(x)\partial_x \mu[c_\infty(x)] = \partial_x \Pi[c_\infty(x)]$ in the bulk, one obtains a more transparent expression for the diffusio-osmotic velocity far from the surface as

$$v_\infty = K_{DO} \partial_x \Pi[c_\infty(x)], \tag{34}$$

with the diffusio-osmotic mobility K_{DO} given as

$$K_{DO} = -\frac{1}{\eta}\int_0^\infty dz'\, z' \left(\frac{c(x,z')}{c_\infty(x)} - 1\right). \tag{35}$$

Note that η can also be assumed to depend on the concentration c. In this case, $1/\eta$ in K_{DO} has to be integrated along z as well. The effect of hydrodynamic slippage on the surface can also be taken into account, along the same lines as in Ref. 14, leading to an enhancement factor $(1 + b/L_s)$, where b is the slip length and L_s is the typical width of the diffuse interface. The results for diffusio-osmosis in Eqs. (34) and (35) are analogous to electro-osmosis and other surface-driven flows, with the mobility defined in terms of the first spatial moment of a density profile (solute concentration profile for diffusio-osmosis and charge density profile in the case of electro-osmosis).

To sum up, a solute gradient generates an interfacial flow of the fluid. As highlighted in Eq. (34), this flow takes its origin in an osmotic pressure gradient occurring within the diffuse layer close to the surface. Quantitatively, this flow is quantified by the value of the diffusio-osmotic mobility K_{DO}, which is non-zero only if there is surface excess or surface depletion of the solute. As a rule of thumb, its sign will be dominantly determined by the adsorption $\Gamma = \int_0^\infty dz'\, (c(x,z')/c_\infty(x) - 1)$. If there is a surface excess ($\Gamma > 0$), the flow of water goes towards the low concentrated area ($K_{DO} < 0$). Respectively, if there is a surface depletion, the flow of water reverses. But in the case of a complex concentration profile, for instance, with an oscillatory spatial dependence on z due to layering, the sign of K_{DO} may be expected to differ from the adsorption Γ. In this case, no obvious conclusion can be made for the direction of the diffusio-osmotic velocity and a full calculation has to be made.

The general expression for the diffusio-osmotic velocity, in Eqs. (34) and (35), is very similar to the corresponding expression for the dilute solution,[14,26,27] but the result in Eq. (34) makes it very clear that the diffusio-osmotic flux is indeed driven by the thermodynamic osmotic pressure gradient $\partial_x \Pi[c_\infty(x)]$.

IV. DISCUSSION AND CONCLUSIONS

We conclude with a few words on possible extensions and implications of the results derived here.

A. Coupling osmosis and diffusio-osmosis

First, while the previous derivations considered osmosis and diffusio-osmosis separately, one may consider a coupled situation in which both phenomena act jointly. Let us consider accordingly a general situation of a *partially* permeable membrane, similar to Fig. 2(b), now with a membrane interface interacting with solute particles. In full generality, the two transport phenomena are intimately coupled in the force balance and the situation is complex to disentangle. However some conclusions can be drawn in the limit where the pore size is large as compared to the interaction range of the surface potential, i.e., a small diffuse layer. In this case, one may decompose the interaction potential into two contributions: $\mathcal{U}(x,z) = \mathcal{U}_\infty(x) + \mathcal{U}_0(x,z)$, where $\mathcal{U}_0(x,z)$ is the surface interaction inside the membrane, which vanishes beyond the diffuse layer close to the surfaces; and $\mathcal{U}_\infty(x)$ is independent of z and describes a global energy barrier associated with the membrane, see Fig. 4. Under this assumption, this situation is amenable to a full calculation, which we report in Appendix B. As shown, the flow across the membrane still obeys a general Kedem–Katchalsky formula as in Eq. (25), with Π the general osmotic force, but with a reflection coefficient which now contains the coupled effects of osmosis and diffusio-osmosis,

$$\sigma = \sigma_O + \sigma_{DO} - \sigma_O \sigma_{DO}, \tag{36}$$

where σ_O is the osmotic reflection coefficient given by Eq. (24) and the diffusio-osmotic reflection coefficient is defined as $\sigma_{DO} = \eta K_{DO}/\kappa$, where K_{DO} given in Eq. (35) is the diffusio-osmotic reflection coefficient and κ the permeability.

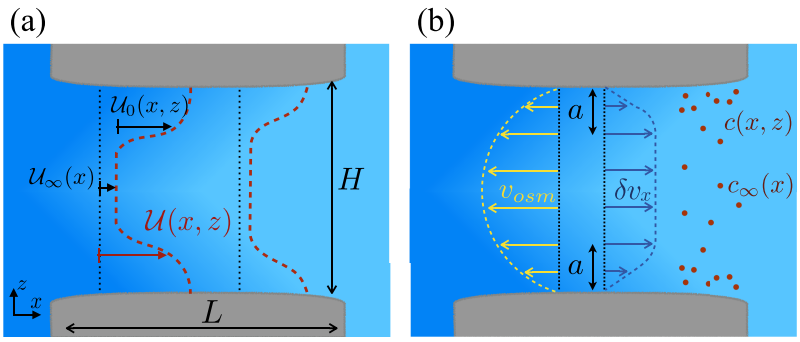

FIG. 4. Geometry of a membrane pore, in which combined osmotic and diffusio-osmotic transport across the membrane takes place. (a) Interaction potential expressed as $\mathcal{U}(x,z) = \mathcal{U}_\infty(x) + \mathcal{U}_0(x,z)$, where $\mathcal{U}_0(x,z)$ vanishes outside the diffuse layers. (b) Illustration of the decomposed velocity profiles $v_x = v_{osm} + \delta v_x$ within the pore. The typical thickness of the diffuse layer is denoted by a and the typical size of the pore by H.

The last term in Eq. (36) accounts for a negative feedback coupling between osmosis and diffusio-osmosis. Although obtained in the limit of the small diffuse layer, it exhibits a proper symmetry, as can be verified by considering various limiting situations. If the membrane is completely semi-permeable with $\sigma_O = 1$, then no solute flux occurs through the membrane and the diffusio-osmotic contribution in $\sigma_{DO}(1 - \sigma_O)$ vanishes. Reversely one also obtains $\sigma = 1$ when $\sigma_{DO} = 1$. A second note is that this coupled contribution hints to numerous possibilities to tune the flux through the membrane. With a given $\sigma_O < 1$, it is possible to enhance (respectively, diminish) σ—and thus the flux through the membrane—with a slight surface depletion (respectively, excess) on the surface. How this result may be generalized to any geometry remains to be explored.

B. Outlook

In summary, we have explored various forms of osmotic transport in the regime of a high solute concentration. Both osmosis across model membranes and diffusio-osmosis at the interface with solid substrates were considered. We have specifically focused our approach on the mechanical balance leading to a solvent flow under solute concentration gradients and explored the regime of a high solute concentration. We demonstrate in particular how the general expression of the osmotic pressure for mixtures, as obtained classically from the thermodynamic framework, emerges from the mechanical balance controlling non-equilibrium transport under solute gradients. The van 't Hoff expression for the osmotic pressure, $\Pi = k_B T c$, is accordingly replaced by its general thermodynamic counterpart, $\Pi = c\,\partial_c f - f[c] + f[c=0]$ (with f the free energy density), which is valid for arbitrary composition of the "solvent"/"solute" mixture. This generalizes the existing results obtained in the dilute solute regime. In the second paper in this series, we will provide a numerical validation of the present results by means of molecular dynamic simulations.[28]

An interesting consequence of the result in Eq. (34) is that a non-linear "sensing" may originate from non-linearities of the osmotic pressure versus the solute concentration. This may occur, e.g., for dense colloidal or polymer suspensions, as well as from a concentration dependent mobility K_{DO} (e.g., in ionic cases where K_{DO} scales as the square of the concentration dependent Debye length). Finally let us discuss again the ingredients required to describe our osmotic membrane. In the case of osmosis, we considered a model membrane, where the details of the membrane are reduced to its minimal ingredients and modeled as an external potential acting on the solute. As shown above, this simplified picture is extremely fruitful to gain insight into the mechanical balance at play. But it also points to the fact that osmosis does not require *per se* a solid membrane to be expressed. One may consider experimental situations where such a potential is built on the basis of optical or electrical forces, using, e.g., optical tweezers to repel "solute" particles or dielectrophoretic potential traps. Such "*osmosis without a membrane*" configuration would be highly interesting to develop, as it would simplify many aspects of clogging and pore blocking which occur for standard porous membranes. However designing such non-solid wells for molecular solutes, such as salts, remains a considerable challenge.

ACKNOWLEDGMENTS

L.B. thanks fruitful discussions with B. Rotenberg, P. Warren, M. Cates, and D. Frenkel on these topics. L.B. acknowledges support from the European Union's FP7 Framework Programme/ERC Advanced Grant Micromegas. S.M. acknowledges funding from a J.-P. Aguilar grant. We acknowledge funding from Agence Nationale de la Recherche (ANR) project BlueEnergy.

APPENDIX A: GENERAL EXPRESSION OF THE OSMOTIC PRESSURE

We recall below the general expression of the osmotic pressure given in Eq. (5). The derivation is directly inspired by the presentation in Ref. 24.

Consider two compartments separated by a perfectly semi-permeable membrane. We consider one side solvent with density ρ_A and solute with density ρ_B. On the other side, there are a solvent with density ρ'_A and solute with density ρ'_B. It is convenient to write the Helmholtz free energy of the mixture

$$F(T, V, N_A, N_B) = -pV + \mu_A N_A + \mu_B N_B, \tag{A1}$$

where V is the system volume, and N_A and N_B are the number of solvent and solute particles, respectively. We used Euler's theorem with $F = U - TS$, with U the internal energy and S the entropy.

The osmotic pressure is the difference in pressure between both sides,

$$\Pi = P - P' = \mu_A(\rho_A - \rho'_A) + \mu_B\rho_B - \mu'_B\rho'_B + f(T, \rho'_A, \rho'_B) - f(T, \rho_A, \rho_B), \tag{A2}$$

where $f = F/V$ is now the free energy density. We also used the fact that the chemical potentials of the solvent at equilibrium are equal on both sides of the membrane,

$$\mu_A = \frac{\partial f(T, \rho'_A, \rho'_B)}{\rho'_A} = \frac{\partial f(T, \rho_A, \rho_B)}{\rho_A}. \tag{A3}$$

Now we define $\rho = \rho_A + \rho_B$ and $c = \rho_B$ in each compartment. As a result (considering constant ρ), we have in this new space variable

$$\mu_A = \frac{\partial f}{\partial c}\frac{\partial c}{\partial \rho_A} = 0 \text{ and } \mu_B = \frac{\partial f}{\partial c}\frac{\partial c}{\partial \rho_B} = \frac{\partial f}{\partial c}. \tag{A4}$$

We can thus express the osmotic pressure directly as

$$\Pi = \frac{\partial f}{\partial c}c - \frac{\partial f}{\partial c'}c' + f(c') - f(c), \tag{A5}$$

which is exactly Eq. (5), with $c' = 0$. In the low density regime, we recall that $f(c) = ck_BT \ln c + (1-c)k_BT \ln(1-c)$ and thus we recover the limit of dilute systems, in which $\Pi = k_BT(c - c')$.

APPENDIX B: COUPLED OSMOTIC AND DIFFUSIO-OSMOTIC FLOWS

Here we examine the case of a membrane with pores of a finite size interacting with the solute. Typically, the geometry under consideration is that of Fig. 4. To simplify calculations, we assume a slit geometry with a planar pore of length L and width H (and invariant by translation in the perpendicular direction). We make also a further hypothesis and assume here that the interaction potential of the membrane with the solute can be decomposed as

$$\mathcal{U}(x,z) = \mathcal{U}_\infty(x) + \mathcal{U}_0(x,z), \tag{B1}$$

where $\mathcal{U}(x,z)$ is non-zero only between $-L/2$ and $L/2$, $\mathcal{U}_\infty(x)$ describes the global energy barrier associated with the membrane, and $\mathcal{U}_0(x,z)$ describes the specific interaction with the membrane pore surface and vanishes for large z. We write a as the typical range of the surface potential, fixing the size of the diffuse layer near the membrane pore surfaces (see Fig. 4). The potential $\mathcal{U}_\infty(x)$ is responsible for the osmotic transport and $\mathcal{U}_0(x,z)$ is responsible for the diffusio-osmotic transport. Here we consider the case where no external pressure difference is applied between the two sides of the membrane; this can be simply superimposed on the driving force as shown in Sec. II. To simplify the derivation, we make several additional simplifications. We assume that the deviation of the concentration profile to the equilibrium rest state is small. Further, we assume that the thickness of the diffusive layer is sufficiently small as compared to the pore size, $a \ll H$. In the following, we show how the reflection coefficients associated with osmotic and diffusio-osmotic transports are combined.

We write the thermodynamic equilibrium along the z direction as

$$\mu[c(x,z)] + \mathcal{U}(x,z) = \mu[c_\infty(x)] + \mathcal{U}_\infty(x). \tag{B2}$$

Here we have used the fact that the potential $\mathcal{U}_0(x,z)$ vanishes for large z. We derive first the osmotic current, following the steps of Sec. II B. We focus on the solute current out of the boundary layer, $z > a$, and compute there the solute profile starting from the Smoluchowski equation

$$J_s^x = -\lambda[c_\infty(x)]c_\infty(x)\partial_x\left(\mu[c_\infty(x)] + \mathcal{U}_\infty(x)\right). \tag{B3}$$

In parallel with the discussion in Sec. II B, we readily obtain the solute profile and then compute the osmotic driving force as

$$\int_{-L/2}^{L/2} dx\, \delta c_\infty(x)(-\partial_x\mathcal{U}_\infty) = \sigma_O \Delta\Pi, \tag{B4}$$

with $\Delta\Pi = c_{\infty,\text{res}}\mu'[c_{\infty,\text{res}}]\delta c_\infty$. The reflection coefficient of the osmotic transport here is defined as

$$\sigma_O = 1 - \frac{\int_{-L/2}^{L/2} \frac{dx'}{\lambda[c_{\infty,0}(x')]}}{\int_{-L/2}^{L/2} \frac{dx'}{\lambda[c_{\infty,0}(x')]}\frac{c_{\infty,\text{res}}}{c_{\infty,0}(x')}}, \tag{B5}$$

where $c_{\infty,0}$ is the stationary concentration (see Sec. II B).

Turning to the diffusio-osmotic part, one deduces the pressure profile from the Stokes equation along z, similarly to Sec. III as

$$p(x,z) - \Pi[c(x,z)] = p_\infty - \Pi[c_\infty(x)]. \tag{B6}$$

The velocity profile is obtained from the Stokes equation along x,

$$\eta\partial_z^2 v_x = -\partial_x(\Pi[c_\infty(x)] - \Pi[c(x,z)]) - c(x,z)(-\partial_x\mathcal{U}_0) - c(x,z)(-\partial_x\mathcal{U}_\infty). \tag{B7}$$

Let us separate the flow into a bulk, pressure-driven, and a surface-driven contribution. We introduce accordingly a velocity profile $v_{osm}(z)$ verifying

$$\eta\partial_z^2 v_{osm} = -c_\infty(x)(-\partial_x\mathcal{U}_\infty), \tag{B8}$$

so that the remaining contribution to the velocity profile, $\delta v_x = v_x - v_{osm}$, verifies the equation,

$$\eta\partial_z^2\delta v_x = -\partial_x(\Pi[c_\infty(x)] - \Pi[c(x,z)]) - c(x,z)(-\partial_x\mathcal{U}_0) - (c(x,z) - c_\infty(x))(-\partial_x\mathcal{U}_\infty), \tag{B9}$$

and only contains surface-driven contributions.

The bulk contribution can be calculated following the very same steps as in Sec. II B. This leads to a Poiseuille-like flow under the osmotic driving and, as in Eq. (25) (with $\Delta p = 0$), the corresponding averaged flux Q_{osm} writes in terms of the permeability κ of the pore as

$$Q_{osm} = \frac{\kappa}{\eta}\sigma_O\frac{\Delta\Pi}{L}. \tag{B10}$$

Here κ scales typically as H^2 (in general, the exact expression for κ will depend on the specific pore geometry).

The surface-driven contribution can be integrated as

$$\eta\,\delta v_x(x,z) = \int_0^z dz'\,z'\left(1 - \frac{c(x,z')}{c_\infty(x)}\right)\partial_x\Pi[c_\infty(x)] + \int_0^z dz'\,z'\,(c(x,z') - c_\infty(x))(-\partial_x\mathcal{U}_\infty), \tag{B11}$$

where we made use of the local equilibrium of Eq. (B2) as $\partial_x\mu[c(x,z)] + \partial_x\mathcal{U}_0 = \partial_x\mu[c_\infty(x)]$. We assumed the no-slip boundary condition at $z = 0$ and a vanishing velocity gradient for any $z \gg a$, see Fig. 4(b). We rewrite the previous velocity profile using the diffusio-osmotic mobility K_{DO}

defined in Eq. (35),

$$\delta v_x(x, z \geq a) = K_{DO}\left(\partial_x \Pi[c_\infty(x)] - c_\infty(x)(-\partial_x \mathcal{U}_\infty)\right). \quad \text{(B12)}$$

To go further and to simplify calculations, we consider now a situation where the (potential) dependence of K_{DO} on x can be neglected. In the dilute regime, it depends on x as $c(x,z)/c_\infty(x) = \exp(-\mathcal{U}_0(x,z)/k_B T)$, so that it is sufficient to require that the surface potential $\mathcal{U}_0$ is weakly dependent on x along the pore surface. Note also that typically $K_{DO} \sim \Gamma \times a$ with Γ the adsorption. One can then calculate the corresponding averaged flux across the membrane thickness (along x) and over its area $\mathcal{A}$, using the assumption $a \ll H$. Interestingly, using Eq. (B4), the last contribution in Eq. (B12) averages to the osmotic driving forces, $\sigma_O \Delta\Pi/L$,

$$\begin{aligned} Q_{surf} &= \frac{1}{\mathcal{A}L}\int d\mathcal{A}\int_{-L/2}^{L/2} dx\, \delta v_x(z) \\ &= K_{DO}(1-\sigma_O)\times\frac{\Delta\Pi}{L}. \end{aligned} \quad \text{(B13)}$$

Note that we assumed here to simplify that the diffusio-osmotic mobility does not depend on x.

Now, adding the two contributions to the flux, Q_{osm} and Q_{surf}, one gets the total flux as

$$\begin{aligned} Q &= Q_{osm} + Q_{surf} \\ &= \frac{\kappa}{\eta}\sigma_O\frac{\Delta\Pi}{L} + K_{DO}(1-\sigma_O)\times\frac{\Delta\Pi}{L}. \end{aligned} \quad \text{(B14)}$$

Defining a diffusio-osmotic reflection coefficient as

$$\sigma_{\rm DO} = \frac{\eta K_{DO}}{\kappa} = \frac{1}{\kappa}\int_0^a dz'\, z'\left(\frac{c(x,z')}{c_\infty(x)} - 1\right), \quad \text{(B15)}$$

(where again the dependence on x in the integral is not considered here for simplification), we then rewrite Eq. (B14) as

$$Q = \mathcal{L}_{\rm hyd}\left(\sigma_{DO} + \sigma_O - \sigma_{DO}\sigma_O\right)\Delta\Pi, \quad \text{(B16)}$$

where, as before, the permeance is defined as $\mathcal{L}_{\rm hyd} = \kappa/(\eta L)$. This equation highlights the introduction of a global reflection coefficient $\sigma = \sigma_{DO} + \sigma_O - \sigma_{DO}\sigma_O$. This gives the expression for the total reflection coefficient of Eq. (36) in the main text.

[1] P. Sheeler and D. E. Bianchi, *Cell and Molecular Biology*, 3rd ed. (Wiley, New York, 1987).
[2] K. H. Jensen, E. Rio, R. Hansen, C. Clanet, and T. Bohr, "Osmotically driven pipe flows and their relation to sugar transport in plants," J. Fluid Mech. **636**, 371–396 (2009).
[3] O. Kedem and A. Katchalsky, "A physical interpretation of the phenomenological coefficients of membrane permeability," J. Gen. Physiol. **45**, 143–179 (1961).
[4] B. E. Logan and M. Elimelech, "Membrane-based processes for sustainable power generation using water," Nature **488**, 313–319 (2012).
[5] A. Siria, P. Poncharal, A.-L. Biance, R. Fulcrand, X. Blase, S. T. Purcell, and L. Bocquet, "Giant osmotic energy conversion measured in a single transmembrane boron nitride nanotube," Nature **494**, 455–458 (2013).
[6] J. R. Werber, C. O. Osuji, and M. Elimelech, "Materials for next-generation desalination and water purification membranes," Nat. Rev. Mater. **1**, 16018 (2016).
[7] J. W. Gibbs, "Semi-permeable films and osmotic pressure," Nature **55**, 461–462 (1897).
[8] E. A. Guggenheim, *Thermodynamics: An Advanced Treatment for Chemists and Physicists*, 7th ed. (Elsevier, Amsterdam, North-Holland, 1985).
[9] I. M. Klotz and R. M. Rosenberg, *Chemical Thermodynamics Basic Concepts and Methods*, 7th ed. (John Wiley & Sons, Inc., 2008).
[10] J. L. Talen and A. J. Staverman, "Osmometry with membranes permeable to solvent and solute," Trans. Faraday Soc. **61**, 2794–2799 (1965); "Negative reflection coefficients," *ibid.* **61**, 2800–2804 (1965).
[11] C. Lee, C. Cottin-Bizonne, A.-L. Biance, P. Joseph, L. Bocquet, and C. Ybert, "Osmotic flow through fully permeable nanochannels," Phys. Rev. Lett. **112**, 244501 (2014).
[12] C. Lee, C. Cottin-Bizonne, R. Fulcrand, L. Joly, and C. Ybert, "Nanoscale dynamics versus surface interactions: What dictates osmotic transport?," J. Phys. Chem. Lett. **8**, 478–483 (2017).
[13] G. S. Manning, "Binary diffusion and bulk flow through a potential-energy profile: A kinetic basis for the thermodynamic equations of flow through membranes," J. Chem. Phys. **49**, 2668–2675 (1968).
[14] A. Ajdari and L. Bocquet, "Giant amplification of interfacially driven transport by hydrodynamic slip: Diffusio-osmosis and beyond," Phys. Rev. Lett. **96**, 186102 (2006).
[15] O. Kedem and A. Katchalsky, "Permeability of composite membranes. Part 1.—Electric current, volume flow and flow of solute through membranes," Trans. Faraday Soc. **59**, 1918–1930 (1963); "Permeability of composite membranes. Part 2.—Parallel elements," *ibid.* **59**, 1931–1940 (1963); "Permeability of composite membranes. Part 3.—Series array of elements," *ibid.* **59**, 1941–1953 (1963).
[16] J. L. Anderson and D. M. Malone, "Mechanism of osmotic flow in porous membranes," Biophys. J. **14**, 957 (1974).
[17] B. Abécassis, C. Cottin-Bizonne, C. Ybert, A. Ajdari, and L. Bocquet, "Boosting migration of large particles by solute contrasts," Nat. Mater. **7**, 785–789 (2008).
[18] V. Yadav, H. Zhang, R. Pavlick, and A. Sen, "Triggered 'on/off' micropumps and colloidal photodiode," J. Am. Chem. Soc. **134**, 15688–15691 (2012).
[19] S. Shin, E. Um, B. Sabass, J. T. Ault, M. Rahimi, P. B. Warren, and H. A. Stone, "Size-dependent control of colloid transport via solute gradients in dead-end channels," Proc. Natl. Acad. Sci. U. S. A. **113**, 257–261 (2016).
[20] N. Shi, R. Nery-Azevedo, A. I. Abdel-Fattah, and T. M. Squires, "Diffusiophoretic focusing of suspended colloids," Phys. Rev. Lett. **117**, 258001 (2016).
[21] P. Debye, "Equilibrium and sedimentation of uncharged particles in inhomogeneous electric fields," in *Ion Transport Across Membranes,* edited by H. T. Clarke (Academic Press, 1954), pp. 273–285.
[22] E. Grim and K. Sollner, "The contributions of normal and anomalous osmosis to the osmotic effects arising across charged membranes with solutions of electrolytes," J. Gen. Physiol. **40**, 887–899 (1957).
[23] C. B. Picallo, S. Gravelle, L. Joly, E. Charlaix, and L. Bocquet, "Nanofluidic osmotic diodes: Theory and molecular dynamics simulations," Phys. Rev. Lett. **111**, 244501 (2013).
[24] J.-L. Barrat and J.-P. Hansen, *Basic Concepts for Simple and Complex Liquids* (Cambridge University Press, 2003).
[25] J. R. Pappenheimer, "Passage of molecules through capillary walls," Physiol. Rev. **33**, 387–423 (1953), available online at http://physrev.physiology.org/content/33/3/387.
[26] E. Ruckenstein, "Can phoretic motions be treated as interfacial tension gradient driven phenomena?," J. Colloid Interface Sci. **83**, 77–81 (1981).
[27] J. L. Anderson, "Colloid transport by interfacial forces," Annu. Rev. Fluid Mech. **21**, 61–99 (1989).
[28] H. Yoshida, S. Marbach, and L. Bocquet, "Osmotic and diffusio-osmotic flow generation at high solute concentration. II. Molecular dynamic simulations," J. Chem. Phys **146**, 194702 (2017).

THE JOURNAL OF CHEMICAL PHYSICS **146**, 194702 (2017)

Osmotic and diffusio-osmotic flow generation at high solute concentration. II. Molecular dynamics simulations

Hiroaki Yoshida,[1,2,a)] Sophie Marbach,[1,b)] and Lydéric Bocquet[1,c)]
[1]*LPS, UMR CNRS 8550, Ecole Normale Supérieure, 24 Rue Lhomond, 75005 Paris, France*
[2]*Toyota Central R&D Labs., Inc., Nagakute, Aichi 480-1192, Japan*

(Received 3 March 2017; accepted 3 April 2017; published online 16 May 2017)

In this paper, we explore osmotic transport by means of molecular dynamics (MD) simulations. We first consider osmosis through a membrane and investigate the reflection coefficient of an imperfectly semi-permeable membrane, in the dilute and high concentration regimes. We then explore the diffusio-osmotic flow of a solute-solvent fluid adjacent to a solid surface, driven by a chemical potential gradient parallel to the surface. We propose a novel non-equilibrium MD (NEMD) methodology to simulate diffusio-osmosis, by imposing an external force on every particle, which properly mimics the chemical potential gradient on the solute in spite of the periodic boundary conditions. This NEMD method is validated theoretically on the basis of linear-response theory by matching the mobility with their Green–Kubo expressions. Finally, we apply the framework to more realistic systems, namely, a water-ethanol mixture in contact with a silica or a graphene surface. *Published by AIP Publishing.* [http://dx.doi.org/10.1063/1.4981794]

I. INTRODUCTION

Transport phenomena involving solute concentration difference or gradient of a solute-solvent fluid emerge in many scientific and industrial fields, from the chemical physics of biological membranes to the development of desalination processes.[1,2] Furthermore, there is a growing interest in applications harnessing concentration gradients to drive flows,[3–9] in particular for energy conversion[10] or storage using nano-scale membranes.[11] There is accordingly a need for a better fundamental understanding of such transport phenomena.

Osmosis across a membrane is a transport phenomenon driven by a solute concentration difference. Let us consider a situation where two fluid reservoirs with solute concentration difference c are separated by a membrane. If the membrane is completely semi-permeable, i.e., only the solvent particles are allowed to pass through the membrane, an osmotic pressure builds up and is well described by the classical van 't Hoff type equation: $\Pi = k_B T c$, with k_B the Boltzmann constant and T the temperature. In contrast, if the membrane is partially semi-permeable, i.e., solute particles are not completely rejected, then also solute flux occurs across the membrane. Transport through the membrane in the latter situation is described by the Kedem–Katchalsky equations,[12–14] which include the reflection coefficient σ as a phenomenological correction to the van 't Hoff equation. Relevant definitions of σ for the low concentration regime were given, e.g., by Manning[15] and extended to arbitrary concentrations in the first paper of this series (Paper I).[16] We also provide there a comprehensive theory to understand the origin of the reflection coefficient σ at a microscopic level.[16]

The diffusio-osmotic flow is a more subtle phenomenon which occurs under solute gradients *in the presence of a fluid-solid interface*. In a bulk fluid, a concentration gradient of a solute will lead to a diffusive flux of both components, but there is no total fluid flow because the forces acting on the solvent and solute particles are balanced. However, in the presence of an interface, the solute concentration in a thin layer near the surface differs from that in the bulk because of either an adsorption or a repulsion of solute particles. Consequently the force balance is broken in this thin layer and the driving force results in the fluid diffusio-osmotic flow. Such an interfacially driven flow is especially relevant to small-scale systems, typically in microfluidic devices with narrow channels and through nanoporous membranes because of the large surface-to-volume ratio.[17] Anderson and co-workers provided a theoretical framework of the diffusio-osmotic flow for the case of low concentration of solute,[18,19] and in Paper I we extended the theory to the high-concentration regime of the solute.[16]

In the present paper, we numerically study the microscopic aspects of these two problems, i.e., the osmosis and the diffusio-osmotic flow, using molecular dynamics (MD) simulations. Our first goal here is to validate the theoretical predictions developed in Paper I,[16] by means of direct measurements of the osmotic pressure and the diffusio-osmotic flow at a microscopic scale. However, in order to achieve this objective, one encounters a methodological difficulty in simulating the diffusio-osmotic flow directly; there is no existing method to implement directly a chemical potential gradient compatible with periodic boundary conditions. In this study, we accordingly introduce a novel non-equilibrium MD (NEMD) technique, which circumvents this difficulty and allows us to impose a proper external forcing representing

a)Electronic mail: h-yoshida@mosk.tytlabs.co.jp
b)Electronic mail: sophie.marbach@lps.ens.fr
c)Electronic mail: lyderic.bocquet@lps.ens.fr

a gradient in the chemical potential of the solute. We find an excellent agreement between our method and the results of a Green–Kubo approach based on linear-response theory, and furthermore validate Onsager's reciprocal relation. The NEMD method is then used to validate the theory and applied to a more realistic system of a water-ethanol mixture in contact with a silica or a graphene surface.

In Sec. II, we examine the osmotic pressure across a membrane, focusing on the evaluation of the reflection coefficient of incomplete semi-permeable membranes at low and high concentrations. We next consider diffusio-osmosis in Sec. III, including the introduction and validation of the new methodology mentioned above. Then a brief summary given in Sec. IV concludes the paper.

II. REFLECTION COEFFICIENT OF PARTIALLY SEMI-PERMEABLE MODEL MEMBRANES

In this section, we first consider the osmotic pressure across a model membrane, which allows us to gain much insight into the osmotic transport, and we introduce a versatile method to measure the osmotic pressure.

A. Theory

For the transport of a solute-solvent fluid across a filtration membrane with pressure and concentration differences between the two sides, the Kedem–Katchalsky model is widely used to describe the volume flux (per unit area) of the solution Q and the particle flux of the solute J_s,

$$Q = -\mathcal{L}_{\rm hyd}\left(\Delta p - \sigma k_{\rm B} T \Delta c\right), \tag{1}$$

$$J_s = -\mathcal{L}_{\rm D}\omega\Delta c + c(1-\sigma)Q, \tag{2}$$

where $\mathcal{L}_{\rm hyd}$ is the permeability coefficient, c is the concentration of the solute, $\mathcal{L}_{\rm D} = D/L$ is the solute permeability with D its diffusion coefficient and L the thickness of the membrane, ω is the factor for the effective mobility value in the membrane, and σ is the reflection coefficient that is a measure of the semi-permeability of the membrane.[15,20,21] The non-dimensional coefficients ω and σ are expected to be related by a linear relationship,[12] as $1-\sigma \propto \omega$.

Most of the approaches so far treat the reflection coefficient as a phenomenological parameter, and discussion on a direct connection with parameters characterizing the membrane is rare. Following our theoretical discussion in Paper I,[16] we consider here a model membrane, taking the form of an energy barrier felt by the solute particles.[16] This simplified situation allows us to obtain an expression for the reflection coefficient which takes the form

$$\sigma = 1 - \frac{\int_{-L/2}^{L/2} \frac{dx'}{\lambda[c(x')]}}{\int_{-L/2}^{L/2} \frac{dx'}{\lambda[c(x')]}\frac{c_0}{c(x')}}, \tag{3}$$

where λ is the mobility of the solute particles and c_0 is the average solute concentration far from the membranes; $c(x)$ is the stationary concentration distribution, see Ref. 16. Since no assumption is made on the magnitude of c_0, this expression is valid beyond the dilute solute limit. In the dilute solute limit, the formula given in Eq. (3) reduces to the one derived by Manning,[15]

$$\sigma = 1 - \frac{L}{\int_{-L/2}^{L/2} dx' \, \exp[+\beta\mathcal{U}(x')]}, \tag{4}$$

where $\mathcal{U}$ denotes the energy barrier representing the membrane.

B. MD simulations

In the present study, we validate the theoretical predictions for the reflection coefficient by means of MD simulations. We use a system of identical Lennard-Jones (LJ) particles for the fluid mixture with a potential barrier model for the membrane, similar to that considered in Ref. 22. Whereas they use a cubic box made of the semi-permeable membrane, here we consider a more direct geometrical setup as shown in Fig. 1. Two reservoirs are separated by a membrane as shown in Fig. 1(a); the membrane is not visible in the figure. The left reservoir contains a pure liquid solvent, while the right reservoir is filled with a liquid solution containing solute particles. The membrane is modeled by an energy barrier $\mathcal{U}$, which acts only on the solute particles, as illustrated in Fig. 1(b). The ends of the reservoirs are closed by rigid walls consisting of an FCC lattice made of the same particles as the solvent. The left wall serves as a piston, maintaining the normal pressure in the left reservoir at $P_L = P_0$ (see below for P_0). On the other hand, the right wall is fixed, and we measure the pressure in the right reservoir P_R from the total force acting on this wall. If the membrane is perfectly semi-permeable, i.e., there is no flux of solute particles across the membrane, then the system reaches the steady state. In the present study, the osmotic pressure is measured as the pressure difference $\Pi = P_R - P_L$; it could be measured alternatively by summing all the forces exerted on each particle by the membrane, which yields identical values. The case of incomplete semi-permeability is less straightforward and described below. Since the right wall is fixed in our setup, there is no net flux of solution; the case of finite flux of mixture across the membrane could also be simulated by controlling the permeability coefficient $\mathcal{L}_{\rm hyd}$, e.g., by introducing a drag force acting on the solvent particles in the membrane (see Ref. 16). For simplicity we do not consider any drag force here.

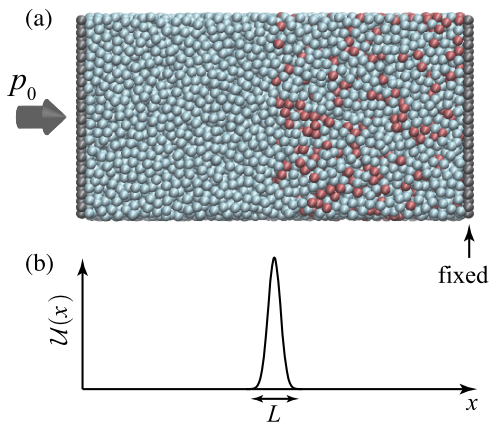

FIG. 1. (a) Simulation setup of two fluid reservoirs separated by a membrane. (b) Illustration of the energy barrier $\mathcal{U}(x)$ felt only by the solute particles (red).

For the inter-particle interactions, we assume a Lennard-Jones (LJ) potential among the solvent and solute particles: $U_{ij}(r) = 4\varepsilon_{ij}^{\mathrm{LJ}}[(\sigma_{ij}^{\mathrm{LJ}}/r)^{12} - (\sigma_{ij}^{\mathrm{LJ}}/r)^6]$. The parameters for the solute-solute, solute-solvent, and solvent-solvent interactions are commonly set as $\varepsilon_{ij}^{\mathrm{LJ}} = \varepsilon_0^{\mathrm{LJ}}$ and $\sigma_{ij}^{\mathrm{LJ}} = \sigma_0^{\mathrm{LJ}}$. The mass of all the particles is m_0. Therefore, the solute and solvent particles are mechanically identical, except that the solute particles feel the energy barrier representing the membrane. The wall particles are also described by the same interaction parameter set. In presenting the simulation results using the LJ potential, we use the units normalized in terms of the LJ parameters $\varepsilon_0^{\mathrm{LJ}}$ and σ_0^{LJ}, i.e., the reference length $\ell_0 = \sigma_0^{\mathrm{LJ}}$, the energy $\varepsilon_0 = \varepsilon_0^{\mathrm{LJ}}$, the force $f_0 = \varepsilon_0/\ell_0$, the pressure $P_0 = f_0/\ell_0^2$, and the time $\tau_0 = \ell_0^2 m_0/\varepsilon_0^{\mathrm{LJ}}$. The energy barrier $\mathcal{U}(z)$ takes the one-dimensional Gaussian form

$$\mathcal{U}(z) = U_0 \exp(-a(z - z_0)^2), \tag{5}$$

where z_0 is the position of the membrane and U_0 controls the height of the energy barrier. The thickness of the membrane is $\sim\sqrt{a}$, where a is fixed at $10/\ell_0^2$. This potential is cut off at a distance ℓ_{cut}, with $\ell_{\mathrm{cut}} = 4\ell_0$. The size of the simulation box in y and z is $22.7 \times 22.7\ \ell_0^2$, and the typical number of particles in one reservoir is 8380. The temperature is kept constant at $k_{\mathrm{B}}T/\varepsilon_0 = 1$ using the Nosé–Hoover thermostat in all directions, and then the density at pressure P_0 is $0.75\ \ell_0^{-3}$. The time integration is carried out with the time step $0.005\tau_0$. For the actual MD implementation, the open-source code LAMMPS is used throughout the paper.[23]

Figure 2(a) shows the MD results of the osmotic pressure as a function of the solute concentration c in the right reservoir. In the case of $U_0 = 30\,\varepsilon_0$, no solute particles cross the membrane during the simulation up to 5×10^6 time steps, i.e., the membrane exhibits complete semi-permeability. In this regime, the reflection coefficient is unity, $\sigma = 1$. The osmotic pressure then converges to the standard van 't Hoff law, $\Pi = k_{\mathrm{B}}Tc$, for dilute solutions. For the larger concentrations, Π departs from the linear line but is still captured by the van 't Hoff law before linearization,

$$\Pi = -\rho_v k_{\mathrm{B}} T \ln(1 - \chi), \tag{6}$$

where χ is the molar fraction of the solute, $\chi = \rho_v^{-1}(1/c - 1/\rho_u + 1/\rho_v)^{-1}$, and ρ_u and ρ_v are the density of the solute and solvent, respectively. On the other hand, when the energy barrier is small ($U_0 = 3\varepsilon_0$), some solute particles permeate through the membrane during the simulations. The membrane is imperfectly semi-permeable and one expects $\sigma < 1$. We observe indeed that the osmotic pressure drops, coherently with $\sigma < 1$. In this situation, the pressure in the right reservoir evolves with time. We accordingly compute the osmotic pressure in the following manner: after equilibration of the system at $U_0 = 30\varepsilon_0$ for at least 10^5 time steps, we set the energy barrier at $U_0 < 30\varepsilon_0$. Then we average the results over 5×10^5 time steps to evaluate the osmotic pressure.

More quantitative data of the reflection coefficient σ for the incomplete semi-permeable membrane are given in Fig. 2(b). Here, the MD values are obtained with $\sigma = \Pi/\Pi_{\mathrm{com}}$, where Π_{com} denotes the value of the complete semi-permeable case, i.e., the data shown in Fig. 2(a) for $U_0 = 30\varepsilon_0$. The MD results are plotted for two values of initial concentration in the right reservoir, $c = 0.036/\ell_0^3$ and $c = 0.36/\ell_0^3$. For comparison,

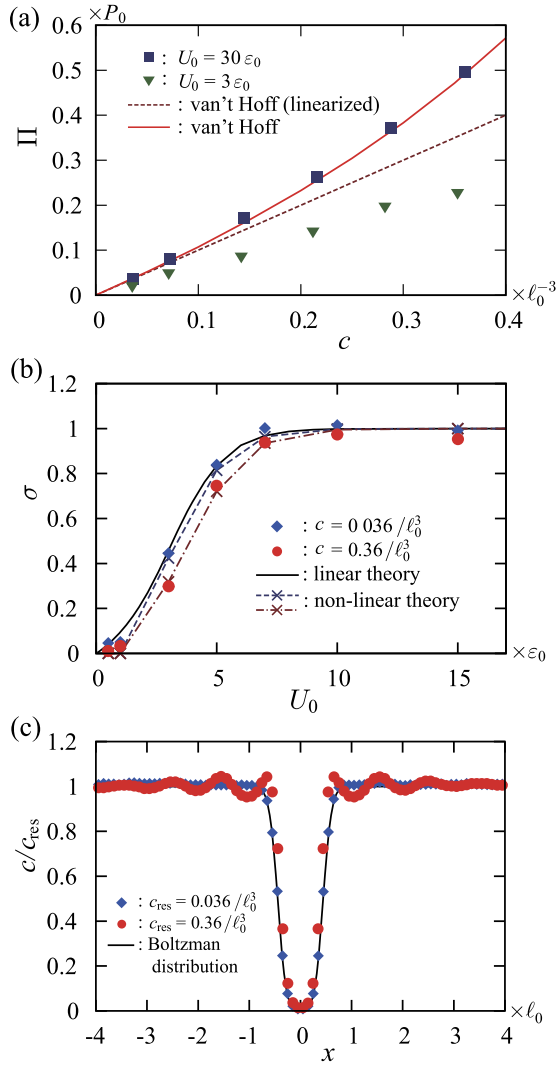

FIG. 2. (a) Osmotic pressure Π versus solute concentration c in the right reservoir. The symbols indicate the MD results and the solid line indicates the van 't Hoff type formula given in Eq. (6). The linearized van 't Hoff law is shown by the dashed line. (b) Reflection coefficient σ versus height of the energy barrier U_0. The MD results are shown by the symbols. While the solid line is the theory for the low concentration regime given in Eq. (4), the dashed line and dashed-dotted line are the results of generalized theory (Eq. (3)). (c) Stationary concentration profiles across the membrane, for the case of $U_0 = 5\varepsilon_0$; here, the concentrations in both reservoirs are identical. The symbols indicate the MD results, which are used to calculate σ using Eq. (3) (and are plotted as crosses and lines in panel (b)). The solid line is the Boltzmann distribution.

the theoretical predictions quoted in Sec. II A are also plotted in the figure. The prediction of Eq. (4), which is valid in the dilute limit, agrees well with the MD data at $c = 0.036/\ell_0^3$. For the high concentration $c = 0.36/\ell_0^3$, however, the MD data depart from the prediction of Eq. (4) and take smaller values.

The prediction of Eq. (3) is evaluated by numerically integrating the concentration profiles of the MD results. Since the solute and solvent particles considered here are mechanically identical, the mobility is independent of the concentration, and thus λ cancels out in Eq. (3). The stationary concentration profiles are obtained at the equilibrium state, with the same concentration in the two reservoirs. Typical concentration profiles are shown in Fig. 2(c) for $U_0 = 5\varepsilon_0$, together with the

Boltzmann distribution valid in the dilute limit, $c = c_0 \exp(-\mathcal{U}/k_B T)$. The deviation from the Boltzmann distribution at $c = 0.36/\ell_0^3$ is a non-linear effect due to high concentration. The interaction between solute particles becomes significant, and it causes the oscillations visible in the concentration profile, similar to fluid density oscillations that generally occur near solid surfaces;[24] the solute-solvent interaction causes a similar oscillation in the solvent density profile (not shown.) Taking into account this effect, Eq. (3) accurately predicts the reflection coefficient as shown in Fig. 2(b). This demonstrates the usefulness of the theoretical prediction for wide concentration ranges beyond the dilute regime, once the concentration profiles are measured or estimated.

III. NON-EQUILIBRIUM SIMULATIONS OF DIFFUSIO-OSMOTIC FLOW

In this section we now consider diffusio-osmosis, i.e., the flow induced by solute gradients, but now tangential to a solid surface. We perform molecular dynamics of diffusio-osmosis for dense solute concentrations. To this end we introduce a new methodology allowing us to simulate the effect of chemical potential gradients numerically.

A. Theory: A reminder

The geometry under consideration is shown in Fig. 3(a), with a chemical potential gradient applied parallel to the surface. In the bulk region, the total force is zero yet solute and solvent fluxes are observed. The solute concentration in a layer adjacent to the surface deviates from that in the bulk because of either a preferential adsorption or a depletion of the solute. The force unbalance in the thin layer is the driving force of the diffusio-osmotic flow. As shown in Paper I,[16] the fluid velocity is linearly proportional to the chemical potential gradient, according to

$$v_x(z) = \frac{1}{\eta}\int_0^z dz' \int_{z'}^{\infty} dz'' \left(c_\infty - c(z'')\right) \nabla_x \mu, \tag{7}$$

where η is the fluid viscosity, c_∞ is the concentration in the bulk region sufficiently far from the surface, and $\nabla_x \mu$ is the chemical potential gradient. This formula correctly recovers the classical result for the dilute solution.[18,19] The diffusio-osmotic mobility K_{DO}, relating the velocity v_∞ far from the surface to the gradient of the chemical potential as $v_\infty = K_{DO} c_\infty \nabla_x \mu$, is then given by

$$K_{DO} = -\frac{1}{\eta}\int_0^\infty dz'\, z' \left(\frac{c(z')}{c_\infty} - 1\right). \tag{8}$$

The mobility K_{DO} is negative for an excess surface concentration at the interface, i.e., the flow of solvent goes towards the low chemical potential area. Respectively, it is positive if there is a surface depletion, and the flow reverses. Note that in the case of slip at the interface with typical slip length b, a slip velocity adds to Eq. (7), such that K_{DO} is enhanced by a factor $(1 + b/L_s)$, with L_s the thickness of the diffusion layer.[25]

B. Principles for an NEMD diffusio-osmosis

In this section, our goal is to develop a method to simulate directly diffusio-osmosis on the basis of non-equilibrium MD (NEMD) simulations. This implies the generation of the diffusio-osmotic flow by applying an external field that is consistent with the application of a chemical potential gradient $-\nabla_x \mu$. A key characteristic of diffusio-osmosis, like all interfacially driven flows—including electro- or thermo-osmosis flows[26,27]—, is that it is a force-free transport phenomenon. This can be demonstrated from the fact that the hydrodynamic velocity profile is flat far away from the surface, so that all forces acting on the surface—direct interactions and hydrodynamics—do vanish in the bulk. Accordingly, if any force is applied to the system (solute+solvent), it should be balanced so that the total force acting on the fluid should

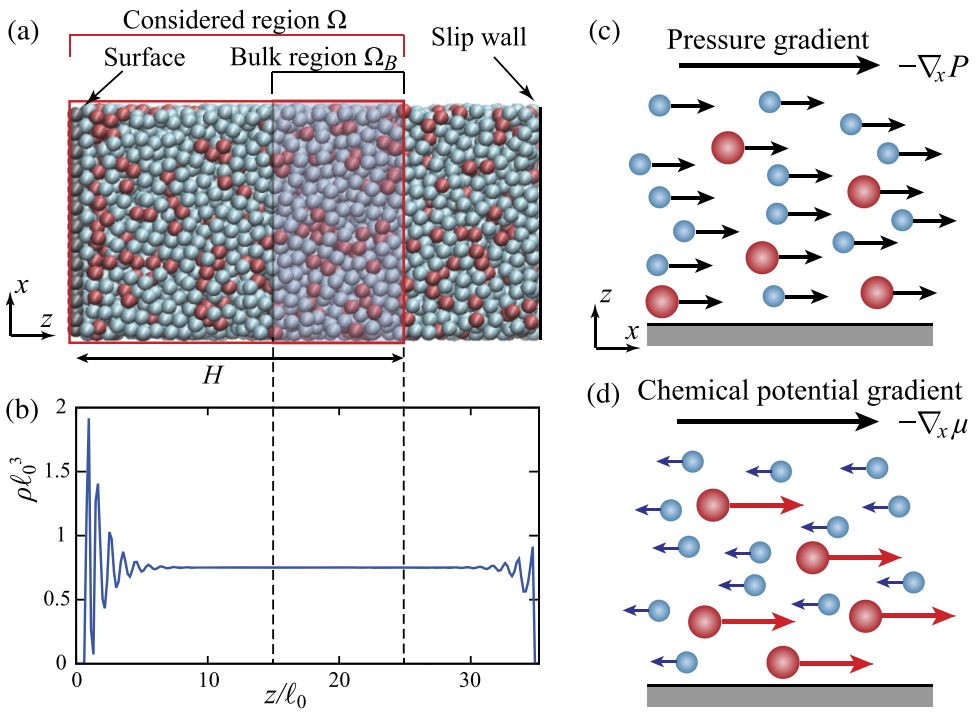

FIG. 3. (a) Computational geometry for the MD simulation for an LJ mixture (solute: red, solvent: blue) in contact with a solid wall (gray). (b) Typical concentration profile along the z direction. (c) Schematic illustration of the NEMD method modeling the pressure gradient. It is modeled by a force acting on each particle. (d) The NEMD method for simulating the chemical potential gradient. It is modeled as a forward force per solute particle (red) and counter force per solvent particle (blue) such that the total force in the bulk is zero.

vanish in the bulk region. This is obviously in contrast with the pressure driven flow. In the MD simulations, for the latter case, an external force F_p is applied commonly to each particle in the fluid, as shown in Fig. 3(c).[28–30] The applied pressure gradient, i.e., the force per volume, is then identified as $-\nabla_x P = F_p N/V$, where N is the number of particles and V is the volume of the whole system Ω.

To simulate diffusio-osmosis, we accordingly propose the following scheme, where we apply a differential force on the solute and on the solvent, see Fig. 3(d):

- An external force F_μ is applied to each solute particle in the whole system Ω.
- A counter force $-[N_s^B/(N^B - N_s^B)]F_\mu$ is applied to each solvent particle in Ω, where N_s^B and N^B are, respectively, the number of solute particles and the total number of particles in the *bulk region*.

Note that the bulk region, denoted by Ω_B, is defined as a volume far from the wall such that the density (and concentration) profile is flat, as depicted in Fig. 3(b). The counter force therefore ensures the force balance in the bulk volume Ω_B. The external force strength is then related to the chemical potential gradient as

$$-\nabla_x \mu = F_\mu N^B/(N^B - N_s^B), \tag{9}$$

as is confirmed below via the Green–Kubo approach.

C. Validation of the NEMD scheme: Green–Kubo relationships

We now validate this methodology on the basis of linear response theory. Indeed due to the Onsager symmetry, one expects that the same diffusio-osmotic mobility will relate two symmetric situations: on the one hand, the solvent flow under a solute chemical gradient and on the other hand, the (excess) solute flux under a pressure drop.[25] This is expressed in the transport matrix as

$$\begin{bmatrix} Q \\ J_s - c_\infty^* Q \end{bmatrix} = \begin{bmatrix} M^{QQ} & M^{QJ} \\ M^{JQ} & M^{JJ} \end{bmatrix} \begin{bmatrix} -\nabla_x P \\ -\nabla_x \mu \end{bmatrix}, \tag{10}$$

where Q and $J_s - c_\infty^* Q$ are the total (volume) flux and the excess solute flux, respectively, as described below. The off-diagonal coefficients in Eq. (10) are expected to be identical $M^{QJ} = M^{JQ}$ due to the Onsager time-reversal, symmetry relationship. Let us therefore demonstrate that our NEMD methodology complies with this symmetry relationship. We will calculate the Green–Kubo expression for both M^{QJ} and M^{JQ} cross coefficients.

We first remind quickly the general statements of linear response theory, i.e., on the response of an observed variable $\mathcal{B}$ to an external potential field $\mathcal{A}(\boldsymbol{x}_i)F_0$, where F_0 is a constant microscopic force and $\mathcal{A}(\boldsymbol{x}_i)$ is a function of the positions of the particles $\boldsymbol{x}_i$. The observed variable is expressed as $\langle \mathcal{B} \rangle = \mathcal{M}^{BA} F_0$, where $\langle \cdot \rangle$ is the ensemble average, and

$$\mathcal{M}^{BA} = \frac{1}{k_B T} \int_0^\infty \langle \mathcal{B}(t) \dot{\mathcal{A}}(0) \rangle dt. \tag{11}$$

In the NEMD approach, the external field is $\mathcal{A} \times F_\mu$ with

$$\mathcal{A} = \sum_{i \in \text{solute}} x_i - \frac{N_s^B}{N^B - N_s^B} \sum_{i \in \text{solvent}} x_i, \tag{12}$$

where x_i is the coordinate along the x axis of particle number i. The observed variable is the total flux, i.e., $\mathcal{B} = Q(t) = (1/N) \sum_{i \in \text{all}} \dot{x}_i$. Injecting these into the definition of $\mathcal{M}^{BA}$ gives the Green–Kubo formula for the diffusio-osmotic flow $\langle Q \rangle$ (abbreviated Q) generated by the NEMD scheme,

$$Q = M^{QJ} \left(\frac{N^B}{N^B - N_s^B} \right) F_\mu, \tag{13}$$

$$\text{with } M^{QJ} = \frac{V}{k_B T} \int_0^\infty \langle Q(t)(J_s - c_\infty^* Q)(0) \rangle dt. \tag{14}$$

Here V is the volume of Ω, and $c_\infty^* = \phi^B \rho_{\text{av}}$, with $\phi^B = N_s^B/N^B$ being the molar fraction of solute in the bulk region Ω^B, and ρ_{av} the density averaged over Ω. The solute flux J_s is calculated in terms of the particle velocity as $J_s = (1/V) \sum_{i \in \text{solute}} \dot{x}_i$.

Similarly, in the reciprocal situation, we measure the solute flux $\mathcal{B} = J_s(t) - c_\infty^* Q(t)$ under a pressure gradient represented by $\mathcal{A} = \sum_{i \in \text{all}} x_i$. We deduce the symmetric formula

$$J_s - c_\infty^* Q = M^{JQ} \left(\frac{N}{V} \right) F_p, \tag{15}$$

$$\text{with } M^{JQ} = \frac{V}{k_B T} \int_0^\infty \langle (J_s - c_\infty^* Q)(t) Q(0) \rangle dt. \tag{16}$$

Comparing Eqs. (14) and (16), we find that $M^{QJ} = M^{JQ}$ so that the proposed scheme complies with Onsager's reciprocal relation. Regarding M^{QJ} and M^{JQ} as the diffusio-osmotic transport coefficients relating the fluxes with the external fields, one may interpret that the microscopic forces F_μ and F_p in terms of the thermodynamic forces

$$-\nabla_x \mu = F_\mu \frac{N^B}{N^B - N_s^B}, \tag{17}$$

and similarly $-\nabla_x P = F_p N/V$.

Equation (17) indicates that, given the chemical potential gradient, the force acting on the solute particles is $F_\mu = -(1 - \phi^B)\nabla_x \mu$ and that on the solvent particles is $-[N_s^B/(N^B - N_s^B)]F_\mu = \phi^B \nabla_x \mu$. Physically, while the force directly originating in $-\nabla_x \mu$ acts only on the solute particles, the counteracting force $\phi^B \nabla_x \mu$ applies to all the particles to ensure a vanishing net force.

D. Numerical validation of the NEMD methodology

We now apply this methodology in NEMD simulations. Our goals are first to highlight the implementation of the NEMD and second to validate the NEMD mobility by comparing it to the equilibrium Green–Kubo estimates.

1. Numerical details

In this section, solvent, solute, and wall particles interact via the LJ potential. While the parameters for the solute-solute, solute-solvent, solvent-solvent, and solvent-wall interactions are commonly set as $\varepsilon_{ij}^{\text{LJ}} = \varepsilon_0^{\text{LJ}} = \varepsilon_0$ and $\sigma_{ij}^{\text{LJ}} = \sigma_0^{\text{LJ}} = \ell_0$, the parameters for the solute-wall interaction $\varepsilon_{\text{solute,wall}}^{\text{LJ}}$ and $\sigma_{\text{solute,wall}}^{\text{LJ}}$ are varied to control the surface excess of solute particles. The wall particles are fixed at $z = 0$, as in Fig. 3(a), on an FCC lattice with lattice constant $\sqrt{2}\ell_0$. In this setting, the hydrodynamic slip at the interface between the wall and the fluid is negligible.[25] An artificial reflecting wall is placed to truncate the computational domain, sufficiently far from the

wall. At this reflecting wall, the incoming atoms are simply reflected with no tangential momentum transfer, i.e., the wall is a complete slip boundary. Since an artificial oscillation of density occurs in the vicinity of the reflecting boundary, we need to exclude this part from all measurements. We thus consider a specific region Ω (shown in Fig. 3(a)) that extends to typically a distance $10\ell_0$ from the reflecting boundary. The particle density is determined such that the normal pressure on the surface is P_0.[26,31]

The lateral dimension of the simulation box is $17\ell_0 \times 17\ell_0$, and the height of domain Ω is $H = 25\ell_0$. The bulk region Ω_B is defined as $z \in [15, 25]\ell_0$. The total number of fluid particles is 7424, and the reflecting wall is typically placed at $z = 35\ell_0$ (this position slightly depends on the interaction parameters). The LJ parameters are varied in the ranges $\varepsilon^{\rm LJ}_{\rm solute,wall}/\varepsilon^{\rm LJ}_0 \in [0.5, 1.5]$ and $\sigma^{\rm LJ}_{\rm solute,wall}/\sigma^{\rm LJ}_0 \in [0.8, 1.5]$. Two concentrations $\bar{c} = 0.15/\ell_0^3$ and $0.04/\ell_0^3$ are considered, where $\bar{c}$ is the solute concentration averaged over Ω. Other computational conditions, as well as notations for the reference parameters, are the same as those described in Sec. II B.

2. NEMD results: Velocity profiles

We show in Fig. 4(a) the velocity profiles obtained using the present NEMD method for different solute-wall interaction parameters. As expected the velocity profile is plug-like at a large distance from the wall, while exhibiting some structuration close to the interface. Here we introduce the solute adsorption Γ, defined as

$$\Gamma = \int_0^\infty dz' \left(\frac{c(z')}{c_\infty} - 1 \right), \tag{18}$$

which is a measure of the surface excess of solute in the layer: Γ is positive for an excess surface concentration and negative for a depletion. In Fig. 4, the two cases of $\Gamma = 3.9\ell_0$ and $-0.9\ell_0$ are shown. The corresponding LJ parameters are $(\varepsilon^{\rm LJ}_{\rm solute,wall}/\varepsilon_0, \sigma^{\rm LJ}_{\rm solute,wall}/\ell_0) = (1.5, 1.5)$ and $(0.5,\ 0.8)$, respectively. The reversal of the velocity profiles is associated with a sign change of the adsorption: the flow is forward for $\Gamma = 3.9\ell_0$ and backward for $\Gamma = -0.9\ell_0$.

Figure 5 plots the diffusio-osmotic mobility calculated from the relationship $K_{DO} = v_\infty/(c_\infty \nabla_x \mu)$ (here shown for $-\nabla\mu_x = 0.025 f_0$). The horizontal axis is the theoretical expression for the mobility given in Eq. (8). It depends on the local concentration profile data which we measure in the simulation, see Fig. 4(b). Clearly all the numerical values drop on the line of slope equal to unity, validating the theoretical prediction in a wide parameter range. We note that we used the value of η calculated from pressure driven flow simulations. One may question whether it is pertinent to use this value to model the flow in the vicinity of the surface, where structuring of the fluid occurs, see Fig. 4(b). However the simulation data show that this provides a fairly accurate prediction for the diffusio-osmotic mobility, using the concentration profile (measured in the equilibrium situation) as an input.

We finally note that the theoretical predictions also allow us to calculate the local velocity profiles in terms of the concentration profile, given in Eq. (7). Here, the integral in

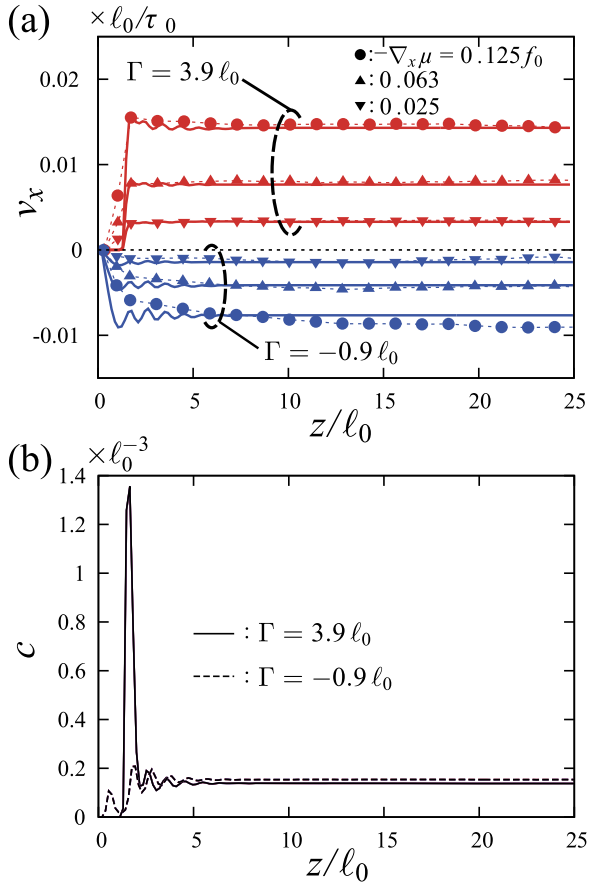

FIG. 4. Velocity profiles of the diffusio-osmotic flow for the case of positive surface excess $\Gamma = 3.9\ell_0$ and negative surface excess $\Gamma = -0.9\ell_0$. The average concentration is $\bar{c} = 0.15/\ell_0^3$. The symbols indicate the MD results, and the solid line in panel (a) indicates the theoretical result given in Eq. (7) where we integrated the concentration profiles shown in panel (b). In panel (b), the concentration profile of $\nabla_x\mu = 0$ is also plotted (black) in addition to the cases of $-\nabla_x\mu = 0.025 f_0$, $0.063 f_0$, and $0.125 f_0$, though the difference is negligible.

Eq. (7) is performed using the concentration profile as shown in Fig. 4(b); the integration range is truncated at $z/\ell_0 = 8\ell_0$, after the concentration converges to the bulk value. The comparison is shown in Fig. 4(a) as solid lines, showing again an excellent agreement with the simulation data.

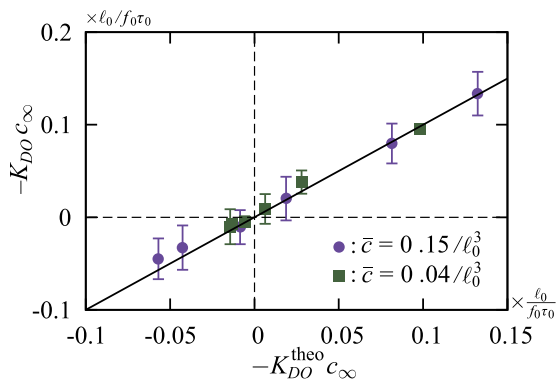

FIG. 5. Numerical values of the diffusio-osmotic mobility $-K_{DO}c_\infty$ obtained using the NEMD method versus its theoretical counterpart $-K_{DO}^{\rm theo}c_\infty$ from Eq. (8). At each point at least four simulation runs have been performed and the average value is plotted, with the error bar indicating the standard deviation. The line indicating a slope equal to unity corresponds to the theoretical prediction.

3. Comparison of mobilities with equilibrium Green–Kubo estimates

As a final check, one can compare the previous values for the mobilities with those obtained from the Green–Kubo relationships in Eqs. (14) and (16). One key difference is that the latter are now evaluated in *equilibrium* simulations.

The calculated correlation functions are displayed in Fig. 6(a). The time integration appearing in Eqs. (14) and (16) suffers from significant noise, and we therefore take an average over a very large time-series sample to compute the time-correlation functions. We accordingly adopt the same strategy as in Refs. 26 and 32, i.e., we perform ten independent MD simulation runs with different initial configurations and average the time-correlation functions over the different samples and time-series. The correlations up to the time difference $t = 1000\tau_0$ are taken, and 4.8×10^6 time-series samples are averaged for each of ten runs.

Then the diffusio-osmotic mobility M^{QJ} and the reciprocal counterpart M^{JQ} are obtained by using Eqs. (14) and (16). Here, we truncate the integration range at $t = 150\,\tau_0$ —after a sufficient decay of the correlation functions—to avoid unnecessary noise. For the example shown in Fig. 6(a), one can check that the two mobilities, calculated using the two correlation functions, do match within the numerical error, i.e., $M^{QJ} = M^{JQ} = 0.12 \pm 0.005\,(\ell_0/f_0\tau_0)$ for the case of $\Gamma = 3.9\ell_0$ and $-0.035 \pm 0.005\,(\ell_0/f_0\tau_0)$ for the case of $\Gamma = -0.9\ell_0$.

Finally, we show in Figs. 6(b) and 6(c) the comparison of the NEMD results (symbols) with the results of the Green–Kubo approach (lines). We apply various values of the chemical potential gradient $-\nabla_x\mu$ (tuning F_μ), and the measured flux Q is plotted in panel (b). A good agreement is obtained, which validates the direct implementation of the diffusio-osmotic flow using the present NEMD method. In panel (c), we also compare the results to the symmetric estimate of the mobility in terms of the excess solute flux under an imposed pressure gradient. The measured solute flux $J_s - c^*_\infty Q$ is plotted for various values of applied pressure drop $-\nabla_x P$ (tuning F_p). Again we find a good agreement with the Green–Kubo results.

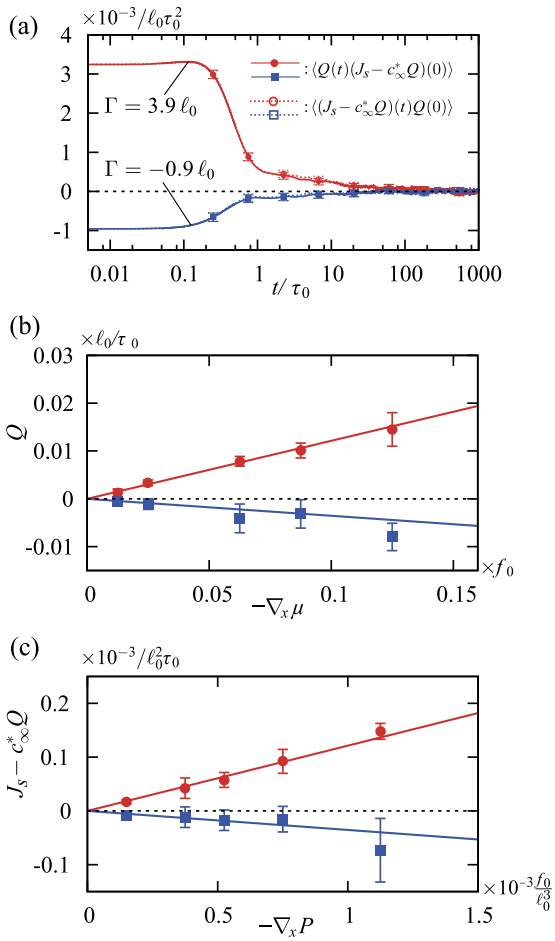

FIG. 6. (a) Time correlation functions appearing in Eqs. (14) and (16), obtained using equilibrium MD simulations, for the case of $\bar{c} = 0.15/\ell_0^3$. The results of ten simulation runs with different initial configurations are averaged, and the standard error is shown with the error bar. (b) Total flux Q versus the chemical potential gradient $-\nabla_x\mu$. (c) Solute flux $J_s - c^*_\infty Q$ versus the pressure gradient $-\nabla_x P$. In panels (b) and (c), the symbols indicate the results of NEMD simulations, and the slopes of the lines indicate the coefficients obtained using Eqs. (14) and (16).

E. Application to the water-ethanol mixture

We finally demonstrate the versatility of the NEMD method by applying it to more realistic systems. Here we keep the same geometry as shown in Fig. 3(a) but replace the fluid with an aqueous ethanol solution and the wall with a silica surface (Fig. 7(a)) or a graphene sheet (Fig. 7(b)). We use the TIP4P/2005 model for water molecules,[33] and the united atom model of the optimized potentials for liquid simulations (OPLS)[34,35] for the ethanol molecules. The model detailed in Ref. 36 is employed for the silica surface, and the interaction parameters for the carbon atoms of the wall are extracted from the AMBER96 force field.[37] The Lorentz–Berthelot mixing rules[38] are used to determine the LJ parameters for the cross-interactions. The temperature is kept at 300 K, using the Nosé–Hoover thermostat for all direction, and the pressure is at 1 atm. The time step is set to 2 fs. The external force is applied to each atom individually, and the value of the force per atom is obtained by dividing the force per molecule by the number of atoms within a molecule.

Here we restrict ourselves to the case of high concentration, i.e., 20% ethanol molar fraction, corresponding to 40 wt. % ethanol. The lateral dimension of the simulation box is 4×4.3 nm^2, and the height of the domain Ω is $H = 4.8$ nm for the case of the silica surface and 6.3 nm for the case of the graphene surface. The thickness of the bulk region Ω_B is $z \in [H - 2\,\text{nm}, H]$.

As in the insets of Figs. 7(a) and 7(b), the pressure driven flow shows no velocity slip on the silica surface and a large slip on the graphene surface.[39] By fitting the formula based on classical continuum theory, $v_x = (-\nabla_x P/2\eta)(2Hb + 2Hz - z^2)$, the slip length for the graphene surface is estimated as $b = 285$ nm (see also Ref. 39). In Figs. 7(c) and 7(d), the diffusio-osmotic flow profiles obtained by the present NEMD are plotted. The flow velocity still shows some noise in spite of the relatively large averages at least over 100 ns (5×10^7 time steps). Nevertheless, the diffusio-osmotic flows are directly observed. The theoretical predictions given in Eq. (7) are also shown in the figure, which exhibit a reasonable agreement with the NEMD data. The applicability of the present NEMD method to a realistic system is thus confirmed. We note that the inverse diffusio-osmotic flow, which has been reported recently for

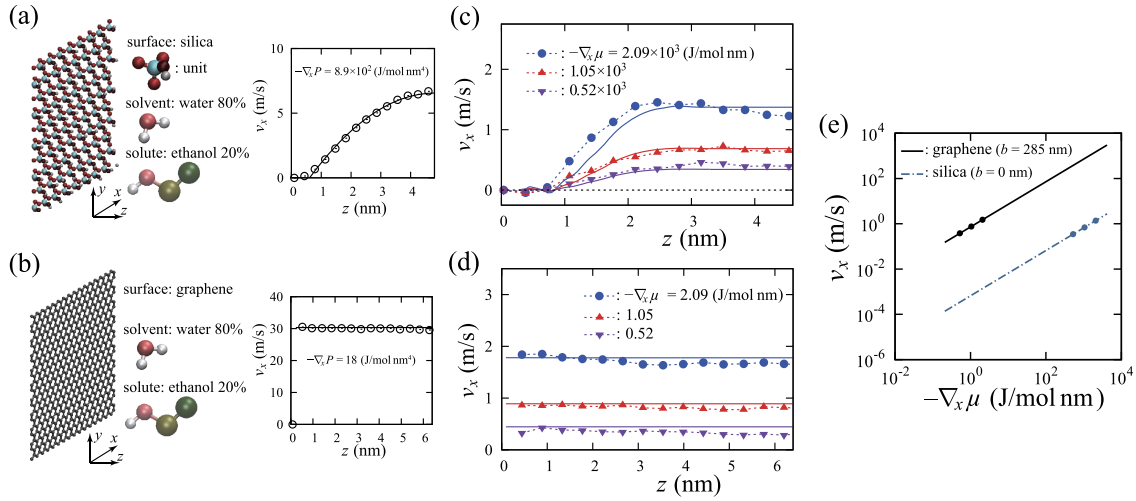

FIG. 7. Illustrations of systems of water-ethanol mixture in contact with (a) silica surface and (b) graphene surface. The velocity profiles under a pressure gradient are also shown in each panel (circles), together with the continuum model (solid line); the z coordinate is measured from the position of Si atoms for the silica surface and from the C atoms for the graphene surface. The velocity profiles of the diffusio-osmotic flow are shown for the case of silica surface in (c), for the case of graphene surface in (d). The symbols indicate the MD results, and the solid lines indicate the theoretical results given in Eq. (7). The slip length is assumed to be 0 in panel (c) and 285 nm in panel (d). (e) Comparison of the diffusio-osmotic velocity obtained using Eq. (8). The solid line indicates the case of the graphene surface, and the dashed-dotted line indicates the case of the silica surface. The dots indicate the points shown in panels (c) and (d).

the system of aqueous ethanol solution with a silica surface,[9] was not observed in the parameter range we considered here.

We finally emphasize that the large slip length for the case of the graphene surface is accounted for by correcting Eq. (7) as remarked in Sec. III A (see also Refs. 16 and 25). The magnitude of the diffusio-osmotic flow is compared in Fig. 7(e), in which v_∞ is plotted as a function of $-\nabla_x\mu$, using Eq. (8); the results corresponding to Figs. 7(c) and 7(d) are indicated by the dots. The diffusio-osmotic flow on the graphene surface is larger than that on the silica surface by about three orders of magnitude. This indicates that the hydrodynamic slip enormously enhances the diffusio-osmotic flow, as expected theoretically, see Ref. 25.

IV. SUMMARY

Transports of fluid mixtures under chemical potential difference have been investigated numerically by means of MD simulations. We first considered osmosis across membranes and examined the reflection coefficient of imperfectly semi-permeable membranes. The theoretical expression given in Eq. (3), which we derived for high solute concentrations, was numerically validated. Next we considered the diffusio-osmotic flow near a solid-liquid interface. We introduced a novel NEMD method allowing us to simulate a chemical potential gradient, involving a mixed force balance acting on solute and solvent molecules, as illustrated in Fig. 3(d). This method allows us to simulate a diffusio-osmotic flow using periodic boundary conditions. We validated the methodology on the basis of linear response theory and numerical calculations of the corresponding Green–Kubo expressions of the transport coefficients. Using the proposed NEMD method, the plug-like velocity profile was directly obtained, as shown in Figs. 4 and 7, both for the LJ fluids and water-ethanol solutions. These results showed a very good agreement with the analytical predictions for both the local velocity profile and mobility.[16]

The proposed methodology can be extended to explore diffusio-phoretic transport involving complex molecules, like polymers, which has not been explored theoretically up to now. Further work in this direction is in progress.

ACKNOWLEDGMENTS

L.B. thanks fruitful discussions with B. Rotenberg, P. Warren, M. Cates, and D. Frenkel on these topics. This work was granted access to the HPC resources of MesoPSL financed by the Region Ile de France and the project Equip@Meso (Reference No. ANR-10-EQPX-29-01) of the programme Investissements d'Avenir supervised by the Agence Nationale de la Recherche (ANR). L.B. acknowledges support from the European Union's FP7 Framework Programme/ERC Advanced Grant Micromegas. S.M. acknowledges funding from a J.-P. Aguilar grant. We acknowledge funding from ANR project BlueEnergy.

[1] O. Kedem and A. Katchalsky, "Thermodynamic analysis of the permeability of biological membranes to non-electrolytes," Biochim. Biophys. Acta **27**, 229–246 (1958).
[2] S. S. Sablani, M. F. A. Goosen, R. Al-Belushi, and M. Wilf, "Concentration polarization in ultrafiltration and reverse osmosis: A critical review," Desalination **141**, 269–289 (2001).
[3] B. Abécassis, C. Cottin-Bizonne, C. Ybert, A. Ajdari, and L. Bocquet, "Boosting migration of large particles by solute contrasts," Nat. Mater. **7**, 785–789 (2008).
[4] V. Yadav, H. Zhang, R. Pavlick, and A. Sen, "Triggered 'on/off' micropumps and colloidal photodiode," J. Am. Chem. Soc. **134**, 15688–15691 (2012).
[5] C. Lee, C. Cottin-Bizonne, A.-L. Biance, P. Joseph, L. Bocquet, and C. Ybert, "Osmotic flow through fully permeable nanochannels," Phys. Rev. Lett. **112**, 244501 (2014).
[6] Y.-X. Shen, P. O. Saboe, I. T. Sines, M. Erbakan, and M. Kumar, "Biomimetic membranes: A review," J. Membr. Sci. **454**, 359–381 (2014).
[7] S. Shin, E. Um, B. Sabass, J. T. Ault, M. Rahimi, P. B. Warren, and H. A. Stone, "Size-dependent control of colloid transport via solute gradients in dead-end channels," Proc. Natl. Acad. Sci. U. S. A. **113**, 257–261 (2016).

[8]S. Marbach and L. Bocquet, "Active osmotic exchanger for efficient nanofiltration inspired by the kidney," Phys. Rev. X **6**, 031008 (2016).
[9]C. Lee, C. Cottin-Bizonne, R. Fulcrand, L. Joly, and C. Ybert, "Nanoscale dynamics versus surface interactions: What dictates osmotic transport?," J. Phys. Chem. Lett. **8**, 478–483 (2017).
[10]A. Siria, P. Poncharal, A.-L. Biance, R. Fulcrand, X. Blase, S. T. Purcell, and L. Bocquet, "Giant osmotic energy conversion measured in a single transmembrane boron nitride nanotube," Nature **494**, 455–458 (2013).
[11]W. J. van Egmond, M. Saakes, S. Porada, T. Meuwissen, C. J. N. Buisman, and H. V. M. Hamelers, "The concentration gradient flow battery as electricity storage system: Technology potential and energy dissipation," J. Power Sources **325**, 129–139 (2016).
[12]O. Kedem and A. Katchalsky, "A physical interpretation of the phenomenological coefficients of membrane permeability," J. Gen. Physiol. **45**, 143–179 (1961).
[13]A. Katchalsky and O. Kedem, "Thermodynamics of flow processes in biological systems," Biophys. J. **2**, 53–78 (1962).
[14]K. S. Spiegler and O. Kedem, "Thermodynamics of hyperfiltration (reverse osmosis): Criteria for efficient membranes," Desalination **1**, 311–326 (1966).
[15]G. S. Manning, "Binary diffusion and bulk flow through a potential-energy profile: A kinetic basis for the thermodynamic equations of flow through membranes," J. Chem. Phys. **49**, 2668–2675 (1968).
[16]S. Marbach, H. Yoshida, and L. Bocquet, "Osmotic and diffusio-osmotic flow generation at high solute concentration. I. Mechanical approaches," J. Chem. Phys. **146**, 194701 (2017).
[17]L. Bocquet and E. Charlaix, "Nanofluidics, from bulk to interfaces," Chem. Soc. Rev. **39**, 1073–1095 (2010).
[18]J. L. Anderson, M. E. Lowell, and D. C. Prieve, "Motion of a particle generated by chemical gradients Part 1. Non-electrolytes," J. Fluid Mech. **117**, 107–121 (1982).
[19]J. L. Anderson, "Colloid transport by interfacial forces," Annu. Rev. Fluid Mech. **21**, 61–99 (1989).
[20]J. L. Talen and A. J. Staverman, "Osmometry with membranes permeable to solvent and solute," Trans. Faraday Soc. **61**, 2794–2799 (1965); "Negative reflection coefficients," *ibid* **61**, 2800–2804 (1965).
[21]J. L. Anderson and D. M. Malone, "Mechanism of osmotic flow in porous membranes," Biophys. J. **14**, 957 (1974).
[22]T. W. Lion and R. J. Allen, "Osmosis in a minimal model system," J. Chem. Phys. **137**, 244911 (2012).
[23]See http://lammps.sandia.gov for the code.
[24]J. N. Israelachvili, *Intermolecular and Surface Forces*, 3rd ed. (Academic Press, 2011).
[25]A. Ajdari and L. Bocquet, "Giant amplification of interfacially driven transport by hydrodynamic slip: Diffusio-osmosis and beyond," Phys. Rev. Lett. **96**, 186102 (2006).
[26]H. Yoshida, H. Mizuno, T. Kinjo, H. Washizu, and J.-L. Barrat, "Molecular dynamics simulation of electrokinetic flow of an aqueous electrolyte solution in nanochannels," J. Chem. Phys. **140**, 214701 (2014).
[27]R. Ganti, Y. Liu, and D. Frenkel, "Molecular simulation of thermo-osmotic slip," preprint arXiv:1702.02499 (2017).
[28]D. K. Bhattacharya and G. C. Lie, "Molecular-dynamics simulations of nonequilibrium heat and momentum transport in very dilute gases," Phys. Rev. Lett. **62**, 897 (1989).
[29]B. D. Todd and D. J. Evans, "Temperature profile for Poiseuille flow," Phys. Rev. E **55**, 2800 (1997).
[30]J.-L. Barrat and L. Bocquet, "Large slip effect at a nonwetting fluid-solid interface," Phys. Rev. Lett. **82**, 4671 (1999).
[31]H. Yoshida and L. Bocquet, "Labyrinthine water flow across multilayer graphene-based membranes: Molecular dynamics versus continuum predictions," J. Chem. Phys. **144**, 234701 (2016).
[32]H. Yoshida, H. Mizuno, T. Kinjo, H. Washizu, and J.-L. Barrat, "Generic transport coefficients of a confined electrolyte solution," Phys. Rev. E **90**, 052113 (2014).
[33]J. L. F. Abascal and C. Vega, "A general purpose model for the condensed phases of water: TIP4P/2005," J. Chem. Phys. **123**, 234505 (2005).
[34]W. L. Jorgensen, J. D. Madura, and C. J. Swenson, "Optimized intermolecular potential functions for liquid hydrocarbons," J. Am. Chem. Soc. **106**, 6638–6646 (1984).
[35]W. L. Jorgensen, "Optimized intermolecular potential functions for liquid alcohols," J. Phys. Chem. **90**, 1276–1284 (1986).
[36]S. H. Lee and P. J. Rossky, "A comparison of the structure and dynamics of liquid water at hydrophobic and hydrophilic surfaces—A molecular dynamics simulation study," J. Chem. Phys. **100**, 3334–3345 (1994).
[37]W. D. Cornell, P. Cieplak, C. I. Bayly, I. R. Gould, K. M. Merz, D. M. Ferguson, D. C. Spellmeyer, T. Fox, J. W. Caldwell, and P. A. Kollman, "A second generation force field for the simulation of proteins, nucleic acids, and organic molecules," J. Am. Chem. Soc. **117**, 5179–5197 (1995).
[38]M. P. Allen and D. J. Tildesley, *Computer Simulation of Liquids* (Oxford University Press, Oxford, 1989).
[39]K. Falk, F. Sedlmeier, L. Joly, R. R. Netz, and L. Bocquet, "Ultralow liquid/solid friction in carbon nanotubes: Comprehensive theory for alcohols, alkanes, OMCTS, and water," Langmuir **28**, 14261–14272 (2012).

Downloaded from https://www.cambridge.org/core. Ecole Supérieure de Chimie Physique Electronique de Lyon CPE, on 24 Aug 2017 at 08:31:43, subject to the Cambridge Core terms of use, available at https://www.cambridge.org/core/terms. https://doi.org/10.1017/jfm.2017.441

J. Fluid Mech. (2017), *vol.* 826, R3, doi:10.1017/jfm.2017.441

JFM RAPIDS
journals.cambridge.org/rapids

The Landau–Squire plume

Eleonora Secchi[1], Sophie Marbach[1], Antoine Niguès[1], Alessandro Siria[1] and Lydéric Bocquet[1,†]

[1]Laboratoire de Physique Statistique, Ecole Normale Supérieure, PSL Research University, 24 rue Lhomond, 75005 Paris, France

(Received 30 April 2017; revised 30 April 2017; accepted 20 June 2017)

In this paper, we analyse the dispersion of a dye by a Landau–Squire plume, generated by a jet flow emerging from a nanocapillary into a reservoir. We demonstrate analytically that the dye concentration profile exhibits a long-range profile decaying as the inverse of the distance to the origin, whereas the plume shape is only a function of a Péclet number defined in terms of the flow characteristics inside the nanocapillary. These predictions are successfully compared with experiments on fluorescent dye dispersion from nanocapillaries under pressure-driven flow. The plume shape allows extraction of the nanojet force characterizing the Landau–Squire velocity profile for a given pressure drop, with results in full agreement with direct velocimetry measurements and finite-element calculations. The peculiarities of the Landau–Squire plume make it a sensitive probe of the flow properties inside the seeding nanocapillary.

Key words: jets, low-Reynolds-number flows, micro-/nano-fluid dynamics

1. Introduction

Nanofluidics, the study of flows down to the nanoscale, has emerged over recent years thanks in particular to the development of new methods to fabricate controlled fluidic systems with nanoscale geometries, as well as of proper instrumentation to quantify transport at these scales (Bocquet & Tabeling 2014). This has allowed the study of ionic and water transport across nanopores and nanotubes made of various materials, thereby revealing a number of exotic transport properties (Siria *et al.* 2013; Geng *et al.* 2014; Joshi *et al.* 2014; Park & Jung 2014; Feng *et al.* 2016; Secchi *et al.* 2016). This opens up new possibilities in the development of innovative processes for desalination, nano-filtration and energy harvesting (Werber, Osuji & Elimelech 2016). However, while measurement of electrical properties across nanochannels is now relatively standard (Branton *et al.* 2008; Siria *et al.* 2013; Stein 2015; Feng *et al.* 2016), measurement of mass flow through nanoscale capillaries remains a considerable challenge due to the minute flow emerging from

† Email address for correspondence: lyderic.bocquet@lps.ens.fr

© Cambridge University Press 2017

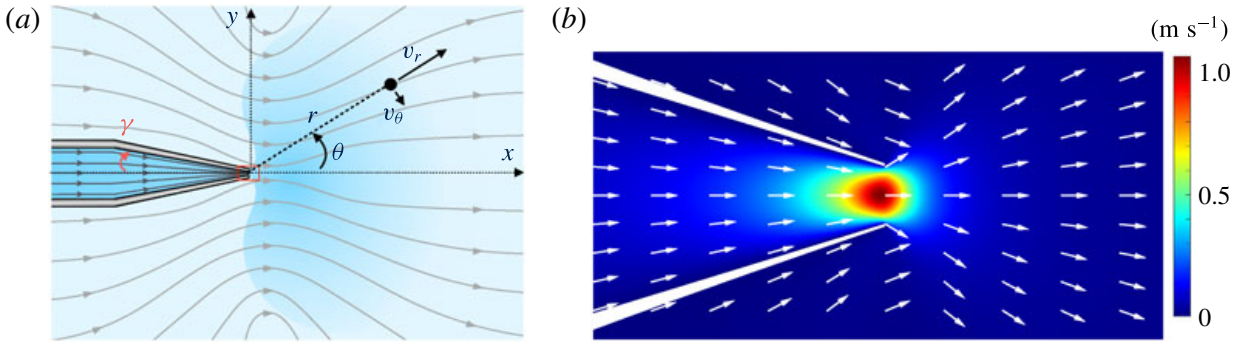

FIGURE 1. Landau–Squire jet flow emerging from a nanocapillary. (*a*) Schematic of pressure-driven streamlines inside the nanocapillary and Landau–Squire streamlines outside; the angle γ defines the internal half-opening-angle of the nanocapillary. (*b*) Close-up view of red box in (*a*); simulated flow amplitude at the nanocapillary tip (box size 1.25 μm × 2.5 μm; nanocapillary tip diameter 250 nm).

such nanopipes (Bocquet & Tabeling 2014; Secchi *et al.* 2016). In this context, it was demonstrated recently that the peculiarities of the nanojet flow emerging from a nanocapillary, the so-called Landau–Squire flow, could be harnessed in order to reach the proper sensitivity to extract the mass transport across a tube down to nanometric sizes (Secchi *et al.* 2016).

The Landau–Squire flow corresponds to a jet flow emerging from the end of a (semi-infinite) narrow tube into a reservoir with infinite dimension; see figure 1. This flow was first solved by Landau and Squire in two seminal works (Squire 1951; Landau & Lifshitz 1959). Its properties were investigated experimentally in recent contributions by Laohakunakorn *et al.* (2013) and Secchi *et al.* (2016). An interesting and peculiar specificity of this flow is that it is completely characterized by the rate of momentum transferred from the tube into the reservoir, i.e. a force – but not by the flow rate. In the viscous (low-Reynolds) regime, the solution for the flow induced in the reservoir is indeed given by a Stokeslet,

$$v_r = \frac{F_P}{4\pi\eta}\frac{\cos\theta}{r}, \qquad v_\theta = -\frac{F_P}{8\pi\eta}\frac{\sin\theta}{r}, \tag{1.1a,b}$$

where the tube tip is taken as the origin for the distance r and the angle θ is measured from the tube axis; η is the fluid viscosity (figure 1). In this equation, F_P has the dimension of a force and corresponds to the fluid momentum transfer. On dimensional grounds, the jet force F_P is accordingly expected to take the form of a Stokes formula in the viscous regime (Secchi *et al.* 2016),

$$F_P = \alpha\eta R_1\overline{v}, \tag{1.2}$$

where R_1 is the characteristic radial dimension of the tube and $\overline{v}$ is the average flow velocity emerging from the tube tip, defined in terms of the fluid flux Q as $\overline{v} = Q/\pi R_1^2$; $\alpha = O(1)$ is a numerical coefficient which depends on the specific geometry of the tip of the nanocapillary. A quantitative estimate of α can be obtained numerically (Secchi *et al.* 2016).

In this paper, we consider a situation in which a dye is added to the capillary and dispersed into the reservoir from the capillary tip under the application of a pressure drop. A stationary plume is created in the reservoir, the shape of which results from

Downloaded from https://www.cambridge.org/core. Ecole Supérieure de Chimie Physique Electronique de Lyon CPE, on 24 Aug 2017 at 08:31:43, subject to the Cambridge Core terms of use, available at https://www.cambridge.org/core/terms. https://doi.org/10.1017/jfm.2017.441

the competition between the convection under the Landau–Squire pressure-driven flow and the molecular diffusion of the dye. In the following, we first solve analytically the convection–diffusion equation for the dye concentration in the reservoir (§ 2); and then compare the results with an experimental investigation of the plume of a fluorescent dye dispersed from nanocapillaries (§ 3).

2. The Landau–Squire plume: theoretical predictions

We show here that the dispersion of dye particles via the Landau–Squire (LS) flow field can be predicted analytically. We consider a situation in which the flowing fluid inside the capillary is seeded with a dye, with concentration C_0 and bulk diffusion coefficient D. The dye emerges into the reservoirs from the tip of the feeding capillary, which therefore acts as a point source with, say, an incoming solute flux Φ_0. The latter is the sum of a convective contribution, QC_0, and a diffusive contribution proportional to $\sim R_1 D C_0$ (with a prefactor whose explicit expression, which depends on the geometry of the seeding capillary tip, will not be needed in the following). Due to the infinite volume of the reservoir, a steady state is reached and the stationary concentration of particles verifies the diffusion–convection equation,

$$D\Delta C - \boldsymbol{v}\cdot\nabla C = 0, \tag{2.1}$$

where $\boldsymbol{v}(\boldsymbol{r})$ is the Landau–Squire (divergence-free) flow field in the reservoir in (1.1). In spherical coordinates, equation (2.1) reads

$$D\frac{1}{r^2}\partial_r(r^2\partial_r C) + D\frac{1}{r^2\sin\theta}\partial_\theta(\sin\theta\,\partial_\theta C) - \frac{F_p}{4\pi\eta r}\cos\theta\,\partial_r C + \frac{F_p}{8\pi\eta r}\frac{\sin\theta}{r}\partial_\theta C = 0. \tag{2.2}$$

We first note that any function of the type $f(\theta)/r^n$, with n a real number, can be a solution of (2.2). However, conservation of the number of dye particles imposes that for any r,

$$\Phi_0 = 2\pi r^2\int_{\theta=0}^{\pi} J_r(r,\theta)\sin\theta\,\mathrm{d}\theta, \tag{2.3}$$

where $J_r(r,\theta) = -D\partial_r C + (F_p\cos\theta/4\pi\eta r)C$ is the radial component of the particle flux and Φ_0 is the total solute flux. This imposes $n=1$, and we deduce $C(r,\theta) = f(\theta)/r$. The differential equation for $f(\theta)$ takes the form

$$D\sin\theta\,\partial_\theta(\sin\theta\,\partial_\theta f) + \frac{F_p}{4\pi\eta}\cos\theta f + \frac{F_p}{8\pi\eta}\sin\theta\,\partial_\theta f = 0. \tag{2.4}$$

The general solution of this equation is obtained as

$$f(\theta) = A\mathrm{e}^{(Pe/2)\cos\theta} + B\mathrm{e}^{(Pe/2)(\cos\theta-1)}\left\{-\mathrm{e}^{Pe}\int_{-(Pe/2)(\cos\theta+1)}^{\infty}\frac{\mathrm{e}^{-t}}{t}\,\mathrm{d}t + \int_{(Pe/2)(1-\cos\theta)}^{\infty}\frac{\mathrm{e}^{-t}}{t}\,\mathrm{d}t\right\}, \tag{2.5}$$

where A and B are two integration constants. This solution introduces an effective Péclet number specific to the Landau–Squire problem and defined as

$$Pe = \frac{F_p}{4\pi\eta D}. \tag{2.6}$$

Downloaded from https://www.cambridge.org/core. Ecole Supérieure de Chimie Physique Electronique de Lyon CPE, on 24 Aug 2017 at 08:31:43, subject to the Cambridge Core terms of use, available at https://www.cambridge.org/core/terms. https://doi.org/10.1017/jfm.2017.441

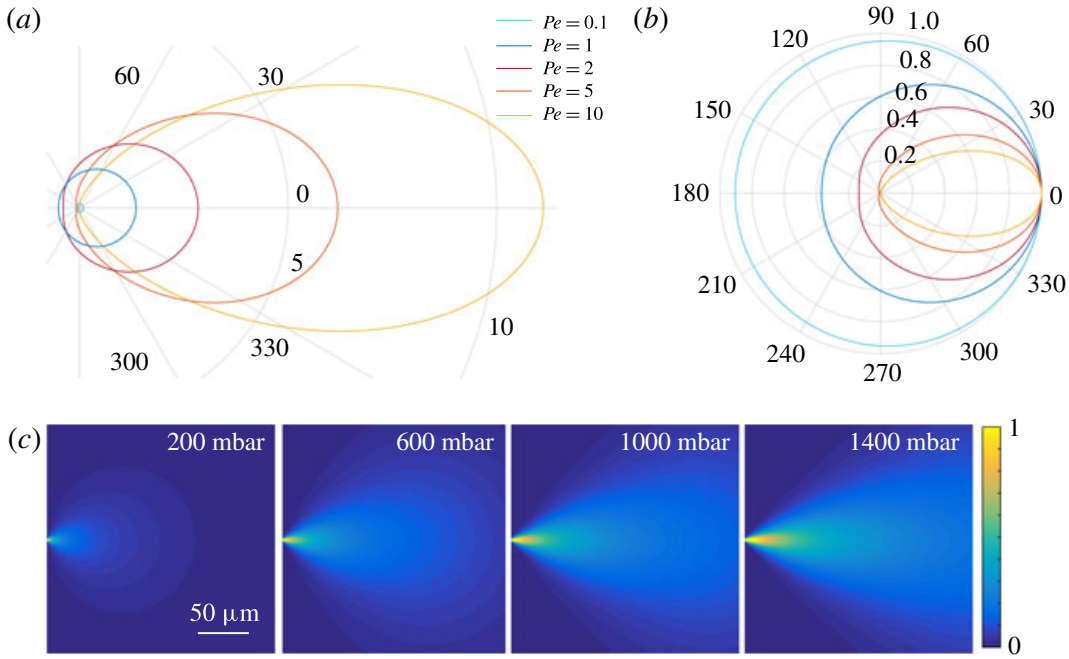

FIGURE 2. The shape of the plume-like concentration profile for different Péclet numbers. (*a*) Iso-concentration profiles derived from $r/r_c = Pe\,\mathrm{e}^{(Pe/2)(\cos\theta-1)}$, with r_c a characteristic length scale independent of Pe, for different Péclet numbers (for illustration, we assumed $\Phi_0 \propto Pe$). (*b*) Renormalized iso-concentration profiles $r/r_{max} = \mathrm{e}^{(Pe/2)(\cos\theta-1)}$ for several Péclet numbers. For small Pe, the profile is very circular, nearly diffusive. For large Pe, the profile is severely distorted in a plume-like shape by the Landau–Squire flow. The colour scale is the same for both plots. (*c*) Simulated concentration profiles in the x, y plane, divided by the largest concentration value measured, for a nanocapillary with dimensions $R_1 = 120$ nm and $\gamma = 4°$.

Imposing that f is a regular function yields $B = 0$, and A is deduced from solute number conservation, equation (2.3). Altogether, the solution of the diffusion–convection problem thus reads

$$C(r,\theta) = \frac{\Phi_0}{4\pi D r}(1+\varepsilon(Pe))\mathrm{e}^{(Pe/2)(\cos\theta-1)}, \tag{2.7}$$

where $\varepsilon(Pe) = (1-(1+Pe)\mathrm{e}^{-Pe})/(Pe-1+(1+Pe)\mathrm{e}^{-Pe})$ is a small contribution of Pe (vanishing for low and high Pe and always smaller than 0.5).

This shows that the concentration profile exhibits an interesting combination of a long-range $1/r$ power-law decay (its amplitude Φ_0 being linearly dependent on the flow Q, see above), with an exponential dependence of the azimuthal shape on the Landau–Squire jet force F_p via Pe. Typical concentration profiles are shown in figure 2(*a*,*b*). We show for illustration a numerical calculation of the full concentration profile evolution with increasing pressure drop in figure 2(*c*). The latter is obtained by combining a finite-element solver for the LS flow following Secchi *et al.* (2016) and a finite-difference solver for the concentration profile in (2.1).

The general properties of the plume as observed in figure 2(*a*), namely the shape and aspect ratio, can be predicted from (2.7). For low Péclet number, the profile is isotropic (circular shape) with an aspect ratio close to unity. For large Péclet number, the concentration profile in (2.7) simplifies to $C(r,\theta) = (\Phi_0/4\pi D r)\exp[-(Pe/4)\theta^2]$, so that the aspect ratio of the plume is accordingly expected to scale sublinearly with the Péclet number, as $1/\bar{\theta} \sim Pe^{1/2}$ for $Pe \gg 1$.

Downloaded from https://www.cambridge.org/core. Ecole Supérieure de Chimie Physique Electronique de Lyon CPE, on 24 Aug 2017 at 08:31:43, subject to the Cambridge Core terms of use, available at https://www.cambridge.org/core/terms. https://doi.org/10.1017/jfm.2017.441

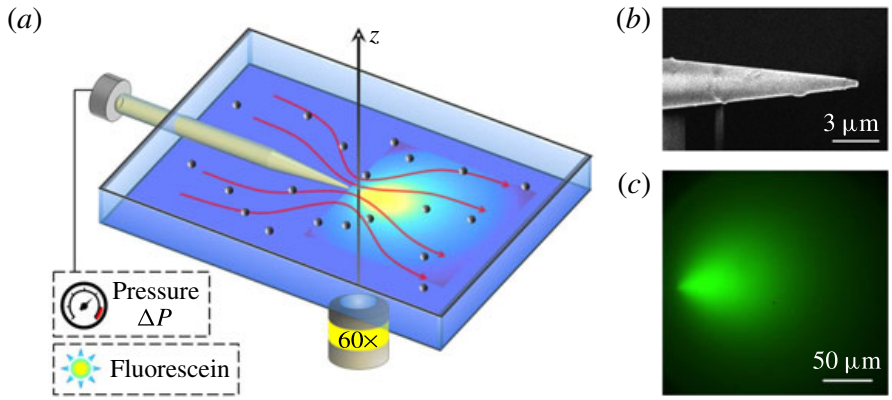

FIGURE 3. Sketch of the experimental set-up. (*a*) Sketch of the experimental set-up for the optical detection of the dye plume emerging from the nanocapillary, and imaging of the flow field via particle tracking of colloids. (*b*) Scanning electron microscope image of a typical glass nanocapillary. (*c*) The fluorescence signal emitted from fluorescein at 1.5 mM emerging from a nanocapillary with $R_1 = 120$ nm and $\gamma = 3°$ at $\Delta P = 1550$ mbar.

3. Experimental investigation of the Landau–Squire flow emerging from a glass nanocapillary

We now turn to an experimental study of the dispersion of a fluorescent dye emerging from a glass nanocapillary.

3.1. *Experimental set-up and procedure*

The experimental set-up is sketched in figure 3. The cell was composed of two macroscopic reservoirs bridged by a nanocapillary. A pressure drop was imposed on the (sealed) reservoir located at the rear, while the front reservoir was kept at ambient pressure. It was constituted of two glass slides, in order to allow visualization of the region in front of the nanocapillary tip. The glass slides were separated by a plastic frame, sealed via two Viton joints (of thickness 0.125 mm) and squeezed between the upper and lower parts of the chamber. The pressure was controlled by an AF1 microfluidic pressure pump from Elveflow.

Nanocapillaries were fabricated on the basis of pulled Pasteur pipettes. Glass capillaries were purchased from Sutter Instrument Company (standard wall borosilicate tubing, internal diameter 0.5 mm, external diameter 1 mm and length 10 cm) and were pulled using a programmable laser puller (P-2000 laser-based microcapillary puller, Sutter Instrument Company). The parameters of the capillary puller were finely tuned in order to fix the outer geometry of the nanocapillary tip and vary the dimension of the opening. The nanopore radius was measured with a scanning electron microscope (SEM, Nova Nanosem). The typical shape of a pulled nanocapillary is presented by the SEM image of the tip in figure 3(*b*).

Fluorescein (Sigma Aldrich) was dispersed in deionized water to a final concentration of 1.5 mM. NaOH was added to the deionized water to reach a pH equal to 8. The water was previously degassed and filtered with syringe filters with 0.2 μm pore size. The glass nanocapillaries were air-plasma treated for 5 min in a low-power plasma cleaner (Harrick Plasma) and immediately filled with the fluorescein solution. The nanocapillary was inserted into the holder and the cell was sealed. The glass reservoir was rinsed with deionized water. For the tracking experiments to characterize the LS

Downloaded from https://www.cambridge.org/core. Ecole Supérieure de Chimie Physique Electronique de Lyon CPE, on 24 Aug 2017 at 08:31:43, subject to the Cambridge Core terms of use, available at https://www.cambridge.org/core/terms. https://doi.org/10.1017/jfm.2017.441

flow, the reservoir was filled with a suspension of polystyrene particles (diameter 0.5 μm, Biovalley) at a volume fraction of $\phi = 10^{-5}$ at pH = 8.

The experimental set-up was mounted on the stage of an inverted optical microscope equipped with epifluorescence (Olympus IX71 equipped with a 60× long working distance objective). The particle tracking experiment was performed in bright-field configuration, while the fluorescein was imaged in epifluorescence configuration with an exposure of 200 ms. A constant pressure was applied to the reservoir at the rear of the capillary for a time interval varying from 1 to 10 min. Flow movies were recorded with a CMOS camera (Orca-Flash V 4.0, Hamamatsu, 16 bit, 2024 × 2024 pixels, 6.5 × 6.5 μm in size). For the particle tracking experiments, a typical run consisted of 8000–12 000 images, acquired with a frame rate of 200–320 f.p.s. and an exposure time of 1.5–3 ms. The procedure was repeated for several pressure values, varying from 20 to 1700 mbar, depending on the dimensions of the glass nanopore. For the plume imaging experiments, the frame rate was lower (typically 0.7 f.p.s.) due to the longer exposure (200 ms). A typical fluorescence plume is shown in figure 3(*c*).

3.2. *Landau–Squire flow data analysis*

Before exploring the fluorescent plume systematically, we first fully characterized the Landau–Squire flow in the reservoir. This was investigated with a standard velocimetry technique, using the polystyrene particles as colloid tracers. This follows the approach described in Secchi *et al.* (2016), and details of the experimental and numerical analysis may be found in the supplementary material of this reference. We recall briefly the method and outline the main results.

A region in front of the nanocapillary tip with dimensions $(\mathrm{d}x, \mathrm{d}y) = (45, 90)$ μm is selected. Image analysis is performed by in-house particle tracking algorithms. The optics has a depth of field comparable to the particle dimension and the algorithm analyses only the particles in focus. This allows the plane to be set at $z = 0$, and the distance from the nanocapillary tip is $r = \sqrt{x^2 + y^2}$. In this configuration, we obtain all the information on the 3D velocity field by analysing the 2D x–y plane passing through the centre of symmetry of the nanocapillary tip. We show in figure 4(*a*,*b*) a typical example for particle tracking, tracer trajectories, and corresponding velocities.

The particle tracking algorithm provides, for each particle, its position (x, y) and velocity components, $v_x(x, y)$ and $v_y(x, y)$. The Landau–Squire theory predicts $v = \sqrt{v_r^2 + v_\theta^2} = (F_P/4\pi\eta)(1/r'(\theta))$, with $r'(\theta) = r \times 2/\sqrt{1 + 3\cos^2\theta}$. Accordingly, for each position (x, y), we calculate $r'(\theta)$ and the velocity modulus v. We repeat the procedure for all of the trajectories. As shown in figure 4(*c*), a linear relation between v and $1/r'$ is measured, as expected from the Landau–Squire theory. The slope of the lines allows the jet force $F_P/4\pi\eta$ to be extracted.

From these experiments, we deduce the pressure dependence of the jet force F_P for a given nanocapillary. The several runs performed at each pressure allow us to check the stability of the flow during time. As an ultimate check, we also vary the dimensions of the analysed area $(\mathrm{d}x, \mathrm{d}y)$, in order to ensure that it does not impact the estimation of F_P. As a final note, it is also possible to analyse the flow in the plane $(x, y, z) = (0, y, z)$, accounting for the 3D nature of the hydrodynamic problem, and we find results in agreement with the Landau–Squire flow.

We finally note that once the F_P parameter is known for a given pressure ΔP, the flow rate Q can be deduced thanks to a proper calibration of α, via (1.2). This follows the approach introduced in Secchi *et al.* (2016), where details can be found in the supplementary material. We show, in particular, that α depends only on the opening

Downloaded from https://www.cambridge.org/core. Ecole Supérieure de Chimie Physique Electronique de Lyon CPE, on 24 Aug 2017 at 08:31:43, subject to the Cambridge Core terms of use, available at https://www.cambridge.org/core/terms. https://doi.org/10.1017/jfm.2017.441

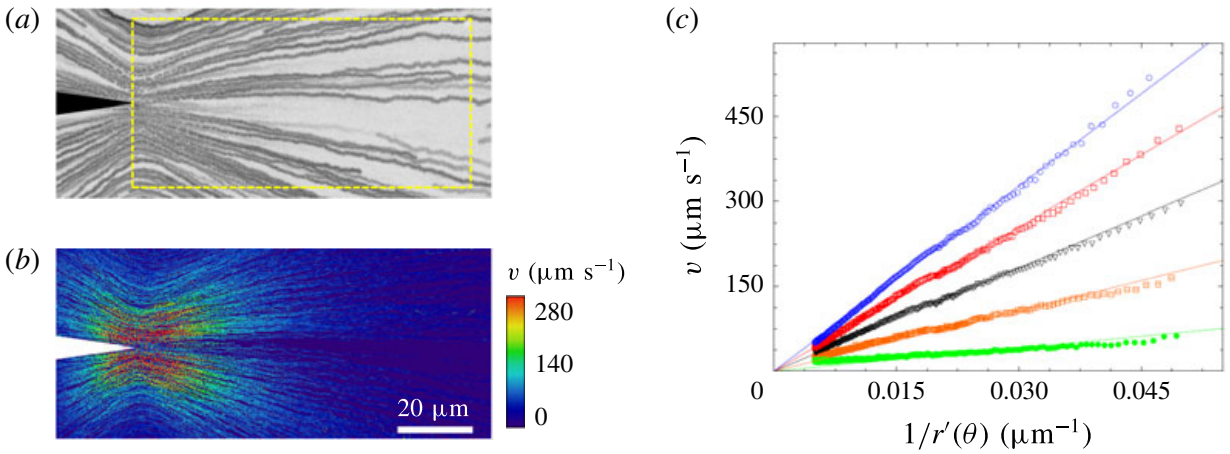

FIGURE 4. Velocimetry measurements of Landau–Squire jet flow. (*a*) Tracer trajectories outside a nanocapillary at $\Delta P = 140$ mbar, revealing a Landau–Squire jet flow. The dashed box highlights the region where image analysis is performed. (*b*) Velocity fields at $\Delta P = 140$ mbar. All data are obtained with a nanocapillary with $R_1 = 200$ nm and $\gamma = 9.7°$. (*c*) Particle velocity as a function of the position-dependent parameter $r'(\theta) = r \times 2/\sqrt{1+3\cos^2\theta}$ for various values of ΔP. From bottom to top, $\Delta P = 20$, 60, 100, 140 and 180 mbar. Here, the nanocapillary geometry is $R_1 = 320$ nm and $\gamma = 12°$. Continuous lines are fits using $v = F_P/(4\pi\eta) \times 1/r'$, allowing estimation of $F_P/4\pi\eta$.

angle γ of the nanocapillary: α is a decreasing function of the angle γ and vanishes as the opening angle γ reaches 90°. We find that in the region of aperture angles γ used in the experiments, the value of α varies between 0.7 and 1.0. However, once the geometry is known for a given nanocapillary (e.g. by SEM imaging), the value of α can be quantitatively predicted for this specific geometry with a 5 % indetermination; see the supplementary material in Secchi *et al.* (2016).

3.3. *Dispersion by the Landau–Squire flow field*

We now turn to the main question of this paper and investigate the dispersion of the fluorescein solution by the LS flow field. Once a pressure drop ΔP is established, a steady state is reached within a few seconds. We checked separately that at these concentrations, the fluorescence intensity maps may be directly correlated to the concentration map of fluorescein and bleaching does not affect our results. We show in figure 5(*a*) the evolution of the intensity signal at steady state with increasing pressure ΔP. The cloud of dispersing fluorescein is clearly distorted into a plume-like shape as the pressure increases, or equivalently as the Péclet number increases. A striking point is that the plume is observed to extend over hundreds of microns, three orders of magnitude larger than the typical nanocapillary aperture, with measurable asymmetry over very long length scales. This is quantified in figure 5(*b*), where the extension of the plume in both the longitudinal (Δx) and lateral (Δy) directions is plotted for various pressure drops, reaching 100 μm in the present conditions, while the nanocapillary aperture is 120 nm in this case. Here, the plume extension is obtained experimentally from an iso-intensity threshold, defined as the line where the detected intensity is half of the maximum intensity; see the red line in the inset of figure 5(*b*). In more detail, we plot in figure 5(*c*) the spatial evolution of the fluorescence intensity along the longitudinal axis in front of the nanocapillary (here normalized by a reference value I_{ref} in the absence of fluorescence). This is shown to

Downloaded from https://www.cambridge.org/core. Ecole Supérieure de Chimie Physique Electronique de Lyon CPE, on 24 Aug 2017 at 08:31:43, subject to the Cambridge Core terms of use, available at https://www.cambridge.org/core/terms. https://doi.org/10.1017/jfm.2017.441

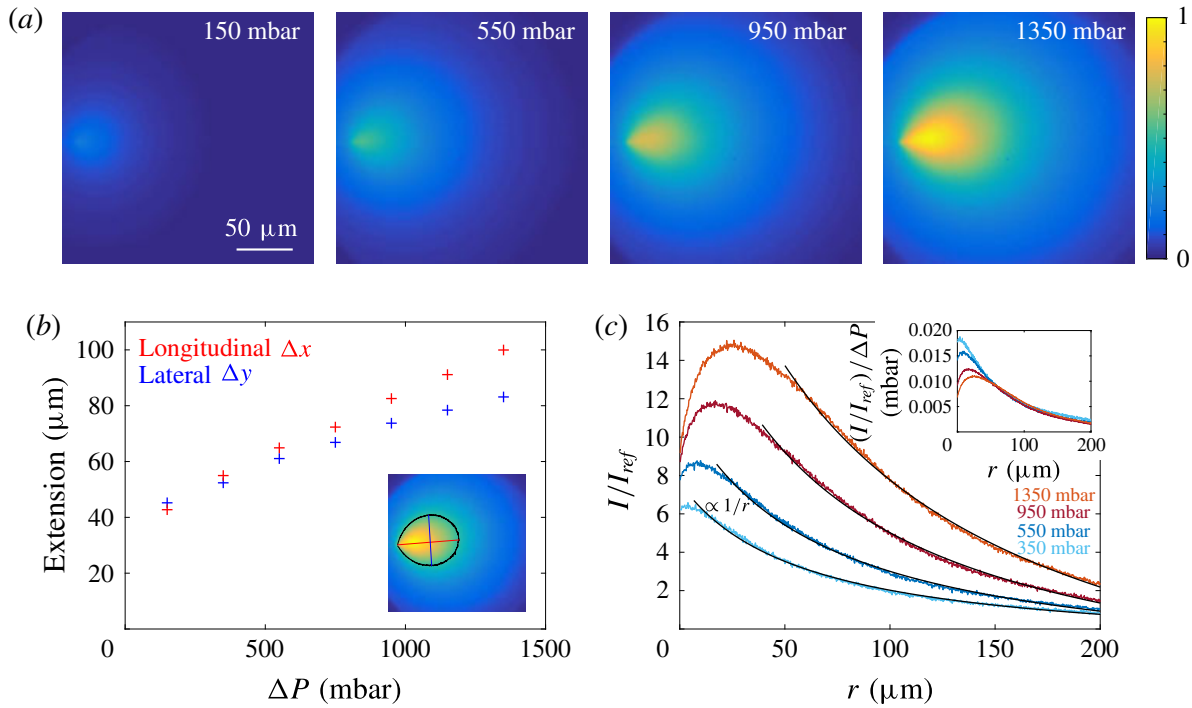

FIGURE 5. Experimental fluorescence profiles with increasing pressure drop. (*a*) Normalized fluorescence maps emerging from a nanocapillary in a deionized water reservoir at pH8, for increasing pressure drop ΔP. The intensity is normalized by the largest pixel intensity measured. The radius of the nanocapillary is $R_1 = 120$ nm and its opening angle is $\gamma = 3°$. (*b*) Longitudinal Δx and lateral Δy extension of the plume as a function of the pressure drop, defined as the longitudinal and lateral extensions (respectively red and blue lines in the inset) of the iso-intensity profile (black line) at maximum intensity of a given map over 2. (*c*) Intensity on the centre horizontal line in front of the nanocapillary for increasing pressure drop as a function of the distance r from the nanocapillary tip. The solid lines are $1/r$ fits. The inset shows the same profiles renormalized by the pressure drop.

exhibit a long-range decay, which is well fitted by the predicted $1/r$ spatial relaxation in the far field, according to (2.7) for $\theta = 0$. Furthermore, its amplitude is shown to scale with the pressure drop ΔP, as highlighted in the inset of figure 5(*c*). The discrepancy at short distances, with a non-monotonic dependence of the intensity, may be attributed to non-trivial point spread dispersion of the optical set-up, which we did not explore exhaustively in this paper.

Going further, more quantitative information on the flow can be obtained from the detailed shape of the iso-intensity lines. Indeed, according to the theoretical prediction in (2.7), the shape of an iso-intensity line is expected to verify

$$r(\theta) = r_{max} \times \exp\left[\frac{Pe}{2}(\cos\theta - 1)\right], \tag{3.1}$$

with $Pe = F_p/4\pi\eta D$ the Péclet number and r_{max} the maximal extension. In figure 6(*a*), we accordingly fit the normalized shape $r(\theta)/r_{max}$ for various pressure drops using this expression. As shown in figure 6(*a*), the profiles are well described by the theoretical prediction using the Péclet number as a single parameter for each pressure drop. Interestingly, the back-diffusion of the plume shape for $\theta = \pi$ is shown to vary strongly with the pressure drop, in particular for small ΔP; see figure 6(*a*). This is in

Downloaded from https://www.cambridge.org/core. Ecole Supérieure de Chimie Physique Electronique de Lyon CPE, on 24 Aug 2017 at 08:31:43, subject to the Cambridge Core terms of use, available at https://www.cambridge.org/core/terms. https://doi.org/10.1017/jfm.2017.441

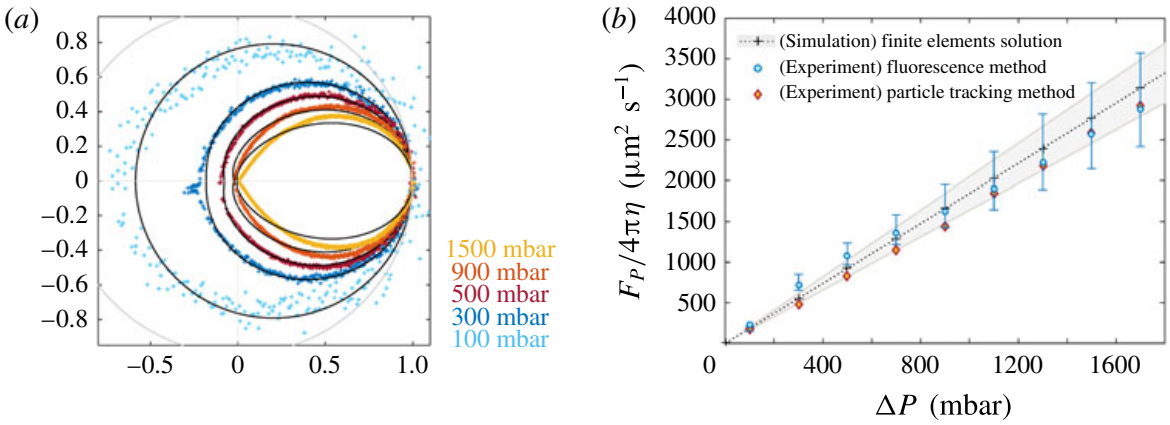

FIGURE 6. Experimental plume shapes and Péclet number. (*a*) Normalized iso-intensity profiles with increasing pressure drop (coloured dots). The profiles are fitted according to the theoretical prediction with *Pe* as the only fitting parameter (nanocapillary with $R_1 = 115$ nm and $\gamma = 3°$). The grey line is the unit circle. (*b*) The LS force parameter $F_p/4\pi\eta = D \times Pe$ for the same nanocapillary, measured from both fluorescence and velocimetry techniques plotted versus the pressure drop ΔP. For the fluorescence technique, F_P is deduced from the values of the Péclet number extracted from the fluorescence profiles in (*a*). For the velocimetry approach, it is extracted from the analysis of the LS flow, as in figure 4. We also report the results obtained from a finite-element calculation (crosses). The shaded area corresponds to a 0.5° uncertainty on γ. The error bars on the fluorescence technique are defined by the variability according to different iso-intensity values.

full agreement with the prediction $r(\theta = \pi)/r_{max} = \exp[-Pe]$ in (3.1). Back-diffusion provides, therefore, a sensitive probe of the Péclet number, in particular for low *Pe*.

In figure 6(*b*), we then plot the extracted LS force $F_p/4\pi\eta = D \times Pe$ as a function of the pressure drop ΔP, showing an expected linear dependence on pressure drop (for small pressure drop); D is the fluorescein diffusion coefficient ($D = 425$ μm^2 s^{-1} (Culbertson, Jacobson & Ramsey 2002)). To assess these results, we compare the pressure dependence of the LS force F_p with alternative measurements obtained from the direct tracking of colloidal particles; see § 3.2. The comparison between the two shows a very good agreement; see figure 6(*b*). For completeness, we also compare these values with the Stokes prediction in (1.2), with the parameter α obtained from numerical finite-element calculation for the nanocapillary geometry under consideration. The latter was obtained along the same lines as in Secchi *et al.* (2016), supplementary material. We emphasize that no fitting parameter is used to compute this estimate.

All three estimates are found to be in very good agreement, confirming that the fluorescence measurement is a proper tool to extract flow information in this Landau–Squire geometry.

4. Summary and concluding remarks

In this paper, we have explored experimentally and theoretically the plume generated by a dye dispersed from a jet flow emerging from the tip of a nanocapillary into a large reservoir, here named the Landau–Squire plume. We have analytically predicted and experimentally assessed the solute concentration profile in the form $C(r, \theta) \sim 1/r \times \mathrm{e}^{(Pe/2)(\cos\theta - 1)}$, where $Pe = F_p/4\pi\eta D$ is the Péclet number associated with the Landau–Squire flow. A key remark is that *Pe* depends only on the flow

Downloaded from https://www.cambridge.org/core. Ecole Supérieure de Chimie Physique Electronique de Lyon CPE, on 24 Aug 2017 at 08:31:43, subject to the Cambridge Core terms of use, available at https://www.cambridge.org/core/terms. https://doi.org/10.1017/jfm.2017.441

characteristics inside the tube, since $Pe \propto R_1 \overline{v}/D$ is defined in terms of the (nanoscale) tube properties, with $\overline{v}$ the averaged flow inside the tube with radius R_1.

The concentration profile thus combines a long-range $1/r$ power-law decay – with an amplitude linear in the flow rate Q – with an exponential dependence of the azimuthal plume shape on the Péclet number Pe. This contrasted dependence makes the shape of the dye plume very sensitive to the flow occurring inside the tube, while being measurable at very long distances from the tip, much longer than the characteristic tip size. This point is particularly obvious in figure 5, where the asymmetric plume extends over hundreds of microns, three orders of magnitude larger than the typical nanocapillary aperture. In practice, a useful remark is that the back-diffusion of the plume shape (for $\theta = \pi$) is exponentially dependent on the Péclet number and thus constitutes a sensitive measurement of Pe, in particular for low Péclet number. Altogether, the Landau–Squire plume bridges the gap between the nanoscale tube flow and the micron scales at which it can be easily characterized.

This feature is a key asset for the measurement of ultra-small flow rates occurring in nanoscale pipes thanks to the dye plume properties. Indeed, the criterion of detectability via the plume is that the Péclet number, which, we emphasize, is defined in terms of inner tube flow properties, is larger than unity. This criterion is much less stringent than direct velocimetry inside the nanochannel and is definitely reachable even for tubes with diameters in the range of nanometres (and even more for tubes that exhibit surface slippage such as carbon nanotubes; see Secchi *et al.* 2016).

Provided that they are successfully attached to the tip of the nanocapillary, the flow through various nanoporous systems can be investigated using analysis of the plume they generate, from small nanotubes to biology-inspired nanosystems like porins. Moreover, other sources of driving, like electro-osmosis or diffusio-osmosis, can also be explored using the same technique. The Landau–Squire plume is a powerful and versatile tool for nanofluidics.

Acknowledgements

We thank D. Stein and U. Keyser for fruitful discussions. E.S., A.N., S.M. and A.S. acknowledge funding from the European Union's H2020 Framework Programme/ERC Starting Grant agreement number 637748 – NanoSOFT. S.M. acknowledges funding from a J.-P. Aguilar grant. We acknowledge funding from ANR project BlueEnergy.

References

BOCQUET, L. & TABELING, E. 2014 Physics and technological aspects of nanofluidics. *Lab on a Chip* **14**, 3143–3158.

BRANTON, D., DEAMER, D. W., MARZIALI, A., BAYLEY, H., BENNER, S. A., BUTLER, T., DI VENTRA, M., GARAJ, S., HIBBS, A., HUANG, X. *et al.* 2008 The potential and challenges of nanopore sequencing. *Nat. Biotechnol.* **26**, 1146–1153.

CULBERTSON, C. T., JACOBSON, S. C. & RAMSEY, J. M. 2002 Diffusion coefficient measurements in microfluidic devices. *Talanta* **56** (2), 365–373.

FENG, J., GRAF, M., LIU, K., OVCHINNIKOV, D., DUMCENCO, D., HEIRANIAN, M., NANDIGANA, V., ALURU, N. R., KIS, A. & RADENOVIC, A. 2016 Single-layer MoS_2 nanopores as nanopower generators. *Nature* **536**, 197–200.

GENG, J., KIM, K., ZHANG, J., ESCALADA, A., TUNUGUNTLA, R., COMOLLI, L. R., ALLEN, F. I., SHNYROVA, A. V., CHO, K. R., MUNOZ, D. *et al.* 2014 Stochastic transport through carbon nanotubes in lipid bilayers and live cell membranes. *Nature* **514** (7524), 612–615.

Downloaded from https://www.cambridge.org/core. Ecole Supérieure de Chimie Physique Electronique de Lyon CPE, on 24 Aug 2017 at 08:31:43, subject to the Cambridge Core terms of use, available at https://www.cambridge.org/core/terms. https://doi.org/10.1017/jfm.2017.441

JOSHI, R. K., CARBONE, P., WANG, F.-C., KRAVETS, V. G., SU, Y., GRIGORIEVA, I. V., WU, H. A., GEIM, A. K. & NAIR, R. R. 2014 Precise and ultrafast molecular sieving through graphene oxide membranes. *Science* **343** (6172), 752–754.

LANDAU, L. D. & LIFSHITZ, E. M. 1959 *Fluid Mechanics*, chap. 2, pp. 81–83. Course of Theoretical Physics, vol. 6. Pergamon.

LAOHAKUNAKORN, N., GOLLNICK, B., MORENO-HERRERO, F., AARTS, D., DULLENS, R., GHOSAL, S. & KEYSER, U. 2013 A Landau–Squire nanojet. *Nano Lett.* **13** (11), 5141–5146.

PARK, H. G. & JUNG, Y. 2014 Carbon nanofluidics of rapid water transport for energy applications. *Chem. Soc. Rev.* **43** (2), 565–576.

SECCHI, E., NIGUES, A., JUBIN, L., SIRIA, A. & BOCQUET, L. 2016 Scaling behavior for ionic transport and its fluctuations in individual carbon nanotubes. *Phys. Rev. Lett.* **116**, 154501.

SECCHI, E., MARBACH, S., NIGUES, A., SIRIA, A. & BOCQUET, L. 2016 Massive radius-dependent flow slippage in carbon nanotubes. *Nature* **537**, 210–213.

SIRIA, A., PONCHARAL, P., BIANCE, A.-L., FULCRAND, R., BLASE, X., PURCELL, S. T. & BOCQUET, L. 2013 Giant osmotic energy conversion measured in a single transmembrane boron nitride nanotube. *Nature* **494** (7438), 455–458.

SQUIRE, H. B. 1951 The round laminar jet. *Q. J. Mech. Appl. Maths* **4** (3), 321–329.

STEIN, D. 2015 Nanopore sequencing: forcing improved resolution. *Biophys. J.* **109**, 2001–2002.

WERBER, J. R., OSUJI, C. O. & ELIMELECH, M. 2016 Materials for next-generation desalination and water purification membranes. *Nat. Rev. Mater.* **1**, 16018.

Downloaded from https://www.cambridge.org/core. Ecole Supérieure de Chimie Physique Electronique de Lyon CPE, on 24 Aug 2017 at 08:31:43, subject to the Cambridge Core terms of use, available at https://www.cambridge.org/core/terms. https://doi.org/10.1017/jfm.2017.441

THE JOURNAL OF CHEMICAL PHYSICS **147**, 154701 (2017)

Active sieving across driven nanopores for tunable selectivity

Sophie Marbach and Lydéric Bocquet[a)]
Laboratoire de Physique Statistique, UMR CNRS 8550, Ecole Normale Supérieure, PSL Research University, 24 Rue Lhomond, 75005 Paris, France

(Received 28 July 2017; accepted 18 September 2017; published online 17 October 2017)

Molecular separation traditionally relies on sieving processes across passive nanoporous membranes. Here we explore theoretically the concept of non-equilibrium active sieving. We investigate a simple model for an active noisy nanopore, where gating—in terms of size or charge—is externally driven at a tunable frequency. Our analytical and numerical results unveil a rich sieving diagram in terms of the forced gating frequency. Unexpectedly, the separation ability is strongly increased as compared to its passive (zero frequency) counterpart. It also points to the possibility of tuning dynamically the osmotic pressure. Active separation outperforms passive sieving and represents a promising avenue for advanced filtration. *Published by AIP Publishing.* https://doi.org/10.1063/1.4997993

I. INTRODUCTION

Filtering specific molecules is a challenge faced for numerous vital needs: from biomedical applications like dialysis to the intensive production of clean water.[1–3] Most modern processes for filtration are based on passive sieving principles: a membrane with specific pore properties allows us to separate the permeating components from the retentate. The domain has been boosted over the last two decades by the possibilities offered by nanoscale materials, such as graphene or advanced membranes.[4–12] Selectivity requires small and properly decorated pores at the scale of the targeted molecules, and this inevitably impedes the flux and transport, making separation processes costly in terms of energy. These traditional sieving membranes are also passive, therefore unable to adapt to external changes, like varying salt or contaminant concentrations in the liquid to filtrate. Furthermore while nature is able to distinguish quasi-similar ions, e.g., like sodium and potassium,[13] no artificial counterpart has been designed up to now to reach such a fine selectivity.

In this context, we explore the possibility of *active sieving*, harnessing non-equilibrium dynamics to separate particles across nanopores. A Maxwell demon is the (utopian) prototypical system able to perform separation on the basis of transfer of information.[14] However designing active pores that can distinguish between nanometer-scale molecules presents the obvious challenge of measuring *in situ* the proper information, i.e., fabricating feedback nanocontrollers.[15–17] Now one may consider a simpler situation of an active nanopore that can change its transmission properties with time thanks to an external energy input. This corresponds accordingly to a non-equilibrium situation, baring some analogy with active matter, which allows us to bypass to some extent the equilibrium constraints for better separation.

Here we explore a simple situation, where an external mechanical or electrical action modifies the pore properties, thus creating some blind, "crazy," Maxwell demon. Typical geometries of driven nanopores under consideration are sketched in Fig. 1: a driven nano-gate, a pore with a fluctuating size, or a pore whose surface charge may be externally gated. Such geometries are of special interest in the present study since they are amenable to further experimental investigations. To model separation across these systems, we build on the pioneering work of Zwanzig in Refs. 18 and 19, who considered the translocation rate of molecules through fluctuating pores. We consider as a supplementary ingredient that the opening of the nanopore is forced externally at a given frequency ω.

II. AN ACTIVE PORE MODEL

A. Effusion of solute through an active pore

We consider the effusion of a solute (with concentration C in a reservoir) across a nanopore. Pore gating that controls the translocation state across the nanopore is characterized by an internal parameter x: for example, the radius of the pore, the door opening, or the surface charge, see Fig. 1. In line with Zwanzig's model in Refs. 18 and 19, we assume that the solute concentration C relaxes according to the following leakage equation:

$$\frac{dC}{dt} = -K(x)C, \tag{1}$$

where $K(x)$ is the x-dependent leakage constant. It is proportional to the mobility of the solute. It also depends on the characteristics of the gating. For steric gating, x is merely geometrical: for the circular pore in Fig. 1(b), x is the radius r of the pore and $K(r) = k' r^2$, while for the nanodoor, x is the aperture of the door and $K(x) = k|x|$. For electric gating, when the pore is charged, see Fig. 1(c), x is proportional to the surface charge of the pore Σ, and for small nanopores, one may model $K(x) = k''\sqrt{1+x^2}$ (see Appendix A for details). The constant k (respectively, k' and k'') defines the mobility of the solute.

[a)]Electronic mail: lyderic.bocquet@lps.ens.fr

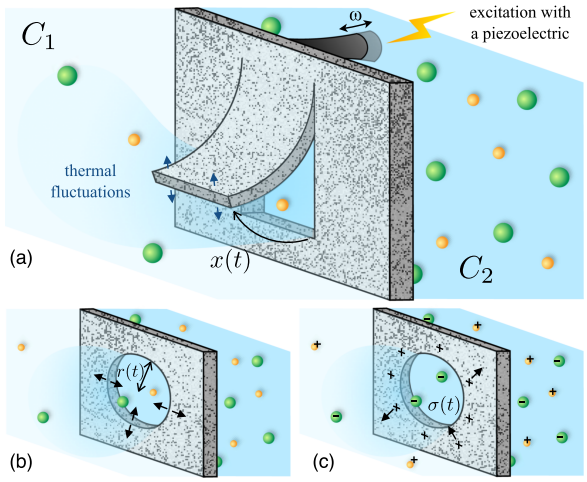

FIG. 1. (a) A driven nanodoor in a membrane, submitted to opening by thermal fluctuations and by external application of a periodic excitation. (b) Circular nanopore with fluctuating size and (c) with fluctuating charge.

We are interested in the separation of small sized particles (say, ions, colloids, polymers, etc.) effusing through nanometric sized pores. Accordingly the internal parameter x is further assumed to evolve dynamically due to (i) thermal noise, expected at the nanoscale, and (ii) some external forcing that drives an oscillation. To simplify the discussion, we assume that the nanopore is excited such that its *average* opening x oscillates at a frequency ω, and we further model the effects of thermal noise by a simple Langevin equation for the excess internal parameter $\delta x = x - \langle x \rangle$,

$$\begin{aligned} \langle x \rangle &= x_0(t) = x_0 \sin(\omega t), \\ \frac{d\,\delta x}{dt} &= -\lambda \delta x + F(t), \end{aligned} \tag{2}$$

where $F(t)$ is the Gaussian white noise. The second moment of δx is $\langle \delta x^2 \rangle = \theta$, and the fluctuation-dissipation theorem at equilibrium imposes $\langle F(t)F(t') \rangle = 2\theta\lambda\delta(t-t')$. The goal now is to obtain more information on the evolution of the solute concentration averaged over the noise: $\langle C(t) \rangle$.

B. From a rate process to the Smoluchowski equation

We turn to the equivalent Fokker-Planck—or Smoluchowski—equation for C. This derivation is inspired by Ref. 18. We denote $f(C,x,t)$ as the probability distribution that the variables C and x have specified values at time t. This function satisfies the Liouville equation

$$\frac{\partial f}{\partial t} = -\frac{\partial}{\partial C}\left(\frac{dC}{dt} f\right) - \frac{\partial \frac{dx}{dt} f}{\partial x} \tag{3}$$

or, substituting the velocities explicitly,

$$\begin{aligned} \frac{\partial f}{\partial t} &= -\frac{\partial}{\partial C}\left(-K(x)Cf\right) \\ &\quad - \frac{\partial\left(-\lambda(x-x_0)f + \frac{dx_0}{dt} f + F(t)f\right)}{\partial x}. \end{aligned} \tag{4}$$

Now we would like to average this stochastic Liouville equation to have the average of f over the noise: $g(C,r,t) = \langle f(C,r,t) \rangle_{\text{noise}}$. We may rewrite the Liouville equation in terms of an operator L such that Eq. (4) is

$$\frac{\partial f}{\partial t} = -Lf - \frac{\partial F(t) f}{\partial x}. \tag{5}$$

It integrates into

$$f(C,r,t) = e^{-tL} f(C,x,0) - \int_0^t ds e^{-(t-s)L} \frac{\partial F(s) f}{\partial x}, \tag{6}$$

which we use to rewrite the differential equation as

$$\frac{\partial f}{\partial t} = -Lf - \frac{\partial F(t)\left(e^{-tL} f(C,r,0) - \int_0^t ds e^{-(t-s)L} \frac{\partial F(s) f}{\partial x}\right)}{\partial x}. \tag{7}$$

Now we can safely average over the noise, using the Gaussian properties of $F(t)$, namely, $\langle F(t) \rangle = 0$ and $\langle F(t)F(t') \rangle = 2\theta\lambda\delta(t-t')$, which gives

$$\frac{\partial g}{\partial t} = -Lg + \frac{\partial \lambda\theta \frac{\partial g}{\partial x}}{\partial x}. \tag{8}$$

Now we look for the average value of C at time t and key feature x: $\bar{C}(x,t) = \int dC C g(C,x,t)$. This yields the following differential equation (Smoluchowski equation):

$$\frac{\partial \bar{C}}{\partial t} = -K(x)\bar{C} + \frac{\partial}{\partial x}\lambda\theta\frac{\partial \bar{C}}{\partial x} + \frac{\partial\left(\lambda(x-x_0) - \frac{dx_0}{dt}\right)\bar{C}}{\partial x}. \tag{9}$$

C. Permeance of the active pore

The time-dependent concentration $\langle C(t) \rangle$ is accordingly defined as $\int \bar{C}(x,t)dx = \langle C(t) \rangle$. For simplicity in the following, we consider that the noise damping parameter λ does not depend on x. The Smoluchowski equation, Eq. (9), can be solved analytically for some specific forms of $K(x)$ [in particular, for $K(x) \propto x^2$]. Alternatively we solve Eq. (9) numerically to deduce the time-dependent averaged concentration $\langle C(t) \rangle$. We show in Fig. 2 an example for the averaged concentration $\langle C(t) \rangle$, here in the case of a nanodoor where $K(x) = k|x|$ [Fig. 1(a)].

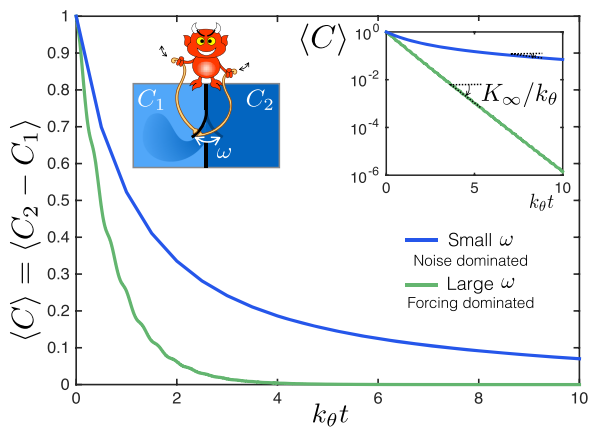

FIG. 2. Relaxation of the difference in concentration between the two sides of a nanodoor, averaged over noise. The data are a simulation result with $\lambda/k_\theta = 10^{-3}$, $\omega/k_\theta = 10^{-3}$, and $\omega/k_\theta = 1$. (*Inset, Left*) Illustration of a demon oscillating the nanodoor. (*Inset, Right*) Log scale of the previous graph and example of the extraction of the long time relaxation constant K_∞, the *permeance* of the system.

As a generic feature, one may show that $\langle C(t)\rangle$ is exponentially decaying at long times,

$$\langle C(t)\rangle \underset{t\to\infty}{\sim} \exp(-K_\infty t), \tag{10}$$

and this allows us to define the *permeance* K_∞ of the system. Fast translocation of the solute corresponds to a large K_∞. The permeance K_∞ depends on the thermal damping λ, noise amplitude θ, but also on the external forcing (frequency ω and amplitude x_0). In the following, our goal is to identify general rules on how the permeance depends on these antagonistic effects. Units of lengths are given by $\sqrt{\theta}$, while time is given in terms of a renormalized parameter k_θ with units of an inverse time: for the nanodoor, $k_\theta = k\sqrt{\theta}$, while for the nanopore, $k_\theta = k'\theta$.

III. TRANSPORT THROUGH THE ACTIVE PORE

Let us first focus on an oscillating circular pore, in which case the leakage law writes as $K(r) = k' r^2$, with r as the pore radius, see Fig. 1(b). We study fluctuations around the averaged forced radius $\langle r(t)\rangle = r_0(1+\epsilon\cos(\omega t))$ with a given amplitude $r_0\epsilon$. In this case, the Smoluchowski equation can be solved analytically (see Appendix B), and the expression for the permeance is written as

$$K_\infty(\omega) = \lambda/2\left(\left(1+\frac{4k'\theta}{\lambda}\right)^{1/2}-1\right)+k' r_0^2\left(1+\frac{4k'\theta}{\lambda}\right)^{-1} + k'\frac{r_0^2\epsilon^2}{2}\left(\frac{\left(1+\frac{4k'\theta}{\lambda}\right)^{-1}}{1+\left(\frac{\omega}{\omega_c(\lambda)}\right)^2}+\frac{\left(\frac{\omega}{\omega_c(\lambda)}\right)^2}{1+\left(\frac{\omega}{\omega_c(\lambda)}\right)^2}\right) \tag{11}$$

with $\omega_c(\lambda) = \sqrt{4k'\theta\lambda+\lambda^2}$ as the cutoff frequency. The first term in Eq. (11) corresponds to the solution for the non-forced case studied by Zwanzig in Ref. 19. In Zwanzig's derivation, only fluctuations of a bottleneck opening are considered (with a hard reflecting barrier at $r = 0$ so that only positive radii are considered). With $r_0 = 0$ and $\omega = 0$, one recovers exactly the exponential factor of Eq. (8) of Ref. 19. The last term corresponds to the supplementary leakage induced by the forced oscillations: it is the combination of a low-pass filter and a high-pass filter. The general behavior of $K_\infty(\omega)$ is plotted in Fig. 3(a). It exhibits complex features that are summarized in the diagram of Fig. 3(b). Although it is presented here only for the nanopore, the diagram is generic to all the systems investigated and represented in Fig. 1.

Let us discuss the various regimes at play. It is first interesting to explore the limiting behaviors at low damping. This regime is actually relevant for ionic or liquid separation systems;[4,20] see, for instance, the experimental study of biological channels in Ref. 21 which is consistent with the low damping limit relaxation with $\lambda \propto 1/\eta$, with η as the fluid viscosity. For low and high frequencies, we can calculate from Eq. (11) (at highest order)

$$\begin{aligned} K_\infty(\omega) &\underset{\substack{\omega\ll\omega_c\\ \lambda\ll k_\theta}}{\sim} \sqrt{k'\lambda\theta}, \\ K_\infty(\omega) &\underset{\substack{\omega\gg\omega_c\\ \lambda\ll k_\theta}}{\sim} k' r_0^2\epsilon^2/2. \end{aligned} \tag{12}$$

These results call for a generic physical interpretation. At high frequency, the forced oscillations become too quick for the thermal damping to rub them out and K_∞ reduces simply to its noise average: $K_\infty \simeq (\omega/2\pi)\int K[x_0(t)]dt$. This is the *forcing dominated regime*; see Fig. 3(d). The behavior at low forcing frequencies ω, where noise dominates [see Fig. 3(c)], is more subtle. According to Eq. (2), the gating variable will mainly diffuse with a diffusion coefficient $\mathcal{D}_x = \theta\lambda$. Over a time τ, the gating variable thus takes a typical value $\bar{x} \sim \sqrt{\mathcal{D}_x\tau}$. Now the passage time is itself fixed by K_∞^{-1} so that one gets a self-consistent estimate for K_∞ as

$$K_\infty \underset{\substack{\omega\ll\omega_c\\ \lambda\ll k_\theta}}{\simeq} K\left[\bar{x}\sim\sqrt{\frac{\lambda\theta}{K_\infty}}\right]. \tag{13}$$

For the circular nanopore, where x is the radius r and $K(r) = k' r^2$, one deduces accordingly $K_\infty \approx \sqrt{k'\lambda\theta}$ as obtained in

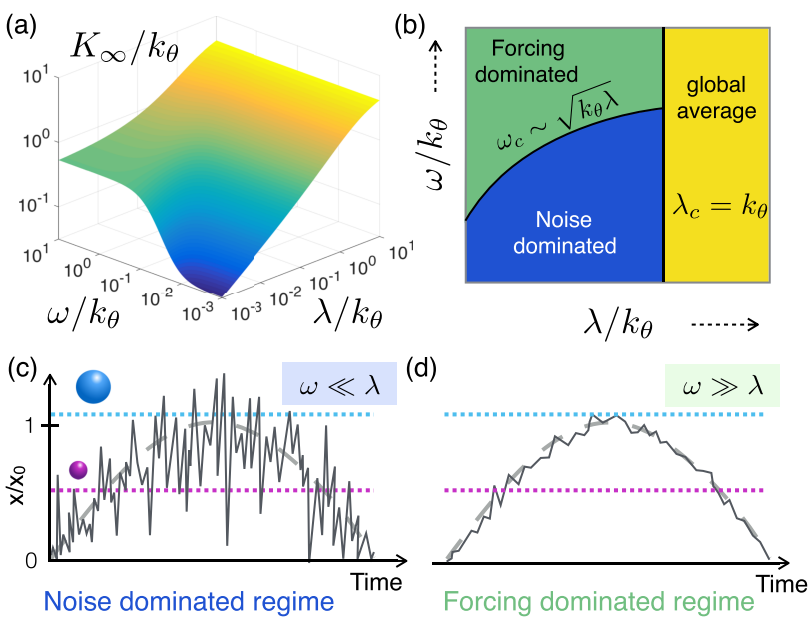

FIG. 3. (a) Analytical solution of the permeance K_∞ as a function of the forcing frequency ω and the thermal damping λ for the forced nanopore system ($r_0 = 2\sqrt{\theta}$ and $\epsilon = 0.5$). (b) Universal phase diagram of the permeance K_∞ with ω and λ. (c) Schematic of the door opening x/x_0 (solid black line) in the noise dominated regime, where $\omega \ll \lambda$, and (d) in the forcing dominated regime, where $\omega \gg \lambda$.

Eq. (12). This interpretation for K_∞ in Eq. (13) can be generalized to the other types of gates. For the nanodoor, for which $K(x) = k|x|$, Eq. (13) predicts $K_\infty \approx (k\lambda\theta)^{1/3}$, as can indeed be verified numerically (see Appendix C).

The transition between the low and high frequency regimes results from the competition between the forced oscillations and the noise. In Eq. (2) the thermal fluctuations $f(t)$ compete with the forced oscillations $dx_0(t)/dt \sim \omega x_0(t)$, and the crossover between the two regimes occurs accordingly when $f(t) \sim dx_0(t)/dt$. Using the fluctuation-dissipation theorem and taking a typical time scale $\tau \sim k_\theta^{-1}$, this yields $\omega_c(\lambda) \sim \sqrt{k_\theta \lambda}$ for the critical frequency. This estimation perfectly matches the scaling obtained numerically for all systems in Fig. 1 and also with the full analytical expression, Eq. (11), for the circular pore in Fig. 1(b).

IV. DYNAMICAL SELECTIVITY

A. Dynamical gating on mobility

The different scalings in Eq. (12) suggest further that the passage rate K_∞ exhibits a strongly contrasted dependence on the particle mobility (via k') in the low and high frequency regimes. Accordingly, at finite frequency, solutes with different mobilities will be separated by the active gate in a very different way as compared to the static (passive) nanopore.

This is highlighted in Figs. 4(a)–4(c), where we show the permeance of the nanopore to particles of different permeabilities, corresponding to particles with different k' (here $k_1/k_2 = 100$ for illustration). The selectivity of the pore, defined in terms of the ratio of the permeances of the two particles, is plotted in Fig. 4(c). What is striking in this plot is that the selectivity is a strongly dependent function of the frequency (and furthermore non-monotonous) so that the relative translocation rate of the two species can be finely tuned by the forcing frequency. This stems from the fact that the critical frequency ω_c for each particle is dependent on the particle mobility (via k'). Thus, a slower-diffusing particle will reach the forcing dominated regime at smaller frequencies. When the slower (blue) particle has just transitioned to the forcing dominated regime, the faster (purple) particle is still in the noise dominated regime, and the selectivity is reduced. This points to various non-trivial avenues for "on demand" sieving.

We emphasize that these results are not dependent on the choice of relative mobility, and here $k_1/k_2 = 100$ is chosen for readability. In a more realistic case of ionic separation, for instance, separating sodium and potassium, we would have $k^{(K^+)}/k^{(Na^+)} = 1.47$.[22] As a consequence, for low frequencies, the selectivity $K_\infty^{(K^+)}/K_\infty^{(Na^+)} \sim \sqrt{k^{(K^+)}/k^{(Na^+)}} \sim 1.21$, and at high frequencies, the selectivity increases: $K_\infty^{(K^+)}/K_\infty^{(Na^+)} \sim k^{(K^+)}/k^{(Na^+)} \sim 1.47$. Note that this does not depend on the value of the noise damping parameter λ: as long as noise is significant in the system, one will always find the critical frequencies from one regime to another.

B. Dynamical gating on size

This behavior is generic to all gatings described in Fig. 1. To highlight this generic feature, we conclude by considering the dynamical selectivity of the nanodoor, represented in Fig. 1(a), with a slightly modified gating process taking explicitly in consideration the effect of the finite size of the particle, see Fig. 4(d). We use a similar gating function as in Ref. 23 so that particles cannot pass if the opening x of the pore is smaller than their size x_p. We modify accordingly the leakage law of Eq. (1) to $K(x - x_p)\mathcal{H}(x - x_p)$, where $\mathcal{H}$ is the Heaviside function. For this leakage law, the Smoluchowski equation cannot be solved analytically and we turn to numerical solutions, see Appendix C. In Fig. 4(e) we compare the measured permeance for three particle sizes: an infinitely small particle (size 0 in grey), a small particle (in purple), and a large particle (in blue). As above, we deduce the corresponding selectivity factor for the two particles with different sizes as the ratio of their permeance. As obtained above for the other gating processes, we find a selectivity that is dependent on the frequency, here a strongly increasing function of the frequency.

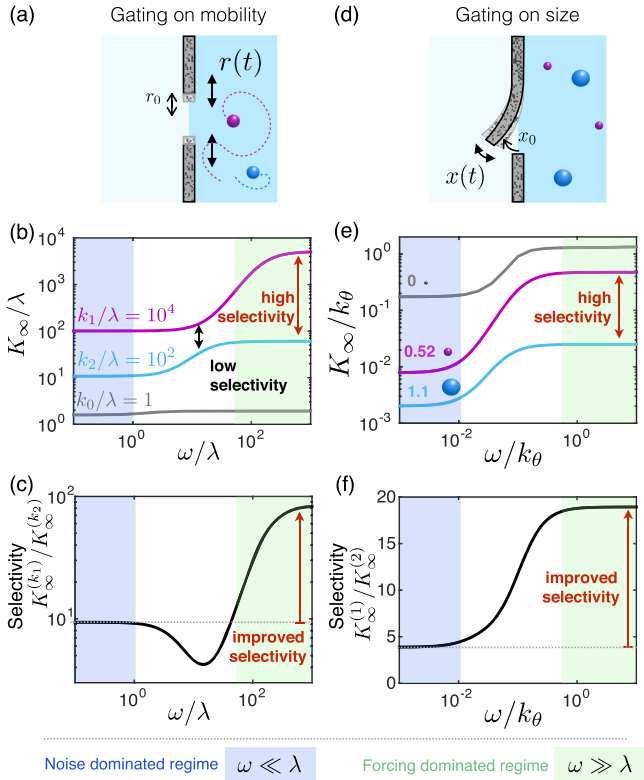

FIG. 4. (a) Schematic of gating through the fluctuating pore relying on mobility differences between particles. (b) Permeance K_∞/λ through the nanopore of two particles with mobility $k_1/\lambda = 10^4$ and $k_2/\lambda = 10^2$ as a function of the forcing frequency ω/λ, for small λ. (c) Selectivity of the nanopore to those particles, defined as the ratio of the permeances. (d) Schematic of gating through the fluctuating door relying on size differences between particles. (e) Permeance K_∞/k_θ through the nanodoor of two particles of different sizes (the smallest, purple, is $0.52x_0$ in radius and the largest, blue, is $1.1x_0$) as a function of the forcing frequency ω/k_θ, for small λ. (f) Selectivity of the nanodoor to those particles, defined as the ratio of their permeances.

V. DISCUSSIONS AND CONCLUSIONS

A. General conclusion

These results show that the selectivity of nanoporous membranes can finely be tuned by an externally forced

gating. Depending on the forcing frequency, dynamical gating allows us to better discriminate particles with different sizes or mobilities. As a rule, in the limit of low damping common in liquid or ionic filtration, an active pore is thus capable of filtering more precisely smaller particles than a standard passive filter with fixed pore size (at zero frequency). Also, in the high frequency regime, an active pore sieves particles in terms of their mobility, which is interesting to separate particles with similar size or charge (as would be needed for the separation of ions, for instance, for distinguishing sodium and potassium that have similar size and charge but different mobilities).[22] Although simple, our model provides a rich diagram, highlighting noise dominated or forcing dominated regimes, with specific selectivity rules. These selectivity properties may be tuned by adjusting the frequency of the excitation and rely on the strong interplay between noise and external excitation.

Numerous extensions can be obviously proposed for the model, which we now plan to explore exhaustively. The model could be easily exploited to explore the consequences of several extensions. If the noise damping parameter λ now depends on x, one expects the critical frequency ω_c and the limiting regimes to be modified in a non-trivial way. Furthermore, since the equations are not linear, when a non-monochromatic excitation is triggered, mode coupling will occur and may result into a broader variety of behaviors. Another underlying question in the prospect of possible applications of this research—in particular within the field of desalination and filtration—is that of the energy consumption of such a device. Obviously the active or dynamical part of the sieving requires some energy input; however, that energy input depends on the specific means of excitation and a detailed energy balance is required to predict the energy efficiency of such dynamical sieving process, a question which we leave for future work.

However the present results already suggest a number of developments for experimental implementations of active pores. Nanoporous materials with piezoelectric or piezomechanical response, e.g., metal organic frameworks,[24,25] are promising candidates in this goal. Furthermore, a nanodoor like in Fig. 1(a) can be designed by nanofabrication techniques, e.g., carving membranes at the sub-micron scale using a focused ion beam. Forcing at a tunable frequency, as well as supplementary white noise, can be provided by piezoelectric systems, allowing us to explore the various domains in the dynamical sieving diagram. These possibilities are a few examples for experimental realizations. They constitute natural routes for a proof of concept of the ideas presented here.

B. Towards an on-demand osmotic pressure

We conclude with a final comment on osmotic pressure. As highlighted by Kedem and Katchalsky in the context of membrane transport, there is an intimate symmetry link between permeance and osmosis.[26] A non-vanishing (respectively, vanishing) osmotic pressure is expressed for a semi-permeable (respectively, fully permeable) membrane. This link is highlighted by the generic expression for the osmotic pressure[26]

$$\Delta\Pi = \sigma \times k_B T \langle C \rangle \tag{14}$$

introducing the rejection coefficient σ, whose value is equal to 1 (respectively, 0) for a semi-permeable (respectively, fully permeable) membrane; for a finite permeance K_∞ of the membrane, one then expects $1 - \sigma \propto K_\infty$.[26] Going to dynamical sieving, the pore opening occurs intermittently with the frequency ω supplemented by thermal noise so that an intermittent osmotic pressure builds up. Let us explicit this link using the extended model with steric gating, with leakage law $K(x - x_p)\mathcal{H}(x - x_p)$ leading to an effective permeance $K_\infty(\omega|x_p)$. The corresponding solute flux $J_s = K_\infty\, \mathcal{V}\langle C \rangle$ (where $\mathcal{V}$ is the volume of the reservoir) can be identified to its definition $J_s = \overline{\mathcal{A}}\frac{D}{e}\kappa\langle C \rangle$, where $\overline{\mathcal{A}}$ is the average opening area of the pore, D is the diffusion coefficient of the solute, and e is the thickness of the membrane; the permeability coefficient κ is accordingly related to σ as $\kappa \propto 1 - \sigma$.[26] Gathering definitions, one thus obtains the dynamical rejection coefficient in terms of selectivity,

$$\sigma(\omega) = 1 - \frac{K_\infty(\omega|x_p)}{K_\infty(\omega|x_p = 0)}, \tag{15}$$

where the permeance of a particle with vanishing size $x_p = 0$ is used as normalization. This leads to a frequency dependent osmotic pressure, $\Delta\Pi(\omega) = \sigma(\omega) \times k_B T \langle C \rangle$. Note that this expression for the osmotic pressure is pertinent on time scales longer than the time-dependent forcing.

Our previous results for $K_\infty(\omega|x_p)$ show that $\Delta\Pi(\omega)$ is a strongly dependent function of ω via active sieving. This frequency dependence of the osmotic pressure is illustrated in Fig. 5 for various solutes. Tuning the frequency of the forcing therefore allows us to modify "on demand" the osmotic pressure across the active membrane. This opens new avenues in terms of separation for active and "on-demand" reverse osmosis.

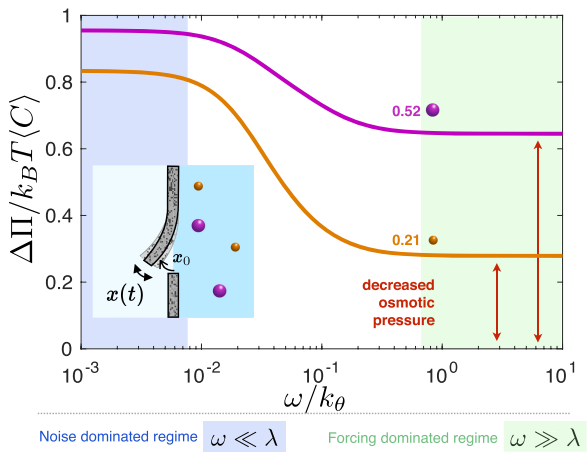

FIG. 5. Frequency dependent osmotic pressure through the nanodoor for two particles of different sizes (the largest, purple, is $0.52x_0$ in radius and the smallest, orange, is $0.21x_0$) as a function of the forcing frequency ω/k_θ for small λ. Inset: schematic of gating through the fluctuating door relying on size differences between particles.

ACKNOWLEDGMENTS

The authors thank R. Netz, A. Siria, and V. Kaiser for valuable discussions. S.M. acknowledges funding from a J.-P. Aguilar grant of the CFM foundation.

APPENDIX A: EXAMPLES OF RATE PROCESS LAWS

1. Strictly diffusion limited processes through pores

The initially concentrated reservoir has volume $\mathcal{V}$. The concentration at the scale of the pore is equilibrating over the typical thickness e of the pore with $\mathcal{A}$ as the pore's apparent section. We can write

$$\frac{dC}{dt} = -\frac{D}{\mathcal{V}e}\mathcal{A}C.$$

In the case of the nanodoor, $\mathcal{A} \sim x(h+w)$, where x is the opening depth of the door (see Fig. 1), h is the height of the door, and w is its width. As a consequence, we find

$$\frac{dC}{dt} = -k|x|C, \text{ with } \mathrm{k} = \frac{\mathrm{D(h+w)}}{\mathcal{V}\mathrm{e}} \tag{A1}$$

for the case of the nanodoor. We find that k is directly proportional to the mobility—or the diffusion coefficient—of the solute.

In the case of the circular pore $\mathcal{A} = \pi r^2$, where r is the radius of the circular pore. As a consequence, we find

$$\frac{dC}{dt} = -k' r^2 C, \text{ with } k' = \frac{D\pi}{\mathcal{V}\mathrm{e}} \tag{A2}$$

for the case of the circular pore. This is the expression used in Ref. 19.

2. Charge influenced rate process

Transport in a narrow charged channel of apparent section $\mathcal{A}$ can be described within the one-dimensional Nernst-Planck model from Ref. 27. For the linear response, the relation between generalized fluxes and potentials is expressed via a transport coefficient matrix,

$$\begin{pmatrix} I \\ \Phi_t \end{pmatrix} = \frac{\mathcal{A}}{e}\begin{pmatrix} K & \mu_K \\ \mu_K & \mu_{\mathrm{eff}} \end{pmatrix} \cdot \begin{pmatrix} -\Delta V \\ -kT\Delta(\log C_s) \end{pmatrix},$$

$$K = 2\mu q^2 \sqrt{C_s^2 + \left(\frac{\Sigma}{h}\right)^2},$$

$$\mu_{\mathrm{eff}} = 2\mu \sqrt{C_s^2 + \left(\frac{\Sigma}{h}\right)^2},$$

$$\mu_K = 2\mu q \frac{\Sigma}{h},$$

where Σ is the number of surface charge, h is the channel height, $\mu = \beta D$ is the ionic mobility, and q is the elementary charge.

We assume small initial concentration difference ΔC_s (around the value C_s) between two reservoirs of volume $\mathcal{V}$; therefore, we approximate $\Delta(\log C_s) \simeq (\Delta C_s)/C_s$. We apply no voltage difference; therefore, we focus on the equation

$$\frac{\mathrm{d}\Delta C_s}{\mathrm{d}t} = \frac{2\Phi_t}{\mathcal{V}} = -\frac{2\mathcal{A}}{e\mathcal{V}}\mu_{\mathrm{eff}} kT\Delta(\log C_s)$$
$$\simeq -\frac{4D\mathcal{A}}{e\mathcal{V}}\sqrt{1+\left(\frac{\Sigma}{hC_s}\right)^2}\Delta C_s$$

and finally

$$\frac{\mathrm{d}C}{\mathrm{d}t} = -k''\sqrt{1+\sigma^2}C, \tag{A3}$$

where we relabeled the variables ($\Delta C_s \to C$, $\Sigma/hC_s \to \sigma$) in the last equation and introduced the characteristic rate $k'' = 4D\mathcal{A}/e\mathcal{V}$. Note that σ is the Dukhin number for the channel.

APPENDIX B: EXACT SOLUTION OF THE RATE PROCESS FOR CIRCULAR NANOPORES

We consider the case where an external force excites the radius of the pore at the frequency ω around a non-zero mean value so that

$$\langle r(t)\rangle_{noise} = r_0(1+\varepsilon\sin(\omega t)). \tag{B1}$$

The Smoluchowski equation (9) becomes

$$\frac{\partial \bar{C}}{\partial t} = -kr^2\bar{C} + \lambda\theta\frac{\partial^2\bar{C}}{\partial r^2} + \frac{\partial}{\partial r}\left([\lambda(r - r_0(1+\varepsilon\sin(\omega t))) - r_0\varepsilon\omega\cos(\omega t)]\,\bar{C}\right). \tag{B2}$$

We assume that the probability distribution $\bar{C}$ initially has its equilibrium value in the absence of leakage, which simply writes as $\bar{C}(r,t=0) = \exp(-\frac{1}{2\theta}(r-r_0)^2)$.

We look for a solution writing as $\bar{C}(r,t) = \exp(a(t) + b(t)r - c(t)r^2)$. This yields the following system of equations:

$$\dot{a}(t) = -2\lambda\theta c + b^2\lambda\theta + \lambda - br_0(\varepsilon\omega\cos\omega t + \lambda(1+\varepsilon\sin\omega t)), \tag{B3a}$$

$$\dot{b}(t) = \lambda b - 4bc\theta\lambda + 2cr_0(\varepsilon\omega\cos\omega t + \lambda(1+\varepsilon\sin\omega t)), \tag{B3b}$$

$$\dot{c}(t) = k - 4c^2\lambda\theta + 2\lambda c. \tag{B3c}$$

We begin with Eq. (B3c) which has the general solution

$$c(t) = \frac{1}{4\theta}\left(1 + S\tanh\left(\lambda S(t-t_0)\right)\right),$$

where t_0 is a constant that can be computed thanks to initial conditions and $S = \left(1+\frac{4k\theta}{\lambda}\right)^{1/2}$. The initial conditions prescribe

$$c(t=0) = \frac{1}{2\theta} = \frac{1}{4\theta}\left(1 + S\tanh\left(-\lambda S t_0\right)\right)$$

so that $\mathrm{th}\,(-\lambda S t_0) = 1/S$. Replacing this result in the expression for c gives

$$c(t) = \frac{1}{4\theta}\left(\frac{2 + (S + 1/S)\tanh\lambda S t}{1 + 1/S\tanh\lambda S t}\right). \tag{B4}$$

The differential Eq. (B3b) is solved using the simple trick to write $b(t) = b_0(t)b_1(t)$, where $b_0(t)$ verifies the time

differential equation involving the terms depending on b only,

$$\dot{b}_0(t) = -\lambda b_0 \left(\frac{1 + S \tanh \lambda St}{1 + 1/S \tanh \lambda St} \right), \tag{B5}$$

and so $b_0(t) = 1/(S \cosh \lambda St + \sinh \lambda St)$. The equation on b_1 is then

$$\dot{b}_1(t) = 2c(t) r_0 (\varepsilon\omega \cos \omega t + \lambda(1 + \varepsilon \sin \omega t))/b_0(t) \tag{B6}$$

and we find the integration constant such that $b(t = 0) = r_0/\theta$. A lengthy but straightforward calculation leads to the solution of this equation as

$$\begin{aligned} b(t) = {} & \frac{r_0}{2S\,(S^2\lambda^2 + \omega^2)\;(S \cosh[St\lambda] + \sinh[St\lambda])} \cdots \\ & \times \Big((-1 + S^2)(\omega^2 + S^2\lambda(\lambda - \varepsilon\omega)) + \cosh[St\lambda] \cdots \\ & \times ((1 + S^2)(S^2\lambda^2 + \omega^2) + S^2(S^2 - 1)\varepsilon\lambda\omega \cos[\omega t] \\ & + S^2\epsilon((1 + S^2)\lambda^2 + 2\omega^2) \sin[\omega t]) \\ & + S(2(S^2\lambda^2 + \omega^2) + (-1 + S^2)\epsilon\lambda\omega \cos[\omega t] \\ & + \epsilon(\omega^2 + S^2(2\lambda^2 + \omega^2)) \sin[\omega t]) \sinh[St\lambda] \Big). \end{aligned} \tag{B7}$$

Using similar lines, one can also calculate the solution for $a(t)$ with the boundary condition $a(t = 0) = -r_0^2/(2\theta)$. The solution is not reported here because it is very lengthy.

We can now derive the average value on noise,

$$\left\langle \bar{C}(t) \right\rangle = \sqrt{\frac{\pi}{c(t)}} \exp\left(a(t) + \frac{b^2(t)}{4c(t)} \right). \tag{B8}$$

We then find that $\left\langle \bar{C}(t) \right\rangle$ behaves as

$$\left\langle \bar{C}(t) \right\rangle = \exp(-K_\infty(\omega)t + k_0(t)), \tag{B9}$$

where $k_0(t)$ is a small and periodic time contribution, which is sublinear in time and thus negligible for long time scales. $K_\infty(\omega)$ is the permeance and is such that

$$\left\langle \bar{C}(t) \right\rangle \underset{t\to\infty}{\sim} \exp(-K_\infty(\omega)t), \tag{B10}$$

with

$$K_\infty(\omega) = \lambda/2(S - 1) + kr_0^2 \left(\frac{1}{S^2} + \frac{\epsilon^2}{2} \frac{\lambda^2 + \omega^2}{S^2\lambda^2 + \omega^2} \right). \tag{B11}$$

By replacing $S = (1 + \frac{4k'\theta}{\lambda})^{1/2}$, we find exactly the result of Eq. (11).

APPENDIX C: NUMERICAL METHODS AND SOLUTIONS

1. Numerical methods

The Smoluchowski equations are solved with a finite difference scheme over 4 orders of magnitude of both ω and λ. Several methods are used to ensure global convergence.

- *Change in space variable.* We define $\tilde{C}(x, t) = \bar{C}(x - x_0(t), t)$ such that $\tilde{C}$ obeys a simpler Smoluchowski equation (no variation of the drift coefficient in time) and solve for $\tilde{C}$ instead of $\bar{C}$.
- *Logarithmic scale.* We define and solve for $\hat{C} = \log \tilde{C}$. This yields a non-linear equation, but the advantage is that high precision is gained—the initial condition is indeed a Gaussian and behaves much better (on a smaller number of orders of magnitude) in the Gaussian scale.
- *Partial Cranck-Nicholson.* We perform the Cranck Nicholson scheme on the linear part and explicit propagation on the non-linear part. Auto-adaptive time scale is used to check for convergence in time.
- The initial time step is chosen via a burning algorithm that allows us to adapt for any kind of parameters in the (ω, λ) parameter space.
- It was found that around a discretization of 1000 space steps usually gave reasonably convergent results. This number had to be adapted for different values in the parameter space anyway to ensure optimal convergence.
- K_∞ was computed as an average over several periods (usually 10) of the relaxation rate, after an initial reasonably long transient phase. A very small amount of configurations (less than 10 over 100 points), with high λ and small ω, would relax to numerically untractable small concentrations before a single oscillation period expired. Averaging over several periods was thus impossible. The data obtained for these very few very small frequencies were equated with the values obtained for higher frequencies at the same λ, for plotting purposes. At these high λ, K_∞ is not expected to depend on ω.

2. Systematic analysis in the absence of forcing

Limiting behaviors in the case of very high damping $\lambda \gg 1$, x has almost the equilibrium distribution at all times, and thus the transition ability can be approximated by

$$K_\infty \underset{\lambda\gg 1}{=} \int K(x)\rho_{eq}(x)dx. \tag{C1}$$

In the case of very low damping, we expect the following scaling discussed in the main paper:

$$K_\infty \underset{\lambda\ll 1}{=} K(\sqrt{\lambda/K_\infty}). \tag{C2}$$

Note that when the leakage law is a power law of the type $K(x) = |x|^n$, with n some integer, then one easily finds

$$K_\infty \sim \lambda^{\frac{n}{2+n}}. \tag{C3}$$

Equivalently, since the mobility λ depends inversely on the viscosity η of the fluid, $K_\infty \sim \eta^{-\frac{n}{2+n}}$.

In the following, we check these scaling laws for different rate processes. The results are summarized within the following paragraphs.

Quadratic rate process: Correspondence between simulations of the quadratic rate process and its exact solution was verified as a benchmark. We do not report this checking procedure here because it adds nothing to the discussion.

Linear rate process: In the following paragraph, we consider the leakage law associated typically with the nanodoor

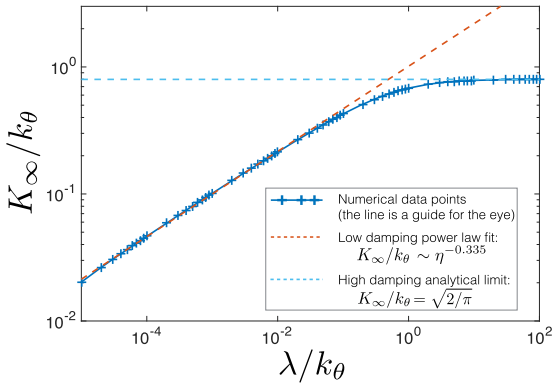

FIG. 6. Linear rate process permeance in the absence of forcing (nanodoor). Simulation results for the permeance K_∞ as a function of the thermal damping λ and comparison to analytical estimates. In this analysis, $k_\theta = k\sqrt{\theta}$. η is the viscosity of the fluid and is proportional to $1/\lambda$.

in Fig. 1(a), $K(x) = k|x|$. In Fig. 6 we show the permeance of the linear rate process as computed numerically. It verifies well the predicted low damping scaling law $K_\infty \sim \lambda^{1/3}$. The high damping limit is computed thanks to Eq. (C1) and is also in very good agreement with numerical calculations.

Note that in order to probe the previous scaling argument, $K_\infty \sim \lambda^{\frac{n}{2+n}}$, we also probed numerically other exponents in the leakage laws. For example, for a cubic leakage law ($n = 3$), the numerical resolution yields an exponent of 0.58, to compare with the analytic estimate of $3/(2+3) = 0.6$.

Charge regulated rate process: We finally consider the leakage law associated typically with the charged nanopore of Fig. 1(c), $K(\sigma) = k''\sqrt{1+\sigma^2}$. In Fig. 7 we show the permeance of the charge regulated process. The process has more features because in the present case θ accounts for the fluctuations of the (dimensionless) surface charge σ. In Fig. 7(a) we observe the permeance at different θ and find that for small λ and large θ, the system behaves as if it had an average leakage law behaving as $K(\sigma) \sim k'' + k''\sigma^2$, i.e., with an exponent $n = 2$. This correspondence is not obvious *a priori* but allows us to predict the scaling behavior for K_∞. Indeed, one may

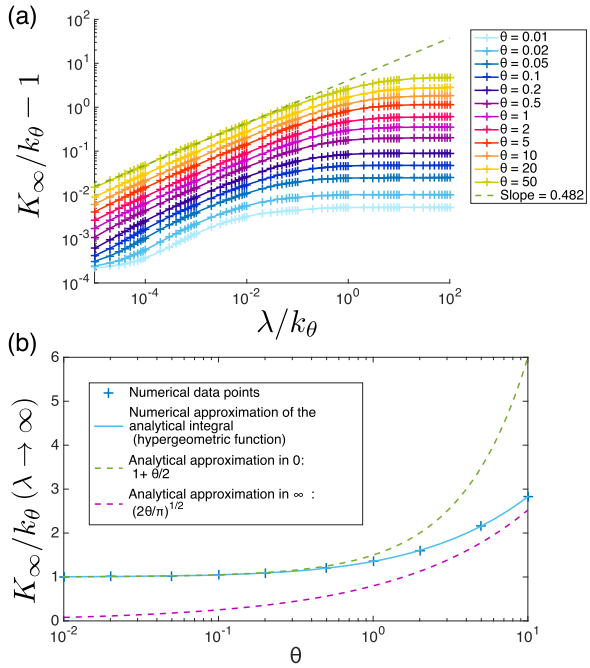

FIG. 7. Charge regulated rate process permeance in the absence of forcing. (a) Simulation results for the permeance K_∞ as a function of the thermal damping λ and comparison to analytical estimates. In this analysis, $k_\theta = k''$. θ is kept in the derivation and varied. The dashed green line verifies $K_\infty/k_\theta - 1 \propto (\lambda/k_\theta)^\beta$ with $\beta \simeq 0.482$. (b) Simulation results for the permeance K_∞ as a function of θ at high thermal damping λ and comparison to analytical estimates.

write that typically the diffusion time scales like $1/(K_\infty - 1)$, and one may then recover from Eq. (C1) that $K_\infty - 1 \sim \lambda^{1/2}$. This scaling prediction is confirmed numerically, see Fig. 7(a). In the regime of high damping, see Fig. 7(b), we find that the system is well described by the analytical expression Eq. (C1) for any θ.

3. Systematic analysis with forcing

We now perform simulations with an external forcing at frequency ω and check that we get for the different

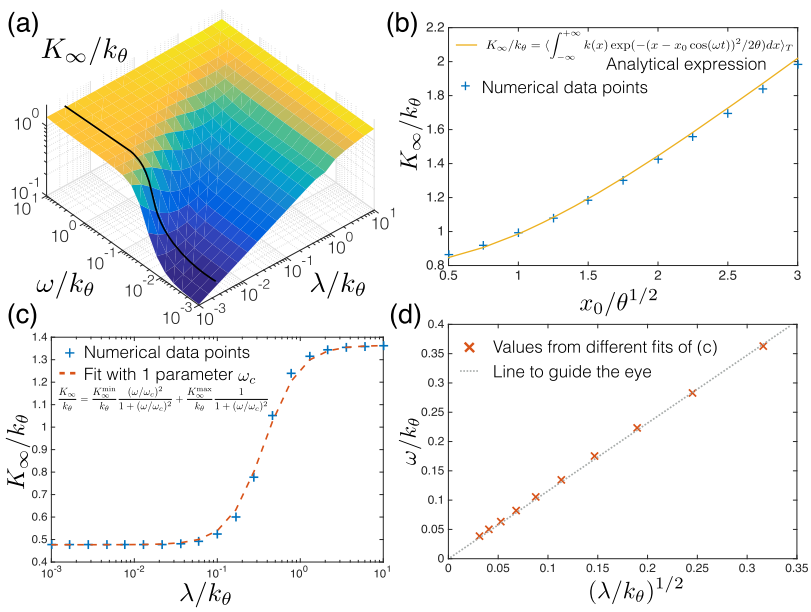

FIG. 8. Linear rate process permeance. (a) Simulation results for the permeance K_∞ as a function of the thermal damping λ and the forcing frequency ω and comparison to analytical estimates. In this analysis, $k_\theta = k\sqrt{\theta}$. The simulation parameter for oscillations around the origin is $x_0/\sqrt{\theta} = 2$. The black line indicates the fitting procedure at a given λ to find ω_c. (b) High plateau value for $\lambda/k_\theta = 10$ and $\omega/k_\theta = 0.1$ for different values of the ratio $x_0/\sqrt{\theta}$, where x_0 is the amplitude of the forcing $x_0(t) = x_0 \cos\omega t$. (c) Example of a filter fit to determine ω_c from the permeance as a function of ω at a fixed $\lambda = 0.1k_\theta$. The type of filter used is given in the legend and the only fitting parameter is ω_c. (d) Plot of ω_c as determined according to (c) as a function of $\sqrt{\lambda}$.

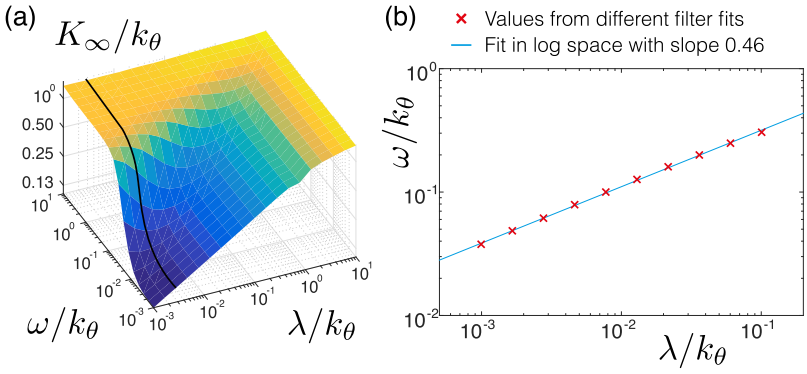

FIG. 9. Charge regulated rate process permeance. (a) Simulation results for the permeance K_∞ as a function of the thermal damping λ and the forcing frequency ω. In this analysis, $k_\theta = k''$. The simulation parameter for oscillations around the origin is $\sigma_0/\sqrt{\theta} = 2$, and $\theta = 1$. The black line indicates the fitting procedure at a given λ to find ω_c. (b) Plot of ω_c as determined from filter fits as a function of λ and power law fit.

systems (nanodoor and charged pore in Figs. 8 and 9) the same "universal features" as for the case of the circular pore. As for the circular nanopores, we indeed find 3 regimes: a forcing dominated regime, a noise dominated regime, and a global average regime, as described in the main text.

We also want to check some analytic scaling laws on the rate process theory with forcing at frequency ω. We have first considered the predicted scaling of the critical frequency with λ (see main text),

$$\omega_c(\lambda) \sim \sqrt{\lambda}. \tag{C4}$$

We performed a fit of each simulation (at constant λ) of K_∞ with the shape of a high pass filter (with a plateau at low frequencies) similar to the function H. We accordingly extract for each λ the value of ω_c and then find the scaling law between λ and ω_c. Overall we have verified that for all systems, the threshold frequency ω_c does obey this scaling law over a range of $\lambda \sim 10^{-3} \to 10^{-1}$.

Furthermore, we can check that the plateau value for the permeance at high λ matches the expected prediction assuming that x reaches its equilibrium distribution [see Fig. 8(b)]. Since the equilibrium distribution of x depends on t (it is periodic over a period $T = \frac{2\pi}{\omega}$), we should also average over a period. This writes as

$$K_\infty \underset{\lambda \gg 1}{=} \left\langle \int K(x)\rho_{eq}(x - x_0(t))dx \right\rangle_T . \tag{C5}$$

Quadratic rate process: As above, the correspondence between simulations of the quadratic rate process at various frequencies and its exact solution was verified before moving onto cases not solvable analytically. This test procedure is not shown here because it does not add to the discussion.

Linear rate process: In this paragraph, we consider the leakage law associated typically with the nanodoor of Fig. 1(a), $K(x) = k|x|$.

In Fig. 8(a) we show the permeance of the nanodoor system over 4 ranges of frequencies and damping. We find the three regimes of permeance (noise dominated regime in blue, forcing dominated regime in orange, and global average in yellow). The fitting procedure, described in Fig. 8(c), allows us to find ω_c for each λ. In Fig. 8(d) we plot ω_c as a function of $\sqrt{\lambda}$ and find a perfect agreement, which confirms the analytical prediction that $\omega_c \propto \sqrt{\lambda}$. The high plateau value [in yellow in Fig. 8(a)] for various forcing amplitudes is shown in Fig. 8(b) and agrees well with the prediction of Eq. (C5).

Charge regulated rate process: Finally we consider the leakage law associated typically with the charged nanopore in Fig. 1(c), $K(\sigma) = k''\sqrt{1+\sigma^2}$. In Fig. 9 we show the permeance of the charged pore over 4 orders of magnitude in frequency and damping. We find the three regimes of permeance (noise dominated regime in blue, forcing dominated regime in orange, and global average in yellow). The fitting procedure yields a typical dependence $\omega_c(\lambda) \sim \lambda^{0.46}$, see Fig. 9(b) very close to the analytical exponent (0.5).

[1] M. Elimelech and W. Phillip, "The future of seawater desalination: Energy, technology, and the environment," Science **333**, 712–717 (2011).
[2] L. Bocquet and P. Tabeling, "Physics and technological aspects of nanofluidics," Lab Chip **14**, 3143–3158 (2014).
[3] J. Werber, C. Osuji, and M. Elimelech, "Materials for next-generation desalination and water purification membranes," Nat. Rev. Mater. **1**, 16018 (2016).
[4] S. Y. Noskov, S. Berneche, and B. Roux, "Control of ion selectivity in potassium channels by electrostatic and dynamic properties of carbonyl ligands," Nature **431**, 830–834 (2004).
[5] T. Humplik, J. Lee, S. C. O'Hern, B. A. Fellman, M. A. Baig, S. F. Hassan, M. A. Atieh, F. Rahman, T. Laoui, R. Karnik, and E. N. Wang, "Nanostructured materials for water desalination," Nanotechnology **22**, 292001 (2011).
[6] J. Lee, T. Laoui, and R. Karnik, "Nanofluidic transport governed by the liquid/vapour interface," Nat. Nanotechnol. **9**, 317–323 (2014).
[7] J. K. Holt, H. G. Park, Y. Wang, M. Stadermann, A. B. Artyukhin, C. P. Grigoropoulos, A. Noy, and O. Bakajin, "Fast mass transport through sub-2-nanometer carbon nano-tubes," Science **312**, 1034 (2006).
[8] R. K. Joshi, P. Carbone, F. C. Wang, V. G. Kravets, Y. Su, I. V. Grigorieva, H. A. Wu, A. K. Geim, and R. R. Nair, "Precise and ultrafast molecular sieving through graphene oxide membranes," Science **343**, 752–754 (2014).
[9] A. Siria, P. Poncharal, A.-L. Biance, R. Fulcrand, X. Blase, S. T. Purcell, and L. Bocquet, "Giant osmotic energy conversion measured in a single transmembrane boron nitride nanotube," Nature **494**, 455–458 (2013).
[10] Z. Siwy and A. Fuliński, "Fabrication of a synthetic nanopore ion pump," Phys. Rev. Lett. **89**, 198103 (2002).
[11] C. B. Picallo, S. Gravelle, L. Joly, E. Charlaix, and L. Bocquet, "Nanofluidic osmotic diodes: Theory and molecular dynamics simulations," Phys. Rev. Lett. **111**, 244501 (2013).
[12] J. Feng, M. Graf, K. Liu, D. Ovchinnikov, D. Dumcenco, M. Heiranian, V. Nandigana, N. R. Aluru, A. Kis, and A. Radenovic, "Single-layer MoS_2 nanopores as nanopower generators," Nature **536**, 197 (2016).
[13] R. Greger and E. Schlatter, "Properties of the basolateral membrane of the cortical thick ascending limb of Henle's loop of rabbit kidney," Pfluegers Arch. Eur. J. Physiol. **396**, 325–334 (1983).
[14] L. Szilard, "Uber die entropieverminderung in einem thermodynamischen system bein eingriffen intelligenter wesen," Z. Phys. **53**, 840–856 (1929).
[15] B. Tavakol, M. Bozlar, C. Punckt, G. Froehlicher, H. A. Stone, I. A. Aksay, and D. P. Holmes, "Buckling of dielectric elastomeric plates for soft, electrically active microfluidic pumps," Soft Matter **10**, 4789–4794 (2014).

[16] J. Koski, V. Maisi, J. Pekola, and D. Averin, "Experimental realization of a Szilard engine with a single electron," Proc. Natl. Acad. Sci. U. S. A. **111**, 13786–13789 (2014).
[17] Y. Jun, M. Gavrilov, and J. Bechhoefer, "High-precision test of Landauer's principle in a feedback trap," Phys. Rev. Lett. **113**, 190601 (2014).
[18] R. Zwanzig, "Rate processes with dynamical disorder," Acc. Chem. Res. **23**, 148–152 (1990).
[19] R. Zwanzig, "Dynamical disorder: Passage through a fluctuating bottleneck," J. Chem. Phys. **97**, 3587–3589 (1992).
[20] E. Secchi, A. Niguès, L. Jubin, A. Siria, and L. Bocquet, "Scaling behavior for ionic transport and its fluctuations in individual carbon nanotubes," Phys. Rev. Lett. **116**, 154501 (2016).
[21] D. Beece, L. Eisenstein, H. Frauenfelder, D. Good, M. Marden, L. Reinisch, A. Reynolds, L. Sorensen, and K. Yue, "Solvent viscosity and protein dynamics," Biochemistry **19**, 5147–5157 (1980).
[22] D. R. Lide, *CRC Handbook of Chemistry and Physics, Volume 85* (CRC Press, 2004).
[23] N. Eizenberg and J. Klafter, "Molecular motion under stochastic gating," Chem. Phys. Lett. **243**, 9–14 (1995).
[24] D.-W. Fu, W. Zhang, and R.-G. Xiong, "The first metal–organic framework (MOF) of imazethapyr and its SHG, piezoelectric and ferroelectric properties," Dalton Trans. 3946–3948 (2008).
[25] A. U. Ortiz, A. Boutin, K. J. Gagnon, A. Clearfield, and F.-X. Coudert, "Remarkable pressure responses of metal–organic frameworks: Proton transfer and linker coiling in zinc alkyl gates," J. Am. Chem. Soc. **136**, 11540–11545 (2014).
[26] O. Kedem and A. Katchalsky, "Permeability of composite membranes. Part 1–3," Trans. Faraday Soc. **59**, 1918–1953 (1963).
[27] L. Bocquet and E. Charlaix, "Nanofluidics, from bulk to interfaces," Chem. Soc. Rev. **39**, 1073–1095 (2010).

Methods and references

Methods

1 Analytical Methods

1.1 Flow calculations

Drag on a sphere in the irrotational boundary condition flow

We compute the stress term for $\boldsymbol{F}_\varepsilon$ in Eq. 4.10:

$$\begin{aligned}
-\int_C \sigma(\boldsymbol{v}^0)\boldsymbol{n} &= \int_{\varphi=0}^{2\pi}\int_{\theta=0}^{\pi} \sin\theta d\theta d\varphi \left(\sigma_{r\theta}\boldsymbol{e}_\theta + \sigma_{rr}\boldsymbol{e}_r\right) \\
&= 3\int_{\varphi=0}^{2\pi}\int_{\theta=0}^{\pi} \sin\theta d\theta d\varphi \left(\cos\theta \boldsymbol{e}_r + \frac{\sin\theta}{2}\boldsymbol{e}_\theta\right) \\
&= 2\pi \int_{\theta=0}^{\pi} \sin\theta d\theta \left((9/2)\cos^2\theta - (3/2)\right)\boldsymbol{e}_z \\
&= 2\pi \left((3/2)[-\cos^3\theta]_0^\pi + 3/2[\cos\theta]_0^\pi\right)\boldsymbol{e}_z = \boldsymbol{0}
\end{aligned} \tag{3.1}$$

Mechanical energy dissipation in the irrotational boundary condition flow

We compute the integral of the full mechanical energy dissipation in the irrotational boundary condition flow. We have according to Eq. 4.6:

$$v_r = \left(1 - \frac{1}{r^3}\right)\cos\theta \quad \text{and} \quad v_\theta = -\left(1 + \frac{1}{2r^3}\right)\sin\theta. \tag{3.2}$$

and

$$\sigma_{r\theta} = \frac{1}{2}\left(\frac{-1}{r}\left(1 - \frac{1}{r^3}\right)\sin\theta + \frac{3}{2r^4}\sin\theta + \frac{1}{r}\left(1 + \frac{1}{2r^3}\right)\sin\theta\right) \tag{3.3}$$

and

$$\sigma_{rr} = -3\left(\frac{1}{r^4}\right)\cos\theta \tag{3.4}$$

and pressure field :

$$p = p_0 - \frac{1}{2}u^2 = p_0 - \frac{1}{2}\left(1 + \frac{1}{r^6}(1 - \frac{3}{4}\sin^2\theta) - \frac{1}{r^3}(2 - 3\sin^2\theta)\right). \tag{3.5}$$

We now compute the mechanical energy dissipation furnished by the sphere on the flow field:

$$\mathcal{P} = -2\pi \int_{\theta=0}^{\pi} v_\theta(r=1)\sigma_{r\theta}(r=1)\sin\theta d\theta + \lim_{R\to\infty} 2\pi R^2 \int_{\theta=0}^{\pi} \boldsymbol{v}(r=R)\boldsymbol{\sigma}_{.r}(r=R)\sin\theta d\theta \tag{3.6}$$

The first term was computed in the main derivation and now we compute the second term:

$$\begin{aligned}
\mathcal{P}_{\text{far}}(R) &= 2\pi R^2 \int_{\theta=0}^{\pi} \boldsymbol{v}(r=R)\boldsymbol{\sigma}_{.r}(r=R)\sin\theta d\theta \\
&= 2\pi R^2 \int_{\theta=0}^{\pi} (v_r\sigma_{rr}(r=R) + v_\theta\sigma_{r\theta})\sin\theta d\theta \\
&= 2\pi R^2 \left(-3\left(1-\frac{1}{R^3}\right)\frac{1}{R^4}\right)\int_{\theta=0}^{\pi}\cos^2\theta\sin\theta d\theta \\
&\qquad - 2\pi R^2\left(1+\frac{1}{2R^3}\right)\frac{1}{2}\left(\frac{-1}{R}\left(1-\frac{1}{R^3}\right)+\frac{3}{2R^4}+\frac{1}{R}\left(1+\frac{1}{2R^3}\right)\right)\int_{\theta=0}^{\pi}\sin^3\theta d\theta \\
&= O(1/R)
\end{aligned} \tag{3.7}$$

and thus the far field boundary term vanishes. Adding the contribution of the pressure field yields the same result.

Mechanical energy dissipation in the partial slip boundary condition flow

The analytical expression for the flow around a sphere can be found in the Stokes regime [235]:

$$v_r = \cos\theta\left(-\frac{1}{r}B + 2C + \frac{2D}{r^3}\right) \quad \text{and} \quad v_\theta = -\sin\theta\left(-\frac{1}{2r}B + 2C - \frac{D}{r^3}\right) \tag{3.8}$$

where $B = (3/2)\frac{1+2b}{1+3b}$ and $C = 1/2$ and $D = (1/4)\frac{1}{1+3b}$ with b the non-dimensional slip length. We compute the stress tensor components:

$$\begin{aligned}
\sigma_{r\theta} &= -\frac{\sin\theta}{2}\left(\left(-\frac{1}{r^2}B + 2C\frac{1}{r} + \frac{2D}{r^4}\right) + \left(\frac{1}{2r^2}B + \frac{3D}{r^4}\right) - \left(-\frac{1}{2r^2}B + 2C\frac{1}{r} - \frac{D}{r^4}\right)\right) \\
&= -3\sin\theta\frac{D}{r^4} \\
\sigma_{rr} &= \cos\theta\left(\frac{1}{r^2}B - \frac{6D}{r^4}\right)
\end{aligned} \tag{3.9}$$

Then we compute the power dissipated by the stresses of the object on the flow:

$$\begin{aligned}
\mathcal{P}_{\text{bound}} &= -6\pi\left(-\frac{1}{2}B + 2C - D\right)D\int_{\theta=0}^{\pi}\sin^3\theta d\theta \\
&= -3\pi\frac{b}{(1+3b)^2}
\end{aligned} \tag{3.10}$$

and going back to the dimensional scale gives the result in the main text. Now computing the far field yields:

$$\begin{aligned}\mathcal{P}_{\text{far}}(R) &= 2\pi R^2 \int_{\theta=0}^{\pi} \boldsymbol{v}(r=R)\boldsymbol{\sigma}_{.r}(r=R)\sin\theta d\theta \\ &= 6\pi R^2 \left(-\frac{1}{2R}B + 2C - \frac{D}{R^3}\right)\frac{D}{R^4}\int_{\theta=0}^{\pi}\sin^3\theta d\theta \\ &\quad + 2\pi R^2\left(\frac{1}{R^2}B - \frac{6D}{R^4}\right)\left(-\frac{1}{R}B + 2C + \frac{2D}{R^3}\right)\int_{\theta=0}^{\pi}\cos^2\theta\sin\theta d\theta\end{aligned} \tag{3.11}$$

and the only non vanishing term when $R \to \infty$ is:

$$\begin{aligned}\mathcal{P}_{\text{far}}(R) &\underset{R\to\infty}{=} 4\pi BC\int_{\theta=0}^{\pi}\cos^2\theta\sin\theta d\theta \\ \mathcal{P}_{\text{far}}(R) &\underset{R\to\infty}{=} 2\pi\frac{1+2b}{1+3b}\end{aligned} \tag{3.12}$$

and going back to the non-dimensional scale: $\mathcal{P}_{\text{far}} = 4\pi\mu U^2 a\frac{1+2b/a}{1+3b/a}$. Adding the contribution of the pressure field yields: $\mathcal{P}_{\text{far}} = 6\pi\mu U^2 a\frac{1+2b/a}{1+3b/a} = \mathcal{F}U$ such that the stresses in the far field generate exactly the energy that compensates for the force acting on the sphere (in the reference of the flow).

Note that the entire derivation may be done in the reference frame of the particle – where the fluid is at rest at infinity. Using the expressions for the velocity field in this regime [431] yields the same result – the far field dissipation vanishes, and the contribution of the power linked to the fact that the sphere is submitted to a force arises from the boundary of the sphere.

1.2 From a noisy process to a Schmoluchowski equations

We establish the equivalent Fokker-Planck – or Smoluchowski – equation for concentration C, where C is submitted to the rate process Eq. 1.1 and Eq. 1.2. This derivation is inspired by [335]. We denote $f(C,x,t)$ the probability distribution that the variables C and x have specified values at time t. This function satisfies a Liouville equation:

$$\frac{\partial f}{\partial t} = -\frac{\partial}{\partial C}\left(\frac{dC}{dt}f\right) - \frac{\partial\frac{dx}{dt}f}{\partial x} \tag{3.13}$$

or, putting in the velocities explicitly,

$$\begin{aligned}\frac{\partial f}{\partial t} = &-\frac{\partial}{\partial C}\left(-K(x)Cf\right) \\ &-\frac{\partial\left(-\lambda(x-x_0)f + \frac{dx_0}{dt}f + F(t)f\right)}{\partial x}.\end{aligned} \tag{3.14}$$

Now we would like to average this stochastic Liouville equation to have the average of f over the noise: $g(C,r,t) = \langle f(C,r,t)\rangle_{\text{noise}}$. We may rewrite the Liouville equation in terms of an

operator L such that Eq. 3.14 is:

$$\frac{\partial f}{\partial t} = -Lf - \frac{\partial F(t) f}{\partial x}. \tag{3.15}$$

It integrates into:

$$f(C,r,t) = e^{-tL} f(C,x,0) - \int_0^t ds e^{-(t-s)L} \frac{\partial F(s) f}{\partial x} \tag{3.16}$$

that we use to rewrite the differential equation as:

$$\frac{\partial f}{\partial t} = -Lf - \frac{\partial F(t) \left(e^{-tL} f(C,r,0) - \int_0^t ds e^{-(t-s)L} \frac{\partial F(s) f}{\partial x} \right)}{\partial x}. \tag{3.17}$$

Now we can safely average over the noise, using the gaussian properties of $F(t)$, namely $\langle F(t) \rangle = 0$ and $\langle F(t) F(t') \rangle = 2\theta\lambda\delta(t-t')$, which gives:

$$\frac{\partial g}{\partial t} = -Lg + \frac{\partial \lambda\theta \frac{\partial g}{\partial x}}{\partial x} \tag{3.18}$$

Now we look for the average value of C at time t and key feature x: $\bar{C}(x,t) = \int dC C g(C,x,t)$. This yields the following differential equation (Schmoluchowski equation):

$$\frac{\partial \bar{C}}{\partial t} = -K(x)\bar{C} + \frac{\partial}{\partial x} \lambda\theta \frac{\partial \bar{C}}{\partial x} + \frac{\partial \left(\lambda(x - x_0) - \frac{dx_0}{dt} \right) \bar{C}}{\partial x} \tag{3.19}$$

1.3 Perturbative theory for the computation of the effective diffusion coefficient in a fluctuating nanoslit

Set up of the initial theory

To simplify further notations we write to first order in the height fluctuations $f_u = \overline{v_x} + D_0 \frac{\partial h}{\partial x}/H$, the total drift in the x direction from the Fokker-Planck equation Eq. 2.1. and drop the $.^\star$ on the marginal probability distribution function for notational convenience. For the initial condition where a particle starts at $x = 0$ at $t = 0$, we can rewrite Eq. 2.1 as:

$$\frac{\partial p}{\partial t} = -\frac{\partial (f_u p)}{\partial x} + D_0 \frac{\partial^2 p}{\partial x^2} + \delta(x)\delta(t) \tag{3.20}$$

We define space-time Fourier transform of the solution by:

$$\tilde{p}(k,\omega) = \int_{-\infty}^{+\infty} dt e^{-i\omega t} \int_{-\infty}^{+\infty} dx e^{-ikx} p(x,t) \tag{3.21}$$

and note the inverse Fourier transform formula :

$$p(x,t) = \int_{-\infty}^{+\infty} \frac{d\omega}{2\pi} e^{i\omega t} \int_{-\infty}^{+\infty} \frac{dk}{2\pi} e^{ikx} \tilde{p}(k,\omega). \tag{3.22}$$

We take the Fourier transform of Eq. 3.20 which gives:

$$i\omega\tilde{p}(k,\omega) = -D_0k^2\tilde{p}(k,\omega) - i\iint \frac{d\nu dq}{(2\pi)^2} k\tilde{f}_u(q,\omega-\nu)\tilde{p}(k-q,\nu) + 1 \tag{3.23}$$

that can be written as:

$$i\omega\tilde{p}(k,\omega) = \tilde{p_0}(k,\omega) - i\tilde{p_0}(k,\omega)\iint \frac{d\nu dq}{(2\pi)^2} k\tilde{f}_u(q,\nu)\tilde{p}(k-q,\omega-\nu) \tag{3.24}$$

where

$$\tilde{p_0}(k,\omega) = \frac{1}{D_0k^2 + i\omega} \tag{3.25}$$

is interpreted as the free-diffusion propagator, i.e. the solution of Eq. 2.1 in the absence of drift *i.e.* when $f_u = 0$. It is this solution about which we are going to construct a perturbation theory. For now we restrict ourselves to the case where the effective drift vanishes (which is true in the case of noise on the interface) and look for the effective diffusion constant of the perturbed solution. The solution to the Fokker-Planck Eq. 3.20 for large t and x should thus have the normal diffusive form but with an effective diffusion constant. In Fourier space this means

$$\tilde{p}(k,\omega) \sim \frac{1}{D_ek^2 + i\omega} \quad \text{for} \quad k,\omega \to 0 \tag{3.26}$$

from which we see that the effective diffusion coefficient D_e can be read off by taking the "static" part of the diffusion propagator ($\omega = 0$) via:

$$\tilde{p}(k,0) \sim \frac{1}{D_ek^2} \quad \text{for} \quad k \to 0 \tag{3.27}$$

Towards the perturbative scheme : non-averaged perturbation theory

In the following section we develop a perturbation expansion to find a solution to Eq. 3.24. The idea is that the drift f_u is a small added contribution (typically in h/H). The perturbation scheme applies actually for any type of drift f_u (though here the drift is explicitly known). We perform this expansion diagrammatically using Feynman diagrams. We represent the free diffusion propagator $\tilde{p_0}(k,\omega)$ as a line with a 2-momentum $K = (k,\omega)$ flowing through it as shown in Fig. 3.1 while the full propagator $\tilde{p}(k,\omega)$ is shown using a thick line.

The Eq. 3.24 can be presented diagrammatically in the following way. To represent the second term on the right hand side of Eq. 3.24 we use a vertex interaction: the ondulated line represents $-ik\tilde{f}_x(Q)/(2\pi)^2$ and the upward 2-momentum Q is integrated over. Notice that the total 2-momentum is conserved, we have K flowing in and Q flowing up such that $K - Q$ is flowing out through the thick line.

Iterating the equation expressed by this diagrammatic representation generates the diagrams shown in Fig. 3.2.

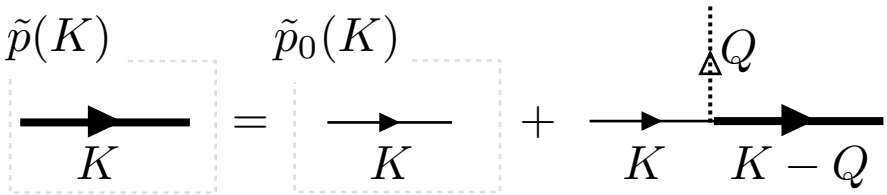

Fig. 3.1: Diagrammatic representation of the Fourier transform of the main Fokker Planck Eq. 3.24

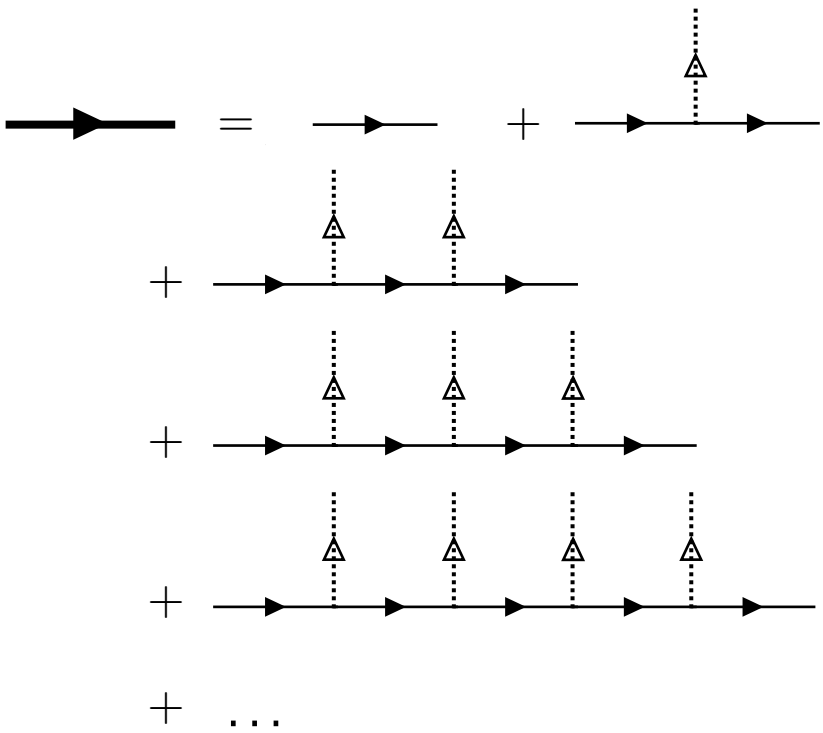

Fig. 3.2: Diagrammatic expansion of the Fourier transform of the main Fokker Planck Eq. 3.24.

Noise-averaged perturbation theory

To proceed we assume that the effective diffusion constant can be read off from the noise-averaged propagator $\langle \tilde{p}(k,\omega)\rangle$. We will assume that the field f_u is Gaussian with zero mean and a short range correlation function invariant under translations in space and time, given by

$$C(x-x', t-t') = \langle f_u(x,t) f_u(x',t')\rangle. \tag{3.28}$$

In the following the field f_u will indeed verify this hypothesis. From there one can see that the correlation function of the Fourier transform of the total drift is:

$$(2\pi)^2 \delta(k+k')\delta(\omega+\omega')\tilde{C}(k,\omega) = \langle \tilde{f}_u(k,\omega)\tilde{f}_u(k',\omega')\rangle \tag{3.29}$$

or in terms of the 2-momentum K:

$$(2\pi)^2\delta(K+K')\tilde{C}(K) = \langle \tilde{f}_u(K)\tilde{f}_u(K')\rangle. \tag{3.30}$$

We write the diagrammatic expansion of $\tilde{p}(K)$ as

$$\tilde{p}(K) = \tilde{p}_0(K) + \tilde{p}_1(K) + \tilde{p}_2(K) + \tilde{p}_3(K) + \tilde{p}_4(K) + ..., \tag{3.31}$$

we can carry out the noise-averaging term by term. Since the field f_u is gaussian with zero average, we find easily that $\langle \tilde{p}_1(K)\rangle = 0$ and also $\langle \tilde{p}_n(K)\rangle = 0$ for any n odd. The first non-zero term for $n > 1$ is the term

$$\begin{aligned}\langle \tilde{p}_2(K)\rangle &= (-i)^2\tilde{p}_0(K)\int \frac{dQdQ'}{(2\pi)^4}k(k-q)\tilde{C}(Q)(2\pi)^2\delta(Q+Q')\tilde{p}_0(K-Q)\tilde{p}_0(K-Q-Q') \\ &= (-i)^2\tilde{p}_0(K)\int \frac{dQ}{(2\pi)^2}k(k-q)\tilde{C}(Q)\tilde{p}_0(K-Q)\tilde{p}_0(K)\end{aligned} \tag{3.32}$$

where we see that 2-momentum Q leaving the first vertex is actually equal to the $-Q'$ the 2-momentum leaving the second vertex. Diagrammatically this is shown in Fig. 3.3 where the line connecting the two vertices now carries a factor $(-i)^2k(k-q)\tilde{C}(q)/(2\pi)^2$. The order 4 term $\langle \tilde{p}_4(K)\rangle$ is shown in Fig. 3.3. Note that there are 3 diagrams according to Wick's theorem. Note that the first diagram of $\tilde{p}_4(K)$ can easily be resummed, while the others not. We keep diagrams that can be resumed in the expansion (the others can actually be discarded at each step because they have lower contributions in $1/k$).

The full propagator can thus we written as a geometric series:

$$\begin{aligned}\tilde{p}(K) &= \tilde{p}_0(K) + \tilde{p}_0(K)\Sigma(K)\tilde{p}_0(K) + \tilde{p}_0(K)\Sigma(K)\tilde{p}_0(K)\Sigma(K)\tilde{p}_0(K) + ... \\ &= \frac{\tilde{p}_0(K)}{1-\Sigma(K)\tilde{p}_0(K)} = \frac{1}{\tilde{p}_0^{-1}(K)-\Sigma(K)}\end{aligned} \tag{3.33}$$

where

$$\Sigma(k,\omega) = (-i)^2\iint \frac{dqd\nu}{(2\pi)^2}\frac{k(k-q)\tilde{C}(q,\nu)}{D_0(k-q)^2 - i(\nu-\omega)}. \tag{3.34}$$

Examining Eq. 3.33 shows that the effective diffusion coefficient can be deduced from $\Sigma(K)$ via

$$\boxed{D_e = D_0 - \lim_{k\to 0}\frac{\Sigma(k,0)}{k^2}} \tag{3.35}$$

Effective diffusion coefficient

We write the incompressibility condition on the fluid

$$\frac{\partial(H+h(x,t))\overline{v_x}(x,t)}{\partial x} = -\frac{\partial h(x,t)}{\partial t} \tag{3.36}$$

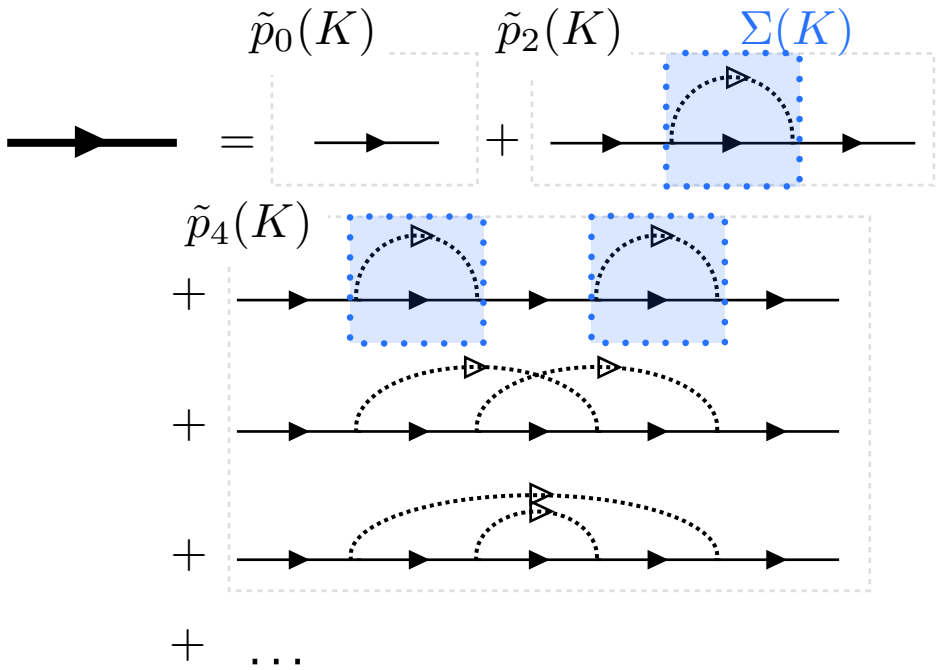

Fig. 3.3: Diagrammatic expansion of the Fourier transform of the main Fokker Planck Eq. 3.24 where the vanishing contributions are eliminated, and the non-vanishing are simplified.

and linearize it for small deformations of the interface, this gives

$$\frac{\partial \overline{v_x}(x,t)}{\partial x} = -\frac{\frac{\partial h(x,t)}{\partial t}}{H}. \tag{3.37}$$

We drop the bar and index x in the following for simplicity. We consider for simplicity that the domain studied is infinite such that the Fourier transforms of u and h are well defined and the incompressibility equation becomes:

$$\tilde{v} = -\frac{\omega}{Hk}\tilde{h}. \tag{3.38}$$

The correlator $C(x-x', t-t')$ of the total drift $f_u = \overline{v_x} + D_0 \partial_x h/H$ in Fourier space is given by

$$\begin{aligned}\tilde{C}(q,\nu)\delta(q+q')\delta(\nu+\nu')(2\pi)^2 &= \left\langle \tilde{f}_u(q,\nu)\tilde{f}_u(q',\nu')\right\rangle \\ &= \left(\left(\frac{\nu}{Hq}\right)^2 + \left(\frac{qD_0}{H}\right)^2\right) S(q,\nu)\delta(q+q')\delta(\nu+\nu')(2\pi)^2.\end{aligned} \tag{3.39}$$

where we defined the form factor of the fluctuating wall as:

$$S(q,\nu)\delta(q+q')\delta(\nu+\nu')(2\pi)^2 = \left\langle \tilde{h}(q,\nu)\tilde{h}(q',\nu')\right\rangle. \tag{3.40}$$

Σ can then be written as:

$$\Sigma(k,0) = -\int \frac{dqd\nu}{(2\pi)^2} \frac{k(k-q)\left(\left(\frac{\nu}{Hq}\right)^2 + \left(\frac{qD_0}{H}\right)^2\right) S(q,\nu)}{D_0(k-q)^2 - i\nu} \tag{3.41}$$

We first expand Σ in terms of k, noting that:

$$\begin{aligned} \frac{k(k-q)}{D_0(k-q)^2 - i\nu} &= \frac{k(k-q)}{D_0q^2 - i\nu - 2D_0kq + D_0k^2} \\ &= \frac{k^2 - kq}{D_0q^2 - i\nu}\left(1 + \frac{2D_0kq}{D_0q^2 - i\nu} + O(k^2)\right) \\ &= -k\frac{q}{D_0q^2 - i\nu} - k^2\frac{D_0q^2 + i\nu}{(D_0q^2 - i\nu)^2} + O(3) \end{aligned} \tag{3.42}$$

The first term in kq leads to a vanishing integral since $S(q,\nu) = S(-q,\nu)$. We thus find:

$$D_e = D_0 - \int \frac{dqd\nu}{(2\pi)^2}\left(\left(\frac{\nu}{Hq}\right)^2 + \left(\frac{qD_0}{H}\right)^2\right) S(q,\nu)\frac{D_0q^2 + i\nu}{(D_0q^2 - i\nu)^2}, \tag{3.43}$$

now symmetrizing the integrand by using that $S(q,\nu) = S(q,-\nu)$ we find:

$$\frac{1}{2}\left(\frac{D_0q^2 + i\nu}{(D_0q^2 - i\nu)^2} + \frac{D_0q^2 - i\nu}{(D_0q^2 + i\nu)^2}\right) = \frac{D_0^3q^6 - 3\nu^2D_0q^2}{(D_0^2q^4 + \nu^2)^2} \tag{3.44}$$

And finally we get the following formulation for the effective diffusion coefficient D_e

$$\boxed{D_e = D_0\left(1 - \int \frac{dqd\nu}{(2\pi)^2H^2}\frac{(D_0q^2)^2 - 3\nu^2}{(D_0q^2)^2 + \nu^2}S(q,\nu)\right)} \tag{3.45}$$

which is exactly the equation given in the main document.

2 Numerical Methods

2.1 Finite elements simulations

Say we are looking for the solution of the Stoke's equation with velocity field $\boldsymbol{v}$ and pressure field p like in Part I, for the simulation of the water flow through a nanocapillary and then through a nanotube. $\boldsymbol{v}$ and p obey a steady state divergence free Stokes equation, with specific boundary conditions. To solve this problem we use a finite elements solver. For problems in complex geometries, and typically elliptic problems, finite elements are well adapted to find numerical solutions. For the problems in this thesis, we used the finite elements software Freefem++ [432].

I give a very broad very naïve introduction to finite elements below – there are number of well written textbooks or see [432] for more information – to give a simple introduction

to what I did. We decompose the space in triangles (finite elements). The idea is to search the unknown function f on the domain Ω that verifies some partial differential equation say $D(f) = 0$ in the form of a linear composition of functions φ_i that "live" on these triangles, so $\varphi_i \in \heartsuit$ where $\heartsuit$ is some function space describing these triangle bound functions. We look for f verifying $D(f) = 0$ in the weak form, e.g. :

$$\forall \varphi \in \heartsuit \ , \iiint_\Omega D(f)\varphi = 0.$$

Most finite element softwares allow to specify for $D(f)$ directly but to some extent this can be an issue (for instance when special boundary conditions want to be implemented, or other). In Freefem++ the equation for f should be specified in the weak form. For the Stoke's equations, they write:

$$\forall (\varphi_x, \varphi_y, \varphi_z, \varphi_p) \in \heartsuit^3 \times \heartsuit \ , \iiint_\Omega \sum_{i=x,y,z} \eta \Delta v_i \varphi_i - (\nabla p)\varphi_i + (\nabla \boldsymbol{v})\varphi_p = 0.$$

As Freefem++ requires to input this equation with only first order derivatives in the field, one should integrate by parts the previous equation – **properly** – and this generally gives the opportunity to account for specific boundary conditions – in particular partial slip boundary conditions or other.

For the problems solved in this thesis, a very tricky thing to solve was to match the very different length scales implied. To model the flow properly, we had to simulate a box of about $200\mu m$ while the inner tube diameter was only $50nm$... So a length scale mismatch of 4 orders of magnitude. For that, the finite elements software had to be very robust in designing the triangles such that very small triangles where used for the flow inside the tube and matched to much larger triangles in the bulk. For that, the function `adaptmesh` of Freefem++ was proven to be especially robust – see Fig. 3.4; while for instance standard adapt mesh solvers in COMSOL 5.0 Multiphysics, where not as robust.

Apart from that, obviously each simulation setup was checked to depend at least as possible on the numerical parameters involved (size of the numerical box, measurement process, etc.).

2.2 Simulating the Fokker-Planck equation

In the following section I will expose some of the "tricks" that I used and found over time to ensure good convergence of a finite difference or finite volume scheme to find numerical solutions for Fokker-Planck equations. In full generality Fokker-Planck equations (in 1D) may be written:

$$\frac{\partial f}{\partial t} = -\frac{\partial}{\partial x}\left(vf - D\frac{\partial f}{\partial x}\right) \tag{3.46}$$

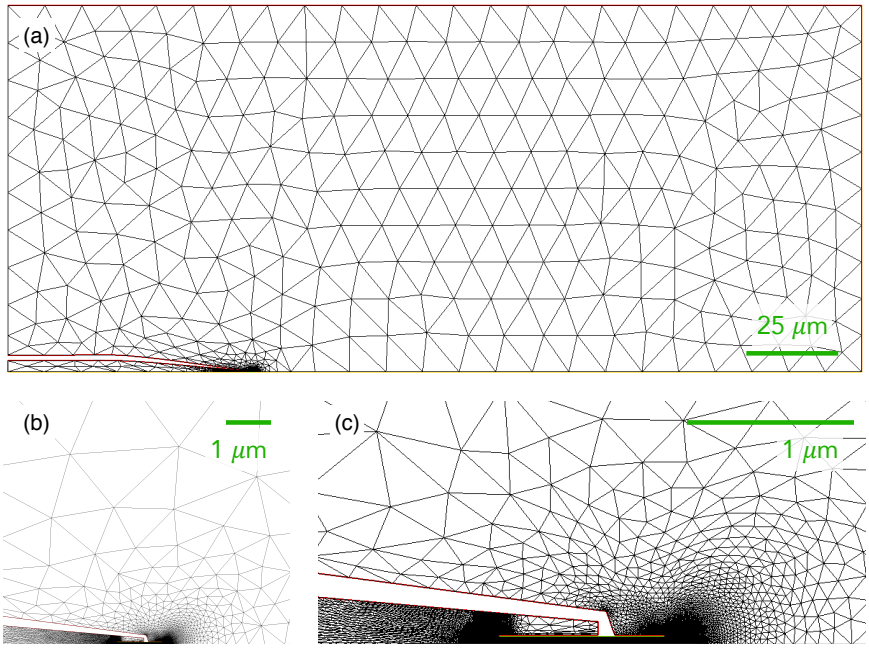

Fig. 3.4: **Adapted finite element mesh for flow measurement**: typical mesh adaptation after 16 iterations to compute the steady flow through a nanotube at the tip of capillary with $(L_t, R_t) = (1\mu m, 50nm)$. (a) total simulation box, the colored lines represent the boundaries with various boundary conditions; (b) and (c) different zooms of the mesh showing how the mesh is extremely refined in the tube.

where f is the function of interest, t is time, x is the space variable, v the velocity field and D the diffusion coefficient. D and v may depend on space and time. The details below are given for this 1D case but can be easily extended to any other dimension.

In the following I talk about *finite differences* or *finite volumes* (nearly equivalent in my perspective to finite differences) numerical schemes to solve the Fokker-Planck equation. The Fokker-Planck equation is a hyperbolic partial difference equation, because of the drift term v. It is possible to solve it with finite elements, but not naturally. In fact in Freefem++ it was not possible to simulate such hyperbolic equations (though this I heard is something that will be a future development).

To put it in a nutshell, *finite differences* consist to discretize space and time (x, t) on discrete points (x_i, t_n) with $(i, n) \in \mathbb{N}^2$ such that $x_i = i\Delta x$ and $t_n = n\Delta t$. Then, the function is discretize as $f(x_i, t_n) = f_i^n$. Then, derivatives are usually written as:

$$\frac{\partial f}{\partial x}(x_i, t_n) = \frac{f_{i+1}^n - f_{i-1}^n}{2\Delta x} \tag{3.47}$$

if the derivatives are centered for example. Then, one is faced with a number of questions: centering derivatives or not ? taking the values on the right side for f_i^n or f_i^{n+1}... and I give hints on most of these questions below.

The trick beyond all: the upstream scheme

I noticed that not many people are aware of this very simple trick – actually named the *upwind* scheme most of the time, but since I am dealing with fluids, I rather talk about *upstream*. The idea is very simple, and highlighted in Fig. 3.5. Suppose that v does not depend on x to start with. How does one discretize $v\frac{\partial f}{\partial x}$? Should the fraction be centered as in Eq. 3.47 ? In fact, since we are talking of an advection term, one has to keep in mind the obvious fact that *you can not advect what is not already there: it is the sand that comes from upstream that will later be downstream.*. As a result, the "rule of thumb" is to look at the sign of v and decide accordingly:

$$\text{If} v > 0 \ , v\frac{\partial f}{\partial x}(x_i) : v\frac{f_i - f_{i-1}}{\Delta x} \text{If} v < 0 \ , v\frac{\partial f}{\partial x}(x_i) : v\frac{f_{i+1} - f_i}{\Delta x} \tag{3.48}$$

and for $v = 0$, you can keep the centered scheme.

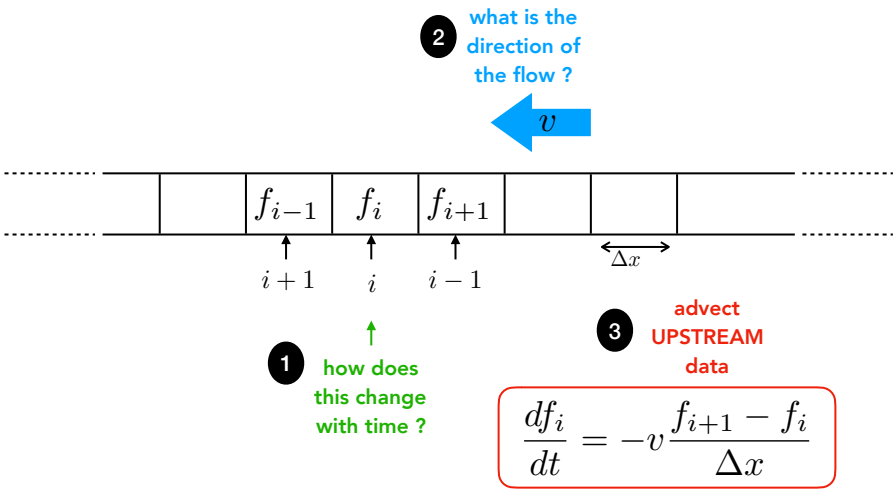

Fig. 3.5: **Upstream finite difference scheme**: typical idea of the upstream scheme; one has to advect (the concentration, particles, or anything else represented by) f_i that is "before" the flow field.

In general v depends on the position and one may decompose $\frac{\partial}{\partial x}(vf) = v\frac{\partial f}{\partial x} + f\frac{\partial v}{\partial x}$. The first term is the usual drift term where this time one checks the sign of v_i and the second term is a source term that can simply be centered. At the end of the day – litterally speaking – you won't know if $v > 0$ corresponds to the first case or the other, especially with all the signs involved, so one should just make the case separation and *try* $v > 0$ for the first condition and then $v < 0$ for the first condition. When the sign is wrong, f diverges immediatly, so you'll know for sure which one is the right one !

Other tricks that may be useful to know

Rescaling and change of origin In full generality, rescaling equations in order to obtain on the one hand non dimensional equations but on the other hand equations on domains that are static in time (for instance rescaling by the length of the system if it is time dependent adds a drift to the equation typically) is a very good idea to avoid having too many parameters to deal with. Also changing the origin for the important variable x can come in handy, for instance if $x - x_0(t)$ looks more convenient.

The logarithmic scale When dealing with Fokker-Planck equations, one is often dealing with dispersion problems, like particle diffusion. In these cases it is frequent to look at the dispersion of a gaussian concentration profile. In general, computers – finite differences – do not deal well with gaussian (or worse exponential) profiles, because the slopes – so in practice the finite differences – involved are very large numbers. As a result, I find that writing the scheme for $g = \ln(f)$ offers better accuracy and better convergence of the scheme with $\Delta x \to 0$.

Crank-Nicolson To put the problem forward I write Eq. 3.46 as $\frac{\partial f_i}{\partial t} = F(f_i)_i$ where F is some linear operator that you know how to discretize, (it is typically a matrix). Now the question is how to write the finite difference in time; knowing that you have f at the initial time and you want to propagate it with time. In full generality one may write:

$$\frac{f_i^{n+1} - f_i^n}{\Delta t} = \alpha F(f_i^n)_i + (1-\alpha) F(f_i^{n+1})_i \tag{3.49}$$

where $\alpha < 1$ is a real number. When $\alpha = 1$ we say that the scheme is *explicit* because you can find f_i^{n+1} directly from f_i^n that is known. When $\alpha = 0$ then the scheme is *implicit* because you can find f_i^{n+1} only implicitely, by inverting the matrix $\mathbb{I} - \Delta t F$. Generally fully implicit schemes are preferred because they will "anticipate" and thus prevent diveregences. However for schemes with drift implied they are not necessarily the best. The Crank-Nicolson scheme consists in taking $\alpha = 1/2$, and thus inverting $A = \mathbb{I} - (\Delta t/2)F$ to find $f_i^{n+1} = A^{-1}(\mathbb{I} + (\Delta t/2)F) f_i^n$. As a rule, the Crank-Nicolson scheme is the best behaved.

Partial Crank-Nicolson Unfortunately some Fokker-Planck equations (with added source terms, or when you pass to logarithmic scaling, etc) may not be linear. One has $\frac{\partial f_i}{\partial t} = F(f_i)_i + N(f_i)_i$ where F is a linear matrix and N a non linear operator. I call *partial Crank-Nicolson* scheme the following scheme:

$$f_i^{n+1} = (\mathbb{I} - (\Delta t/2)F)^{-1}(\mathbb{I} + (\Delta t/2)F + \Delta t N)(f_i^n) \tag{3.50}$$

and it is also the best compromise in this case since a fully implicit method is hardly possible. But how to choose Δt ?

The typical time step The upstream scheme is generally stable if the following Courant - Friedrichs - Lewy condition is satisfied [433]

$$\frac{\Delta x}{\Delta t} \geq v \tag{3.51}$$

e.g. the *numerical speed* of update is greater than the *physical speed.* If it is not the case things will be advected faster than we may track for them. Obviously sometimes this condition is not sufficient to ensure sufficient convergence, and one requires for example smaller time steps (this is mostly true to account for the diffusive terms, or other things that can come into play). For this purpose sometimes it is useful to perform an adaptation of the time step.

Auto adaptative time step To check if the scheme is well converged, something that is generally used is to check dynamically that if the time step were divided by two, it would not change too much the solution. In practice one computes: $f_i^{n+1} = B(f_i^n)$ where B is the finite difference operator. Then one also computes $g_i^{n+1/2} = B_{1/2}(f_i^n)$ where $B_{1/2}$ is the B operator but with $\Delta t \to \Delta t/2$, and finally $g_i^{n+1} = B_{1/2}(g_i^{n+1/2})$. Then one computes some norm for example the L^2 norm $d = ||f^{n+1} - g^{n+1}||_2$. If $d \leq \varepsilon$ where ε is a predefined convergence criteria, then the time step Δt is appropriate. If not, Δt should be divided at least by 2, and the scheme is repeated until the convergence criteria is met. Note that one can also perform that scheme to increase the time step when the dynamics are slowing down. However each of these adaptation steps costs a lot of computational time, and most times they are only used – and not at every time step – to decrease the time step intelligently.

2.3 Molecular dynamics simulations

General setting of a graphene layer on top of water

In the molecular dynamics (MD) simulations, the interaction potential employed for water molecules is the TIP4P model. The water-graphene interaction potential is determined by the Lorentz-Berthelot mixing rule, employing the Lenard-Jones (LJ) parameters of AMBER96 for carbon atoms (specifically the dihedral coefficient for the graphene layers is taken to be 3.125 kcal/mole) . The MD simulations are implemented using the open-source code LAMMPS. The number of molecules and the size of the simulation box are fixed during each simulation, while the temperature is maintained at 300 K using the Nosé-Hoover thermostat (in the NVT ensemble). The time integration is carried out with the time step 1 fs, and SHAKE algorithm is employed to maintain the water molecules as rigid. The LJ interactions are treated using the standard method with spherical cutoff at 9.8 Å, while the long-range Coulomb interactions are treated using the particle-particle particle-mesh (PPPM) method. The bottom layer is kept fixed, while on the top layer a pressure of 1 atm is distributed on every carbon of the graphene sheet. The position of the graphene atoms of the flexible layer is monitored with time and averaged to obtain the position of the top layer when it is fixed.

The water molecules are disposed randomly initially (with an average distance corresponding to the final density), and then their positions are relaxed using a first minimisation algorithm to minimise the potential energy. The water molecules are relaxed for 10 ps keeping the top layer fixed, and then the top layer is allowed to move and the simulation runs for $20 - 100ns$ depending on the simulation size. To integrate the Newton equations of motion, a Verlet algorithm is then used. The number of water molecules varies typically between 1500 and 8000 molecules, while the graphene layers constitute about 4000 to 8000 atoms depending on the dimensions of the simulation box.

Validation of numerical results with respect to numerical parameters

We report here the results for mainly two simulations (# 1 and # 2) of graphene layers sandwiching a water layer. The graphene layers are each made of 3680 carbon atoms. The number of water molecules is specified in the table below. The only difference between # 1 and # 2 is that in # 2 the number of water molecules is doubled and thus the water layer is doubled. See insets of Figs. Fig. 3.6 and Fig. 3.7 for a visual presentation of the simulations.

Simulation number	**Number of water molecules**	**Height H of the layer** (Å)	**Average number of water layers**	**Width of the simulation box**
# 1	2372	10.9	2-3	40
# 2	4744	18.6	5-6	40

We perform simulations in 3 cases. (a) any carbon atom of the top graphene layer is free to move with a 1 atm pressure constraint distributed on every carbon of the graphene sheet; the average height H of the graphene layer is monitored with time and recorded, as well as the mean deviation of the height $\langle h^2 \rangle^{1/2}$. This situation is referred to as *thermal flexibility*. We use 6 independent runs to measure the mean square displacement of water molecules within the sheets; (b) all carbon atoms of the top graphene layer are fixed to the height H. This situation is labeled as *fixed flat*. Here, 6 independent runs are also made to measure the mean square displacement of water molecules within the sheets; (c) all carbon atoms of the top graphene layer are frozen in an undulated state that was obtained from the *thermal flexibility* case. For # 1 simulations, 4 independent frozen states are taken, for each of which 6 independent runs are made to measure the mean square displacement of water molecules within the sheets. For # 2 simulations we use the same protocol but on only 2 independent frozen states. The results were found to vary only very weakly from one frozen state to another. This situation is labeled as *fixed undulated*.

The results for these simulations are reported in the tabular and in Figs. Fig. 3.6 and Fig. 3.7 below.

Simulation number	**Diffusion within flexible layer** ($\times 10^{-9}$ m^2/s)	**Height fluctuations** $\langle h^2 \rangle^{1/2}$ (Å)	**Diffusion within flat layer** ($\times 10^{-9}$ m^2/s)	**Diffusion within fixed undulated** ($\times 10^{-9}$ m^2/s)
# 1	3.8 ± 0.2	1.37	2.6 ± 0.1	2.2 ± 0.1
# 2	4.4 ± 0.4	1.35	3.4 ± 0.2	2.8 ± 0.1

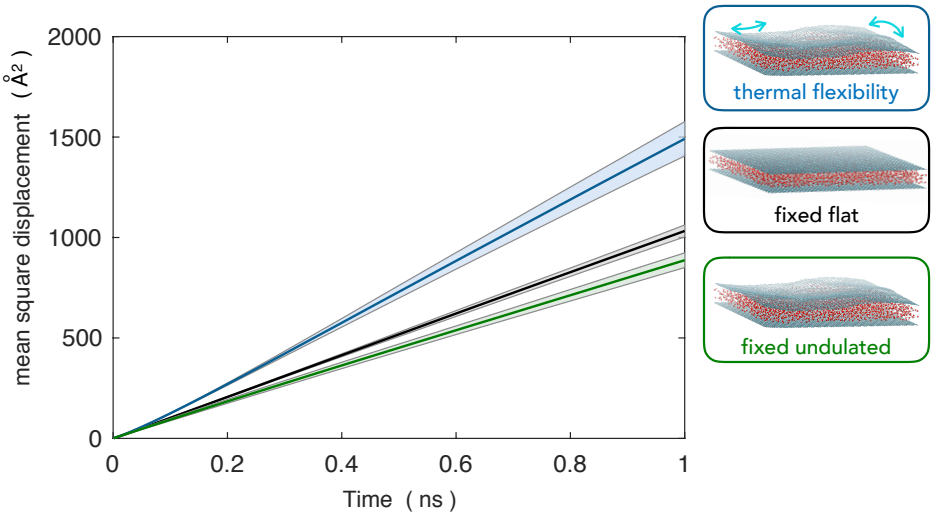

Fig. 3.6: Molecular dynamics simulation results for simulation # 1 detailed in the text. The mean square displacement of water molecules is computed on 6 to 24 independent runs, for the 3 situations detailed in the text, *thermal flexibility*, *fixed flat* and *fixed undulated*.

We find that diffusion within the water layer is always enhanced when the top graphene layer is flexible, compared to the flat case. This corresponds to enhancement when the dynamics of the fluctuating layer are fast. On the contrary, when the top graphene layer is fixed in an undulated configuration, then diffusion is always decreased as compared to the fixed flat case: this corresponds to the traditional Fick-Jacobs entropic slow down.

Note that in all these cases, the typical enhancement factor $\langle h^2 \rangle / H^2 \sim 0.01$ is much smaller than the effects actually observed. One could argue that here the proper H to define is actually the height of the water layer itself (computed for instance from shear simulations) and not the distance between the two graphene sheets. This would slightly diminish H and thus increase $\langle h^2 \rangle / H^2$ but still be smaller than the enhancement of the diffusion coefficient that here is of order 0.5.

Between simulation # 1 and # 2, all diffusion coefficients increase when the layer is thicker, this is due to diminution of the diffusion coefficient upon confinement [378, 434].

Note that the sensitivity of these results were also tested with respect to the lateral

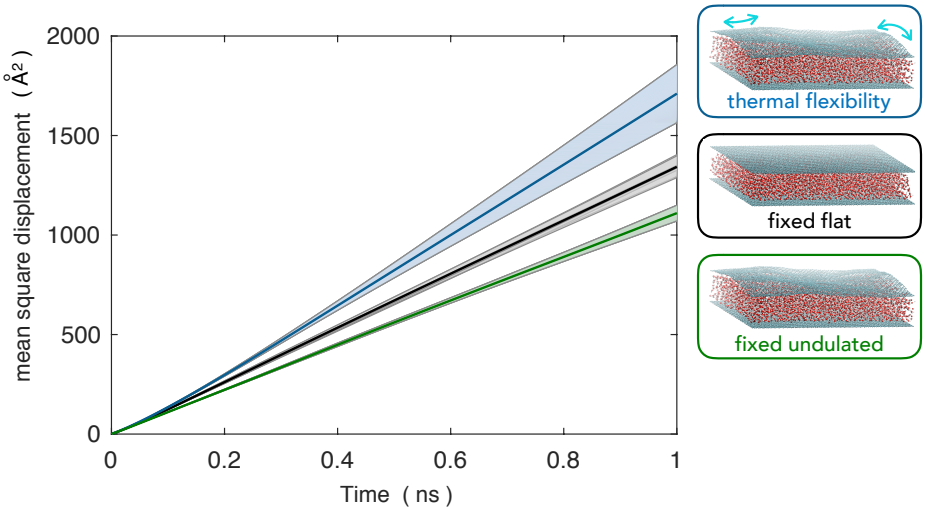

Fig. 3.7: Molecular dynamics simulation results for simulation # 2 detailed in the text. The mean square displacement of water molecules is computed on 6 to 12 independent runs, for the 3 situations detailed in the text, *thermal flexibility*, *fixed flat* and *fixed undulated*.

dimension of the simulation box. Although some effect is noted as the simulation box increases ($\langle h^2 \rangle$ increases slightly, all diffusion coefficients diminish slightly) we still find the same clear ordering between the different situations.

3 Experimental Methods

In the following I describe some of the experimental methods used to measure ionic currents through the nano-door in Part III.

3.1 Cell and membrane preparation

Preliminary steps Use gloves, place the device on a tissue sheet to avoid (and detect!) spilling, the cell should have been previously entirely cleaned and dried.

Cell mounting The steps to mount the cell are described also in Fig. 3.8.

1. Place the bottom cell part with the metal bars on the main metal support such that the cell does not move during membrane positioning. Place the first rubber O-ring in the appropriate location.
2. Place the membrane in the slit designed for it, and beware of the side to put it in, in general I place it as in Fig. 3.8-a, with the flat interface at the top. (At this stage it is

possible to put just a drop of red silicon glue on the PEEK on the side, that will ensure that the setup moves less during filling, unfilling etc).

3. Add the second O-ring in the top cell part, and place the top cell part through the metal bars and carefully on top of the membrane.

4. Place carefully on top the glass screwing device, hold the PEEK cell in place, and screw carefully both parts together. Screw one last turn when the whole thing is starting to be pinched together. This is the crucial step to ensure that there will be no leaks in the device.

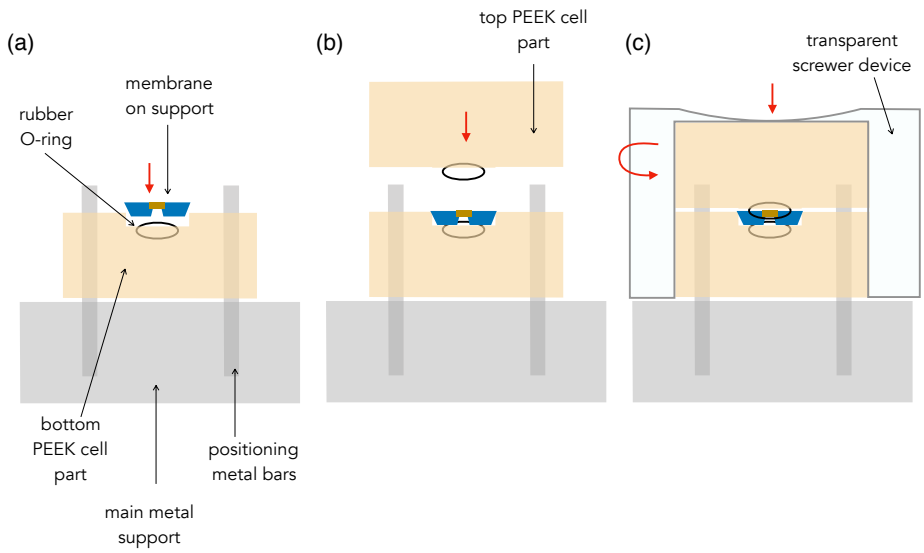

Fig. 3.8: **Steps to mount a cell** (a) insertion of the membrane (b) position of the upper cell part (c) assembly and screwing for hermiticity.

Filling and cell closing The steps to fill and close the cell are the following, according to the fragility of the membrane, they may be more or less hard to perform without breaking the membrane.

1. Bring the syringe with desired solution as close as possible to the membrane support, and press slowly (very slowly if the membrane is fragile, because the pressure itself brought by the syringe can be lethal). Push the bubbles that appeared by injecting solution close to them. Bubbles are the hardest thing to get rid of.

2. screw with delicacy the cork, pump the water spilling with another syringe, add a quarter of a turn with the wrench. If the cell is turned upside down it should not spill. If it does, the membrane is broken...

3.2 Solution preparation

I used KCl ionic solutions. The solutions are prepared by dissolving KCl (Sigma Aldrich in deionized water. The molar mass of KCl is $74.55g/mol$ such that for $1mol/L$ solution (or equivalently $1M$) one requires $3.727g$ of salt in $50mL$ or $7.455g$ in $100mL$. Different concentrations are then obtained by standard dissolution. The conductivity of the solutions were measured using a conductance meter (Hanna Instruments, HI 2550) before the experiments. The solutions were filtered using syringe filters with a $0.2\mu m$ pore size (Corning Syringe Filters, Sigma Aldrich).

3.3 Ionic and streaming measurements

The electrodes are 1 mm diameter silver wires. Their surface is periodically activated by immersion in NaClO for 15 min. Electrical transport is measured with a Keithley 2410 1100V SourceMeter (Tektronix) connected to an acquisition card (National Instruments) and controlled by a custom software (python). The resolution is $1pA$. During electrical measurements, the setup is placed inside a Faraday cage to shield it from electrical noise. Sometimes, 4 wire measurements were performed, in which case current is imposed via Platinum electrodes.

Pressure is applied thanks to a connector that is linked to a tube arriving in the cell, and carefully sealed to the cell cork. The pressure is applied by an AF1 Microfluidic Pressure Pump (Elveflow) and controlled by a custom software (python).

Programs for ionic and streaming measurements: I coded the programs to acquire current measurements with time (`IvsV.py`) and current measurements with time, applying at the same time pressure ramps (`IvsVwithP.py`). Each of these scripts is well commented and easily changed to acquire different profiles (and is using the `makeIvsVcurve.py` to plot curves during acquisition).

3.4 Optical fiber measurements

To acquire resonance profiles of the nanodoor, a membrane with a carved nanodoor is placed on a support. A standard piezo is connected to the support and can be connected to a frequency excitor (Zürich Instruments). An optical fiber is mounted on a micropositioning stage (x,y,z directions from Mechonics). The stage is connected to a card (Mechonics) to the computer and controlled by a custom software (C++). The optical fiber is fed by a laser source 51 nanoFI with wavelength $\lambda = 661nm$ and maximum power $P = 6mW$ (Schäfter + Kirchhoff). The return deconvoluted signal is sent to a photodiode DET 26A/M (Thorlabs) and the resulting voltage to an amplifier DLPCA-200 Amp (Laser Components). The signal

is then send to data acquisition card (National Instruments) and read by a custom software (python).

Programs for optical fiber measurements: I coded the programs to acquire x y z maps of return optical signal from the fiber. The compiled program `ApplicationMecho1.exe` is able to move the Mechonics stage according to a specific order in a text file `Order`, which indicates the step and the speed and the direction to move. `MeasureDAQTest.py` is a simple program that reads and outputs the voltage value acquired at the instant, and useful to ensure that the setup is working out. `LaunchMap.py` performs a z direction single scan and measures the return signal, `LaunchMapxy.py` produces an x y map and `LaunchMapxyfast.py` is a bit faster. The three previous programs call `ApplicationMecho1.exe` and `MeasureDAQ.py`. Generating a map is especially difficult because the microcontrollers are not extremely robust: after a number of iterative move, there is a slight drift in one direction.

References

[1] Richard W Baker, "Membrane technology and applications", *Membrane Technology* (2004).

[2] Anna Lee, Jeffrey W Elam et Seth B Darling, "Membrane materials for water purification: design, development, and application", *Environmental Science: Water Research & Technology* 2(1), 17–42 (2016).

[3] T Christopher Dickenson, *Filters and filtration handbook*, Elsevier (1997).

[4] Jay R Werber, Chinedum O Osuji et Menachem Elimelech, "Materials for next-generation desalination and water purification membranes", *Nature Reviews Materials* 1(5), 16018 (2016).

[5] TLFi, *Le Trésor de la Langue Française informatisé*, (1971-1994).

[6] thesaurus, *Thesaurus dictionnary*, (2018).

[7] Alfred Ernout et Antoine Meillet, *Dictionnaire étymologique de la langue latine. Histoire des mots*, Paris, Klincksieck (1951, 4th edition, 2001).

[8] Douglas Brinkley, *History of the United States*, Viking Penguin. New York (1998).

[9] Bernard de Montfaucon, *Antiquity Explained, and Represented in Sculptures, Volumes 3 to 4*, J. Tonson and J. Watts (1722).

[10] Ian Spencer Hornse, *A history of Beer and Brewing*, Cambridge, Royal Society of Chemistry (2003).

[11] Robert J Forbes, *A short history of the art of distillation: from the beginnings up to the death of Cellier Blumenthal*, Brill (1970).

[12] Kenneth S Sutherland et George Chase, *Filters and filtration handbook*, Elsevier (2011).

[13] Geoffrey M Geise, Donald R Paul et Benny D Freeman, "Fundamental water and salt transport properties of polymeric materials", *Progress in Polymer Science* 39(1), 1–42 (2014).

[14] Phillip Sheeler et Donald E Bianchi, *Cell and molecular biology*, Wiley New York etc. (1987).

[15] Kaare H Jensen, Emmanuelle Rio, Rasmus Hansen, Christophe Clanet et Tomas Bohr, "Osmotically driven pipe flows and their relation to sugar transport in plants", *Journal of Fluid Mechanics* 636, 371–396 (2009).

[16] O Kedem et A Katchalsky, "A physical interpretation of the phenomenological coefficients of membrane permeability", *The Journal of general physiology* 45(1), 143–179 (1961).

[17] Bruce E Logan et Menachem Elimelech, "Membrane-based processes for sustainable power generation using water", *Nature* 488(7411), 313 (2012).

[18] Alessandro Siria, Philippe Poncharal, Anne-Laure Biance, Rémy Fulcrand, Xavier Blase, Stephen T Purcell et Lydéric Bocquet, "Giant osmotic energy conversion measured in a single transmembrane boron nitride nanotube", *Nature* 494(7438), 455 (2013).

[19] Jacobus Henricus Van't Hoff, *Etudes de dynamique chimique*, volume 1, Muller (1884).

[20] Jacobus H van't Hoff, "Die Rolle des osmotischen Druckes in der Analogie zwischen Lösungen und Gasen", *Zeitschrift für physikalische Chemie* 1(1), 481–508 (1887).

[21] J Willard Gibbs, "Semi-permeable films and osmotic pressure", *Nature* 55(1429), 461 (1897).

[22] Edward Armand Guggenheim, "Thermodynamics-an advanced treatment for chemists and physicists", *Amsterdam, North-Holland, 1985, 414 p.* (1985).

[23] Irving Myron Klotz et Robert M Rosenberg, *Chemical thermodynamics: basic concepts and methods*, Wiley Online Library (2008).

[24] Wilhelm Pfeffer, *Osmotische untersuchungen: studien zur zellmechanik*, W. Engelmann (1877).

[25] JB Dandeno, "Osmotic Theories, with Special Reference to Van't Hoff's Law", *Bulletin of the Torrey Botanical Club* 36(6), 283–298 (1909).

[26] MM Meyer et JH van'T Hoff, "Sur la pression osmotique", *Recueil des Travaux Chimiques des Pays-Bas* 9(7), 157–161 (1890).

[27] S Sourirajan, "Sea Water Demineralization by the "Surface Skimming" Process", *UCLA Dept. of Engineering, June-Aug* pages 58–65 (1958).

[28] Samuel Terrill Yuster, S Sourirajan et Karl Bernstein, *Sea Water Demineralization by the" surface Skimming" Process*, volume 58, University of California, Department of Engineering (1958).

[29] Sidney Loeb. "The loeb-sourirajan membrane: How it came about". ACS Publications, (1981).

[30] Sidney Loeb et Srinivasa Sourirajan. "Sea water demineralization by means of an osmotic membrane". ACS Publications, (1962).

[31] Milagro Marroquin, Terri Bruce, John Pellegrino, S Ranil Wickramasinghe et Scott M Husson, "Characterization of asymmetry in microporous membranes by cross-sectional confocal laser scanning microscopy", *Journal of membrane science* 379(1-2), 504–515 (2011).

[32] Seetha S Manickam et Jeffrey R McCutcheon, "Understanding mass transfer through asymmetric membranes during forward osmosis: A historical perspective and critical review on measuring structural parameter with semi-empirical models and characterization approaches", *Desalination* 421, 110–126 (2017).

[33] Takeshi Matsuura, "Progress in membrane science and technology for seawater desalination—a review", *Desalination* 134(1-3), 47–54 (2001).

[34] Mathias Ulbricht, "Advanced functional polymer membranes", *Polymer* 47(7), 2217–2262 (2006).

[35] Yun Wang, Ken S Chen, Jeffrey Mishler, Sung Chan Cho et Xavier Cordobes Adroher, "A review of polymer electrolyte membrane fuel cells: technology, applications, and needs on fundamental research", *Applied energy* 88(4), 981–1007 (2011).

[36] Youngpil Chun, Dennis Mulcahy, Linda Zou et In S Kim, "A short review of membrane fouling in forward osmosis processes", *Membranes* 7(2), 30 (2017).

[37] World Health Organization, *Progress on sanitation and drinking water: 2015 update and MDG assessment*, World Health Organization (2015).

[38] Kelvin B Gregory, Radisav D Vidic et David A Dzombak, "Water management challenges associated with the production of shale gas by hydraulic fracturing", *Elements* 7(3), 181–186 (2011).

[39] Radisav D Vidic, Susan L Brantley, Julie M Vandenbossche, David Yoxtheimer et Jorge D Abad, "Impact of shale gas development on regional water quality", *Science* 340(6134), 1235009 (2013).

[40] Devin L Shaffer, Laura H Arias Chavez, Moshe Ben-Sasson, Santiago Romero-Vargas Castrillón, Ngai Yin Yip et Menachem Elimelech, "Desalination and reuse of high-salinity shale gas produced water: drivers, technologies, and future directions", *Environmental science & technology* 47(17), 9569–9583 (2013).

[41] Viviani C Onishi, Juan A Reyes-Labarta et José A Caballero. "Zero-liquid discharge desalination of hypersaline shale gas wastewater: Challenges and future directions". In *Euro-Mediterranean Conference for Environmental Integration*, pages 65–67. Springer, (2017).

[42] Viviani C Onishi, Alba Carrero-Parreno, Juan A Reyes-Labarta, Eric S Fraga et José A Caballero, "Desalination of shale gas produced water: A rigorous design approach for zero-liquid discharge evaporation systems", *Journal of Cleaner Production* 140, 1399–1414 (2017).

[43] CNRS, "Dossier scientifique: l'eau", (http://www.cnrs.fr/cw/dossiers/doseau/decouv/cycle/stocksEau.html).

[44] Arjen Y Hoekstra et Mesfin M Mekonnen, "The water footprint of humanity", *Proceedings of the national academy of sciences* 109(9), 3232–3237 (2012).

[45] JD Birkett, "The history of desalination before large-scale use, encyclopedia of desalination and water resources (desware)"(2012).

[46] L Henthorne, "Desalination–a critical element of water solutions for the 21st century", *The International Desalination Association* (2009).

[47] Raphael Semiat, "Energy issues in desalination processes", *Environmental science & technology* 42(22), 8193–8201 (2008).

[48] Matthew E Suss, Theodore F Baumann, William L Bourcier, Christopher M Spadaccini, Klint A Rose, Juan G Santiago et Michael Stadermann, "Capacitive desalination with flow-through electrodes", *Energy & Environmental Science* 5(11), 9511–9519 (2012).

[49] Yoram Oren, "Capacitive deionization (CDI) for desalination and water treatment—past, present and future (a review)", *Desalination* 228(1-3), 10–29 (2008).

[50] Marc A Anderson, Ana L Cudero et Jesus Palma, "Capacitive deionization as an electrochemical means of saving energy and delivering clean water. Comparison to present desalination practices: Will it compete?", *Electrochimica Acta* 55(12), 3845–3856 (2010).

[51] Isela Victoria Arámburo-Miranda et Emmanuel Hammurabi Ruelas-Ramírez, "Desalination of sea water with aquatic lily (Eichhornia crassipes)", *Environmental Science and Pollution Research* 24(33), 25676–25681 (2017).

[52] Jaime M Amezaga, Anna Amtmann, Catherine A Biggs, Tom Bond, Catherine J Gandy, Annegret Honsbein, Esther Karunakaran, Linda Lawton, Mary Ann Madsen, Konstantinos Minas et al., "Biodesalination: a case study for applications of photosynthetic bacteria in water treatment", *Plant physiology* 164(4), 1661–1676 (2014).

[53] K Minas, E Karunakaran, Thomas Bond, C Gandy, A Honsbein, M Madsen, J Amezaga, A Amtmann, MR Templeton, CA Biggs et al., "Biodesalination: an emerging technology for targeted removal of Na+ and Cl- from seawater by cyanobacteria", *Desalination and Water Treatment* 55(10), 2647–2668 (2015).

[54] Daosheng Deng, E Victoria Dydek, Ji-Hyung Han, Sven Schlumpberger, Ali Mani, Boris Zaltzman et Martin Z Bazant, "Overlimiting current and shock electrodialysis in porous media", *Langmuir* 29(52), 16167–16177 (2013).

[55] Sung Jae Kim, Sung Hee Ko, Kwan Hyoung Kang et Jongyoon Han, "Direct seawater desalination by ion concentration polarization", *Nature Nanotechnology* 5(4), 297 (2010).

[56] Kim Choon Ng, Kyaw Thu, Youngdeuk Kim, Anutosh Chakraborty et Gary Amy, "Adsorption desalination: an emerging low-cost thermal desalination method", *Desalination* 308, 161–179 (2013).

[57] Yunlong Luo, Wenshan Guo, Huu Hao Ngo, Long Duc Nghiem, Faisal Ibney Hai, Jian Zhang, Shuang Liang et Xiaochang C Wang, "A review on the occurrence of micropollutants in the aquatic environment and their fate and removal during wastewater treatment", *Science of the Total Environment* 473, 619–641 (2014).

[58] Lynn Williams Stephens, Rob Lindsay, Michael Milne, Adam Klein, Valerie Fuchs et Lisa Rodenburg, "PCBs: The Next Frontier In Microconstituent Regulation-A Case Study of Municipal Wastewater Treatment", *Proceedings of the Water Environment Federation* 2016(8), 5423–5429 (2016).

[59] Jeremy S Guest, Steven J Skerlos, James L Barnard, M Bruce Beck, Glen T Daigger, Helene Hilger, Steven J Jackson, Karen Karvazy, Linda Kelly, Linda Macpherson et al., "A new planning and design paradigm to achieve sustainable resource recovery from wastewater"(2009).

[60] Xu Wang, Perry L McCarty, Junxin Liu, Nan-Qi Ren, Duu-Jong Lee, Han-Qing Yu, Yi Qian et Jiuhui Qu, "Probabilistic evaluation of integrating resource recovery into wastewater treatment to improve environmental sustainability", *Proceedings of the National Academy of Sciences* 112(5), 1630–1635 (2015).

[61] Daniel Puyol, Damien J Batstone, Tim Hülsen, Sergi Astals, Miriam Peces et Jens O Krömer, "Resource recovery from wastewater by biological technologies: opportunities, challenges, and prospects", *Frontiers in microbiology* 7, 2106 (2017).

[62] Wen-Wei Li, Han-Qing Yu et Zhen He, "Towards sustainable wastewater treatment by using microbial fuel cells-centered technologies", *Energy & Environmental Science* 7(3), 911–924 (2014).

[63] Mark A Shannon, Paul W Bohn, Menachem Elimelech, John G Georgiadis, Benito J Marinas et Anne M Mayes, "Science and technology for water purification in the coming decades", *Nature* 452(7185), 301 (2008).

[64] Yuan Zhou et Richard SJ Tol, "Evaluating the costs of desalination and water transport", *Water resources research* 41(3) (2005).

[65] Kader Gaid et Yvan Treal, "Le dessalement des eaux par osmose inverse: l'expérience de Véolia Water", *Desalination* 203(1-3), 1–14 (2007).

[66] Menachem Elimelech et William A Phillip, "The future of seawater desalination: energy, technology, and the environment", *science* 333(6043), 712–717 (2011).

[67] "World Development Indicators | Data", *data.worldbank.org* (retrieved on March 2nd, 2018).

[68] Sangwoo Shin, Jesse T Ault, Patrick B Warren et Howard A Stone, "Accumulation of Colloidal Particles in Flow Junctions Induced by Fluid Flow and Diffusiophoresis", *Physical Review X* 7(4), 041038 (2017).

[69] Lloyd M Robeson, "Correlation of separation factor versus permeability for polymeric membranes", *Journal of membrane science* 62(2), 165–185 (1991).

[70] Amit Mehta et Andrew L Zydney, "Permeability and selectivity analysis for ultrafiltration membranes", *Journal of Membrane Science* 249(1-2), 245–249 (2005).

[71] O Kedem et A Katchalsky, "Permeability of composite membranes. Part 1.—Electric current, volume flow and flow of solute through membranes", *Transactions of the Faraday Society* 59, 1918–1930 (1963).

[72] Leos Zeman et Michael Wales. "Polymer solute rejection by ultrafiltration membranes". ACS Publications, (1981).

[73] John Douglass Ferry, "Ultrafilter membranes and ultrafiltration.", *Chemical Reviews* 18(3), 373–455 (1936).

[74] PHILIP L Paine et P Scherr, "Drag coefficients for the movement of rigid spheres through liquid-filled cylindrical pores.", *Biophysical journal* 15(10), 1087 (1975).

[75] Seiichi Mochizuki et Andrew L Zydney, "Theoretical analysis of pore size distribution effects on membrane transport", *Journal of membrane science* 82(3), 211–227 (1993).

[76] Geoffrey M Geise, Ho Bum Park, Alyson C Sagle, Benny D Freeman et James E McGrath, "Water permeability and water/salt selectivity tradeoff in polymers for desalination", *Journal of Membrane Science* 369(1-2), 130–138 (2011).

[77] Christopher Bellona, Jörg E Drewes, Pei Xu et Gary Amy, "Factors affecting the rejection of organic solutes during NF/RO treatment?a literature review", *Water research* 38(12), 2795–2809 (2004).

[78] Katsuki Kimura, Gary Amy, Jörg E Drewes, Thomas Heberer, Tae-Uk Kim et Yoshimasa Watanabe, "Rejection of organic micropollutants (disinfection by-products, endocrine disrupting compounds, and pharmaceutically active compounds) by NF/RO membranes", *Journal of membrane science* 227(1-2), 113–121 (2003).

[79] Jay R Werber, Akshay Deshmukh et Menachem Elimelech, "The critical need for increased selectivity, not increased water permeability, for desalination membranes", *Environmental Science & Technology Letters* 3(4), 112–120 (2016).

[80] Rajindar Singh, "Production of high-purity water by membrane processes", *Desalination and Water Treatment* 3(1-3), 99–110 (2009).

[81] Yu Miyashita, Sang-Hyuck Park, Hoon Hyung, Ching-Hua Huang et Jae-Hong Kim, "Removal of N-nitrosamines and their precursors by nanofiltration and reverse osmosis membranes", *Journal of Environmental Engineering* 135(9), 788–795 (2009).

[82] Takahiro Fujioka, Kenneth P Ishida, Takuji Shintani et Hitoshi Kodamatani, "High rejection reverse osmosis membrane for removal of N-nitrosamines and their precursors", *Water research* 131, 45–51 (2018).

[83] Sukanyah Shanmuganathan, Paripurnanda Loganathan, Christian Kazner, MAH Johir et Saravanamuthu Vigneswaran, "Submerged membrane filtration adsorption hybrid system for the removal of organic micropollutants from a water reclamation plant reverse osmosis concentrate", *Desalination* 401, 134–141 (2017).

[84] Douglas L Gin et Richard D Noble, "Designing the next generation of chemical separation membranes", *Science* 332(6030), 674–676 (2011).

[85] William J Koros et Chen Zhang, "Materials for next-generation molecularly selective synthetic membranes", *Nature materials* 16(3), 289 (2017).

[86] Khaled A Mahmoud, Bilal Mansoor, Ali Mansour et Marwan Khraisheh, "Functional graphene nanosheets: The next generation membranes for water desalination", *Desalination* 356, 208–225 (2015).

[87] Oishi Sanyal, Chen Zhang, Graham B Wenz, Shilu Fu, Nitesh Bhuwania, Liren Xu, Meha Rungta et William J Koros, "Next generation membranes?using tailored carbon", *Carbon* 127, 688–698 (2018).

[88] Lydéric Bocquet et Elisabeth Charlaix, "Nanofluidics, from bulk to interfaces", *Chemical Society Reviews* 39(3), 1073–1095 (2010).

[89] Lyderic Bocquet et Patrick Tabeling, "Physics and technological aspects of nanofluidics", *Lab on a Chip* 14(17), 3143–3158 (2014).

[90] Peter Agre, "The aquaporin water channels", *Proceedings of the American Thoracic Society* 3(1), 5–13 (2006).

[91] Gregory M Preston, Tiziana Piazza Carroll, William B Guggino et Peter Agre, "Appearance of water channels in Xenopus oocytes expressing red cell CHIP28 protein", *Science* 256(5055), 385–387 (1992).

[92] Kazuyoshi Murata, Kaoru Mitsuoka, Teruhisa Hirai, Thomas Walz, Peter Agre, J Bernard Heymann, Andreas Engel et Yoshinori Fujiyoshi, "Structural determinants of water permeation through aquaporin-1", *Nature* 407(6804), 599 (2000).

[93] Benoît Roux, Jean-Yves Lapointe et Daniel G Bichet, "Structure de l'aquaporine 1 ou comment bloquer un bâton de relais (le proton) qui se déplace plus vite que le coureur (l'eau)?", (2001).

[94] Thomas Walz, Barbara L Smith, Mark L Zeidel, Andreas Engel et Peter Agre, "Biologically active two-dimensional crystals of aquaporin CHIP.", *Journal of Biological Chemistry* 269(3), 1583–1586 (1994).

[95] Haixin Sui, Bong-Gyoon Han, John K Lee, Peter Walian et Bing K Jap, "Structural basis of water-specific transport through the AQP1 water channel", *Nature* 414(6866), 872 (2001).

[96] Simon Gravelle, Laurent Joly, François Detcheverry, Christophe Ybert, Cécile Cottin-Bizonne et Lydéric Bocquet, "Optimizing water permeability through the hourglass shape of aquaporins", *Proceedings of the National Academy of Sciences* 110(41), 16367–16372 (2013).

[97] Emad Tajkhorshid, Peter Nollert, Morten Ø Jensen, Larry JW Miercke, Joseph O'connell, Robert M Stroud et Klaus Schulten, "Control of the selectivity of the aquaporin water channel family by global orientational tuning", *Science* 296(5567), 525–530 (2002).

[98] Jianping Gao, Robert Szoszkiewicz, Uzi Landman, Elisa Riedo et al., "Structured and viscous water in subnanometer gaps", *Physical Review B* 75(11), 115415 (2007).

[99] Simona Dalla Bernardina, Erwan Paineau, Jean-Blaise Brubach, Patrick Judeinstein, Stéphan Rouzière, Pascale Launois et Pascale Roy, "Water in carbon nanotubes: the peculiar hydrogen bond network revealed by infrared spectroscopy", *Journal of the American Chemical Society* 138(33), 10437–10443 (2016).

[100] Kumar Varoon Agrawal, Steven Shimizu, Lee W Drahushuk, Daniel Kilcoyne et Michael S Strano, "Observation of extreme phase transition temperatures of water confined inside isolated carbon nanotubes", *Nature nanotechnology* 12(3), 267 (2017).

[101] G Algara-Siller, O Lehtinen, FC Wang, RR Nair, U Kaiser, HA Wu, AK Geim et IV Grigorieva, "Square ice in graphene nanocapillaries", *Nature* 519(7544), 443 (2015).

[102] Kenichiro Koga, GT Gao, Hideki Tanaka et Xiao Cheng Zeng, "Formation of ordered ice nanotubes inside carbon nanotubes", *Nature* 412(6849), 802 (2001).

[103] Alexander I Kolesnikov, Jean-Marc Zanotti, Chun-Keung Loong, Pappannan Thiyagarajan, Alexander P Moravsky, Raouf O Loutfy et Christian J Burnham, "Anomalously soft dynamics of water in a nanotube: a revelation of nanoscale confinement", *Physical review letters* 93(3), 035503 (2004).

[104] Uri Raviv, Pierre Laurat et Jacob Klein, "Fluidity of water confined to subnanometre films", *Nature* 413(6851), 51 (2001).

[105] Eric Lauga, Michael Brenner et Howard Stone. "Microfluidics: the no-slip boundary condition". In *Springer handbook of experimental fluid mechanics*, pages 1219–1240. Springer, (2007).

[106] J Goyon, A Colin, G Ovarlez, A Ajdari et L Bocquet, "Spatial cooperativity in soft glassy flows", *Nature* 454(7200), 84 (2008).

[107] Kazuko T Mashiyama et Hazime Mori, "Origin of the Landau-Lifshitz hydrodynamic fluctuations in nonequilibrium systems and a new method for reducing the Boltzmann equation", *Journal of Statistical Physics* 18(4), 385–407 (1978).

[108] François Detcheverry et Lydéric Bocquet, "Thermal fluctuations in nanofluidic transport", *Physical review letters* 109(2), 024501 (2012).

[109] Jiandong Feng, Michael Graf, Ke Liu, Dmitry Ovchinnikov, Dumitru Dumcenco, Mohammad Heiranian, Vishal Nandigana, Narayana R Aluru, Andras Kis et Aleksandra Radenovic, "Single-layer MoS 2 nanopores as nanopower generators", *Nature* 536(7615), 197 (2016).

[110] Jiandong Feng, Ke Liu, Roman D Bulushev, Sergey Khlybov, Dumitru Dumcenco, Andras Kis et Aleksandra Radenovic, "Identification of single nucleotides in MoS 2 nanopores", *Nature nanotechnology* 10(12), 1070 (2015).

[111] Stefano Pagliara, Simon L Dettmer et Ulrich F Keyser, "Channel-facilitated diffusion boosted by particle binding at the channel entrance", *Physical review letters* 113(4), 048102 (2014).

[112] Chang Young Lee, Wonjoon Choi, Jae-Hee Han et Michael S Strano, "Coherence resonance in a single-walled carbon nanotube ion channel", *Science* 329(5997), 1320–1324 (2010).

[113] Wonjoon Choi, Zachary W Ulissi, Steven FE Shimizu, Darin O Bellisario, Mark D Ellison et Michael S Strano, "Diameter-dependent ion transport through the interior of isolated single-walled carbon nanotubes", *Nature communications* 4, 2397 (2013).

[114] Eleonora Secchi, Sophie Marbach, Antoine Niguès, Derek Stein, Alessandro Siria et Lydéric Bocquet, "Massive radius-dependent flow slippage in carbon nanotubes", *Nature* 537(7619), 210–213 (2016).

[115] Ramya H Tunuguntla, Robert Y Henley, Yun-Chiao Yao, Tuan Anh Pham, Meni Wanunu et Aleksandr Noy, "Enhanced water permeability and tunable ion selectivity in subnanometer carbon nanotube porins", *Science* 357(6353), 792–796 (2017).

[116] Pramod Nednoor, Vasilis G Gavalas, Nitin Chopra, Bruce J Hinds et Leonidas G Bachas, "Carbon nanotube based biomimetic membranes: mimicking protein channels regulated by phosphorylation", *Journal of Materials Chemistry* 17(18), 1755–1757 (2007).

[117] RR Nair, HA Wu, PN Jayaram, IV Grigorieva et AK Geim, "Unimpeded permeation of water through helium-leak–tight graphene-based membranes", *Science* 335(6067), 442–444 (2012).

[118] A Esfandiar, B Radha, FC Wang, Q Yang, S Hu, S Garaj, RR Nair, AK Geim et K Gopinadhan, "Size effect in ion transport through angstrom-scale slits", *Science* 358(6362), 511–513 (2017).

[119] Mainak Majumder, Alessandro Siria et Lydéric Bocquet, "Flows in one-dimensional and two-dimensional carbon nanochannels: Fast and curious", *MRS Bulletin* 42(4), 278–282 (2017).

[120] Alessandro Siria, Marie-Laure Bocquet et Lydéric Bocquet, "New avenues for the large-scale harvesting of blue energy", *Nature Reviews Chemistry* 1(11), 0091 (2017).

[121] Nicholas AW Bell, Christian R Engst, Marc Ablay, Giorgio Divitini, Caterina Ducati, Tim Liedl et Ulrich F Keyser, "DNA origami nanopores", *Nano letters* 12(1), 512–517 (2011).

[122] Martin Langecker, Vera Arnaut, Thomas G Martin, Jonathan List, Stephan Renner, Michael Mayer, Hendrik Dietz et Friedrich C Simmel, "Synthetic lipid membrane channels formed by designed DNA nanostructures", *Science* 338(6109), 932–936 (2012).

[123] Michael I Walker, Krystian Ubych, Vivek Saraswat, Edward A Chalklen, Philipp Braeuninger-Weimer, Sabina Caneva, Robert S Weatherup, Stephan Hofmann et Ulrich F Keyser, "Extrinsic cation selectivity of 2D membranes", *ACS nano* 11(2), 1340–1346 (2017).

[124] Francesco Fornasiero, Hyung Gyu Park, Jason K Holt, Michael Stadermann, Costas P Grigoropoulos, Aleksandr Noy et Olgica Bakajin, "Ion exclusion by sub-2-nm carbon nanotube pores", *Proceedings of the National Academy of Sciences* 105(45), 17250–17255 (2008).

[125] Jiandong Feng, Ke Liu, Michael Graf, Dumitru Dumcenco, Andras Kis, Massimiliano Di Ventra et Aleksandra Radenovic, "Observation of ionic Coulomb blockade in nanopores", *Nature materials* 15(8), 850 (2016).

[126] Jason K Holt, Hyung Gyu Park, Yinmin Wang, Michael Stadermann, Alexander B Artyukhin, Costas P Grigoropoulos, Aleksandr Noy et Olgica Bakajin, "Fast mass transport through sub-2-nanometer carbon nanotubes", *Science* 312(5776), 1034–1037 (2006).

[127] Mainak Majumder, Nitin Chopra, Rodney Andrews et Bruce J Hinds, "Nanoscale hydrodynamics: enhanced flow in carbon nanotubes", *Nature* 438(7064), 44 (2005).

[128] Max Whitby, Laurent Cagnon, Maya Thanou et Nick Quirke, "Enhanced fluid flow through nanoscale carbon pipes", *Nano letters* 8(9), 2632–2637 (2008).

[129] Wai-Fong Chan, Eva Marand et Stephen M Martin, "Novel zwitterion functionalized carbon nanotube nanocomposite membranes for improved RO performance and surface anti-biofouling resistance", *Journal of Membrane Science* 509, 125–137 (2016).

[130] Robert L McGinnis, Kevin Reimund, Jian Ren, Lingling Xia, Maqsud R Chowdhury, Xuanhao Sun, Maritza Abril, Joshua D Moon, Melanie M Merrick, Jaesung Park et al., "Large-scale polymeric carbon nanotube membranes with sub–1.27-nm pores", *Science advances* 4(3), e1700938 (2018).

[131] Alessandro Bianciardi, Caterina Credi, Marinella Levi, Francesco Rosa et Alessandro Zecca, "Biomimicry thinking: methodological improvements and practical implementation", *Bioinspired, Biomimetic and Nanobiomaterials* 6(2), 87–101 (2017).

[132] Bryan D McCloskey, Ho Bum Park, Hao Ju, Brandon W Rowe, Daniel J Miller et Benny D Freeman, "A bioinspired fouling-resistant surface modification for water purification membranes", *Journal of membrane science* 413, 82–90 (2012).

[133] Haeshin Lee, Shara M Dellatore, William M Miller et Phillip B Messersmith, "Mussel-inspired surface chemistry for multifunctional coatings", *science* 318(5849), 426–430 (2007).

[134] Yan Lv, Hao-Cheng Yang, Hong-Qing Liang, Ling-Shu Wan et Zhi-Kang Xu, "Nanofiltration membranes via co-deposition of polydopamine/polyethylenimine followed by cross-linking", *Journal of Membrane Science* 476, 50–58 (2015).

[135] Hongcai Gao, Yimin Sun, Jiajing Zhou, Rong Xu et Hongwei Duan, "Mussel-inspired synthesis of polydopamine-functionalized graphene hydrogel as reusable adsorbents for water purification", *ACS applied materials & interfaces* 5(2), 425–432 (2013).

[136] DE Azzi, Marc El Beyrouthy et al., "How Emerging Technologies and Biomimicry can Help Solving Water Problems: Desert case Studies", *Adv Crop Sci Tech* 3, e130 (2015).

[137] José Guadarrama-Cetina, Anne Mongruel, M-G Medici, Enrique Baquero, AR Parker, I Milimouk-Melnytchuk, Wenceslao González-Viñas et D Beysens, "Dew condensation on desert beetle skin", *The European Physical Journal E* 37(11), 109 (2014).

[138] Natalia Vladimirovna Chevtchik, Michele Fedecostante, Jitske Jansen, Milos Mihajlovic, Martijn Wilmer, Marieke Rüth, Rosalinde Masereeuw et Dimitrios Stamatialis, "Upscaling of a living membrane for bioartificial kidney device", *European journal of pharmacology* 790, 28–35 (2016).

[139] Anthony P Davis, David N Sheppard et Bradley D Smith, "Development of synthetic membrane transporters for anions", *Chemical Society Reviews* 36(2), 348–357 (2007).

[140] Kai Xiao, Lu Chen, Ganhua Xie, Pei Li, Xiang-Yu Kong, Liping Wen et Lei Jiang, "Bio-Inspired Dumbbell-Shaped Nanochannel with Controllable Structure and Ionic Rectification", *Nanoscale* (2018).

[141] Jongho Lee, Anthony P Straub et Menachem Elimelech, "Vapor-gap membranes for highly selective osmotically driven desalination", *Journal of Membrane Science* (2018).

[142] Jieke Jiang, Hengdi Zhang, Wenqing He, Tianzhong Li, Hualin Li, Peng Liu, Meijin Liu, Zhaoyue Wang, Zuankai Wang et Xi Yao, "Adhesion of Microdroplets on Water-Repellent Surfaces toward the Prevention of Surface Fouling and Pathogen Spreading by Respiratory Droplets", *ACS applied materials & interfaces* 9(7), 6599–6608 (2017).

[143] Han Chen, Hao-Ran Liu, Xi-Yun Lu et Hang Ding, "Entrapping an impacting particle at a liquid–gas interface", *Journal of Fluid Mechanics* 841, 1073–1084 (2018).

[144] Marc Fouet, M-A Mader, Sabri Iraïn, Zineb Yanha, Antoine Naillon, Sébastien Cargou, A-M Gué et Pierre Joseph, "Filter-less submicron hydrodynamic size sorting", *Lab on a Chip* 16(4), 720–733 (2016).

[145] Ghulam Destgeer, Kyung Heon Lee, Jin Ho Jung, Anas Alazzam et Hyung Jin Sung, "Continuous separation of particles in a PDMS microfluidic channel via travelling surface acoustic waves (TSAW)", *Lab on a Chip* 13(21), 4210–4216 (2013).

[146] Armaghan Fakhfouri, Citsabehsan Devendran, David J Collins, Ye Ai et Adrian Neild, "Virtual membrane for filtration of particles using surface acoustic waves (SAW)", *Lab on a Chip* 16(18), 3515–3523 (2016).

[147] JA McCammon, "Protein dynamics", *Reports on Progress in Physics* 47(1), 1 (1984).

[148] Prabuddha Mukherjee, Itamar Kass, Isaiah T Arkin et Martin T Zanni, "Picosecond dynamics of a membrane protein revealed by 2D IR", *Proceedings of the National Academy of Sciences of the United States of America* 103(10), 3528–3533 (2006).

[149] Katherine Henzler-Wildman et Dorothee Kern, "Dynamic personalities of proteins", *Nature* 450(7172), 964–972 (2007).

[150] A Joshua Wand, "Dynamic activation of protein function: a view emerging from NMR spectroscopy", *Nature Structural & Molecular Biology* 8(11), 926–931 (2001).

[151] Sergei Yu Noskov, Simon Berneche et Benoît Roux, "Control of ion selectivity in potassium channels by electrostatic and dynamic properties of carbonyl ligands", *Nature* 431(7010), 830–834 (2004).

[152] Gira Bhabha, Jeeyeon Lee, Damian C Ekiert, Jongsik Gam, Ian A Wilson, H Jane Dyson, Stephen J Benkovic et Peter E Wright, "A dynamic knockout reveals that conformational fluctuations influence the chemical step of enzyme catalysis", *Science* 332(6026), 234–238 (2011).

[153] Guanghong Wei, Wenhui Xi, Ruth Nussinov et Buyong Ma, "Protein ensembles: how does nature harness thermodynamic fluctuations for life? The diverse functional roles of conformational ensembles in the cell", *Chemical reviews* 116(11), 6516–6551 (2016).

[154] Toby W Allen, Serdar Kuyucak et Shin-Ho Chung, "Molecular dynamics study of the KcsA potassium channel", *Biophysical journal* 77(5), 2502–2516 (1999).

[155] Orr H Shapiro, Vicente I Fernandez, Melissa Garren, Jeffrey S Guasto, François P Debaillon-Vesque, Esti Kramarsky-Winter, Assaf Vardi et Roman Stocker, "Vortical ciliary flows actively enhance mass transport in reef corals", *Proceedings of the National Academy of Sciences* 111(37), 13391–13396 (2014).

[156] Klaus F Rinne, Stephan Gekle, Douwe Jan Bonthuis et Roland R Netz, "Nanoscale pumping of water by AC electric fields", *Nano letters* 12(4), 1780–1783 (2012).

[157] Jia Geng, Kyunghoon Kim, Jianfei Zhang, Artur Escalada, Ramya Tunuguntla, Luis R Comolli, Frances I Allen, Anna V Shnyrova, Kang Rae Cho, Dayannara Munoz et al., "Stochastic transport through carbon nanotubes in lipid bilayers and live cell membranes", *Nature* 514(7524), 612 (2014).

[158] Gerhard Hummer, Jayendran C Rasaiah et Jerzy P Noworyta, "Water conduction through the hydrophobic channel of a carbon nanotube", *Nature* 414(6860), 188 (2001).

[159] Hyung Gyu Park et Yousung Jung, "Carbon nanofluidics of rapid water transport for energy applications", *Chemical Society Reviews* 43(2), 565–576 (2014).

[160] Shirui Guo, Eric R Meshot, Tevye Kuykendall, Stefano Cabrini et Francesco Fornasiero, "Nanofluidic transport through isolated carbon nanotube channels: Advances, controversies, and challenges", *Advanced Materials* 27(38), 5726–5737 (2015).

[161] Abdelhamid Maali, Touria Cohen-Bouhacina et Hamid Kellay, "Measurement of the slip length of water flow on graphite surface", *Applied Physics Letters* 92(5), 053101 (2008).

[162] RK Joshi, Paola Carbone, Feng-Chao Wang, Vasyl G Kravets, Ying Su, Irina V Grigorieva, HA Wu, Andre K Geim et Rahul Raveendran Nair, "Precise and ultrafast molecular sieving through graphene oxide membranes", *science* 343(6172), 752–754 (2014).

[163] Sony Joseph et NR Aluru, "Why are carbon nanotubes fast transporters of water?", *Nano letters* 8(2), 452–458 (2008).

[164] Davide Mattia et Yury Gogotsi, "Static and dynamic behavior of liquids inside carbon nanotubes", *Microfluidics and Nanofluidics* 5(3), 289–305 (2008).

[165] M Whitby et N Quirke, "Fluid flow in carbon nanotubes and nanopipes", *Nature Nanotechnology* 2(2), 87 (2007).

[166] Kerstin Falk, Felix Sedlmeier, Laurent Joly, Roland R Netz et Lydéric Bocquet, "Molecular origin of fast water transport in carbon nanotube membranes: superlubricity versus curvature dependent friction", *Nano letters* 10(10), 4067–4073 (2010).

[167] John A Thomas et Alan JH McGaughey, "Reassessing fast water transport through carbon nanotubes", *Nano letters* 8(9), 2788–2793 (2008).

[168] Haitao Liu, Jin He, Jinyao Tang, Hao Liu, Pei Pang, Di Cao, Predrag Krstic, Sony Joseph, Stuart Lindsay et Colin Nuckolls, "Translocation of single-stranded DNA through single-walled carbon nanotubes", *Science* 327(5961), 64–67 (2010).

[169] Eleonora Secchi, Antoine Niguès, Laetitia Jubin, Alessandro Siria et Lydéric Bocquet, "Scaling behavior for ionic transport and its fluctuations in individual carbon nanotubes", *Physical review letters* 116(15), 154501 (2016).

[170] Xingcai Qin, Quanzi Yuan, Yapu Zhao, Shubao Xie et Zhongfan Liu, "Measurement of the rate of water translocation through carbon nanotubes", *Nano letters* 11(5), 2173–2177 (2011).

[171] Ulrich J Lorenz et Ahmed H Zewail, "Observing liquid flow in nanotubes by 4D electron microscopy", *Science* 344(6191), 1496–1500 (2014).

[172] Kyunghoon Kim, Jia Geng, Ramya Tunuguntla, Luis R Comolli, Costas P Grigoropoulos, Caroline M Ajo-Franklin et Aleksandr Noy, "Osmotically-driven transport in carbon nanotube porins", *Nano letters* 14(12), 7051–7056 (2014).

[173] Isaac Newton, *Philosophiae naturalis principia mathematica*, volume 1, G. Brookman (1833).

[174] Daniel Bernoulli, *Hydrodynamica: sive de viribus et motibus fluidorum commentarii*, (1738).

[175] Jean Le Rond d'Alembert, *Essai d'une nouvelle théorie de la résistance des fluides*, David l'aîné (1752).

[176] L Euler, "Principes généraux du mouvement de fluides, mémoire de l'académie des Sciences de Berlin, 11", (1755).

[177] CLMH Navier, "Mémoire sur les lois du mouvement des fluides", *Mémoires de l'Académie Royale des Sciences de l'Institut de France* 6(1823), 389–440 (1823).

[178] Georges Gabriel Stokes, "On the theories of the internal friction of fluids in motion, and of the equilibrium and motion of elastic solids", *Transactions of the Cambridge Philosophical Society* 8 (1880).

[179] O Reynolds, "An experimental investigation of the circumstances which determine whether the motion of water shall be direct or sinuous, and of the law of resistance in parallel channels", *Philosophical Trans Royal Society of* 1, 935–82 (1883).

[180] Ludwig Prandtl, "Über Flussigkeitsbewegung bei sehr kleiner Reibung", *Verhandl. III, Internat. Math.-Kong., Heidelberg, Teubner, Leipzig, 1904* pages 484–491 (1904).

[181] L. Boltzmann, "Weitere Studien über das Wärmegleichgewicht unter Gasmolekülen", *Sitzungs. Akad. Wiss. Wien* 66, 275?370 (1872).

[182] James Clerk Maxwell et al., "IV. On the dynamical theory of gases", *Philosophical transactions of the Royal Society of London* 157, 49–88 (1867).

[183] Sydney Chapman, "VI. On the law of distribution of molecular velocities, and on the theory of viscosity and thermal conduction, in a non-uniform simple monatomic gas", *Phil. Trans. R. Soc. Lond. A* 216(538-548), 279–348 (1916).

[184] David Enskog, "Kinetische Theorie der Vorgänge in mässig verdünnten Gasen.", (1917).

[185] J Clerk Maxwell, "On Stresses in Rarefied Gases Arising from Inequalities of Temperature.", *Proceedings of the Royal Society of London* 27, 304–308 (1878).

[186] François Coron, "Derivation of slip boundary conditions for the Navier-Stokes system from the Boltzmann equation", *Journal of Statistical Physics* 54(3-4), 829–857 (1989).

[187] François Golse, "From the Boltzmann equation to the Euler equations in the presence of boundaries", *Computers & Mathematics with Applications* 65(6), 815–830 (2013).

[188] Nader Masmoudi et Laure Saint-Raymond, "From the Boltzmann equation to the Stokes-Fourier system in a bounded domain", *Communications on pure and applied mathematics* 56(9), 1263–1293 (2003).

[189] Lydéric Bocquet et Jean-Louis Barrat, "Flow boundary conditions from nano-to micro-scales", *Soft matter* 3(6), 685–693 (2007).

[190] Lydéric Bocquet et Jean-Louis Barrat, "Hydrodynamic boundary conditions, correlation functions, and Kubo relations for confined fluids", *Physical review E* 49(4), 3079 (1994).

[191] Jean-Louis Barrat et Lydéric Bocquet, "Large slip effect at a nonwetting fluid-solid interface", *Physical review letters* 82(23), 4671 (1999).

[192] Elizabeth D Smith, Mark O Robbins et Marek Cieplak, "Friction on adsorbed monolayers", *Physical Review B* 54(11), 8252 (1996).

[193] Eric Lauga et Howard A Stone, "Effective slip in pressure-driven Stokes flow", *Journal of Fluid Mechanics* 489, 55–77 (2003).

[194] Cécile Cottin-Bizonne, Jean-Louis Barrat, Lydéric Bocquet et Elisabeth Charlaix, "Low-friction flows of liquid at nanopatterned interfaces", *Nature materials* 2(4), 237 (2003).

[195] Chiara Neto, Drew R Evans, Elmar Bonaccurso, Hans-Jürgen Butt et Vincent SJ Craig, "Boundary slip in Newtonian liquids: a review of experimental studies", *Reports on Progress in Physics* 68(12), 2859 (2005).

[196] Jacob N Israelachvili et Gayle E Adams, "Measurement of forces between two mica surfaces in aqueous electrolyte solutions in the range 0–100 nm", *Journal of the Chemical Society, Faraday Transactions 1: Physical Chemistry in Condensed Phases* 74, 975–1001 (1978).

[197] Gerd Binnig, Calvin F Quate et Ch Gerber, "Atomic force microscope", *Physical review letters* 56(9), 930 (1986).

[198] Jacob N Israelachvili, "Measurement of the viscosity of liquids in very thin films", *Journal of colloid and interface science* 110(1), 263–271 (1986).

[199] C Cottin-Bizonne, S Jurine, J Baudry, J Crassous, F Restagno et E Charlaix, "Nanorheology: an investigation of the boundary condition at hydrophobic and hydrophilic interfaces", *The European Physical Journal E* 9(1), 47–53 (2002).

[200] CL Henry, C Neto, DR Evans, S Biggs et VSJ Craig, "The effect of surfactant adsorption on liquid boundary slippage", *Physica A: Statistical Mechanics and its Applications* 339(1-2), 60–65 (2004).

[201] Eleonora Secchi, Sophie Marbach, Antoine Niguès, Alessandro Siria et Lydéric Bocquet, "The Landau–Squire plume", *Journal of Fluid Mechanics* 826 (2017).

[202] Nadanai Laohakunakorn, Benjamin Gollnick, Fernando Moreno-Herrero, Dirk GAL Aarts, Roel PA Dullens, Sandip Ghosal et Ulrich F Keyser, "A landau–squire nanojet", *Nano letters* 13(11), 5141–5146 (2013).

[203] Jens Eggers et Emmanuel Villermaux, "Physics of liquid jets", *Reports on progress in physics* 71(3), 036601 (2008).

[204] He B Squire, "The round laminar jet", *The Quarterly Journal of Mechanics and Applied Mathematics* 4(3), 321–329 (1951).

[205] Lev Davidovich Landau et EM Lifshitz, *Course of Theoretical Physics Vol. 6 Fluid Mechanies*, Pergamon Press (1959).

[206] Ralph Allen Sampson, "On Stokes's current function", *Philosophical Transactions of the Royal Society of London. A* 182, 449–518 (1891).

[207] Uffe Høgsbro Thygesen et Thomas Kiørboe, "Diffusive transport in Stokeslet flow and its application to plankton ecology", *Journal of mathematical biology* 53(1), 1–14 (2006).

[208] Davide Mattia, Hannah Leese et Kah Peng Lee, "Carbon nanotube membranes: from flow enhancement to permeability", *Journal of Membrane Science* 475, 266–272 (2015).

[209] Mihail Barboiu, "Artificial water channels–incipient innovative developments", *Chemical Communications* 52(33), 5657–5665 (2016).

[210] Francesco Calabrò, KP Lee et D Mattia, "Modelling flow enhancement in nanochannels: Viscosity and slippage", *Applied Mathematics Letters* 26(10), 991–994 (2013).

[211] Davide Mattia et Francesco Calabrò, "Explaining high flow rate of water in carbon nanotubes via solid–liquid molecular interactions", *Microfluidics and Nanofluidics* 13(1), 125–130 (2012).

[212] Patricia Ternes, Alejandro Mendoza-Coto et Evy Salcedo, "Single-file mobility of water-like fluid in a generalized Frenkel-Kontorova model", *The Journal of chemical physics* 147(3), 034510 (2017).

[213] ME Suk, AV Raghunathan et NR Aluru, "Fast reverse osmosis using boron nitride and carbon nanotubes", *Applied Physics Letters* 92(13), 133120 (2008).

[214] Tamsyn A Hilder, Daniel Gordon et Shin-Ho Chung, "Salt rejection and water transport through boron nitride nanotubes", *Small* 5(19), 2183–2190 (2009).

[215] Gabriele Tocci, Laurent Joly et Angelos Michaelides, "Friction of water on graphene and hexagonal boron nitride from ab initio methods: very different slippage despite very similar interface structures", *Nano letters* 14(12), 6872–6877 (2014).

[216] Benoit Grosjean, Clarisse Pean, Alessandro Siria, Lydéric Bocquet, Rodolphe Vuilleumier et Marie-Laure Bocquet, "Chemisorption of hydroxide on 2D materials from DFT calculations: graphene versus hexagonal boron nitride", *The journal of physical chemistry letters* 7(22), 4695–4700 (2016).

[217] JB Sokoloff, "Enhancement of the water flow velocity through carbon nanotubes resulting from the radius dependence of the friction due to electron excitations", *Physical Review E* 97(3), 033107 (2018).

[218] Xingfei Wei et Tengfei Luo, "Effects of Electrostatic Interaction and Chirality on the Friction Coefficient of Water Flow Inside Single-Walled Carbon Nanotubes and Boron Nitride Nanotubes", *The Journal of Physical Chemistry C* 122(9), 5131–5140 (2018).

[219] Michael Thomas et Ben Corry, "A computational assessment of the permeability and salt rejection of carbon nanotube membranes and their application to water desalination", *Phil. Trans. R. Soc. A* 374(2060), 20150020 (2016).

[220] Dietrich Einzel, Peter Panzer et Mario Liu, "Boundary condition for fluid flow: curved or rough surfaces", *Physical review letters* 64(19), 2269 (1990).

[221] Dragoş Iftimie et Franck Sueur, "Viscous boundary layers for the Navier–Stokes equations with the Navier slip conditions", *Archive for rational mechanics and analysis* 199(1), 145–175 (2011).

[222] BV Levich, "Bubble motion at high Reynolds numbers", *Zh. Eksp. Theoret. Fiz.* 19, 18–24 (1949).

[223] DW Moore, "The boundary layer on a spherical gas bubble", *Journal of Fluid Mechanics* 16(2), 161–176 (1963).

[224] Jacques Louis Lions, "Quelques méthodes de résolution des problemes aux limites non linéaires", (1969).

[225] Yuelong Xiao et Zhouping Xin, "On the vanishing viscosity limit for the 3D Navier-Stokes equations with a slip boundary condition", *Communications on pure and applied mathematics* 60(7), 1027–1055 (2007).

[226] H Beirao da Veiga et Francesca Crispo, "Concerning the Wk, p-inviscid limit for 3-D flows under a slip boundary condition", *Journal of Mathematical Fluid Mechanics* 13(1), 117–135 (2011).

[227] Luigi C Berselli et Stefano Spirito, "On the Boussinesq system: regularity criteria and singular limits", *Methods and Applications of Analysis* 18(4), 391–416 (2011).

[228] Lizhen Wang, Zhouping Xin et Aibin Zang, "Vanishing viscous limits for 3D Navier–Stokes equations with a Navier-slip boundary condition", *Journal of Mathematical Fluid Mechanics* 14(4), 791–825 (2012).

[229] Siegfried Maier et Juergen Saal, "Stokes and Navier-Stokes equations with perfect slip on wedge type domains", *Discrete and Continuous Dynamical Systems, Series S* 7(5), 1045–1063 (2014).

[230] Xin Zhong, "Vanishing viscosity limits for the 3D Navier-Stokes equations with a slip boundary condition", *Proceedings of the American Mathematical Society* 145(4), 1615–1628 (2017).

[231] F Brochard et PG De Gennes, "Shear-dependent slippage at a polymer/solid interface", *Langmuir* 8(12), 3033–3037 (1992).

[232] Peter A Thompson et Sandra M Troian, "A general boundary condition for liquid flow at solid surfaces", *Nature* 389(6649), 360 (1997).

[233] Mark Ilton, Thomas Salez, Paul D Fowler, Marco Rivetti, Mohammed Aly, Michael Benzaquen, Joshua D McGraw, Elie Raphaël, Kari Dalnoki-Veress et Oliver Bäumchen, "Beyond the Navier-de Gennes paradigm: slip inhibition on ideal substrates", *arXiv preprint arXiv:1708.03420* (2017).

[234] Ken Kamrin et Howard A Stone, "The symmetry of mobility laws for viscous flow along arbitrarily patterned surfaces", *Physics of Fluids* 23(3), 031701 (2011).

[235] John Happel et Howard Brenner, *Low Reynolds number hydrodynamics: with special applications to particulate media*, volume 1, Springer Science & Business Media (2012).

[236] Dirk Olbers, Jürgen Willebrand et Carsten Eden, *Ocean dynamics*, Springer Science & Business Media (2012).

[237] HH Winter, "Viscous dissipation term in energy equations", *Calculation and Measurement Techniques for Momentum, Energy and Mass Transfer* 7, 27–34 (1987).

[238] Jingxian Zhang, Haiping Tian, Zhaohui Yao, Pengfei Hao et Nan Jiang, "Evolutions of hairpin vortexes over a superhydrophobic surface in turbulent boundary layer flow", *Physics of Fluids* 28(9), 095106 (2016).

[239] Michael B Martell, J Blair Perot et Jonathan P Rothstein, "Direct numerical simulations of turbulent flows over superhydrophobic surfaces", *Journal of Fluid Mechanics* 620, 31–41 (2009).

[240] Robert J Daniello, Nicholas E Waterhouse et Jonathan P Rothstein, "Drag reduction in turbulent flows over superhydrophobic surfaces", *Physics of Fluids* 21(8), 085103 (2009).

[241] Angela Busse, Neil D Sandham, Glen McHale et Michael I Newton, "Change in drag, apparent slip and optimum air layer thickness for laminar flow over an idealised superhydrophobic surface", *Journal of Fluid Mechanics* 727, 488–508 (2013).

[242] Pranesh Muralidhar, Nangelie Ferrer, Robert Daniello et Jonathan P Rothstein, "Influence of slip on the flow past superhydrophobic circular cylinders", *Journal of Fluid Mechanics* 680, 459–476 (2011).

[243] Dominique Legendre, Eric Lauga et Jacques Magnaudet, "Influence of slip on the dynamics of two-dimensional wakes", *Journal of fluid mechanics* 633, 437–447 (2009).

[244] Ivan U Vakarelski, Jeremy O Marston, Derek YC Chan et Sigurdur T Thoroddsen, "Drag reduction by Leidenfrost vapor layers", *Physical review letters* 106(21), 214501 (2011).

[245] Ivan U Vakarelski, Joseph D Berry, Derek YC Chan et Sigurdur T Thoroddsen, "Leidenfrost vapor layers reduce drag without the crisis in high viscosity liquids", *Physical review letters* 117(11), 114503 (2016).

[246] Joseph D Berry, Ivan U Vakarelski, Derek YC Chan et Sigurdur T Thoroddsen, "Navier slip model of drag reduction by Leidenfrost vapor layers", *Physics of Fluids* 29(10), 107104 (2017).

[247] Lin Guo, Shiyi Chen et Mark O Robbins, "Slip boundary conditions over curved surfaces", *Physical Review E* 93(1), 013105 (2016).

[248] Ben Corry, "Designing carbon nanotube membranes for efficient water desalination", *The Journal of Physical Chemistry B* 112(5), 1427–1434 (2008).

[249] Bruce J Hinds, Nitin Chopra, Terry Rantell, Rodney Andrews, Vasilis Gavalas et Leonidas G Bachas, "Aligned multiwalled carbon nanotube membranes", *Science* 303(5654), 62–65 (2004).

[250] Mainak Majumder, Nitin Chopra et Bruce J Hinds, "Effect of tip functionalization on transport through vertically oriented carbon nanotube membranes", *Journal of the American Chemical Society* 127(25), 9062–9070 (2005).

[251] Ben Corry, "Water and ion transport through functionalised carbon nanotubes: implications for desalination technology", *Energy & Environmental Science* 4(3), 751–759 (2011).

[252] Wai-Fong Chan, Hang-yan Chen, Anil Surapathi, Michael G Taylor, Xiaohong Shao, Eva Marand et J Karl Johnson, "Zwitterion functionalized carbon nanotube/polyamide nanocomposite membranes for water desalination", *Acs Nano* 7(6), 5308–5319 (2013).

[253] Tian-Yin Liu, Hao-Ge Yuan, Qian Li, Yuan-Hui Tang, Qiang Zhang, Weizhong Qian, Bart Van der Bruggen et Xiaolin Wang, "Ion-responsive channels of zwitterion-carbon nanotube membrane for rapid water permeation and ultrahigh mono-/multivalent ion selectivity", *ACS nano* 9(7), 7488–7496 (2015).

[254] Hui Ying Yang et Rohit Karnik, "Membrane for filtrating water"(2018). US Patent 9,873,092.

[255] Jia Liu, Chuan Wang, Xiaomin Tu, Bilu Liu, Liang Chen, Ming Zheng et Chongwu Zhou, "Chirality-controlled synthesis of single-wall carbon nanotubes using vapour-phase epitaxy", *Nature Communications* 3, 1199 (2012).

[256] Juan Ramon Sanchez-Valencia, Thomas Dienel, Oliver Gröning, Ivan Shorubalko, Andreas Mueller, Martin Jansen, Konstantin Amsharov, Pascal Ruffieux et Roman Fasel, "Controlled synthesis of single-chirality carbon nanotubes", *Nature* 512(7512), 61 (2014).

[257] Meagan S Mauter, Menachem Elimelech et Chinedum O Osuji, "Nanocomposites of vertically aligned single-walled carbon nanotubes by magnetic alignment and polymerization of a lyotropic precursor", *Acs Nano* 4(11), 6651–6658 (2010).

[258] Chao Xu, Aiju Cui, Yuelian Xu et Xianzhi Fu, "Graphene oxide–TiO2 composite filtration membranes and their potential application for water purification", *Carbon* 62, 465–471 (2013).

[259] B Radha, A Esfandiar, FC Wang, AP Rooney, K Gopinadhan, A Keerthi, A Mishchenko, A Janardanan, P Blake, L Fumagalli et al., "Molecular transport through capillaries made with atomic-scale precision", *Nature* 538(7624), 222 (2016).

[260] TC Broyer, "The movement of materials into plants Part I. Osmosis and the movement of water into plants", *The Botanical Review* 13(1), 1–58 (1947).

[261] SM Henton, AJ Greaves, GJ Piller et PEH Minchin, "Revisiting the Münch pressure–flow hypothesis for long-distance transport of carbohydrates: modelling the dynamics of solute transport inside a semipermeable tube", *Journal of Experimental Botany* 53(373), 1411–1419 (2002).

[262] R Greger et U Windhorst, "Comprehensive human physiology", *From Cellular Mechanisms to Integration* 2 (1996).

[263] P. H. Baylis, "Water and salt homeostasis in hearlth and disease-foreword"(1989).

[264] John L Stephenson, "Concentration of urine in a central core model of the renal counterflow system", *Kidney international* 2(2), 85–94 (1972).

[265] Paul J Palatt et Gerald M Saidel, "Countercurrent exchange in the inner renal medulla: vasa recta-descending limb system", *Bulletin of mathematical biology* 35(4), 431–447 (1973).

[266] S Randall Thomas, "Inner medullary lactate production and accumulation: a vasa recta model", *American Journal of Physiology-Renal Physiology* 279(3), F468–F481 (2000).

[267] David Foster, John A Jacquez et Eugene Daniels, "Solute concentration in the kidney—II. Input-output studies on a central core model", *Mathematical Biosciences* 32(3-4), 337–360 (1976).

[268] Anita T Layton, "A mathematical model of the urine concentrating mechanism in the rat renal medulla. I. Formulation and base-case results", *American Journal of Physiology-Renal Physiology* 300(2), F356–F371 (2010).

[269] Aurélie Edwards, "Modeling transport in the kidney: investigating function and dysfunction", *American Journal of Physiology-Renal Physiology* 298(3), F475–F484 (2009).

[270] Sophie Marbach et Lydéric Bocquet, "Active osmotic exchanger for efficient nanofiltration inspired by the kidney", *Physical Review X* 6(3), 031008 (2016).

[271] Gambro, "Phoenix x 36 brochure"(2009).

[272] Jeffrey T Borenstein, Eli J Weinberg, Brian K Orrick, Cathryn Sundback, Mohammad R Kaazempur-Mofrad et Joseph P Vacanti, "Microfabrication of three-dimensional engineered scaffolds", *Tissue engineering* 13(8), 1837–1844 (2007).

[273] Jeong Chul Kim, Francesco Garzotto, Federico Nalesso, Dinna Cruz, Ji Hyun Kim, Eungtaek Kang, Hee Chan Kim et Claudio Ronco, "A wearable artificial kidney: technical requirements and potential solutions", *Expert review of medical devices* 8(5), 567–579 (2011).

[274] Paolo Armignacco, Francesco Garzotto, Mauro Neri, Anna Lorenzin et Claudio Ronco, "Wak engineering evolution", *Blood purification* 39(1-3), 110–114 (2015).

[275] R. Greger et E. Schlatter, "Properties of the basolateral membrane of the cortical thick ascending limb of henle's loop of rabbit kidney", *Pflügers Arch.* 396, 325–334 (1983).

[276] C.-L. Chou, M.A. Knepper, A.N. Hoek, D. Brown, B. Yang, T. Ma et A.S. Verkman, "Reduced water permeability and altered ultrastructure in thin descending limb of Henle in aquaporin-1 null mice", *J. Clin. Invest.* 103, 491–496 (1999).

[277] S. Nielsen, J. Frøkiaer, D. Marples, T.H. Kwon, P. Agre et Knepper M.A., "Aquaporins in the kidney: from molecules to medicine", *Physiol. Rev.* 82, 205–244 (2002).

[278] R. Greger et E. Schlatter, "Presence of luminal K+, a prerequisite for active NaCl transport in the cortical thick ascending limb of henle's loop of rabbit kidney", *Pflügers Arch.* 392, 92–94 (1981).

[279] J. A. Jacquez, D. Foster et E. Daniels, "Solute concentration in the kidney - I. A model of the renal medulla and its limit cases", *Mathematical biosciences* 32, 307–335 (1976).

[280] J. Stephenson, "Concentration engines and the kidney : I. Central core model of the renal medulla", *Biophys. J.* 13, 512–545 (1973).

[281] J. Stephenson, "Concentration engines and the kidney : II. Multisolute central core systems", *Biophys. J.* 13, 546–567 (1973).

[282] J. Stephenson, "Concentration engines and the kidney : III - Canonical mass balance equation for multinephron models of the renal medulla", *Biophys. J.* 16, 1273–1286 (1976).

[283] J. Stephenson, R. Tewarson et R. Mejia, "Quantitative analysis of mass and energy balance in non-ideal models of the renal counterflow system", *Proc. Nat. Acad. Sci. USA* 71, 1618–1622 (1974).

[284] J. Stephenson, "Models of the urinary concentrating mechanism", *Kidney Int.* 31, 648–661 (1987).

[285] M. A. Knepper, R. A. Danielson, Saidel G. M. et R. S. Post, "Quantitative analysis of renal medullary anatomy in rats and rabbits", *Kidney Int.* 12, 313–323 (1977).

[286] L. Koepsell, W. Kriz et J. Schnermann, "Pattern of luminal diameter changes along the descending and ascending thin limbs of the loop of Henle in the inner medullary zone of the rat kidney", *Z. Anat. Entwickl.-Gesch.* 138, 321–328 (1972).

[287] Finkelstein A., *Water movement through lipid bilayers, pores, and plasma membranes*, John Wiley & Sons (1987).

[288] B. Yang et J. M. Sands, *Urea Transporters*, Springer Science+ Business Media Dordrecht (2014).

[289] R. P. Garay et P. J. Garrahan, "The interaction of sodium and potassium with the sodium pump in red cells", *J. Physiol.* 231, 297–325 (1973).

[290] J. Newburgh, "The changes which alter renal osmotic work", *J. Clin. Invest.* 22, 439–446 (1943).

[291] A. Layton, "Mathematical modeling of kidney transport", *Wiley Interdiscip. Rev. Syst. Biol. Med.* 5, 557–73 (2013).

[292] B. Hargitay et W. Kuhn, "The multiplication principle as the basis for concentrating urine in the kidney", *J. Am. Soc. Nephrol.* (2001).

[293] S. Hervy et S. Randall Thomas, "Inner medullary lactate production and urine-concentrating mechanism: a flat medullary model", *Am. J. Physiol. Renal Physiol.* (2003).

[294] B. Alberts, Julian Lewis, Martin Raff, Keith Roberts et Peter Walter, *Molecular Biology of the Cell, 4th edition*, Garland-Science, New-York (2002).

[295] J. W. Post, Joost Veerman, Hubertus V.M. Hamelers, Gerrit J.W. Euverink, Sybrand J. Metz, Kitty Nymeijer et Cees J.N. Buisman, "Salinity-gradient power: evaluation of pressure-retarded osmosis and reverse electrodialysis", *J. Memb. Sci.* 288, 218–230 (2007).

[296] B. B. Sales, M. Saakes, J. W. Post, C. J. N. Buisman, P. M. Biesheuvel et H. V. M. Hamelers, "Direct power production from a water salinity difference in a membrane-modified supercapacitor flow cell", *Environ. Sci. Technol.* 44, 5661–5665 (2010).

[297] J. de Jong, R. G. H. Lammerink et M. Wessling, "Membranes and microfluidics: a review", *Lab Chip* 6, 1125–1139 (2006).

[298] Drago Sticker, Mario Rothbauer, Sarah Lechner, Marie-Therese Hehenberger et Peter Ertl, "Multi-layered, membrane-integrated microfluidics based on replica molding of a thiol–ene epoxy thermoset for organ-on-a-chip applications", *Lab on a Chip* 15(24), 4542–4554 (2015).

[299] Bor-han Chueh, Dongeun Huh, Christina R Kyrtsos, Timothée Houssin, Nobuyuki Futai et Shuichi Takayama, "Leakage-free bonding of porous membranes into layered microfluidic array systems", *Analytical chemistry* 79(9), 3504–3508 (2007).

[300] W.H. Fissell, H.D. Humes, A.J. Fleischman et Roy S., "Dialysis and Nanotechnology: Now, 10 Years, or Never?", *Blood Purif.* 25, 12–17 (2007).

[301] Allen R Nissenson, Claudio Ronco, Gayle Pergamit, Martin Edelstein et Richard Watts, "The human nephron filter: toward a continuously functioning, implantable artificial nephron system", *Blood purification* 23(4), 269–274 (2005).

[302] Allen R Nissenson, Claudio Ronco, Gayle Pergamit, Martin Edelstein et Richard Watts, "Continuously functioning artificial nephron system: the promise of nanotechnology", *Hemodialysis International* 9(3), 210–217 (2005).

[303] E Weinberg, M Kaazempur-Mofrad et J Borenstein, "Concept and computational design for a bioartificial nephron-on-a-chip", *The International journal of artificial organs* 31(6), 508–514 (2008).

[304] Laura Ha, Kyung-Jin Jang et Kahp-Yang Suh. "Kidney on a chip". In *Microfluidics for Medical Applications*, pages 19–39. (2014).

[305] Ye Gu et Norihisa Miki, "Multilayered microfilter using a nanoporous PES membrane and applicable as the dialyzer of a wearable artificial kidney", *Journal of Micromechanics and Microengineering* 19(6), 065031 (2009).

[306] Hongkai Wu, Teri W Odom, Daniel T Chiu et George M Whitesides, "Fabrication of complex three-dimensional microchannel systems in PDMS", *Journal of the American Chemical Society* 125(2), 554–559 (2003).

[307] Antoine Naillon, Hajar Massadi, Rémi Courson, Jean Bekhit, Lucie Seveno, Pierre-François Calmon, Marc Prat et Pierre Joseph, "Quasi-static drainage in a network of nanoslits of non-uniform depth designed by grayscale laser lithography", *Microfluidics and Nanofluidics* 21(8), 131 (2017).

[308] Vincent Liu, Yong-Ak Song et Jongyoon Han, "Capillary-valve-based fabrication of ion-selective membrane junction for electrokinetic sample preconcentration in PDMS chip", *Lab on a Chip* 10(11), 1485–1490 (2010).

[309] A Caliò, J Leng, J Decock, L De Stefano et JB Salmon, "Microscopy assisted fabrication of a hydrogel-based microfluidic filter", *Journal of the European Optical Society-Rapid publications* 10 (2015).

[310] Jérémy Decock, Mathias Schlenk et Jean-Baptiste Salmon, "In-situ photo-patterning of pressure-resistant hydrogel membranes with controlled permeabilities in PEGDA microfluidic channels", *Lab on a Chip* (2018).

[311] Z Siwy et A Fuliński, "Fabrication of a synthetic nanopore ion pump", *Physical Review Letters* 89(19), 198103 (2002).

[312] L. Bankir, N. Bouby, M.-M. Trinh-Trang-Tan et B. Kaissling, "Thick ascending limb - anatomy and function: role in urine concentrating mechanisms", *Adv. Nephrol.* 16, 69–102 (1987).

[313] David L Goldstein et Eldon J Braun, "Proportions of mammalian-type and reptilian-type nephrons in the kidneys of two passerine birds", *journal of Morphology* 187(2), 173–179 (1986).

[314] Fouad Khalil et Joseph Tawfic, "Some observations on the kidney of the desert J. jaculus and G. gerbillus and their possible bearing on the water economy of these animals", *Journal of Experimental Zoology Part A: Ecological Genetics and Physiology* 154(3), 259–271 (1963).

[315] William H Dantzler et Eldon J Braun, "Comparative nephron function in reptiles, birds, and mammals", *American Journal of Physiology-Regulatory, Integrative and Comparative Physiology* 239(3), R197–R213 (1980).

[316] CAROL A Beuchat, "Body size, medullary thickness, and urine concentrating ability in mammals", *American Journal of Physiology-Regulatory, Integrative and Comparative Physiology* 258(2), R298–R308 (1990).

[317] RJ Gibson, "The Atlantic salmon in fresh water: spawning, rearing and production", *Reviews in fish biology and fisheries* 3(1), 39–73 (1993).

[318] Neil Hammerschlag, "Osmoregulation in elasmobranchs: a review for fish biologists, behaviourists and ecologists", *Marine and Freshwater Behaviour and Physiology* 39(3), 209–228 (2006).

[319] Neil Hazon, Alan Wells, Richard D Pillans, Jonathan P Good, W Gary Anderson et Craig E Franklin, "Urea based osmoregulation and endocrine control in elasmobranch fish with special reference to euryhalinity", *Comparative Biochemistry and Physiology Part B: Biochemistry and Molecular Biology* 136(4), 685–700 (2003).

[320] WS Marshall et M Grosell, "Ion transport, osmoregulation, and acid-base balance", *The physiology of fishes* 3, 177–230 (2006).

[321] C. Fritzmann, J. Löwenberg, T. Wintgens et T. Melin, "State-of-the-art reverse osmosis desalination", *Desalination* 216, 1–76 (2007).

[322] R. K. Nagarale, G. S. Gohil et V. K. Shahi, "Recent developments on on-exchange membranes and electro-membrane processes.", *Adv. Colloid Interface Sci.* 119, 97–130 (2006).

[323] J. Li, Ma-li Zhou, Jiu-yang Lin, Wen-yuan Ye, Yan-qing Xu, Jiang-nan Shen, Cong-jie Gao et Bart Van der Bruggen, "Mono-valent cation selective membranes for electrodialysis by introducing polyquaternium-7 in a commercial cation exchange membrane", *Journal of Membrane Science* 486, 89–96 (2015).

[324] S. C. O'Hern, Michael S. H. Boutilier, Juan-Carlos Idrobo, Yi Song, Jing Kong, Tahar Laoui, Muataz Atieh et Rohit. Karnik, "Selective ionic transport through tunable subnanometer pores in single-layer graphene membranes", *Nano Lett.* 14, 1234–1241 (2014).

[325] Avi Ring et John Sandblom, "Measurement of channel lifetime in artificial lipid membranes: dimerization kinetics of gramicidin A", *Journal of Membrane Science* 16, 319–337 (1983).

[326] Martin Karplus, J Andrew McCammon et Warner L Peticolas, "The internal dynamics of globular protein", *Critical Reviews in Biochemistry* 9(4), 293–349 (1981).

[327] Emmanuel Haldoupis, Taku Watanabe, Sankar Nair et David S Sholl, "Quantifying Large Effects of Framework Flexibility on Diffusion in MOFs: CH4 and CO2 in ZIF-8", *ChemPhysChem* 13(15), 3449–3452 (2012).

[328] Ming Ma, François Grey, Luming Shen, Michael Urbakh, Shuai Wu, Jefferson Zhe Liu, Yilun Liu et Quanshui Zheng, "Water transport inside carbon nanotubes mediated by phonon-induced oscillating friction", *Nature nanotechnology* 10(8), 692–695 (2015).

[329] Ming Ma, Gabriele Tocci, Angelos Michaelides et Gabriel Aeppli, "Fast diffusion of water nanodroplets on graphene", *Nature Materials* 15(1), 66 (2016).

[330] Eduardo R Cruz-Chú, Ermioni Papadopoulou, Jens H Walther, Aleksandar Popadić, Gengyun Li, Matej Praprotnik et Petros Koumoutsakos, "On phonons and water flow enhancement in carbon nanotubes", *Nature nanotechnology* 12(12), 1106 (2017).

[331] K Herterich et K Hasselmann, "The horizontal diffusion of tracers by surface waves", *Journal of Physical Oceanography* 12(7), 704–711 (1982).

[332] L. Szilard, "Uber die Entropieverminderung in einem thermodynamischen System bein Eingriffen intelligenter Wesen", *Z. Phys.* 53, 840–856 (1929).

[333] Helen M Berman, John Westbrook, Zukang Feng, Gary Gilliland, Talapady N Bhat, Helge Weissig, Ilya N Shindyalov et Philip E Bourne. "The protein data bank, 1999–". In *International Tables for Crystallography Volume F: Crystallography of biological macromolecules*, pages 675–684. Springer, (2006).

[334] Sophie Marbach et Lydéric Bocquet, "Active sieving across driven nanopores for tunable selectivity", *The Journal of Chemical Physics* 147(15), 154701 (2017).

[335] Zwanzig R., "Rate processes with dynamical disorder", *Acc. Chem. Res.* 23, 148–152 (1990).

[336] R. Zwanzig, "Dynamical disorder: passage through a fluctuating bottleneck", *J. Chem. Phys.* 97, 3587–3589 (1992).

[337] D Beece, L Eisenstein, H Frauenfelder, D Good, MC Marden, L Reinisch, AH Reynolds, LB Sorensen et KT Yue, "Solvent viscosity and protein dynamics", *Biochemistry* 19(23), 5147–5157 (1980).

[338] David R Lide, *CRC handbook of chemistry and physics*, volume 85, CRC press (2004).

[339] Yusuke Sakiyama, Adam Mazur, Larisa E Kapinos et Roderick YH Lim, "Spatiotemporal dynamics of the nuclear pore complex transport barrier resolved by high-speed atomic force microscopy", *Nature nanotechnology* 11(8), 719 (2016).

[340] James M Gere et Barry J Goodno, "Mechanics of Materials 5th", *Brooks Cole* (2001).

[341] A Khan, J Philip et P Hess, "Young's modulus of silicon nitride used in scanning force microscope cantilevers", *Journal of Applied Physics* 95(4), 1667–1672 (2004).

[342] Khashayar Babaei Gavan, Hidde JR Westra, Emile WJM van der Drift, Warner J Venstra et Herre SJ van der Zant, "Size-dependent effective Young's modulus of silicon nitride cantilevers", *Applied Physics Letters* 94(23), 233108 (2009).

[343] Sophie Marbach, David S. Dean et Lydéric Bocquet, "Transport and dispersion across wiggling nano-pores", *submitted* (2018).

[344] Geoffrey Taylor. "Dispersion of soluble matter in solvent flowing slowly through a tube". In *Proceedings of the Royal Society of London A: Mathematical, Physical and Engineering Sciences*, volume 219, pages 186–203. The Royal Society, (1953).

[345] Rutherford Aris. "On the dispersion of a solute in a fluid flowing through a tube". In *Proceedings of the Royal Society of London A: mathematical, physical and engineering sciences*, volume 235, pages 67–77. The Royal Society, (1956).

[346] David Reguera et JM Rubi, "Kinetic equations for diffusion in the presence of entropic barriers", *Physical Review E* 64(6), 061106 (2001).

[347] Paolo Malgaretti, Ignacio Pagonabarraga et J Miguel Rubi, "Entropic electrokinetics: recirculation, particle separation, and negative mobility", *Physical review letters* 113(12), 128301 (2014).

[348] Karen Alim, Gabriel Amselem, François Peaudecerf, Michael P Brenner et Anne Pringle, "Random network peristalsis in Physarum polycephalum organizes fluid flows across an individual", *Proceedings of the National Academy of Sciences* 110(33), 13306–13311 (2013).

[349] Shigeru Kuroda, Seiji Takagi, Toshiyuki Nakagaki et Tetsuo Ueda, "Allometry in Physarum plasmodium during free locomotion: size versus shape, speed and rhythm", *Journal of experimental biology* 218(23), 3729–3738 (2015).

[350] M Tlalka, DP Bebber, PR Darrah, SC Watkinson et MD Fricker, "Emergence of self-organised oscillatory domains in fungal mycelia", *Fungal Genetics and Biology* 44(11), 1085–1095 (2007).

[351] Vincent Démery et David S Dean, "Perturbative path-integral study of active-and passive-tracer diffusion in fluctuating fields", *Physical review E* 84(1), 011148 (2011).

[352] Günther Grün, Klaus Mecke et Markus Rauscher, "Thin-film flow influenced by thermal noise", *Journal of Statistical Physics* 122(6), 1261–1291 (2006).

[353] Klaus Mecke et Markus Rauscher, "On thermal fluctuations in thin film flow", *Journal of Physics: Condensed Matter* 17(45), S3515 (2005).

[354] Cosima Stubenrauch et Regine Von Klitzing, "Disjoining pressure in thin liquid foam and emulsion films—new concepts and perspectives", *Journal of Physics: condensed matter* 15(27), R1197 (2003).

[355] Renate Fetzer, M Rauscher, R Seemann, Karin Jacobs et Klaus Mecke, "Thermal noise influences fluid flow in thin films during spinodal dewetting", *Physical Review Letters* 99(11), 114503 (2007).

[356] Simon Gravelle, Christophe Ybert, Lydéric Bocquet et Laurent Joly, "Anomalous capillary filling and wettability reversal in nanochannels", *Physical Review E* 93(3), 033123 (2016).

[357] F Heslot, N Fraysse et AM Cazabat, "Molecular layering in the spreading of wetting liquid drops", *Nature* 338(6217), 640–642 (1989).

[358] Armand Ajdari et Jacques Prost, "Free-flow electrophoresis with trapping by a transverse inhomogeneous field.", *Proceedings of the National Academy of Sciences* 88(10), 4468–4471 (1991).

[359] Peter Reimann, Christian Van den Broeck, H Linke, Peter Hänggi, JM Rubi et A Pérez-Madrid, "Giant acceleration of free diffusion by use of tilted periodic potentials", *Physical review letters* 87(1), 010602 (2001).

[360] Peter Reimann, Christian Van den Broeck, H Linke, Peter Hänggi, JM Rubi et A Pérez-Madrid, "Diffusion in tilted periodic potentials: Enhancement, universality, and scaling", *Physical Review E* 65(3), 031104 (2002).

[361] T Guérin et DS Dean, "Kubo formulas for dispersion in heterogeneous periodic nonequilibrium systems", *Physical Review E* 92(6), 062103 (2015).

[362] Alessandro Siria et Antoine Niguès, "Electron beam detection of a Nanotube Scanning Force Microscope", *Scientific Reports* 7(1), 11595 (2017).

[363] Walter Fischer et Jürgen Brickmann, "Ion-specific diffusion rates through transmembrane protein channels: a molecular dynamics study", *Biophysical chemistry* 18(4), 323–337 (1983).

[364] Annalisa Fasolino, JH Los et Mikhail I Katsnelson, "Intrinsic ripples in graphene", *Nature materials* 6(11), 858–861 (2007).

[365] Changgu Lee, Xiaoding Wei, Jeffrey W Kysar et James Hone, "Measurement of the elastic properties and intrinsic strength of monolayer graphene", *science* 321(5887), 385–388 (2008).

[366] Hu Qiu, Rong Shen et Wanlin Guo, "Vibrating carbon nanotubes as water pumps", *Nano Research* 4(3), 284–289 (2011).

[367] AM Rao, E Richter, Shunji Bandow, Bruce Chase, PC Eklund, KA Williams, S Fang, KR Subbaswamy, M Menon, A Thess et al., "Diameter-selective Raman scattering from vibrational modes in carbon nanotubes", *Science* 275(5297), 187–191 (1997).

[368] Vera Sazonova, Yuval Yaish, Hande Üstünel, David Roundy, Tomás A Arias et Paul L McEuen, "A tunable carbon nanotube electromechanical oscillator", *Nature* 431(7006), 284–287 (2004).

[369] Daniel Garcia-Sanchez, A San Paulo, MJ Esplandiu, F Perez-Murano, L Forró, A Aguasca et A Bachtold, "Mechanical detection of carbon nanotube resonator vibrations", *Physical review letters* 99(8), 085501 (2007).

[370] Philippe Poncharal, ZL Wang, Daniel Ugarte et Walt A De Heer, "Electrostatic deflections and electromechanical resonances of carbon nanotubes", *science* 283(5407), 1513–1516 (1999).

[371] Sushil K Sarna. "Colonic motility: from bench side to bedside". In *Colloquium Series on Integrated Systems Physiology: From Molecule to Function*, volume 2, pages 1–157. Morgan & Claypool Life Sciences, (2010).

[372] Johannes M Froehlich, Michael A Patak, Constantin von Weymarn, Christoph F Juli, Christoph L Zollikofer et Klaus-Ulrich Wentz, "Small bowel motility assessment with magnetic resonance imaging", *Journal of Magnetic Resonance Imaging* 21(4), 370–375 (2005).

[373] Jonas Cremer, Igor Segota, Chih-yu Yang, Markus Arnoldini, John T Sauls, Zhongge Zhang, Edgar Gutierrez, Alex Groisman et Terence Hwa, "Effect of flow and peristaltic mixing on bacterial growth in a gut-like channel", *Proceedings of the National Academy of Sciences* page 201601306 (2016).

[374] M Tlalka, SC Watkinson, PR Darrah et MD Fricker, "Continuous imaging of amino-acid translocation in intact mycelia of Phanerochaete velutina reveals rapid, pulsatile fluxes", *New Phytologist* 153(1), 173–184 (2002).

[375] P. A. Stewart et B. T. Stewart, "Protoplasmic movement in slime mold plasmodia: The diffusion drag force hypothesis", *Exp. Cell Res.* 17, 44 (1959).

[376] Sophie Marbach, Karen Alim, Natalie Andrew, Anne Pringle et Michael P Brenner, "Pruning to increase Taylor dispersion in Physarum polycephalum networks", *Physical review letters* 117(17), 178103 .

[377] P Girard, J Prost et P Bassereau, "Passive or active fluctuations in membranes containing proteins", *Physical review letters* 94(8), 088102 (2005).

[378] Pauline Simonnin, Benoit Noetinger, Carlos Nieto Draghi, Virginie Marry et Benjamin Rotenberg, "Diffusion under confinement: hydrodynamic finite-size effects in simulation", *Journal of Chemical Theory and Computation* (2017).

[379] Arnold J Storm, Cornelis Storm, Jianghua Chen, Henny Zandbergen, Jean-Francois Joanny et Cees Dekker, "Fast DNA translocation through a solid-state nanopore", *Nano letters* 5(7), 1193–1197 (2005).

[380] Stefan W Kowalczyk, David B Wells, Aleksei Aksimentiev et Cees Dekker, "Slowing down DNA translocation through a nanopore in lithium chloride", *Nano letters* 12(2), 1038–1044 (2012).

[381] Ulrich F Keyser, "Controlling molecular transport through nanopores", *Journal of The Royal Society Interface* page rsif20110222 (2011).

[382] Lorenz J Steinbock, Roman D Bulushev, Swati Krishnan, Camille Raillon et Aleksandra Radenovic, "DNA translocation through low-noise glass nanopores", *Acs Nano* 7(12), 11255–11262 (2013).

[383] Ke Liu, Jiandong Feng, Andras Kis et Aleksandra Radenovic, "Atomically thin molybdenum disulfide nanopores with high sensitivity for DNA translocation", *ACS nano* 8(3), 2504–2511 (2014).

[384] Grégory F Schneider, Stefan W Kowalczyk, Victor E Calado, Grégory Pandraud, Henny W Zandbergen, Lieven MK Vandersypen et Cees Dekker, "DNA translocation through graphene nanopores", *Nano letters* 10(8), 3163–3167 (2010).

[385] Jeroen Rodenburg, Marjolein Dijkstra et René van Roij, "Van't Hoff's law for active suspensions: the role of the solvent chemical potential", *Soft matter* 13(47), 8957–8963 (2017).

[386] Thomas W Lion et Rosalind J Allen, "Osmosis with active solutes", *EPL (Europhysics Letters)* 106(3), 34003 (2014).

[387] Alexandre P Solon, Joakim Stenhammar, Michael E Cates, Yariv Kafri et Julien Tailleur, "Generalized thermodynamics of phase equilibria in scalar active matter", *Physical Review E* 97(2), 020602 (2018).

[388] Alexandre P Solon, Y Fily, Aparna Baskaran, Mickael E Cates, Y Kafri, M Kardar et J Tailleur, "Pressure is not a state function for generic active fluids", *Nature Physics* 11(8), 673 (2015).

[389] JL Talen et AJ Staverman, "Osmometry with membranes permeable to solvent and solute", *Transactions of the Faraday Society* 61, 2794–2799 (1965).

[390] JL Talen et AJ Staverman, "Negative reflection coefficients", *Transactions of the Faraday Society* 61, 2800–2804 (1965).

[391] C Lee, C Cottin-Bizonne, A-L Biance, P Joseph, L Bocquet et C Ybert, "Osmotic flow through fully permeable nanochannels", *Physical review letters* 112(24), 244501 (2014).

[392] C Lee, C Cottin-Bizonne, R Fulcrand, L Joly et C Ybert, "Nanoscale dynamics versus surface interactions: What dictates osmotic transport?", *The journal of physical chemistry letters* 8(2), 478–483 (2017).

[393] Gerald S Manning, "Binary Diffusion and Bulk Flow through a Potential-Energy Profile: A Kinetic Basis for the Thermodynamic Equations of Flow through Membranes", *The Journal of Chemical Physics* 49(6), 2668–2675 (1968).

[394] Armand Ajdari et Lydéric Bocquet, "Giant amplification of interfacially driven transport by hydrodynamic slip: Diffusio-osmosis and beyond", *Physical review letters* 96(18), 186102 (2006).

[395] O Kedem et A Katchalsky, "Permeability of composite membranes. Part 2.—Parallel elements", *Transactions of the Faraday Society* 59, 1931–1940 (1963).

[396] O Kedem et A Katchalsky, "Permeability of composite membranes. Part 3.—Series array of elements", *Transactions of the Faraday Society* 59, 1941–1953 (1963).

[397] John L Anderson et Dermot M Malone, "Mechanism of osmotic flow in porous membranes", *Biophysical journal* 14(12), 957–982 (1974).

[398] Sophie Marbach, Hiroaki Yoshida et Lydéric Bocquet, "Osmotic and diffusio-osmotic flow generation at high solute concentration. I. Mechanical approaches", *The Journal of Chemical Physics* 146(19), 194701 (2017).

[399] Petrus Josephus Wilhelmus Debye, PP Debye, BH Eckstein, WH Barber et GJ Arquette, *Equilibrium and sedimentation of uncharged particles in inhomogeneous electric fields*, Academic Press (1954).

[400] Eugene Grim et Karl Sollner, "The contributions of normal and anomalous osmosis to the osmotic effects arising across charged membranes with solutions of electrolytes", *The Journal of general physiology* 40(6), 887–899 (1957).

[401] Clara B Picallo, Simon Gravelle, Laurent Joly, Elisabeth Charlaix et Lydéric Bocquet, "Nanofluidic osmotic diodes: Theory and molecular dynamics simulations", *Physical review letters* 111(24), 244501 (2013).

[402] Hiroaki Yoshida, Sophie Marbach et Lydéric Bocquet, "Osmotic and diffusio-osmotic flow generation at high solute concentration. II. Molecular dynamics simulations", *The Journal of Chemical Physics* 146(19), 194702 (2017).

[403] Eli Ruckenstein, "Can phoretic motions be treated as interfacial tension gradient driven phenomena?", *Journal of Colloid and Interface Science* 83(1), 77–81 (1981).

[404] John L Anderson, "Colloid transport by interfacial forces", *Annual review of fluid mechanics* 21(1), 61–99 (1989).

[405] Benjamin Abécassis, C Cottin-Bizonne, C Ybert, A Ajdari et L Bocquet, "Boosting migration of large particles by solute contrasts", *Nature materials* 7(10), 785 (2008).

[406] Vinita Yadav, Hua Zhang, Ryan Pavlick et Ayusman Sen, "Triggered "on/off" micropumps and colloidal photodiode", *Journal of the American Chemical Society* 134(38), 15688–15691 (2012).

[407] Sangwoo Shin, Eujin Um, Benedikt Sabass, Jesse T Ault, Mohammad Rahimi, Patrick B Warren et Howard A Stone, "Size-dependent control of colloid transport via solute gradients in dead-end channels", *Proceedings of the National Academy of Sciences* 113(2), 257–261 (2016).

[408] Nan Shi, Rodrigo Nery-Azevedo, Amr I Abdel-Fattah et Todd M Squires, "Diffusiophoretic focusing of suspended colloids", *Physical review letters* 117(25), 258001 (2016).

[409] Tom Chou, "Kinetics and thermodynamics across single-file pores: solute permeability and rectified osmosis", *The Journal of Chemical Physics* 110(1), 606–615 (1999).

[410] Charles Linder et Ora Kedem, "Asymmetric ion exchange mosaic membranes with unique selectivity", *Journal of Membrane Science* 181(1), 39–56 (2001).

[411] Pavel Y Apel, Irina V Blonskaya, Nikolay E Lizunov, Katarzyna Olejniczak, Oleg L Orelovitch, María E Toimil-Molares et Christina Trautmann, "Osmotic Effects in Track-Etched Nanopores", *Small* (2018).

[412] George Eisenman et Richard Horn, "Ionic selectivity revisited: the role of kinetic and equilibrium processes in ion permeation through channels", *The Journal of membrane biology* 76(3), 197–225 (1983).

[413] P Läuger, W Stephan et E Frehland, "Fluctuations of barrier structure in ionic channels", *Biochimica et Biophysica Acta (BBA)-Biomembranes* 602(1), 167–180 (1980).

[414] H Schröder, "Rate theoretical analysis of ion transport in membrane channels with elastically bound ligands", *The Journal of chemical physics* 79(4), 1997–2005 (1983).

[415] Jean-Louis Barrat et Jean-Pierre Hansen, *Basic concepts for simple and complex liquids*, Cambridge University Press (2003).

[416] Ludmila V Schagina, AE Grinfeldt et AA Lev, "Interaction of cation fluxes in gramicidin A channels in lipid bilayer membranes", *Nature* 273(5659), 243 (1978).

[417] FJ Sigworth. "Fluctuations in the current through open ach-receptor channels". In *BIOPHYSICAL JOURNAL*, volume 37, pages A309–A309. BIOPHYSICAL SOCIETY 9650 ROCKVILLE PIKE, BETHESDA, MD 20814-3998, (1982).

[418] Aleksandar Donev, John B Bell, Anton De la Fuente et Alejandro L Garcia, "Enhancement of diffusive transport by non-equilibrium thermal fluctuations", *Journal of Statistical Mechanics: Theory and Experiment* 2011(06), P06014 (2011).

[419] Rep Kubo, "The fluctuation-dissipation theorem", *Reports on progress in physics* 29(1), 255 (1966).

[420] BA Wallace, "Common structural features in gramicidin and other ion channels", *Bioessays* 22(3), 227–234 (2000).

[421] Devaki A Kelkar et Amitabha Chattopadhyay, "The gramicidin ion channel: a model membrane protein", *Biochimica et Biophysica Acta (BBA)-Biomembranes* 1768(9), 2011–2025 (2007).

[422] Alan Finkelstein et Olaf Sparre Andersen, "The gramicidin A channel: a review of its permeability characteristics with special reference to the single-file aspect of transport", *The Journal of membrane biology* 59(3), 155–171 (1981).

[423] Peter Läuger, "Mechanisms of biological ion transport—carriers, channels, and pumps in artificial lipid membranes", *Angewandte Chemie International Edition* 24(11), 905–923 (1985).

[424] RP Swenson Jr et CM Armstrong, "K+ channels close more slowly in the presence of external K+ and Rb+", *Nature* 291(5814), 427 (1981).

[425] Al L Hodgkin et RD Keynes, "The potassium permeability of a giant nerve fibre", *The Journal of Physiology* 128(1), 61–88 (1955).

[426] AL Hodgkin et RD Keynes, "Active transport of cations in giant axons from Sepia and Loligo", *The Journal of physiology* 128(1), 28–60 (1955).

[427] PAUL A Rosenberg et ALAN Finkelstein, "Interaction of ions and water in gramicidin A channels: streaming potentials across lipid bilayer membranes.", *The Journal of general physiology* 72(3), 327–340 (1978).

[428] Bertrand Coste, Bailong Xiao, Jose S Santos, Ruhma Syeda, Jörg Grandl, Kathryn S Spencer, Sung Eun Kim, Manuela Schmidt, Jayanti Mathur, Adrienne E Dubin et al., "Piezo proteins are pore-forming subunits of mechanically activated channels", *Nature* 483(7388), 176 (2012).

[429] Jason Wu, Amanda H Lewis et Jörg Grandl, "Touch, tension, and transduction–the function and regulation of Piezo ion channels", *Trends in biochemical sciences* 42(1), 57–71 (2017).

[430] Laetitia Jubin, Anthony Poggioli, Alessandro Siria et Lydéric Bocquet, "Dramatic pressure-sensitive ion conduction in conical nanopores", *Proceedings of the National Academy of Sciences* page 201721987 (2018).

[431] A Sellier, "Stokes flow about a slip arbitrary-shaped particle", *Computer Modeling in Engineering & Sciences(CMES)* 87(2), 157–176 (2012).

[432] F. Hecht, "New development in FreeFem++", *J. Numer. Math.* 20(3-4), 251–265 (2012).

[433] Richard Courant, Eugene Isaacson et Mina Rees, "On the solution of nonlinear hyperbolic differential equations by finite differences", *Communications on Pure and Applied Mathematics* 5(3), 243–255 (1952).

[434] François Detcheverry et Lydéric Bocquet, "Thermal fluctuations of hydrodynamic flows in nanochannels", *Physical Review E* 88(1), 012106 (2013).

Résumé

La filtration de molécules est un enjeu vital dans les domaines biomédicaux tels que la dialyse jusqu'à la production à grande échelle d'eau potable. Dans les dernières décennies, des matériaux nanoporeux ont permis des avancées significatives, mais s'appuient toujours sur une géométrie de type "passoire" où une membrane avec de petits trous permet la sélection des molécules cibles. Ceci entraîne notamment une diminution du transport à travers ces trous, et rend les procédés de séparation coûteux en énergie.
Ici je développe plusieurs approches innovantes pour la filtration, inspirées par des filtres biologiques (les reins humains, les aquaporines). Je définis de nouveaux concepts pour la séparation, en m'appuyant sur des modèles simples. J'explore notamment des arrangements topologiques différents mais aussi l'idée d'une passoire active, où la taille des trous peut par exemple varier dans le temps. Tous ces principes pourraient être implémentés à partir d'éléments existants et fournir des alternatives pour la dialyse ou le recyclage des eaux usées.
Ces recherches amènent aussi des questions fondamentales originales en physique. En particulier, des grandeurs définies traditionnellement à l'équilibre comme la pression osmotique ou la perméabilité d'un pore ne sont pas bien définies quand le pore a des propriétés qui dépendent du temps. Pour autant, on imagine aisément qu'il est possible d'étendre ces concepts hors d'équilibre, et que cela aura de nombreuses conséquences pour la filtration, et même le pompage ionique.

Mots Clés

Nanofluidique – Osmose

Abstract

Filtering specific molecules is a challenge faced for several vital needs: from biomedical applications like dialysis to the intensive production of clean water. The domain has been boosted over the last decades by the possibilities offered by nanoscale materials. Filtration is however always designed according to a sieving perspective: a membrane with small and properly decorated pores allows for the selection of the targeted molecules. This inevitably impedes the flux and transport, making separation processes costly in terms of energy.
Here I investigate several innovative approaches to separation and filtration. I draw inspiration from biological systems (the human kidney, biological channels like aquaporins) and rationalize some new concepts for sieving, based on simple models. These approaches rely on different alternative strategies: either exploring new topologies or the idea of active sieving, with dynamically responsive channels and pores. All these principles could be readily mimicked using existing technologies to build artificial dialysis devices or alternatives for advanced water recycling.
In a broader perspective, these approaches open fundamental questions in the fields of statistical physics and fluid dynamics. In particular, traditional in equilibrium quantities like osmotic pressure and permeability are not defined when the pore has an active component, yet one easily imagines that such concepts could be extended to these out-of-equilibrium situations. This has numerous consequences on filtration and desalination, but also on ionic pumping and sorting.

Keywords

Nanofluidics – Osmosis